POLITECNICO DI TORINO

SCUOLA DI DOTTORATO

Dottorato in Elettronica e Comunicazioni - XXVI ciclo

Tesi di Dottorato

Power Management, Attitude Determination and Control Systems of Small Satellites

Anwar Ali

Tutore
Prof. Leonardo M. Reyneri

Coordinatore del corso di dottorato
Prof. Ivo Montrosset

February 2014

DEDICATED

To

My late father

Who taught me to trust in Allah and believe in myself

Acknowledgements

I will start “In the name of Allah, the Beneficent, the Merciful”. I thank Allah for giving me the courage and the strength to fulfill my PhD thesis.

First of all, I would like to express my special appreciation and gratitude to my supervisor Professor Leonardo M. Reyneri, for providing me an opportunity to work in the AraMiS group. You have been a great teacher for me during these three years. I would like to thank you for encouraging my research and for the patience you had in helping me. Your advice on both research as well as on my career have been priceless. I would also like to thank the whole AraMiS team at Politecnico di Torino for their help during these three years, in particular Prof. Claudio Sansoè and Prof. Dante Del Corso. Special thanks to Alberto Vallan for his help and supervision during thermal measurements. I should be thankful to Danilo Roascio and Juan Carlos de Los Rios for their help in learning different tools and laboratory machines.

I would especially like to thank my PhD colleagues, Haider Ali and Muhammad Rizwan Mughal for their continuous support to strive towards my goal. Their company made these three years really pleasant and enjoyable here at Politecnico.

Last but not least, I am very thankful to my family and especially my wife and sweet daughter who spent these three years in Pakistan without me. Their prayers and sacrifices for me was what sustained me thus far.

Torino, February 10th, 2014

Anwar Ali

Summary

Satellites have always been considered to be extremely expensive and risky business, which not only requires extensive knowledge and expertise in this field but also huge budget. Primarily, this concept was based on initial development and launching cost. Secondly, it was also impossible to repair and substitute parts (this was true up to 1993: the first Hubble Space Telescope servicing mission), which makes design more tough because it requires advanced fault tolerance solutions and extreme reliability. But with the passage of time many space actors entered in this market. Low cost design techniques played an important role in the aerospace market growth in the past years, but they can still play a major part in future developments. At present, several private companies are also providing launch services which further lower the accumulative cost. Many universities and SMEs (Small Medium Enterprises) worldwide are also trying to reduce satellite costs. The Department of Electronics and Telecommunication (DET) at Politecnico di Torino has been working on NanoSatellites since 2002 and developed their first NanoSatellite called PiCPoT, which was intended to be launched together with other university satellites by a DNEPR LV rocket in July 2006. Unfortunately a problem in the first stage of the carrier led to the destruction of all satellites. After that DET started work on a comprehensive NanoSatellite project called AraMiS (Italian acronym for Modular Architecture of Satellites). The main idea of the AraMiS is modularity at mechanical, electronic and testing levels using Commercial-Off-The-Shelf (COTS) components. These modules can be assembled together to get the targeted mission, which allows an effective cost sharing between multiple missions. AraMiS satellites have mass up to 5kg with different shapes and dimensions. AraMiS-C1 is a CubeSat Standard satellite developed on the AraMiS approach. Four sides of the AraMiS-C1 are equipped with identical tiles called 1B8_CubePMT that mount solar panels on the exterior and a combined power management, attitude control and computing subsystem on the interior. The other two sides are devoted to the telecommunication tiles called 1B9_CubeTCT which carry a commercial deployable UHF antenna (one side) and a patch type SHF antenna (the other side).

Thesis discusses in detail the design, implementation and testing of the 1B8_CubePMT module. It is developed on the design approach of AraMiS architecture with dimension $98\times82.5\times1.6\ mm^3$. 1B8_CubePMT module contains electric power supply (EPS) and attitude determination & control subsystems (ADCS) of AraMiS-C1 satellite. The integration of such a large number of systems in a small area was not a trivial job. Several techniques were employed for reduction of size, weight and power consumption of the different subsystems while still achieving best performances. COTS components were selected for the EPS subsystems, on the basis of power loss analysis and minimum dimensions which helped in efficiency enhancement and also miniaturization of the subsystems. ADCS subsystems components were also selected on the basis of minimum dimensions and lower power consumptions while still achieving targeted performances. The most interesting feature of the 1B8_CubePMT module is the design and integration of a reconfigurable magnetorquer coil within four internal layers occupying no excess space. Coils in each layer are treated separately and can be attached/detached through straps. Changing the arrangement of these straps make the magnetorquer reconfigurable. Different housekeeping sensors have been employed at various points of the 1B8_CubePMT module.

Thesis also discusses thermal modeling of CubeSat, AraMiS-C1 satellite and 1B8_CubePMT module. Thermal resistance and temperature differences between different sides of the satellites

and individual tiles have been found. At the end, preliminary thermal and spin analysis of NanoSatellites have been presented.

Chapter 1 gives an introduction to the problem and proposed solutions which will be discussed in this thesis. Chapter 2 presents an introduction to AraMiS project and AraMiS-C1 satellite. Chapter 3 discusses different satellite design flow configurations and their comparison.

Chapter 4 discusses 1B8_CubePMT module which is a CubeSat standard power management tile, developed on the AraMiS concept, for AraMiS-C1 satellite. It has EPS and ADCS subsystems which are the most essential elements of any aerospace mission.

Chapter 5 deals with the design and development of the EPS system of AraMiS-C1 satellite. This chapter discusses how to reduce the size, weight and power consumption of the EPS subsystems while achieving better efficiency and fulfilling satellite power requirements. The selection of COTS components on the basis of power loss analysis and minimum dimensions is discussed in detail. Housekeeping sensors such as current, voltage and temperature sensors which are employed at different points of the 1B8_CubePMT module to cope with anomalies, have been discussed in detail in this chapter. At the end of the chapter, the designed EPS is evaluated on the basis of AraMiS-C1 power budget.

Chapter 6 discusses design and implementation of attitude determination sensors (ADS) of the AraMiS-C1 satellite. 1B8_CubePMT has three types of attitude determination sensors: sun sensor, magnetometer and gyroscope. This chapter discusses in detail the design and operation of these sensors. Chapter 7 discusses the attitude control (ADC) system of AraMiS-C1 satellite. The design and implementation of a reconfigurable magnetorquer coil which is embedded inside the 1B8_CubePMT module, is discussed in detail. The designed magnetorquer has been evaluated on different parameters and compared with the magnetic actuator already available in the market. In chapter 8 testing procedure and results of 1B8_CubePMT subsystems are discussed in detail.

Chapter 9 presents thermal modelling of NanoSatellites. Detailed and simplified thermal models of CubeSat panel have been discussed. Thermal resistances measured through both models are compared. Generic thermal model of a CubeSat is presented. Utilizing the proposed models, thermal resistance of 1B8_CubePMT and AraMiS-C1 are measured. In order to verify the theoretical results, the thermal resistance of the AraMiS-C1 is measured through an experimental setup.

Chapter 10 discusses preliminary thermal and spin analysis of NanoSatellites in space environment. All the heat sources and their effects on the satellite have been discussed. A thermal balance equation has been established and satellite temperature for different structures and various conditions has been found. At the end a satellite spin analysis on the basis of different absorption coefficient related with colors, has been discussed.

CONTENTS

List of Acronyms

SMEs	Small Medium Enterprises
EPS	Electric Power Supply
ADCS	Attitude Determination & Control Subsystems
COTS	Commercial-Off-The-Shelf
CubePMT	CubeSat Power Management Panel
CubeTCT	CubeSat Tele-Communication Tile
DET	Department of Electronics & Telecommunication
LEO	Low Earth Orbit
POD	Pico-satellite Orbital Deployer
OBC	On-Board Computer
PMTs	Power Management Tiles
PDB	Power Distribution Bus
OBDH	On-board Data Handling
UCS	Unified Clock System
VLO	Very-Low-power low-frequency Oscillator
REFO	Low Frequency Oscillator
DCO	Digitally Controlled Oscillator
FLL	Frequency Locked Loop
ACLK	Auxiliary clock
MCLK	Main clock
SMCLK	Sub-Main clock
ADC	Analog to Digital Converter
USCI	Universal Serial Communication Interface
MPP	Maximum Power Point

MPPT	Maximum Power Point Tracker
OV	Open Voltage
P&O	Perturb and Observe
IC	Incremental Conductance
SC	Short Current pulse
CV	Constant Voltage
ESR	Equivalent Series Resistance
RMS	Root Mean Square
ESL	Equivalent Series Inductance
ADS	Attitude Determination System
ACS	Attitude Control System
AMR	Anisotropic Magneto Resistance
FG	Fluxgates
GMR	Giant Magneto Resistance
MI	Magneto Impedance
TMR	Tunnel Magneto Resistance
SDT	Spin Dependent Tunnel)
SPI	Serial Peripheral Interface
PCB	Printed Circuit Board

Chapter 1

Introduction

The market of NanoSatellite is on continuous rise due to its low cost space missions. The main reason is the availability of COTS components and already developed subsystems in the market. Universities and SMEs (Small Medium Enterprises) are also attracted by the low cost to build up their own satellites. In this regard the first real NanoSatellite is CubeSat, developed by California Polytechnic State University in collaboration with Stanford University. Dimensions of 1U CubeSat are $10\times10\times10$ cm^3 with weight up to 1.33kg [1]. Department of Electronic & Telecommunication (DET) at Politecnico di Torino also developed their first NanoSatellite called PiCPoT [2], which was intended to be launched together with other university satellites by a DNEPR LV rocket in July 2006. Unfortunately a problem in the first stage of the carrier led to destruction of all satellites. After that DET started work on another project called AraMiS [3]. The feature of AraMiS design approach is its modularity and scalability. These modules can be reused for multiple missions which helps in significant reduction of the overall budget, development and testing time. One has just to reassemble the required subsystems to achieve the targeted specific mission. COTS components have been used for AraMiS project implementation which are low cost and easily available from the market. The target environment for AraMiS satellites is the Low Earth Orbit (LEO) with an expected operation life of 5 years. AraMiS provides low-cost and higher performance space missions with dimensions equal to or larger than CubeSats.

The design process of AraMiS is based on tiles. Tiles or panel bodies are printed circuit board with solar panel on exterior side and other electronic subsystems on interior side. 1B8_CubePMT is the power management, attitude determination and control tile developed for AraMiS-C1 and other NanoSatellites of CubeSat standard. AraMiS-C1 is a CubeSat standard NanoSatellite developed on the AraMiS project design approach. Four sides of the AraMiS-C1 are equipped with 1B8_CubePMT modules. The remaining two sides are devoted to the telecommunication tiles called 1B9_CubeTCT modules. 1B9_CubeTCT has RF frontend and carry a commercial deployable UHF antenna (one side) and a patch type SHF antenna (the other side). Inside the satellite there is room for batteries and payload boards.

1B8_CubePMT is developed on a single eight layers PCB with dimensions $98.0\times82.5\times1.6$ mm3. It has EPS and ADCS subsystems of AraMiS-C1. The top side (layer-1) has two solar cells and sun sensor while the bottom side (layer-8) contains all the electronic subsystems. EPS includes solar panel, boost converter, load switches and different linear and switching regulators. ADCS consists of magnetometer, gyroscope, magnetorquer coil, sun detector, housekeeping sensors and different connectors. A commercial microcontroller MSP430 from Texas Instruments performs power management, data processing and various control operations. Magnetorquer coil with 200 turns, is integrated inside the 1B8_CubePMT four internal layers (layer 2, 3, 4 & 5). Layer-6 has the ground plan while layer-7 contains partial ground plans and some PCB traces to connect the components in layer-8.

1.1 Problem Statement

The main goal of the thesis is the design and implementation of EPS and ADCS subsystems on a single CubeSat dimension tile called 1B8_CubePMT. Reducing the weight, cost, power consumption and space occupation of the subsystems in such a way to maintain the system performance and operation in safe margins. EPS should meet the power requirement while ADCS should fulfill orientation and stabilization requirements of AraMiS-C1.

The second goal of the thesis is to present generalized thermal models of CubeSat tiles in general and particularly the power management tile and CubeSat standard NanoSatellites. Applying the proposed models to the 1B8_CubePMT module and AraMiS-C1 satellite and measure their thermal resistances. Also perform thermal and spin analysis of a small satellite in space environment.

1.2 Proposed Solutions

1B8_CubePMT is developed on the design approach of AraMiS project. The main feature of the AraMiS design is the scalability and modularity of all the subsystems. These are the two most important characteristics this innovative architecture possess. The most efficient way to reduce the cost of a NanoSatellite missions is to reduce design and non-recurrent fabrication costs as much as possible, which usually accounts for more than half of the overall budget. Design and non-recurrent fabrication costs reduction is possible by sharing the design among multiple missions. Design reuse is the main feature of the AraMiS project, that is, to have a modular architecture based on a small number of modules which can be reused in multiple missions.

COTS components have been used for 1B8_CubePMT implementation which is the second main feature of AraMiS project. COTS components were selected on the basis of minimum dimensions, less weight and lower price. Efficiency enhancement of the EPS system was achieved by using different COTS components and selecting the best one on the basis of power loss analysis and minimum dimensions. COTS components greatly help in reducing mission cost but they required proper safety margins to be considered during design to allow safe operations in the harsh space environment.

For miniaturization and weight reduction purposes, a reconfigurable magnetorquer coil has been designed and integrated in four internal layers of the 1B8_CubePMT module. Magnetorquer coil is a better choice for attitude control and stabilization of NanoSatellites. Magnetorquer coil has small dimensions, weight and low heat dissipation. The designed magnetorquer coil is reconfigurable and integrated within the PCB internal layers occupying no excess space on 1B8_CubePMT module.

From thermal modeling, theoretical values of thermal resistances of 1B8_CubePMT and AraMiS-C1 satellite were found. In order to verify these theoretical results, practical values of the thermal resistances were measured inside the vacuum chamber available in the laboratory.

1.3 Thesis Organization

This thesis will deal with the design and development of EPS and ADCS subsystems of AraMiS-C1 satellite on a single CubeSat standard module. The integration of such a large number of systems on a single tile was not a trivial job. Several techniques were employed for reduction of size, weight and power consumption while still achieving best performances. COTS components were used for 1B8_CubePMT systems implementation. COTS for EPS subsystems were selected on the basis of power loss analysis which helped in efficiency enhancement and also miniaturization of the subsystems. ADCS subsystems components were also selected on the basis of minimum dimensions and lower power consumptions while still achieving targeted performances. A reconfigurable magnetorquer coil has been designed and implemented inside four internal layers of the 1B8_CubePMT module. In order to cope with the anomalies of the 1B8_CubePMT subsystems different housekeeping sensors have been employed at various points of the tile. Thesis also discusses thermal modeling and thermal analysis of small satellites.

Chapter 2 presents an introduction to AraMiS project and AraMiS-C1 satellite. Chapter 3 discusses different satellite design flow configurations.

Chapter 4 discusses 1B8_CubePMT module. 1B8_CubePMT is the CubeSat standard power management tile developed for AraMiS-C1 and other NanoSatellites of CubeSat standard. It has EPS and ADCS which are the most essential elements of any aerospace mission.

Chapter 5 deals with the design and development of the electric power supply (EPS) system of AraMiS-C1 satellite. This chapter discusses how to reduce the size and weight of the EPS subsystems while achieving better efficiency and fulfilling satellite power requirements. The selection of COTS components on the basis of power loss analysis and minimum dimensions is discussed in detail. Housekeeping sensors are employed at different points of the 1B8_CubePMT module to cope with anomalies. At the end of the chapter, designed EPS is evaluated on the basis of AraMiS-C1 power budget.

Chapter 6 discusses design and implementation of ADS of AraMiS-C1 satellite. 1B8_CubePMT has three types of attitude determination sensors: sun sensor, magnetometer and gyroscope. This chapter discusses in detail the design and operation of these sensors. Chapter 7 discusses the ADC system of AraMiS-C1 satellite. The design and implementation of a reconfigurable magnetorquer coil which is embedded inside the 1B8_CubePMT module, is discussed in detail. The designed magnetorquer has been evaluated on different parameters and discussed with the magnetic actuator already available in the market. In chapter 8 testing procedure and results of 1B8_CubePMT subsystems are discussed in detail.

Chapter 9 presents thermal modelling of NanoSatellites. Detailed and simplified thermal models of CubeSat panel have been discussed. Thermal resistances measured through both models are compared and the results are in close agreement. Generic thermal model of a CubeSat is also presented. Utilizing the proposed models, thermal resistance of 1B8_CubePMT and AraMiS-C1 are measured. In order to verify the theoretical results, the thermal resistance of the AraMiS-C1 is measured through an experimental setup. Chapter 10 discusses preliminary thermal and spin analysis of NanoSatellites in space environment. All the heat sources and their effect on the satellite have been discussed. A thermal balance equation has been found and satellite temperature for different structures and various conditions has been found. At the end a satellite spin analysis on the basis of different absorption coefficient related with color has been discussed.

Chapter 2

Introduction to Small Satellites

Small satellites market has considerably grown over the last decade. This has been made possible due to the availability of low cost launch vectors. This cost reduction has made it feasible for universities and small industries to enter the satellite market. In 2001, Professor Robert Twiggs at Stanford University, USA, in collaboration with Professor Jordi Puig-Suari at California Polytechnic State University, have defined and implemented the standard for small satellite called CubeSat [4-5]. CubeSat identifies the standard for small satellite with dimensions $10\times10\times10$ cm^3 and a maximum mass of 1.33 kg, having a structure adapted to the launcher POD (Pico-satellite Orbital Deployer). Another feature of CubeSat is the use of low-cost commercial components (COTS: Commercial Off -The-Shelf). These features greatly help in the reduction of cost and development time. In addition, the weight reduction allows the use of less expensive launchers. Satellites based on CubeSat standard have made it possible for potential clients to buy and assemble their own satellites. This (CubeSat) standard laid the foundation for several projects of NanoSatellites by many universities and SMEs worldwide. Different universities across Europe such as University of Wurzburg in Germany, the Norwegian University of Science and Technology and Italian universities including; the University of Rome La Sapienza , the University of Trieste and Politecnico di Torino.

Practically, any artificial satellite of low mass and low volume can be considered as a small satellite. However, the definition can be extended to any system designed with the small satellite philosophy. This may include features such as commercial off the shelf components, modular systems, less redundancy, open sourcing, incremental missions, etc.

Small satellites are encouraging spacecrafts to test and try novel methods and technologies (E.g. open source hardware and software, formation flying), which might not be under the purview of large scale satellites This remains the reasons as to why small satellites have been considered a disruptive technology by numerous space mission experts. Small satellite programs are particularly attractive since they are "affordable". There shall be no surprises in the near future, if more and more developing countries, groups from the academic world or even small teams of space enthusiasts develop their own space mission based on small satellites. The small satellite platform is catering to new actors such as developing countries, students and amateurs.

2.1 PiCPoT

The Department of Electronics & Telecommunication Engineering, in collaboration with the Department of Aerospace Engineering at Politecnico di Torino started work on the PICPOT (Small Cube of Politecnico di Torino) project in January 2004. The major objective of the project was to design, implement and launch experimental satellite into LEO with the aim of:

- Training and educating the students, therefore PiCPoT was primarily developed by students cooperation.

- Check the operation and reliability of COTS components in space
- Acquire and transmit to Earth Station several images and measurements carried into orbit by the onboard sensors
- Taking Earth's surface images
- Encouraging and creating interdisciplinary activities to enhance the interaction and coordination of various departments, faculty members, PhD students and other students of the Politecnico.

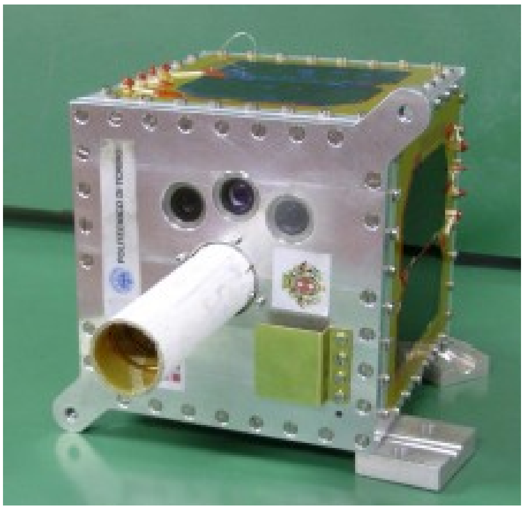

Figure 2.1: Photograph of PiCPoT satellite

PICPOT is a satellite of cubic structure with dimensions 13×13× 13cm^3 and a mass of 2.5 kg. The six external faces are made of aluminum alloy type 5000 AlMn. Photograph of PiCPoT is shown in figure 2.1. Solar panels are mounted on the five external faces which provide power to the PiCPoT. The sixth face have test connector and three cameras. There are two antennas (for 437 MHz and 2.4 GHz) which are used to communicate with the ground station. PiCPoT also contain two Kill-Switches which can guarantee the absence of power until the satellite is not completely detached from the launcher. The interior of the satellite houses two types of batteries (NiCd and NiMh) to power the satellite in the absence of the solar power. The satellite have the following electronic circuit boards:

- **Power Supply:** recharge the batteries by converting incoming voltage from the solar panels and also maintain the temperature of the satellite.
- **Power Switch:** converts the battery voltage to different voltage levels required by all the other subsystems onboard PiCPoT.
- **RxTx**: receives and transmits signals between the ground station and satellite via 437 MHz and 2.4 GHz channels that operate in half duplex mode.
- **ProcA and ProcB**: are the two on-board computer implemented on separate PCBs. They duplicate the same functions. These processors and boards are built with different technologies and different components that provide redundancy to avoid possible failure. They both also acquire telemetry data and communicate with Payload and RxTx. These

processors are not operated simultaneously for efficient utilization of the onboard available power.

- **Payload**: is responsible for acquiring earth images via onboard photo/video cameras. It also compress these images to JPEG and send them to the ProcA or ProcB, which manages their transmission to the ground.

2.2 AraMiS Project

AraMiS (Modular architecture for Satellites) is a project that wants to take further the CubeSat concept and create a true modular architecture. The design approach of AraMiS architecture is to provide low-cost and high performance space missions with dimensions larger than CubeSats. The feature of AraMiS design approach is modularity and scalability. These modules can be reused for multiple missions which helps in significant reduction of the overall budget, development and testing time. One has just to reassemble the required subsystems to achieve the targeted specific mission.

This architecture is intended for different satellite missions, from small systems weighing from 1kg to larger missions. Figure 2.2 depicts a number of configurations that show the potential capabilities of the proposed architecture. Modularity has been implemented in different ways. From the mechanical perspective, larger satellite structures can be conveniently realized by combining several small modular structures. The modularity concept has also been intended from electronic standpoint. Most of the internal subsystems are developed in such a manner they can be composed together to enhance performance. One such example is the power management subsystem. In conventional missions: to get maximum solar power, solar cells are mounted on all the available surfaces but their number can be different in various missions, thus requiring to re-design each time. This new modular approach makes use of a standard module, as can be seen in figure 2.2 which can be replicated many time to fit mission requirements [6].

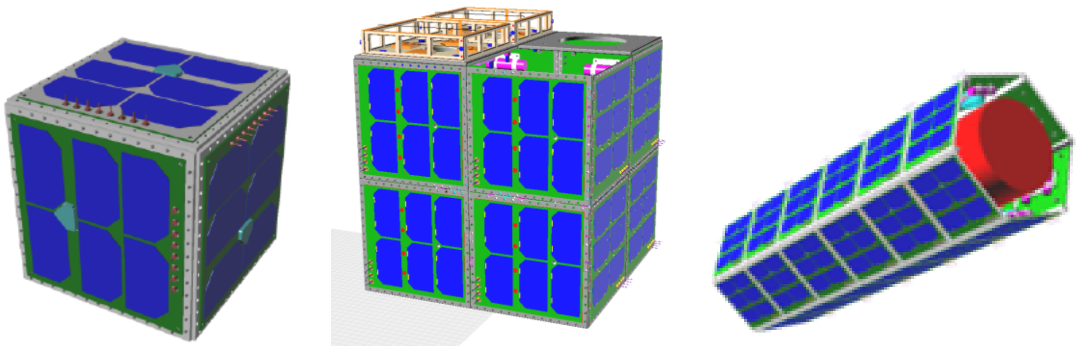

Figure 2.2: Different AraMiS satellites architecture

2.3 AraMiS Satellite Subsystems

The AraMiS satellites can achieve the desired flexibility level by combination of several subsystems together. The main subsystems of this architecture are:

- Mechanical
- Power management
- Attitude determination and control

- Telecommunication

2.3.1 Mechanical subsystem

The mechanical subsystem is the backbone of a satellite. It provides physical structure to the satellite and holds in place all the subsystem together and also protect them from environment conditions. The main material used for building the AraMiS structure is Aluminum, used in particular for its light weight. The structure skeletal is made by metallic square rods while the power management and telecommunication sub-systems are mounted on thin panels that are screwed to the rods. The power management tiles cover the satellite with solar panels mounted on the external face. The number of these tiles mainly depends on satellite size and power requirement. This provides a degree freedom to mission designers since size and generated power can be increased by simply adding more modules.
All the tiles are connected on the external faces of the satellite and the payload is mounted inside which can be altered by the mission requirement. Figure 2.3 shows the Aluminum frames of AraMiS structure.

Figure 2.3: AraMiS mechanical structures

2.3.2 Power management subsystem

The power management subsystem is responsible for generating, storing and delivering power to all the other satellite subsystems. It is one of the most critical subsystem as a failure here can lead to shutting down everything. Fault tolerance is an important parameter and most of the design solutions were selected for this reason.

Conventionally, power management is mission dependent which requires ad-hoc development for the specific needs. This tends to increase overall system cost and testing time. For this reason the AraMiS project uses modular power management system that can be adapted for various missions. Figure 2.4 shows different solar panels of AraMiS satellites.

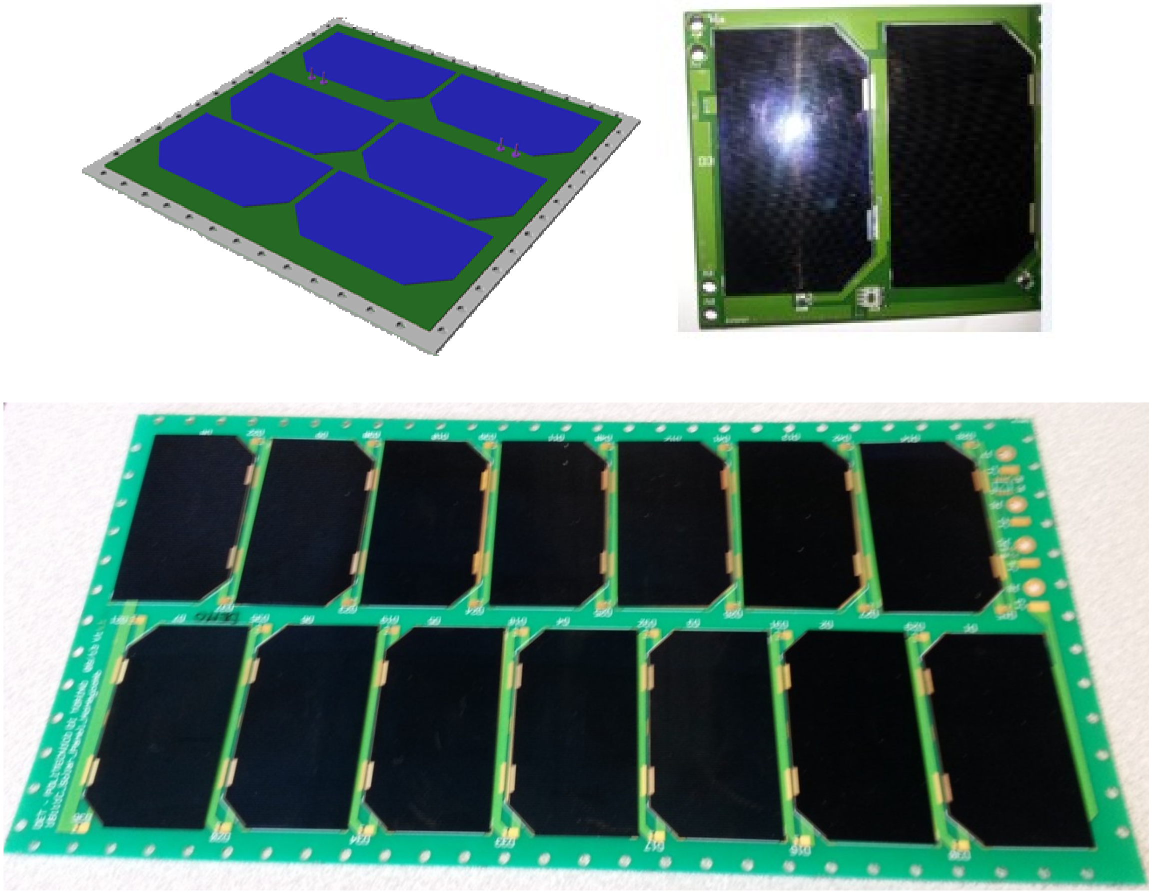

Figure 2.4: AraMiS solar panels

2.3.3 AraMiS Telecommunications Subsystem

The AraMiS telecommunications subsystem follows the modularity concept. There is a basic telecommunication tile that is provided in a standard AraMiS satellite. In case of special applications, dedicated tiles can be added to meet mission criteria. This module is used to receive command and control packets from the ground station and to send back telemetry and status information. The bandwidth needed to exchange this kind of information is usually low, so the RF link was designed for low speed and low power. The module has been designed using COTS components which were selected to achieve good fault tolerance level. There are two different frequency bands used for satellite and ground communication: the UHF 437MHz band and the SHF 2.4 GHz band. To reduce occupied bandwidth, both channels are implemented using half-duplex protocol, sharing the same frequency for downlink and uplink. AraMiS telecommunication module are shown in figure 2.5.

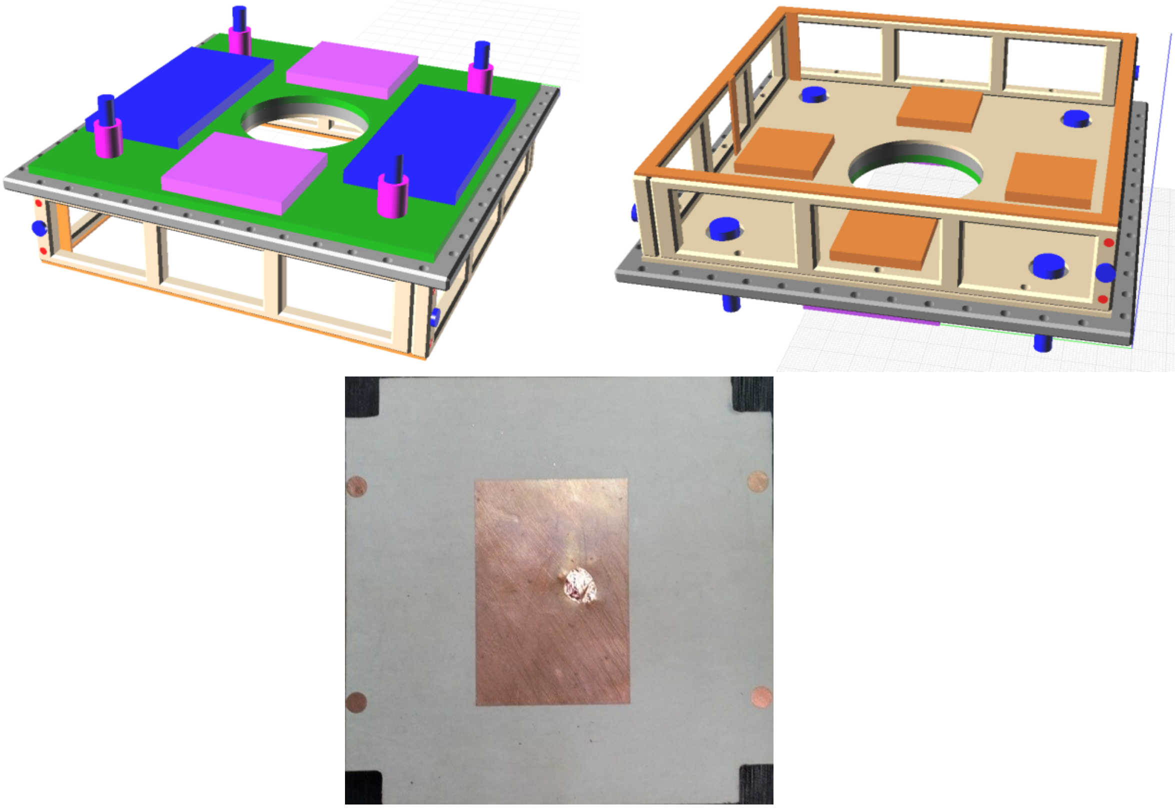

Figure 2.5: AraMiS telecommunication module

2.3.4 Tile Computer subsystem

Tile Computer (OBC) used in AraMiS satellites consist of redundant MSP430 microcontrollers and FPGAs, that are mainly responsible for overall satellite system management. Some of the key responsibilities perform by OBC includes:

- Creating and transmitting (by Transceiver board) Beacon packets,
- Decoding and executing commands,
- Executing attitude control algorithm,
- Storing housekeeping data,
- Controlling Payload sub-systems.

2.3.5 Attitude determination and control subsystem

This subsystem is mainly responsible for sensing and modifying satellite orientation for keeping the tile subsystems pointing at their targets. Attitude control can be performed in passive or active way: passive attitude control is usually achieved by mounting a permanent magnet in the satellite which acts as a compass in the Earth magnetic field. This system is extremely simple and consume no power. The main drawback is lack of spin control due to the variable Earth magnetic field. Active control is performed using controlled actuators that modify satellite attitude on OBC commands. In AraMiS, attitude control is automatically performed by the satellite using magnetorquer and reaction wheels.

For attitude determination, three types of attitude sensors are used: magnetic, spin and Sun sensors. These sensors consist of COTS components which were selected on the basis of small dimension, light weight and low power consumption while achieving better performances.

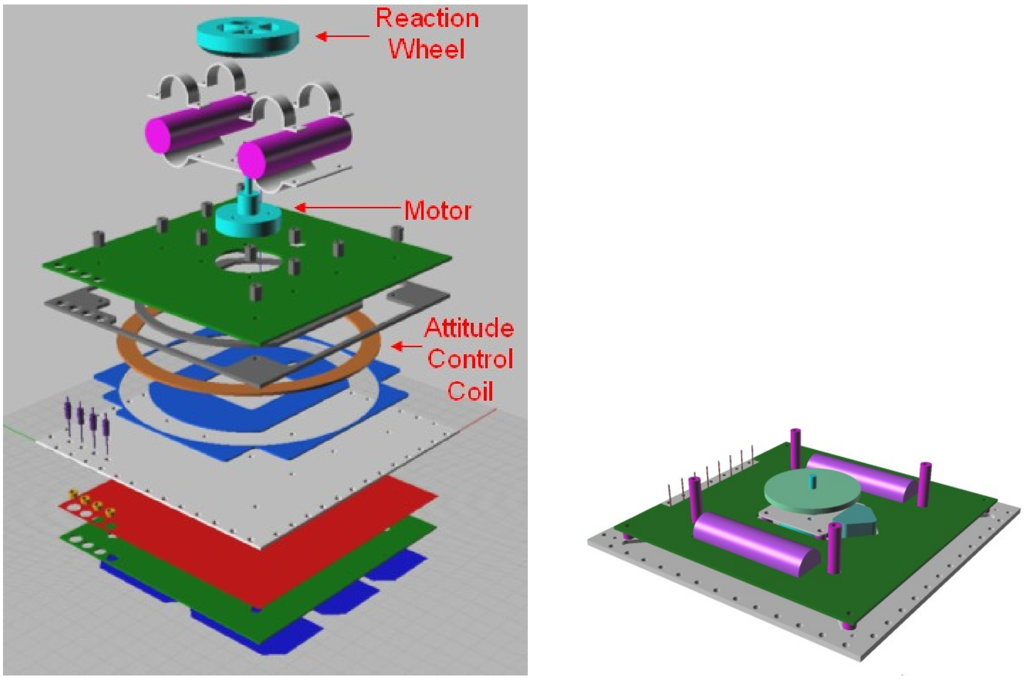

Figure 2.6: AraMiS ADCS modules

2.3.6 Payload

The payload is heavily mission dependent and the architecture was developed to allow high flexibility on it: the main requirements that the AraMiS architecture impose on the payload is its compatibility with the tile power distribution and data bus. Different payloads can be fitted in the various configurations but mechanical fixtures should be developed to connect them to the mechanical structure. A view of the payload inside AraMiS is shown in figure 2.7.

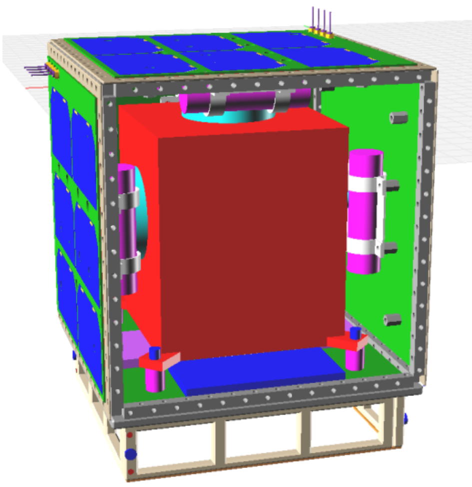

Figure 2.7: Payload inside AraMiS

2.4 AraMiS-C1

AraMiS-C1 is a 1U CubeSat standard NanoSatellite built as a demonstrator of the AraMiS modular architecture developed since 2007 at Politecnico di Torino. Four sides of the satellite are equipped with identical "tiles" that mount solar panels on the exterior and a combined power management, attitude control and computing subsystem on the interior. The other two sides are devoted to the telecommunication links and carry a commercial deployable UHF antenna (one side) and a patch type SHF antenna (the other side) on the exterior. Inside the satellite there is room for batteries and payload boards. Once deployed, the ISIS - Deployable Antenna System for CubeSats will release four antenna baffles. No drag augmenting device and no other deployable device (except antennas) is installed.

AraMiS-C1 is based on the modular architecture AraMiS, which is modular at electrical, mechanical and software level. In this architecture, major bus functionalities are split over a number of identical modules that are placed in a proper manner in each tile (integrated inside the same PCB), making the design, maintenance, manufacturing, testing and integration very simple. The modules interconnect and dynamically exchange data and power in a distributed and self configuring architecture, which is flexible because standardized interfaces between components are specified. Product variations can then take place substituting modular components without affecting the rest of the system. AraMiS-C1 is made by assembling a number of tiles developed at Politecnico di Torino, as detailed further, plus a few commercial off-the-shelf subsystems from ISIS's CubeSat shop. Photograph of 1U AraMiS-C1 with four 1B8_CubePMT and two communication tiles is shown in figure 2.8.

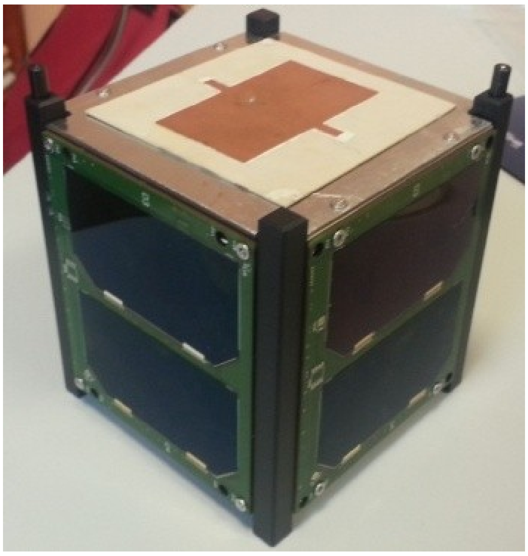

Figure 2.8: Photograph of AraMiS-C1

The AraMiS-C1 is designed to be functional over a period of two to three years on LEO in the 500 km range, but even lower orbits with higher atmospheric drag that will guarantee a few months in space are acceptable for our purposes. Obviously longer orbital life (at least one year) will be more appropriate for the scientific objectives of the mission.

AraMiS-C1 have the following subsystems:

- ISIS - 1-Unit CubeSat Structure

- 1B8_CubePMT modules
- 1B9_CubeTCT modules
- Payload
- Battery pack
- UHF antenna
- Harness
- Onboard data handling
- On-Board Computer (OBC)

2.4.1 ISIS - 1-Unit CubeSat Structure

The ISIS 1-Unit CubeSat structure is developed as a generic, modular satellite structure based upon the CubeSat standard. The design created by ISIS allows for multiple mounting configurations, giving CubeSat developers maximum flexibility in their design process. The stack of PCBs and other flight modules can be build up first in the secondary structure and integrated with the load carrying frames at the end of the process, ensuring accessibility of the flight avionics. In addition, the use of a load carrying frame and detachable shear panels allows for access to all parts of the spacecraft avionics, even after final integration by removing one or more of the shear panels. The modular structure allows up to two 1-Unit stacks of PCBs, or other modules, to be mounted inside the structure. ISIS-1-Unit CubeSat structure is shown in figure 2.9 while the structure characteristics are given in table 2.1.

Figure 2.9: ISIS-1-Unit CubeSat structure (an example)

Parameter	Value	Unit
Part production tolerances	0.1	mm
Maximum supported mass (total)	2000	g
Primary Structure Mass	100	g
Primary + Secondary Structure Mass	200	g
Outside Envelope (l × w × h)	100 × 100 × 113.5	mm^3
Inside Envelope (l×w × h)	98.4 × 98.4 × 98.4	mm^3
Thermal Range (min - max)	-40 to +80	°C

Table 2.1: Characteristic parameters of the ISIS-1-Unit CubeSat structure

2.4.2 1B8_CubePMT Module

EPS and ADCS are the most essential elements of any aerospace mission. Efficient EPS and precise ADCS are the core of any spacecraft mission. So keeping in mind their importance, they have been integrated and developed on a single tile called 1B8_CubePMT module. This module is built on a single 8-layers FR4 PCB with dimension 82.5 × 96 ×1.6 mm^3 which also acts as mechanical structure for AraMiS-C1 satellite. It has solar panels and sun sensor on the external side while internal side contains components of power management and attitude subsystems. A reconfigurable magnetorquer coil is embedded inside the four internal layers of the 1B8_CUbePMT PCB.

Modular power management tiles (PMTs) are already available in the market but they are less efficient, heavier in weight, consume more power and contain less number of subsystems. COTS components have been used for 1B8_CubePMT implementation which are low cost and easily available from the market. 1B8_CubePMT is developed on the design approach of AraMiS architecture.

1B8_CubePMT subsystems include:

- 1B111B Solar Panel
- 1B1121D Boost converter
- 1B1251 Switching and linear regulators
- Housekeeping Sensors
- 1B221 Magnetometer
- 1B211B Gyroscope
- 1B235 Sun Sensor
- 1B222 Magnetic torque actuator)
- 1B223 Magnetorquer coil
- 1B4222 Tile Processor

1B8_CubePMT and its subsystems are discussed in detail in chapters 4, 5, 6, 7 and 8.

2.4.3 1B9_CubeTCT

1B9_CubeTCT is a four layered PCB with dimensions 98.0 × 98.0 × 1.55mm^3. The components are mounted on the bottom layer (layer 4) while the top layer (layer 1) contains a feed point for mounting detachable S-band patch antenna (2.4 GHz). The routing for RF, Power and other analog traces are performed on the bottom surface. All the digital traces are routed on the third layer (3). The second and fourth layers are ground planes which help in shielding RF, Power and analog traces from digital signals. Therefore, ensures a considerably better signal integrity. The 1B9_CubeTCT communicates with onboard computer (OBC) through a 6 pin SPI connector. Power Distribution Bus (PDB) is made available using a separate 4 pin connector. Two 8 pin connectors are available for separate programming and debugging of the Texas Instruments CC2510 Transmitter TX and Receiver RX. The data processing, monitoring and various control operation for 1B9_CubeTCT is also perform by these commercially available transceivers which has an internal 8051 core microcontroller. A photograph of 1B9_CubeTCT module is shown in figure 2.10 [7].

The main focus for 1B9_CubeTCT design is to realize a high bandwidth communication link using low cost COTS components which are available in market. This has made it feasible for the universities and SMEs to enter the field of satellite design. Moreover, a modular architecture approach has been employed for complete nano-satellite design. This modular approach makes the redesign convenient by the reuse of the identical modules.

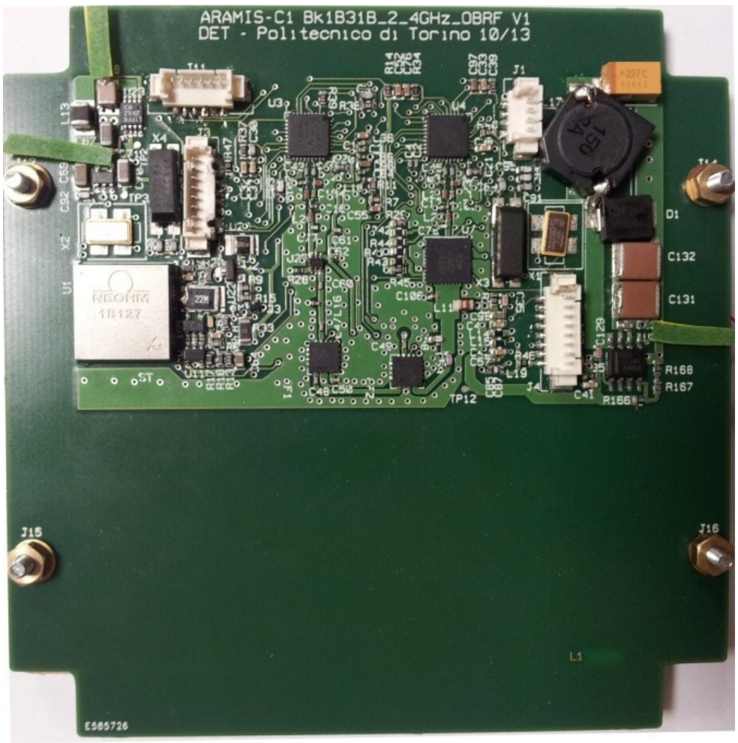

Figure 2.10: Photograph of 1B9_CubeTCT module

2.4.4 1B31A Tile Radio Frequency Module (437MHz)

UHF Module is used both as a transmitter and receiver, in half duplex configuration mode. It consists of MSP430 microcontroller performing protocol functions and two CC1020 transceivers that are configured separately as a transmitter and receiver respectively. As shown in the figure

2.11, the RF front end consists of Power Amplifier, LNA that are connected to transmitting cc1020 and receiving cc1020 which is then fed to a four element monopole antenna via Solid State Switch.

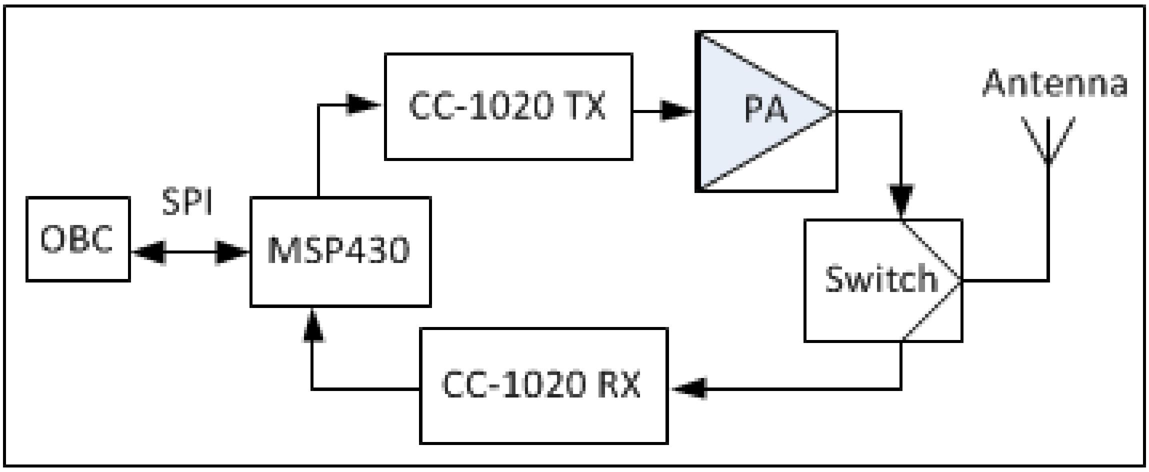

Figure 2.11: UHF Band Communication Block Scheme.

2.4.5 ISIS - Deployable Antenna System for CubeSats

The ISIS deployable antenna system contains up to four tape spring antennas of up to 55 cm length. The system can accommodate up to four monopole antennas, which deploy from the system after orbit insertion.

The wires are melted using two redundant heating elements per wire. RF phasing / BalUn circuitry ties the antennas together in for instance a turnstile configuration, two dipoles, or just one dipole. ISIS can configure the antenna system to be compatible with all UHF and VHF radios which are typically used for CubeSats.

Depending on the configuration, one or two radios in the CubeSat can connect to the antenna system by means of miniature RF connectors. Furthermore, the top face of the antenna system can accommodate a two solar cells solar panel and provisions have been made such that it can be customized for customers who require sensors or other systems to protrude to the exterior, e.g. camera apertures.

The antenna system has been designed for maximum compatibility with existing COTS CubeSat components. It is compatible with any UHF and/or VHF radio system. It can be mounted on top and bottom faces of all ISIS CubeSat structures and Pumpkin rev C and rev D CubeSat structures. For custom made structures, which adhere to the CubeSat standard mechanical envelope, mounting should also be possible.

2.4.6 1B31B Tile Radio Frequency Module (2.4GHz)

CC2510 transceivers that are configured separately as a transmitter and receiver, respectively. The Protocol functions are performed by the Embedded 8051 core tile each cc2510 transceivers. The RF front end consists of Power Amplifier, LNA that are connected to transmitting CC2510 and receiving CC2510 which is then fed to a four element monopole antenna via Solid State Switch as shown in figure 2.12.

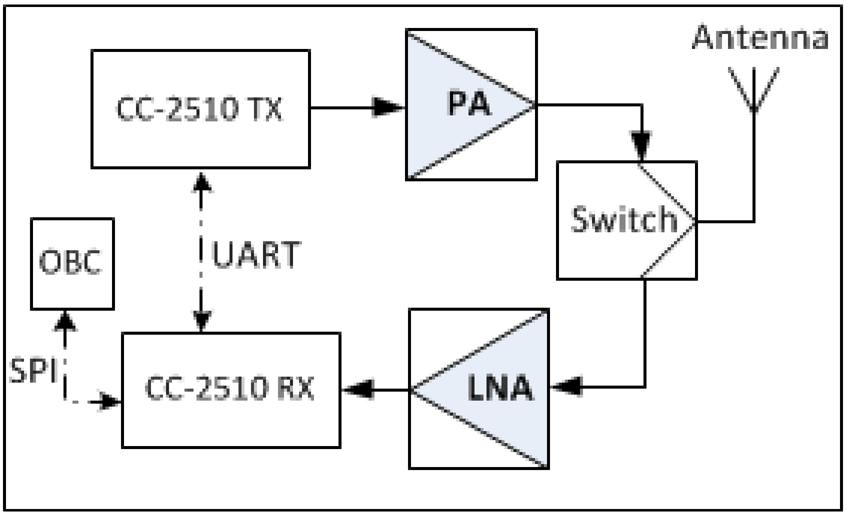

Figure 2.12: S-Band Communication Block Scheme.

2.4.7 1B3211 - Single Patch Rodgers Antenna

For S-Band communication Link, single patch antenna has been selected that is operated at 2.45 GHz. The compact design allows it to be mounted on external face of TCT. It is fed via coax feed from the internal S-Band Module. Among the available materials, Rodgers' Duroid Substrate 6002 was selected which has a relative permittivity 'ε_r'= 2.94 and thickness 't' = 30mil/0.762mm.

2.4.8 Payload

The payload is a scientific/technological payload composed of three independent boards, developed by different groups. All of them have the common aim of comparing the sensitivity to radiations of commercial microcontrollers in order to make results available to the scientific community. The same (or a similar) program will run on all the boards, aimed at counting the SEUs which accumulate during the lifetime of a microcontroller in LEO orbit, under similar conditions. The three boards will host:

- Payload - Board 1: a Texas Instrument's MSP430F5438 microcontroller
- Payload - Board 2: a Microchip's PIC microcontroller
- Payload - Board 3: a few flavors of Xilinx's PicoBlaze soft-core on an Actel ProAsic FPGA, with different levels of HW radiation hardening. This payload has been developed at University of Alicante (E)

Characteristics common to Payload-Board 1, Payload-Board 2 and Payload-Board 3 are:

- mass: 35g
- size 80 × 80 mm^2
- power consumption: 100mW average
- data rate requirements: about 50B every minute

2.4.9 Harness

The harness of AraMiS - C1 is very simple. Each AraMiS - C1 has:

- MOLEX-4 pins PicoBlade header connector for Power Distribution Bus; 12V nominal; max 200mA, except for the 1B9_CubeTCT tile, which can sink up to 800mA. This also shares ground node and kill switch connection.
- MOLEX-5 pins PicoBlade header for tile data bus (I2C)
- MOLEX-8 pins PicoBlade header for JTAG programming of microcontroller, to be used only on ground for microcontroller configuration

The power harness is therefore a bus connection for power Distribution Bus; one plug for each tile and the payload (7 plugs).
The data harness is therefore a bus connection for I2C; one plug for each tile and the payload (7 plugs).
The RF harness is a coax cable from the 1B9_CubeTCT tile to the opposite ISIS - Deployable Antenna System for CubeSats.
All harnesses are tied to the Internal Structure of the AraMiS-C1. Connectors are fixed by means of appropriate silicone resin.

2.4.10 Battery Pack

A pack of ten rechargeable secondary batteries from SANYO. They are assembled in two packs of five batteries each has.

- Nominal Voltage = 7V
- Capacity = 900mAh
- Mass = 230g
- Min Temperature = -20 °C
- Max Temperature = +60 °C

2.4.11 1B45 Tile Data Handling (OBDH) and Software

On Board Data Handling Subsystem is one of the critical subsystems of any satellite mission [8]. A lot of design effort needs to be done for reliable way of data handling among different modules (sensors, actuators, etc.). The following sections show the detailed documentation of On Board Data Handling and Software sections of AraMiS-C1.

2.4.11.1 Tile Data Handling Bus

All the data handling of AraMiS-C1 takes place in accordance with the Basic Protocol for communication between one or more subsystems developed at Politecnico di Torino, which supports in a transparent way, several physical layers. The Master is any processor willing to communicate (exchange data and commands) with a Slave. Master may either be the On Board Computer or a Tile Processor (MSP430F5438 from Texas Instruments). The Slave may be a Tile or any other subsystem. Master communicates with the Slave via either SPI, OBDB, or I2C protocols. The Master, via the interface, can at least:

- Send/Receive designer-defined messages to/from the Slave (namely, Read Data/Write Data operation);
- Send Designer-defined commands to the Slave (namely, Command Only operation);
- Acquire Designer-defined housekeeping information from the Slave (e.g. internal voltages, currents, temperatures; see use case Housekeeping Management);
- Set the Slave to sleep mode or wake it up

- Configure the Slave (e.g. enable/disable subsystems)

The Basic Protocol supports the following actions

- Write Data - when a Master wants to transfer up to 256B of data to a Slave;
- Read Data - when a Master wants to read up to 256B of data from a Slave;
- Command Only - when a Master wants to deliver a data-less command to a Slave.
- Broadcast Write Data - when a Master wants to transfer up to 256B of data to all Slaves;
- Broadcast Command Only -Command Only - when a Master wants to deliver a data-less command to all Slaves.

Most data transfers contain an appropriate START element; an 8-bit Master address; 8-bit Slave address ; a 16-bits command;
an 8-bit data length field (only for Write Data and Broadcast Write Data); data (1B to 256B; except read data); a 16-bit CRC
check and an appropriate STOP element. For AraMiS-C1, we select I2C physical layer for all connections.

2.4.12 On-board Computer

On-Board Computer (OBC) is the heart of any satellite mission. Use case diagrams of figure 2.13 shows the main functions of OBC. Some salient features of the OBC to provide the satellite flight segment with the following features:

- Processing resources for the flight mission software
- Telemetry and telecomm-and services and interfaces with the RF communication chain
- General communication services with the Avionics and payload equipment through an on-board communication bus.
- Time synchronization and distribution
- Failure tolerance architecture based on the use of redundancy implementation principle
- Managing payload data on the satellite and then transmitting it to ground station in proper format and efficiently.

One of the 1B8_CubePMT tile processors acts as the On Board Computer (OBC) for AraMiS-C1.

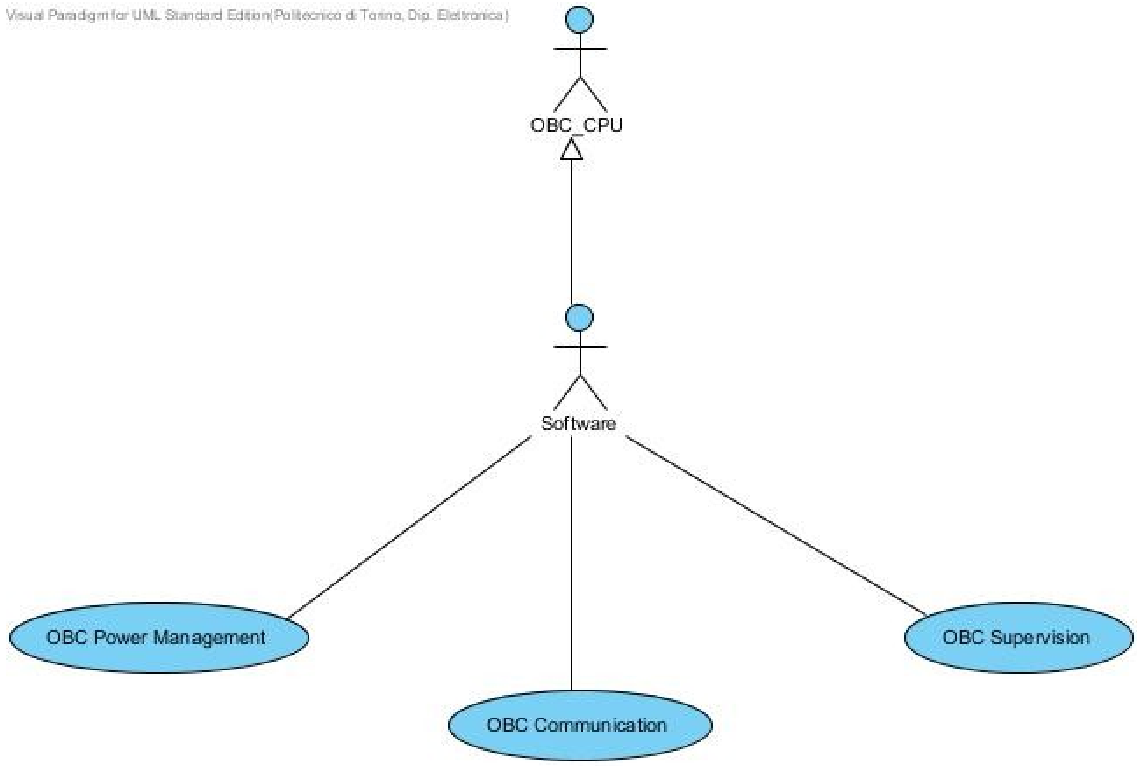

Visual Paradigm for UML Standard Edition(Politecnico di Torino, Dip. Elettronica)
OBC_CPU
Software
OBC Power Management
OBC Communication
OBC Supervision

(a)

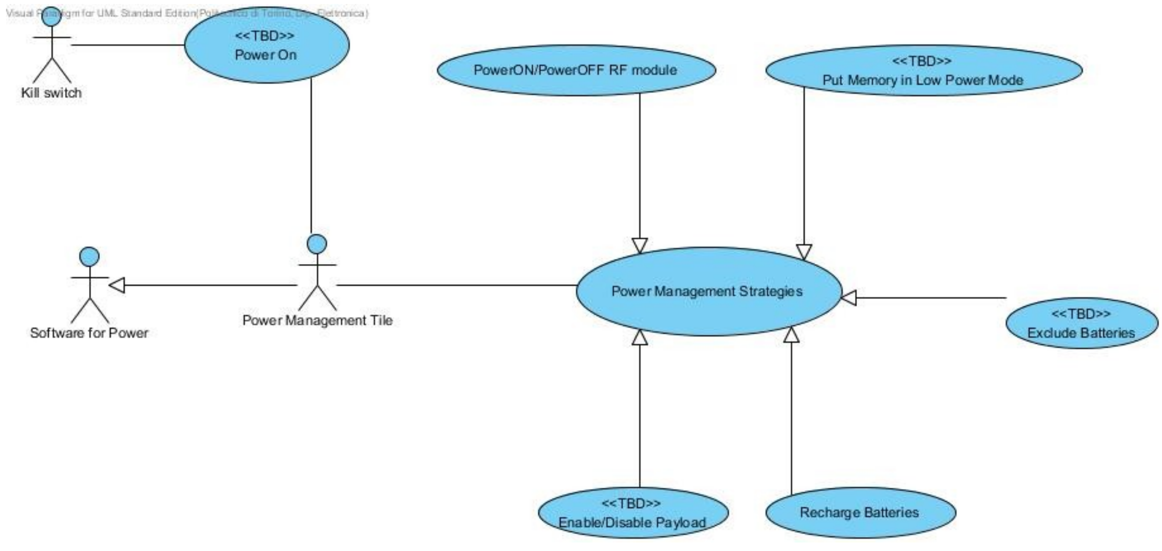

Kill switch
<<TBD>>
Power On
PowerON/PowerOFF RF module
<<TBD>>
Put Memory in Low Power Mode
Software for Power
Power Management Tile
Power Management Strategies
<<TBD>>
Exclude Batteries
<<TBD>>
Enable/Disable Payload
Recharge Batteries

(b)

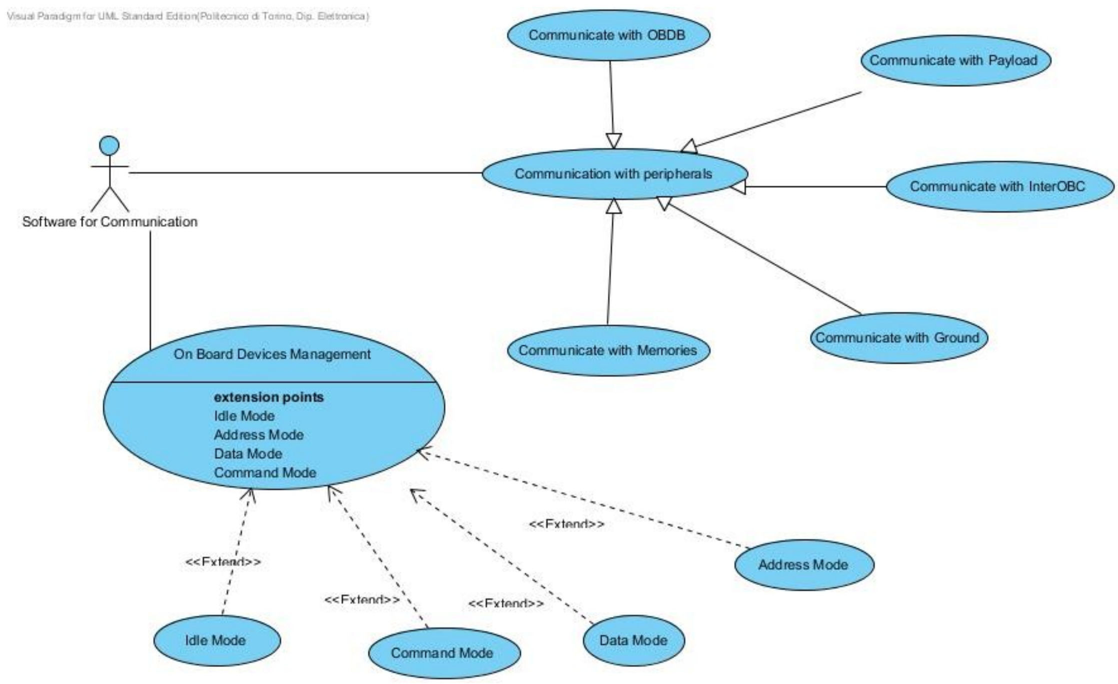

(c)

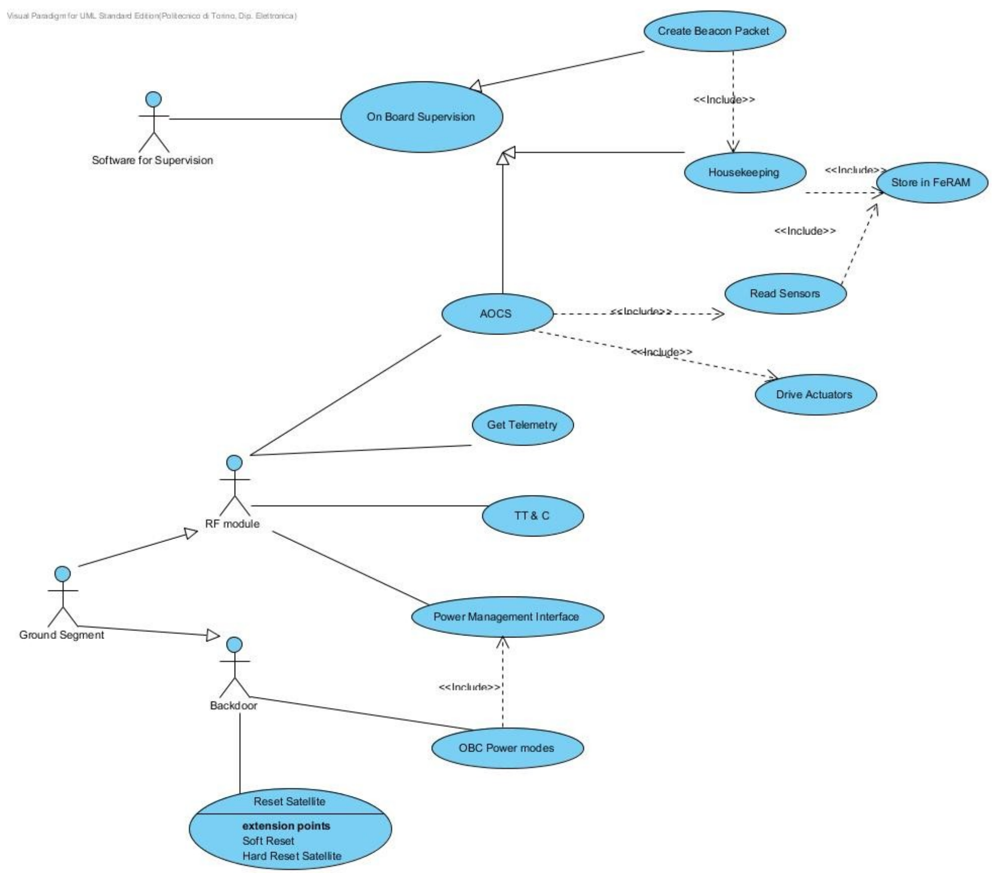

(d)

Figure 2.13: Major functions of OBC (a) OBC use cases (b) OBC power management (c) OBC communication (d) OBC supervision

Chapter 3

Satellite Design Flow

3.1 Introduction

In this chapter we are going to discuss the design configuration of AraMiS tiles and modules. Basically three types of design configurations are used. These configurations are discussed here and at the end a trade off analysis of using modules in different spacecraft configurations has been given.

3.2 Design flow Configurations

The design technique of the AraMiS tiles and modules is quite flexible and a number of spacecraft configurations are possible including physical, logical and satellite on demand. The key design flow sequence is described as follows.

- Design the new subsystems either on single, double or quadruple module configuration.
- Test the subsystems on ground using development board. The tiles having processors and pluggable connectors can be transformed very easily into the development boards for the functional testing of modules.
- Integrate each module on the tile connectors in a physical module based satellite configuration. The specific module can be used only if the desired mission needs it.
- Embed the logical modules in the main tile for a logical module based satellite configuration. This configuration is permanent and cannot be altered after the design phase.
- Integrate physical and logical modules on a single tile for a custom satellite on demand configuration. This approach takes advantages of both physical and logical configurations.

3.2.1 Physical Module Based Configuration

This configuration uses standard tiles hosting multiple connectors and the individual subsystems are developed on physical daughter boards, connected to the tile via pluggable connectors. The subsystem modules are used only if the specific mission needs it. This configuration achieves high level of design flexibility, testability and upgradability. The testing of modules, tiles and the whole satellite is needed in this type of configuration. This configuration is mostly employed for teaching/research purposes because the integration of the physical modules causes highly integration complexities.

3.2.2 Satellite on Demand Configuration

This configuration embeds the already developed and tested modules inside the PCB of the tile. Therefore in this configuration, the design of physical modules in a permanent configuration. Testing at tile and mission level is required and not at the module level. The CubeSat standard tile is built using this approach

3.2.3 Reusable Design Configuration

The reusable design configuration is an optimized spacecraft configuration based on the customer requirements. This configuration reuses the satellite on demand configuration with minor addition or removal of specific subsystems on customer demands. This configuration actually follows the Cheaper-Faster-Better philosophy. The testing is performed only at mission level as the modules and tiles of the previously tested configurations are used in this spacecraft.

3.3 Design Trade-off analysis

A design trade-off was performed for using different types of modules in the above mentioned satellite configurations. Physical module based configuration has high level of design flexibility, testability and can easily be upgraded but the shortcomings are increased mass/weight because of using separate modules, less space for payload and difficult integration of physical modules on the tile connectors. Logical module based configuration cannot be upgraded once designed. Moreover it has lower testability than the other schemes. The detailed comparison of the above configurations is depicted in figure 3.1. In [9], we have presented design and test of bus interface circuit on single module emphasizing the concept of plug and play approach.

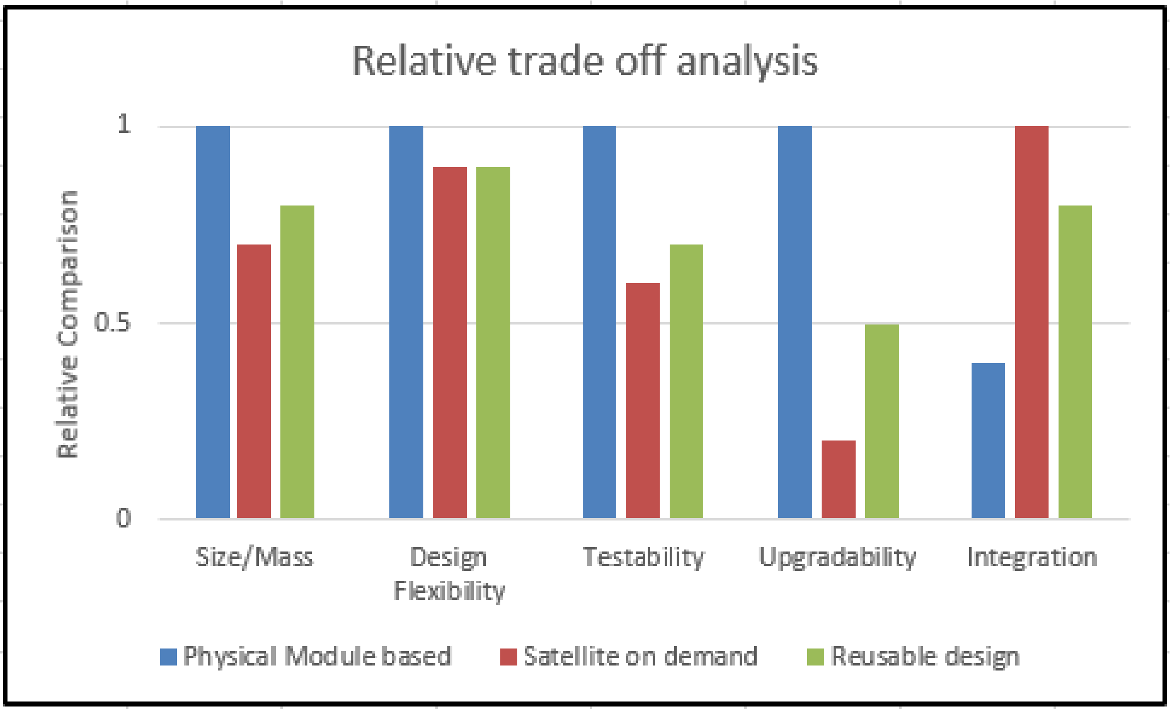

Figure 3.1: Trade off analysis of using modules in different spacecraft configurations

Chapter 4

CubeSat Power Management Tile: 1B8_CubePMT

4.1 Introduction

1B8_CubePMT is the power management, attitude determination and control tile for AraMiS-C1 satellite. 1B8_CubePMT is mounted on the four external faces of the AraMiS-C1 satellite. The other two sides have the telecommunication tiles called 1B9_CubeTCT. The photos of the AraMiS-C1 are shown in figure 4.1.

Electric power supply (EPS) and attitude determination & control subsystem (ADCS) are the most essential elements of any aerospace mission. Efficient EPS and precise ADCS are the core of any spacecraft mission. So keeping in mind their importance, they have been integrated and developed on a single tile called 1B8_CubePMT module [10]. Modular power management tiles (PMTs) are already available in the market but they are less efficient, heavier in weight, consume more power and contain less number of subsystems. The goal of this work is to implement EPS and ADCS subsystems in a single module focusing on the main issues and adding some additional features. 1B8_CubePMT is developed on the design approach of AraMiS architecture using the satellite on demand design flow configuration (discussed in chapter 3).

In this chapter we will discuss 1B8_CubePMT in general. Subsystems design, implementation and testing details are given in chapter 5, 6, 7 and 8.

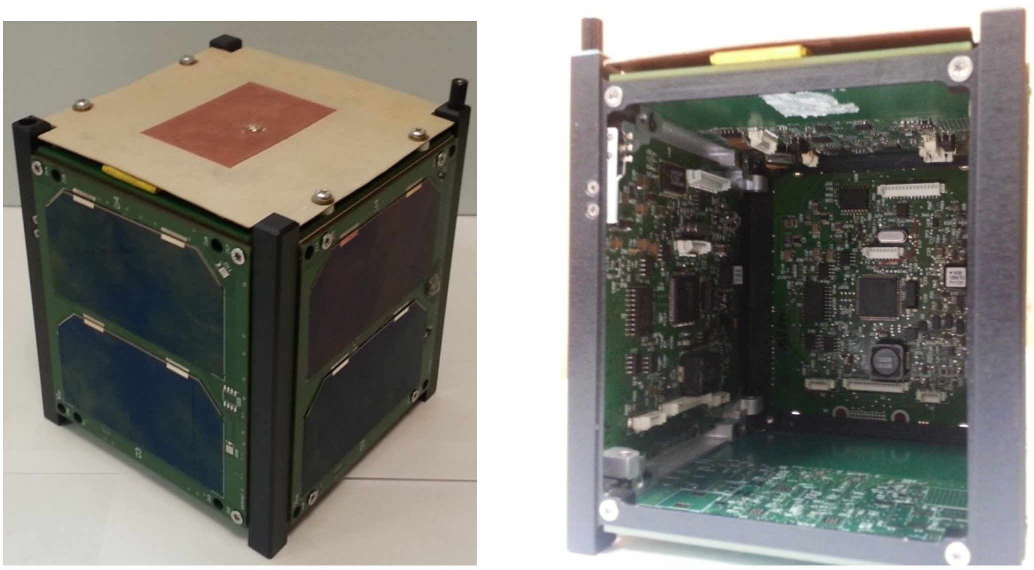

Figure 4.1: Photos of AraMiS-C1 external and internal views

4.1.1 1B8_CubePMT Subsystems Nomenclature

The 1B8_CubePMT module subsystems names are according to the nomenclature used for these subsystems inside UML diagrams [11].

UML (Unified Modeling Language), a widely used modeling language in high level object oriented designs is becoming a standard in vast application areas. UML provides a lot of independent diagrams, including the usecase diagram, class diagram, sequence diagram, requirement diagram, state diagram etc. Different diagrams exhibit system properties in different views. The choice of the diagram usually depends upon the characteristics of the system [12].

UML has been used for the design and documentation of the AraMiS project. All the subsystems blocks and their functionalities have been described using the UML. Hardware/software architecture of AraMiS, detailed documentation of each subsystem has been implemented using UML. The design methodology employs UML class diagram for every module. With the proposed approach, every subsystem is composed of a hardware (HW) part and a corresponding SW support.

1B8_CubePMT UML class diagram is given in figure 4.2. All the subsystems names are according to the nomenclature used for their classes in UML. In this thesis, we will used the corresponding UML names of all the subsystems.

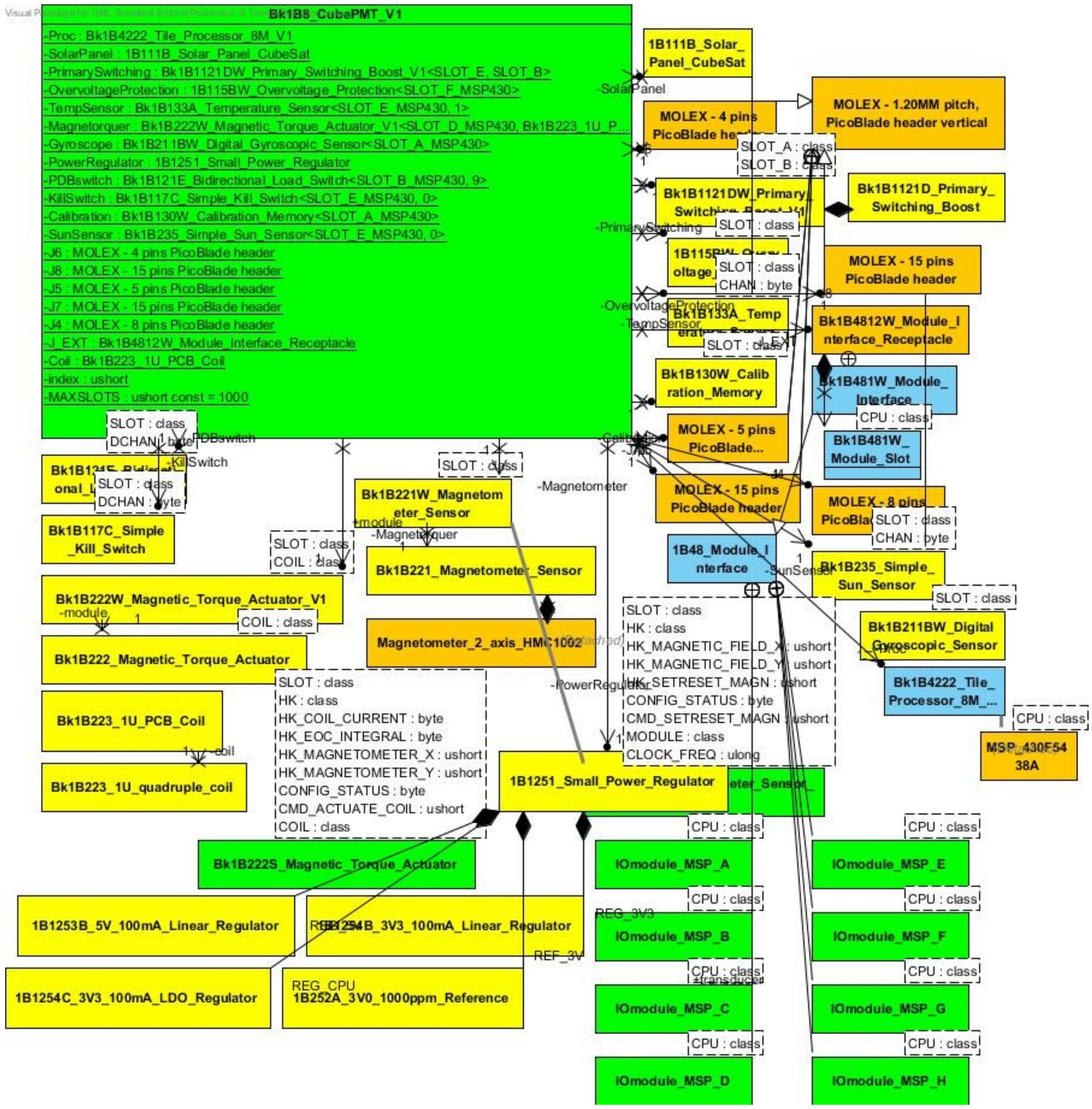

Figure 4.2: UML class diagram of 1B8_CubePMT.

4.1.2 1B8_CubePMT Subsystems

1B8_CubePMT has EPS and ADCS subsystems. EPS is responsible for power generation while ADCS provides pointing to the antennas, direct solar panels towards sun and controls the satellites spin rate. EPS includes solar panel, boost converter, load switches and different linear and switching regulators. ADCS consists of magnetometer, gyroscope, sun sensor, magnetic torque actuator and magnetorquer coil. Different housekeeping sensors are mounted at different points of the CubePMT tile. For harness data and power, 1B8_CubePMT has different connectors. A commercial microcontroller MSP430F5438 from Texas Instruments performs power management, data processing and various control operations [13].

The external face of 1B8_CubePMT module has two solar cells and sun sensor while the internal face contains all the EPS and ADCS subsystems components. The solar cells are triple junction space qualified providing an efficiency of 26%. They are connected in series to achieve an output voltage of approximately 4.4V (each cell generating 2.2V). The external face also has a simple sun sensor that is used as a sun directional sensor. The inner face has a boost converter which step up the solar panel voltage from 4.4V to 14V (power distribution bus voltage). The inner face also has a magnetometer and a yaw rate gyroscope with dynamic range of ±80°/s which is connected to the tile processor through SPI bus. A magnetorquer coil with 200 turns, is integrated inside the PCB four internal layers, thus occupy no extra space in the spacecraft. MSP430 microcontroller is mounted on the inner face for monitoring and control operations of the whole system. Block diagram of 1B8_CubePMT is shown in figure 4.3 while photographs of 1B8_CubePMT are shown in figure 4.4 and figure 4.5.

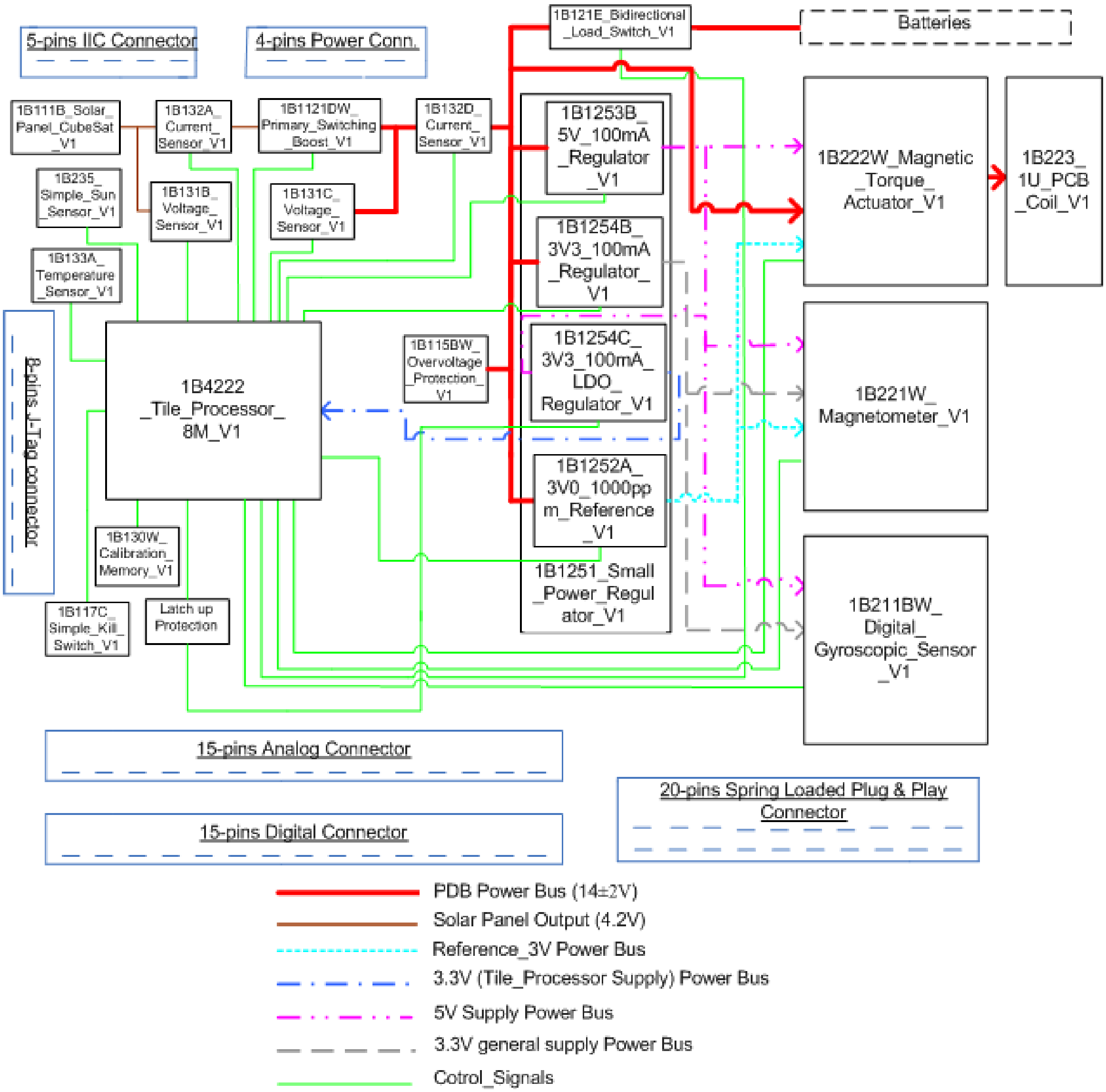

Figure 4.3: Block diagram of the 1B8_CubePMT subsystems.

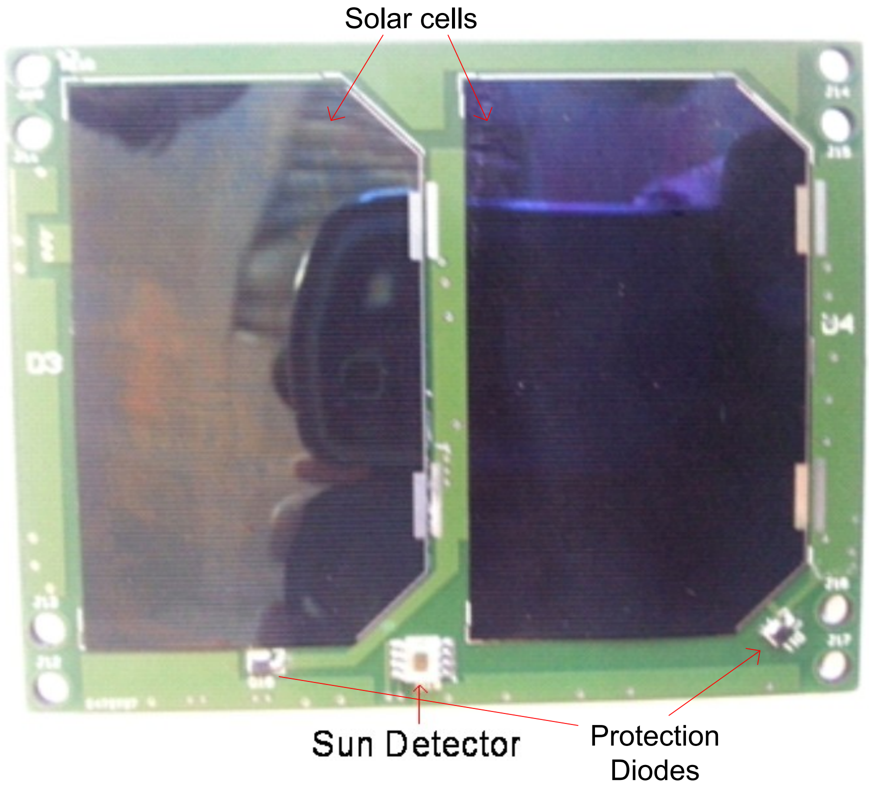

Figure 4.4: Photographs of 1B8_CubePMT module's solar panel side.

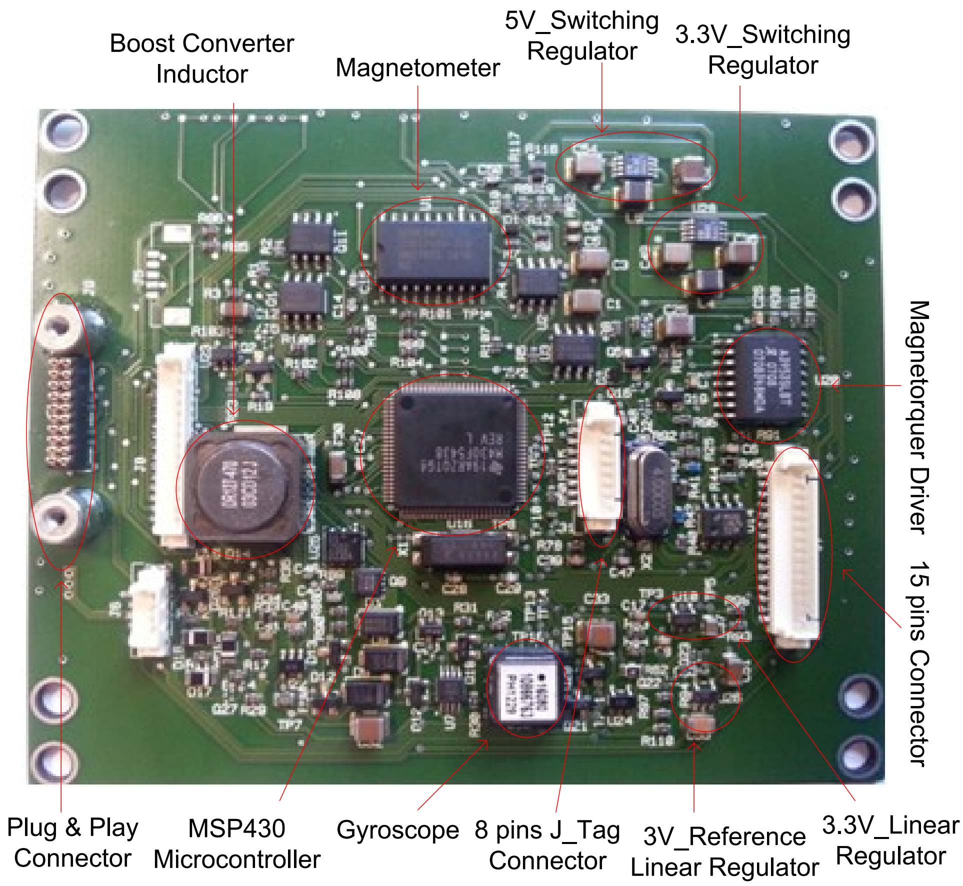

Figure 4.5: Photographs of 1B8_CubePMT module's component side.

4.1.1 Cross-Sectional View

Cross sectional view of the 1B8_CubePMT module is shown in figure 4.6. Two solar cells are attached with layer-1 through resin. Magnetorquer coil with 200 turns, is integrated inside the PCB four internal layers (layer 2, 3, 4 & 5). Layer-6 has the ground plan while layer-7 contains partial ground plans and PCB traces to connect the components in layer-8.

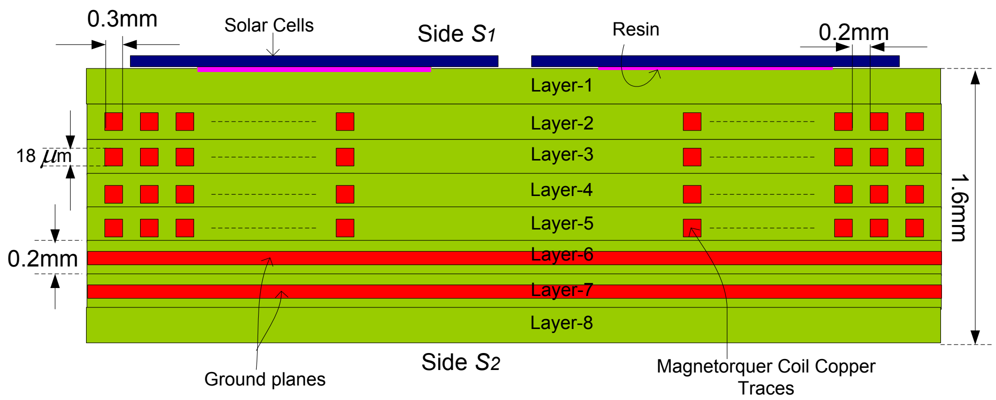

Figure 4.6: Cross sectional view of the 1B8_CubePMT module.

4.1.1 Dimensions

1B8_CubePMT is developed on a single eight layers PCB with dimensions 98.0×82.5×1.6 mm^3. The top side (layer-1) has two solar cells and sun sensor while the bottom side (layer-8) contains all the electronic subsystems. All analog and digital signals of the subsystems are available on two 15 pins connectors. Power distribution bus (PDB) and solar panel outputs are available on a separate four pins connector. Eight pins J-tag connector is available for programming and debugging of tile processor and a five pins I2C connector for communication with other tiles. A spring loaded 20-pins plug and play connector is used for connecting any external subsystem on one of the eight ports of tile processor. Figure 4.7 shows 1B8_CubePMT dimensions of solar panel and component sides. Table 4.1 shows the 1B8_CubePMT module imporatant dimension parameters.

Parameter	Dimensions	Unit
PCB dimensions of 1B8_CubePMT module	98.0×82.5×1.6	mm^3
Total thickness of 1B8_CubePMT with components	9.15	mm
Mass of 1B8_CubePMT module	40	g
Dimensions of a single solar cell	70×40×0.15	mm^3
Height of PicoBlade Molex connector	4.7	mm
Height of Boost Converter inductor	7.5	mm
Height of Gyroscope	5.2	mm

Table 4.1: 1B8_CubePMT dimensions

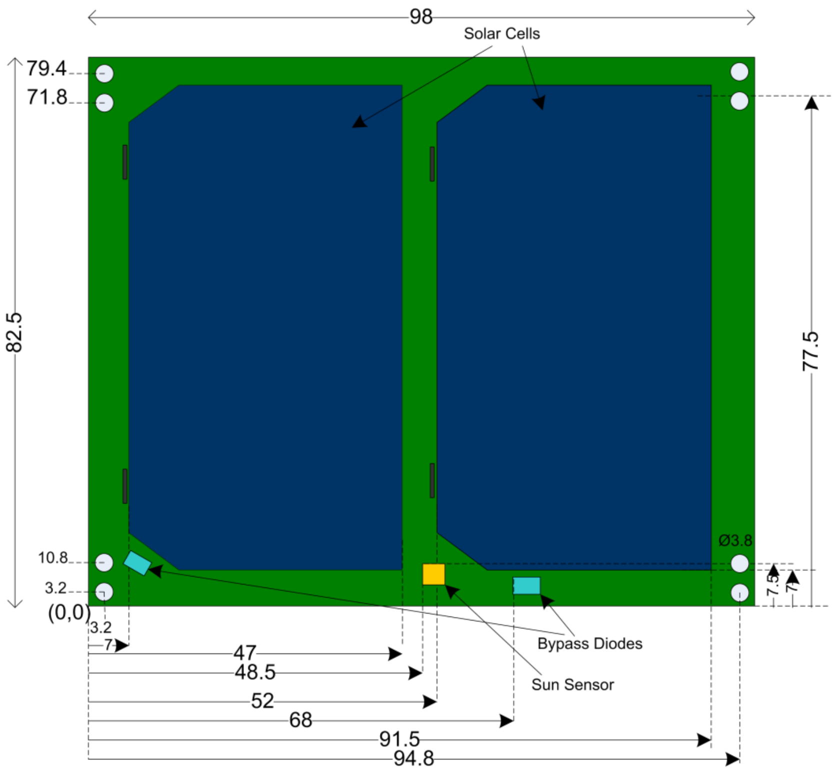

(a)

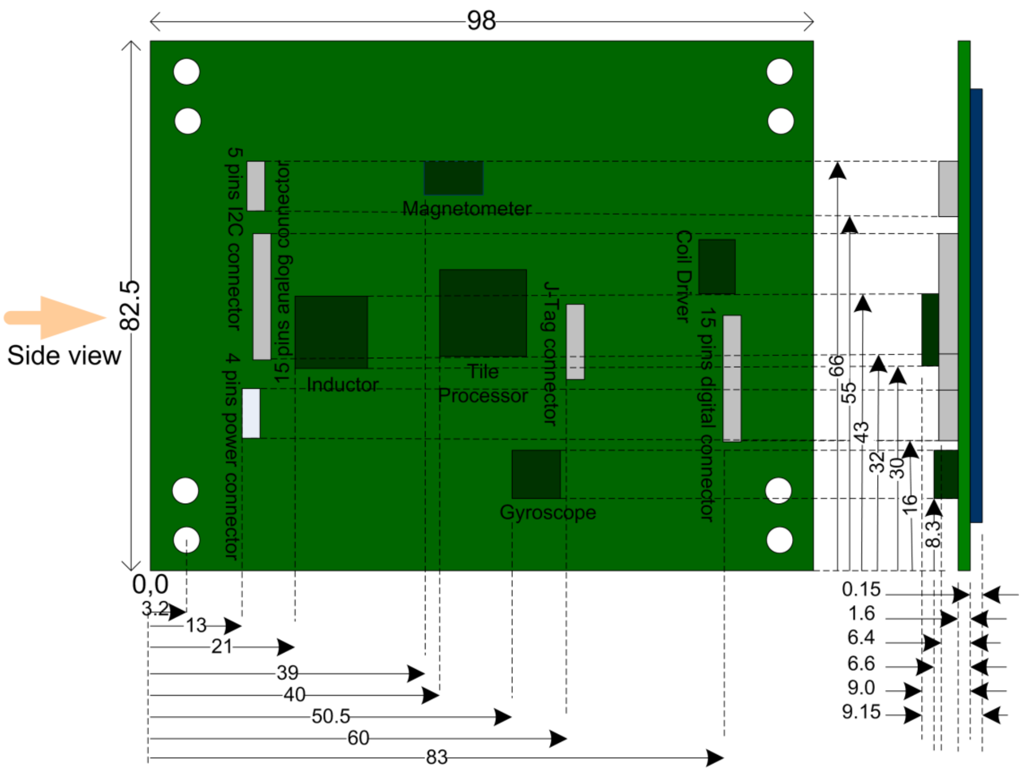

(b)

Figure 4.7: 1B8_CubePMT dimensions (mm) (a) Solar panel side (b) component side

4.1.2 Power and Data Interface

The data and power interfaces of 1B8_CuibePMT is very simple. It has six different connectors :

- MOLEX-4 pins PicoBlade connector (J6): On this connector solar panel output and PDB of the 1B8_CubePMT module are available.
- MOLEX-5 pins PicoBlade connector (J5): This connector has on-board data bus (I2C) and kill switch connection. 3.3V supply is also available on this connector.
- MOLEX-8 pins PicoBlade JTAG connector (J4): This connector is used for programming and debugging purposes of the tile processor.
- MOLEX-15 pins PicoBlade analog connector (J8): All the analog signals of different sensors are available on this connector. 5V supply and 3V reference supply are also available on this connector.
- MOLEX-15 pins PicoBlade digital connector (J7): This connector has all the critical digital signals for testing purposes.
- Plug and Play Spring Loaded connector (J9): This connector is attached to the tile processor on port G (also called module G). It is a 20 pins optional connector and an external module (subsystem) can be connected to the tile processor through this connector.

4.1.3 1B4222 Tile Processor

Tile processor is the heart of 1B8_CubePMT module and is mainly responsible for managing the system, in particular:

- Processing resources of the 1B8_CubePMT
- General communication services of the subsystems of 1B8_CubePMT with avionics and payload equipment of AraMiS-C1 through I2C bus
- Power management and scheduling task
- Storing and processing housekeeping data
- Decoding and executing commands of all the subsystems

Commercial MSP430F5438 [13] ultra low power 16-Bit RISC architecture microcontroller is used as tile processor which can support up to 25 MHz system clock. The MSP430F5438 has one active mode and six software selectable low-power modes. An interrupt event can wake up the device from any low-power modes, service the request, and restore back to low-power mode on return from the interrupt program. It is an eleven ports microcontroller. A separate subsystem is attached on each port. These subsystems are called modules, therefore each port on the tile processor is also called module as shown in figure 4.8. On each module a subsystem of 1B8_CubePMT is connected. One of these module has an optional spring loaded plug and play male connector . External subsystem with female connector can be connected on this module. Tile processor has a J-Tag connector for programming and debugging purpose. A single tile module contains eight digital and two analog signals as shown in the UML class diagram of figure 4.9.

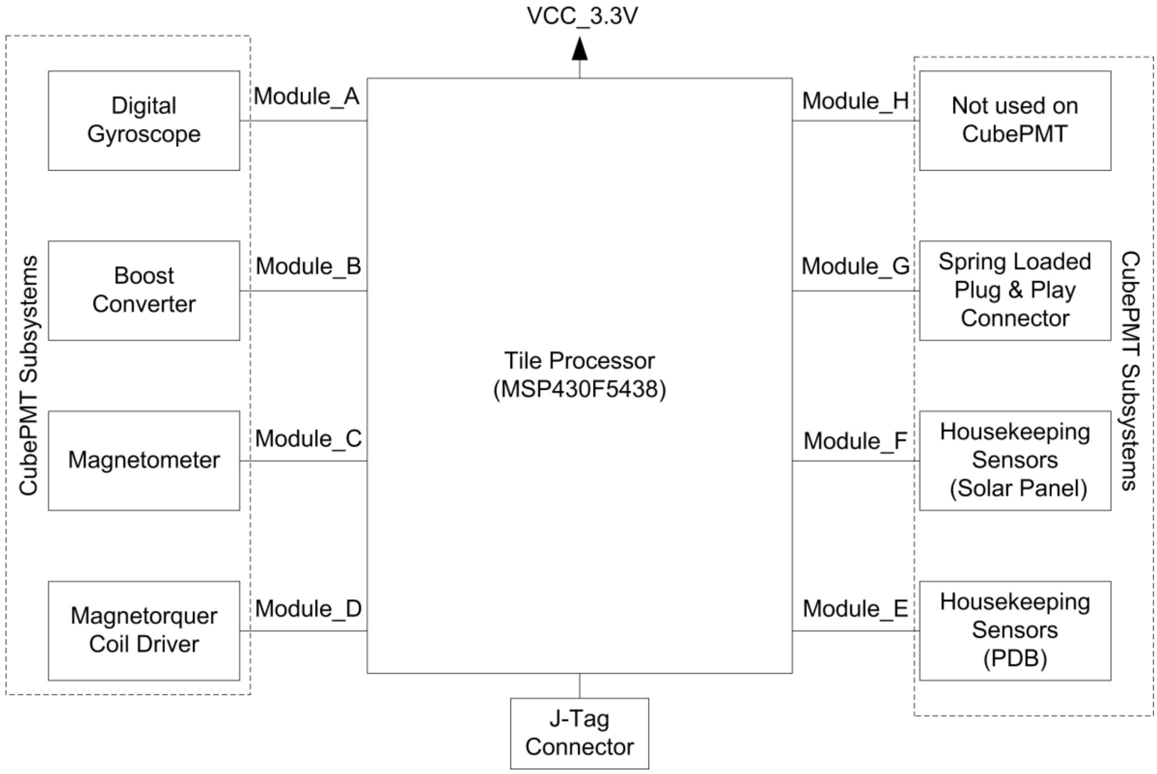

Figure 4.8: 1B8_CubePMT architecture with respect to Tile processor.

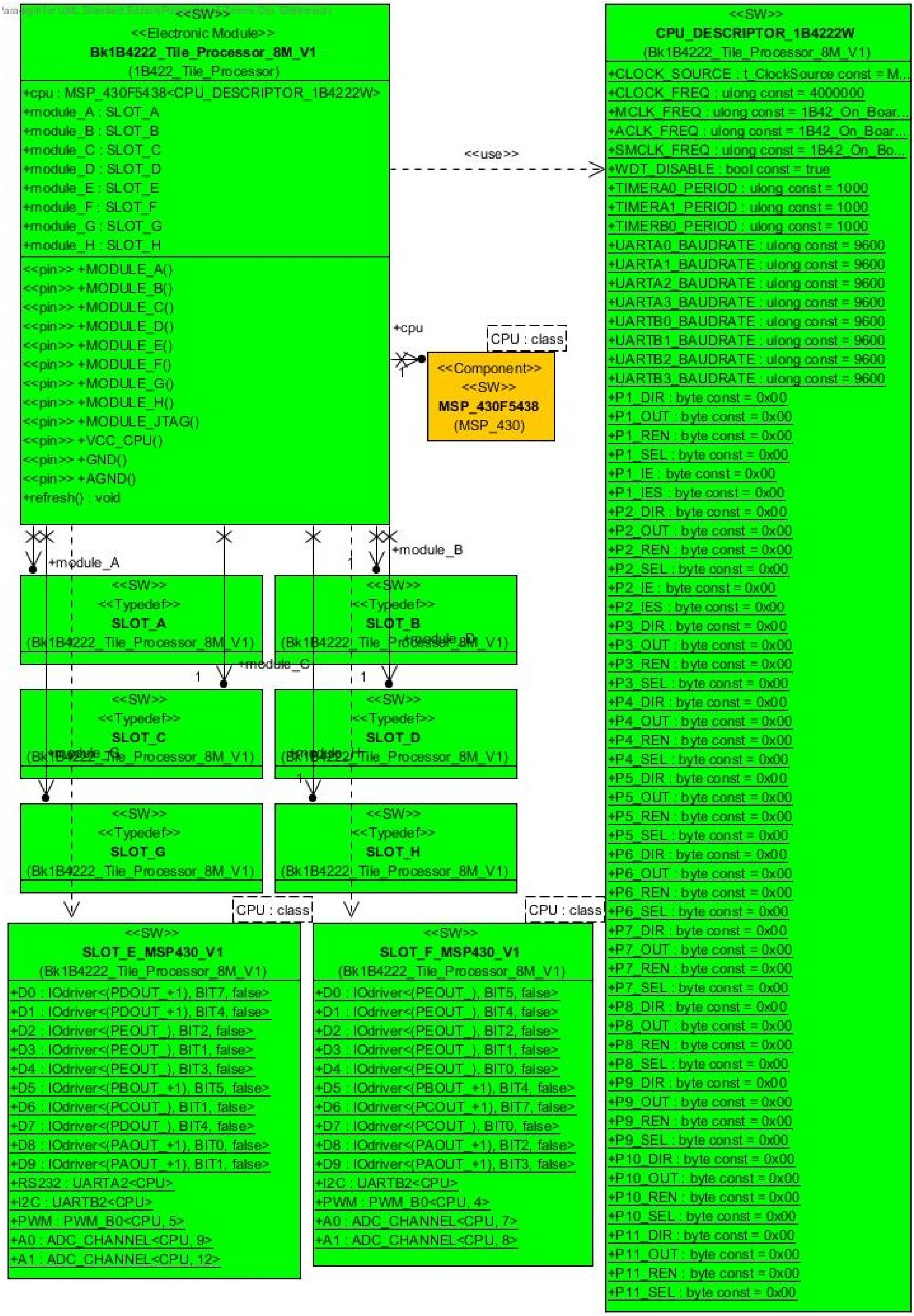

Figure 4.9: UML class diagram shows the signals of 8-slots (ports) of the tile processor 1B4222

4.1.3.1 Digital I/O

There are up to ten 8-bit I/O ports implemented: For 100-pin options, P1 through P10 are complete. P11 contains three individual I/O bits [13].

- All individual I/O bits are independently programmable.
- Any combination of input, output, and interrupt conditions is possible

4.1.3.2 Oscillator and System Clock

The clock system in the MSP430x5xx family of devices is supported by the Unified Clock System (UCS) module that includes support for a 32-kHz watch crystal oscillator (XT1 LF mode), an internal very-low-power low-frequency oscillator (VLO), an internal trimmed low-frequency oscillator (REFO), an integrated internal digitally controlled oscillator (DCO), and a high-frequency crystal oscillator (XT1 HF mode or XT2). The UCS module features digital frequency locked loop (FLL) hardware that, in conjunction with a digital modulator, stabilizes the DCO frequency to a programmable multiple of the selected FLL reference frequency. The internal DCO provides a fast turn-on clock source and stabilizes in less than 5 μs. The UCS module provides the following clock signals [13]:

- Auxiliary clock (ACLK), sourced from a 32-kHz watch crystal, a high-frequency crystal, the internal low-frequency oscillator (VLO), the trimmed low-frequency oscillator (REFO), or the internal digitally controlled oscillator DCO.
- Main clock (MCLK), the system clock used by the CPU. MCLK can be sourced by same sources made available to ACLK.
- Sub-Main clock (SMCLK), the subsystem clock used by the peripheral modules. SMCLK can be sourced by same sources made available to ACLK.
- ACLK/n, the buffered output of ACLK, ACLK/2, ACLK/4, ACLK/8, ACLK/16, ACLK/32

4.1.3.3 Timer (TA0, TA1, TB0)

This device contains 16-bit timer/counters TA0, TA1, TB0 with five, three and seven capture/compare registers respectively. It can support multiple capture/compares, PWM outputs, and interval timing. It also has extensive interrupt capabilities. Interrupts may be generated from the counter on overflow conditions and from each of the capture/compare registers [13].

4.1.3.4 Analog to Digital Converter (ADC)

The ADC12 module supports fast 12-bit analog-to-digital conversions. The module implements a 12-bit SAR core, sample select control, reference generator, and a 16-word conversion-and-control buffer. The conversion-and-control buffer allows up to 16 independent ADC samples to be converted and stored without any CPU intervention [13].

4.1.3.5 Universal Serial Communication Interface (USCI)

The USCI modules are used for serial data communication. The USCI module supports synchronous communication protocols such as SPI (3 or 4 pin) and I2C, and asynchronous communication protocols such as UART, enhanced UART with automatic baudrate detection, and IrDA. Each USCI module contains two portions, A and B.

The USCI_An module provides support for SPI (3 pin or 4 pin), UART, enhanced UART, or IrDA. The USCI_Bn module provides support for SPI (3 pin or 4 pin) or I2C.

4.1.4 EPS and ADCS

1B8_CubePMT Subsystems are divided into two subsystems, EPS and ADCS. EPS will be discussed in detail in chapter 5 while ADCS will be discussed in chapter 6 and chapter 7.

4.2 Latch-up Protection

The MOSFET devices are normally prone to radiations (latch-up). The latch-up problem can be solved by using bipolar devices, which are immune to latch-up, since they require an extremely high energy to trigger this event. But the processors are MOSFET based and required latch-up protection circuits.

The latch-up protection circuit designed for 1B8_CubePMT is shown in figure 4.10. EN_CPU is going to enable the power supply of the tile processor. The voltage divider network of resistors R117 and R116 provides 3.3V to the tile processor. When there is a latch-up occurred, the B_D5_PWM signal from the tile processor connected with C50 will connected to the ground as the whole tile processor is short to the ground. The voltage on the point A which is connected to the enable pin of the tile processor is also becomes zero and supply of the tile processor is disabled. When the latch-up period is passed away, C50 is again charged through R117 from the PDB. The time for which the tile processor will be off is selected by the R117 and C50 values. The current draw by the enable supply of the tile processor is 1µA.

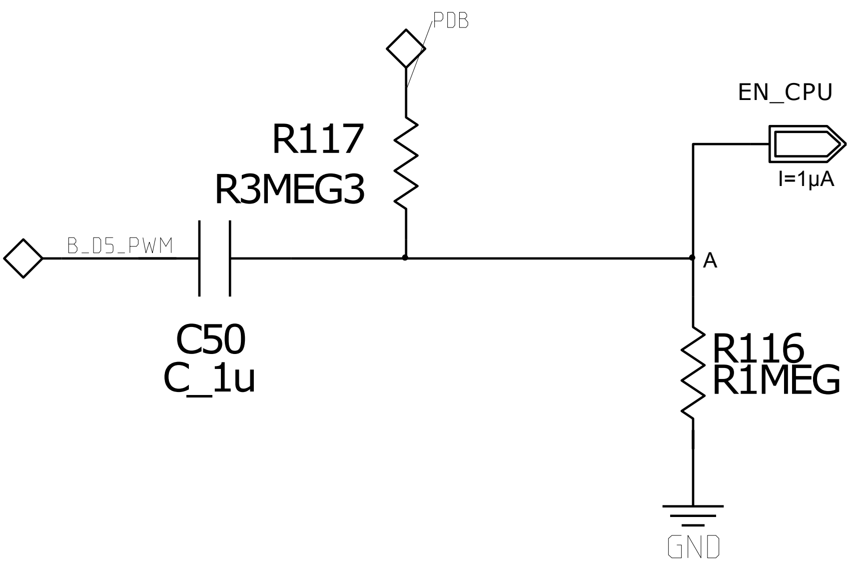

Figure 4.10: Latch-up protection circuit designed for 1B8_CubePMT

$$PDB.\frac{R116}{R116+R117}-1\mu A.\frac{R116\times R117}{R116+R117}=3.3V \tag{4-1}$$

$$18V-1\mu A\times R117=3.3V\,\frac{R116+R117}{R116}$$

$$18V-3.3V=3.3V\left(1+\frac{R117}{R116}\right)$$

$$\frac{R117}{R116}=3.45$$

$$Let$$

$$R116=1M\Omega$$

$$R117=3.3M\Omega$$

Chapter 5

Tile Level Electric Power Supply

5.1 Introduction

In this chapter we will discuss the design, implementation and operation of all the subsystems of AraMiS-C1 EPS at tile level in detail. As already discussed that AraMiS-C1 has four power management tiles (1B8_CubePMT). All of them are identical and have EPS and ADCS subsystems. Here in this chapter we will discuss just one tile EPS subsystems.

The aim of electric power supply (EPS) unit is to generate, distribute and convert power to different voltage levels. NanoSatellites dimensions and space environment constraints limit the design of an ideal EPS system. 1B8_CubePMT is CubeSat standard tile with dimensions 98× 82.5 × 1.6 mm^3, have solar panel on one side and all the subsystem components of EPS and ADCS on the other side. To accommodate such a large number of subsystems in a small space, require to reduce the dimension of all the subsystems. The main goals in the EPS design are to achieve higher efficiency and to reduce the size of all components used. Therefore COTS components were selected for EPS on the basis of power loss analysis and small dimensions [14].

The desired functionalities guide the EPS design. The designed EPS must produce sufficient energy to supply all the subsystems of the AraMiS-C1 satellite. Enough energy has to be stored to supply the satellite during the satellite night. The EPS must also provide several power outputs (3V, 3.5V, 5V etc) with stabilized voltages. There should also be different sensors mounted at different point on the EPS, in order to monitor the operation limits [15].

5.2 EPS Subsystems

EPS of AraMiS-C1 at tile levels contains the following subsystems,

- 1B111B Solar panel
- 1B1121D Boost converter
- 1B121E Bi-directional Load Switch
- 1B114 Batteries
- 1B115B Over voltage protection
- 1B1251 Switching & linear regulators and
- 1B121 Load switches

Boost converter steps up the solar panel voltage (4.4V) to power distribution bus (PDB) voltage level (14V±2V). Maximum power point tracker (MPPT) operates solar cells at maximum power point. Energy is stored on a single pack of NiCd rechargeable batteries (external to the 1B8_CubePMT module). The pack contains ten NiCd elements each provides 1.2V. Storage capacity of each NiCd cell is 0.9Ah. Batteries are charged from PDB and provide power to the 1B8_CubePMT subsystems in the absence of solar power. Over voltage protection circuit keeps the PDB voltage within the operation limits. Switching and linear regulators step down the PDB

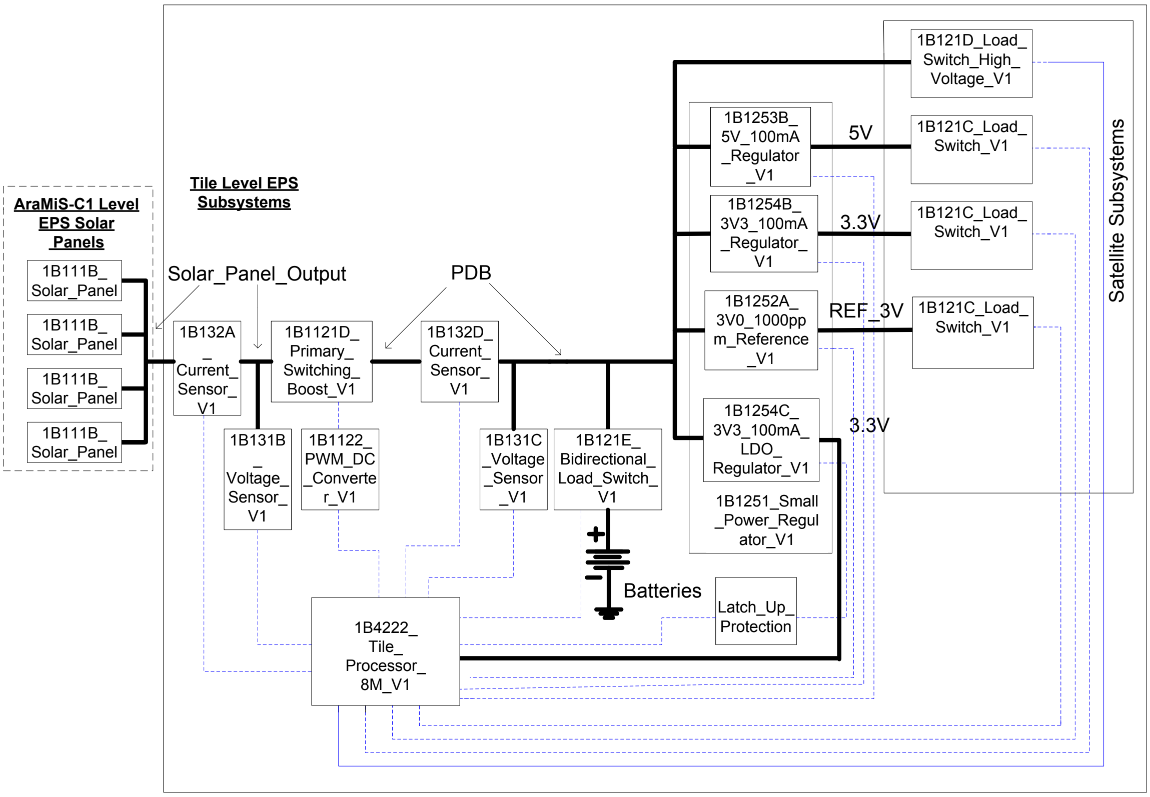

Figure 5.1: EPS Block diagram at tile level

voltage to different voltage levels required for all the subsystem components. Load switches supply and cutoff power from the subsystems through enable signal from the tile processor.

Housekeeping sensors such as voltage, current and temperature sensors are employed at different points of the EPS in order to monitor the operation and inform the tile processor in case of abnormalities. Block diagram of the EPS subsystem is shown in figure 5.1.

5.3 1B111B Solar Panel

Two triple junction GaAs solar cells with 26% efficiency are connected in series. Each cell generates 2.2V and their series combination provides an output voltage of approximately 4.4V. Bypass diode is connected in parallel to each solar cell which ensures proper operation of the single cell in case, one of them is damaged. Single solar cell power/voltage (P-V) characteristics of the 1B8_CubePMT module are plotted at two different temperatures (25˚C & 45˚C) as shown in figure 5.2. With increase in temperature, the performance of solar cell degrades in terms of output voltage and power. Figure 5.3 shows the photo of 1B8_CubePMT module solar panel side.

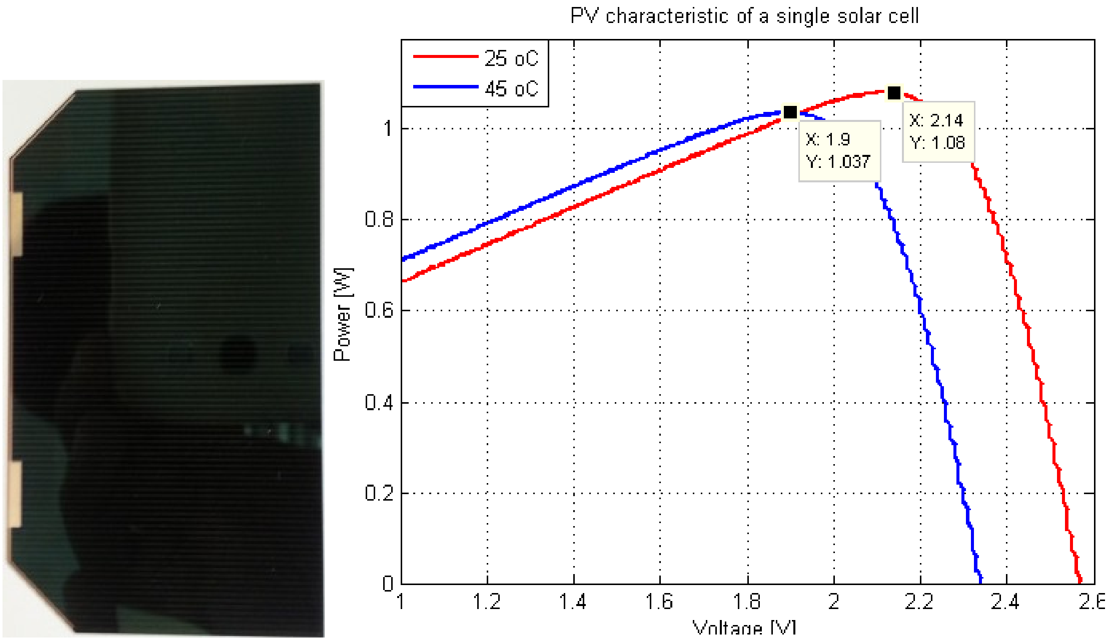

Figure 5.2. 1B8_CubePMT module single solar cell photo and P-V characteristics.

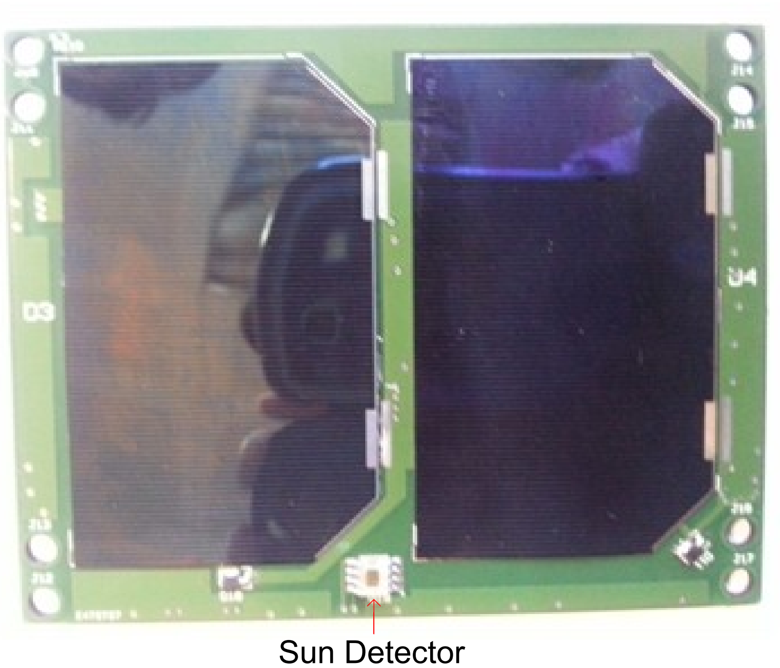

Figure 5.3: Photo of1B8_CubePMT module solar panel

5.3.1 1B111B Solar Panel Fault Tolerance Analysis

Simple fault tolerance analyses have been performed for two series connected solar cells ofAraMiS-C1. In this analysis, a case of short and open circuits of a single solar cell (single fault) is considered. The simulation circuit [16] of a single solar cell is shown in figure 5.3.

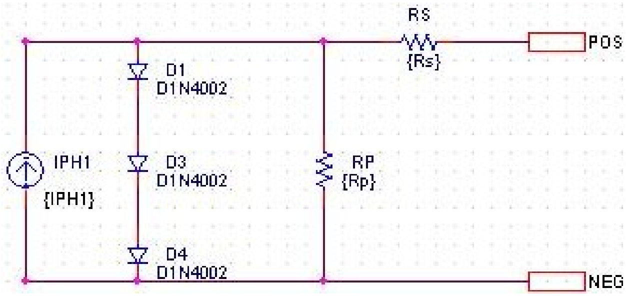

Figure 5.4. Simulation circuit of a single solar cell.

In figure 5.3 IPH, RS and RP are solar current, series and parallel resistor parameters respectively. By changing the values of these parameters one can easily simulate solar cells with different behavior.

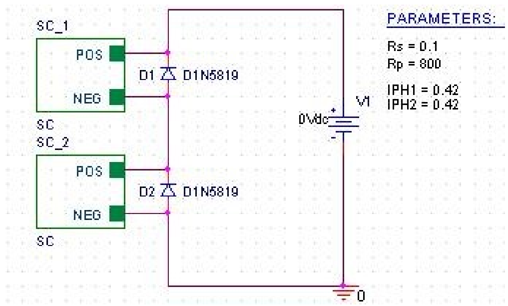

(a)

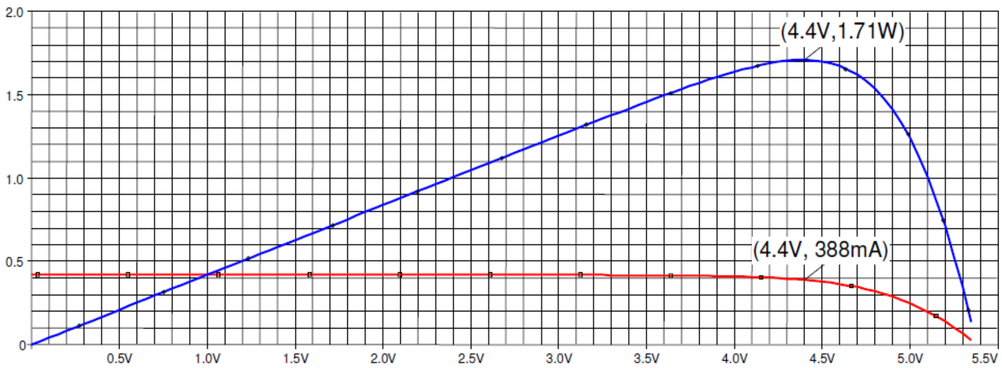

(b)

Figure 5.5: Two series connected solar cells (a) Schematic (b) Current and power vs voltage

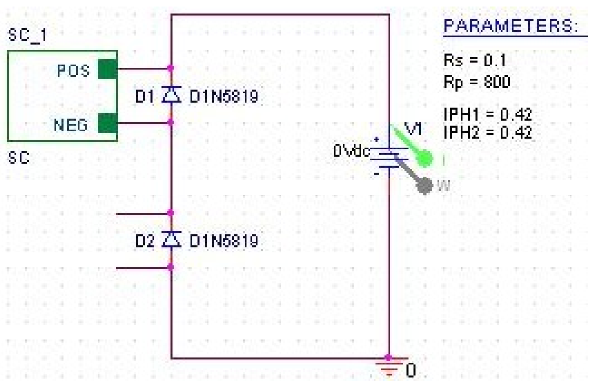

(a)

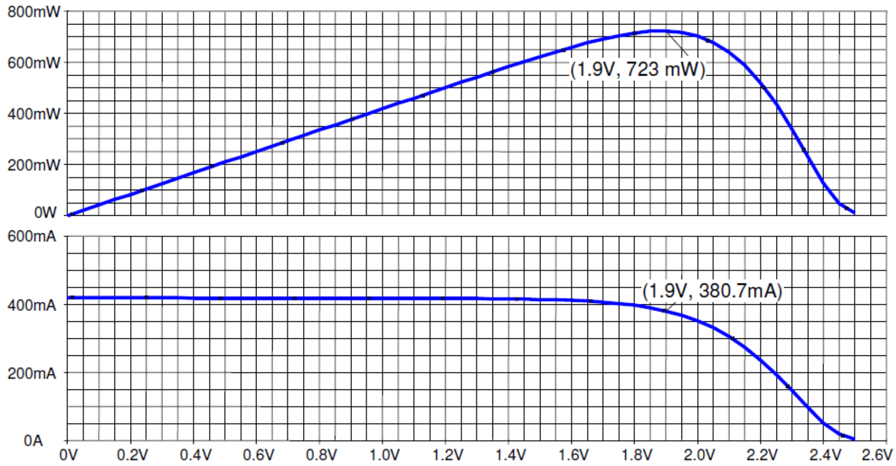

(b)

Figure 5.6: Two series connected solar cells with one cell open circuit (a) Schematic (b) Voltage, current and power plots

Figure 5.4 shows output current, voltage and power waveforms for the solar panel of AraMiS-C1. The output voltage and current for two solar cells connected in series are 4.4V and 388mA at their maximum power point (MPP). In figure 5.5 schematic and plots are shown (output voltage, current and power) for two series connected solar cells with one cell open circuit.

5.4 1B1121D Boost Converter

The boost converter is also called a step-up power converter because the required output voltage is always higher than the input voltage. The polarity remains the same and has no input output isolation. It has a continuous input and a pulsating output current. Output discontinuous current is due to the diode which conducts only for a portion of the switching cycle. The output capacitor supplies the load current for the rest of the cycle [17].

Ideal DC-DC converter is one which converts all the input energy to the output without losses. But in reality, it is impossible to realize such a system. Practical converters have losses due to internal resistance of the inductor, ESR of capacitors, MOSFET switching and on resistance, forward voltage drop on diodes and so on. We have to reduce all these losses to the lowest possible level in order to increase the overall efficiency of the converter.

Higher efficiency and minimum dimensions are main concerns for any converter. Boost converter is a type of switching-mode power supply containing two semiconductor switches (diode and transistor) and at least one energy storage element (an inductor). Our main aim is to increase the efficiency and reduce the area of the components for the converter. We used COTS components for our design. Each component for our design was selected on the basis of power loss analysis in order to achieve minimum power loss and maximum efficiency. This converter is designed for CubeSat standard power management tiles.

5.4.1 MPPT algorithms

Maximum power point (MPP) of the solar panel is not constant and varies with environment conditions as depicted in figure 5.2. In order to operate solar cells at MPP, converter with MPPT are needed. A simple boost converter just connects the solar panel module directly to the batteries. This forces solar panels to follow the battery voltage, which is not the suitable operating point and results in power loss [18]. MPPT boost converter steps up the solar panel voltage to PDB voltage level extracting maximum power from solar panel according to the environment conditions.

For MPPT, a number of algorithms are used, but the most common are open voltage (OV) method, perturb and observe (P&O) method, incremental conductance (IC) method, short current pulse (SC) method and constant voltage (CV) method [19-20]. Each algorithm has some advantages and disadvantages depend on the application. For the MPPT of 1B8_CubePMT EPS, the requirement is low power consumption, minimum space occupation and higher efficiency. So the preferred algorithm is constant voltage (CV) method. It is based on analog devices and does not require microcontroller for its operation which reduces the space occupation and power consumption [21-22].

Efficiency of EPS mainly depends on the boost converter. Components responsible for the efficiency are the boost converter's input/output capacitors, inductor, diode and MOSFET switch. Power losses through MPPT components are very low and can be neglected.

5.4.2 Components responsible for losses

This converter is designed for the AraMiS-C1 satellite power management tile, 1B8_CubePMT which is the most essential module and the boost converter is an integral part of it. The designed boost converter has one MOSFET, two capacitors, an inductor and a diode. It converts 4.4V to 14V. In MOSFET we have three main power losses. Power loss due to the internal resistance of MOSFET. Power loss due to the gate capacitance. The third one is due to rise and fall times of the switch. We analyzed different devices on the bases of these three parameters and selected the best one. Power loss in capacitors is mainly due to the ESR (Equivalent Series Resistance). In order to have low power losses in capacitors, we have to select them with minimum ESR values. Lower is the ESR of capacitor, higher will be the ripple current capability of the component. Similar to the capacitor, the internal resistance is also responsible for power loss in inductor. Boost converter efficiency decrease as the inductor internal resistance value increases. As a result, smaller the internal resistance of the inductor, smaller the power loss will be. The power loss through the diode is related to the current flowing through the diode and forward voltage drop on it. Due to the MOSFET on and off switching, current will never flow through the diode continuously. For this purpose we selected a diode with very low forward voltage drop.

Different components were analyzed in Spice simulations and the best amongst them were selected on the basis of minimum losses and small dimensions. After selection of proper components, the implemented MPPT boost converter resulted in 93% efficiency [23].

5.5 The proposed Boost Converter

5.5.1 PSpice Simulation Circuit

The PSpice simulation circuit diagram of the proposed boost converter is shown in figure 5.6. The whole system is divided into four parts which have two series connected solar cells, boost converter, driver and load. The two solar cells, simulated with current generators and diodes, are connected in series. They generates a voltage of 4.2V (each cell provides 2.1V). The boost converter transforms this 4.2V generated by solar cells to PDB (power distribution bus) voltage level which is 14V. The boost converter consists of a MOSFET, Schottky diode, an inductor and two ceramic capacitors. Schottky diode is used instead of a normal silicon diode because it has a very low forward voltage drop due to hot carrier metal-semiconductor junction. Low forward voltage drop result in less power consumption. Ceramic capacitors also have very low ESR values as compared to other capacitors results in reduced power dissipation.

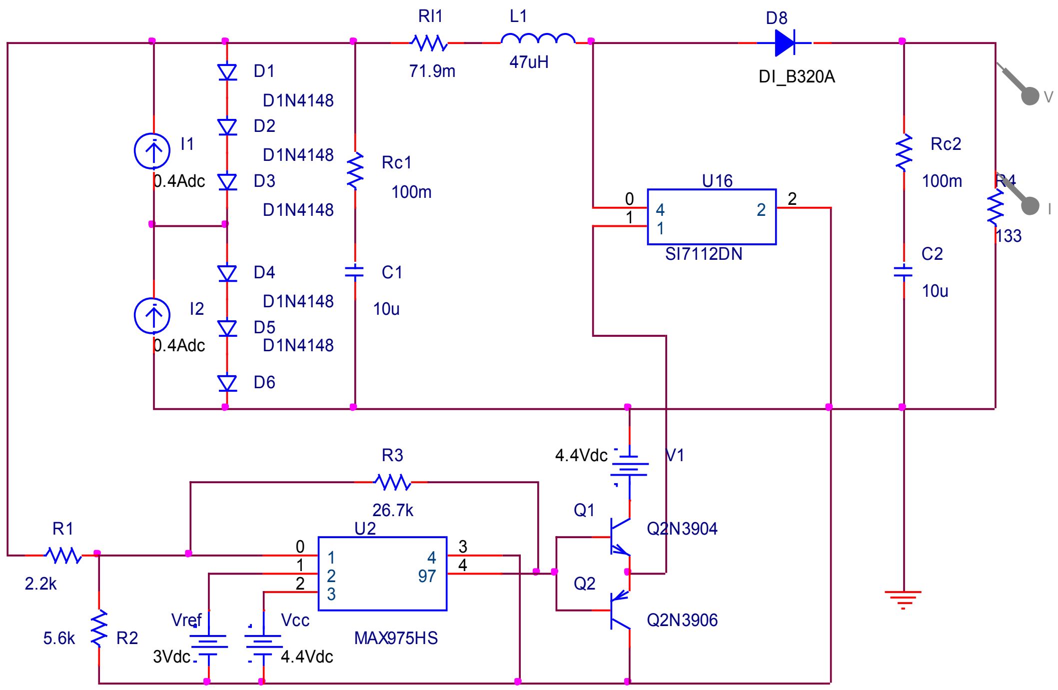

Figure 5.7: PSpice simulation circuit diagram of the proposed boost converter

The boost driver also called Maximum Power Point Tracker (MPPT), operate the two solar cells at its maximum power point. Comparator hysteresis loop is used to get the maximum power from the series connections of the two solar cells. Internal hysteresis helps the comparator to avoid oscillation due to noise signal. In this design a hysteresis of about 400mV is added to the comparator. PWM DC Converter fixes the reference voltage for the comparator.

MOSFET ON state

During ON state of the MOSFET switch Q1 is turned on by the control driver and diode D1 is off. Current flows through the inductor L1 and MOSFET Q1 to ground. In this stage the inductor stores energy in its magnetic field. On the load side the current flows from the capacitor C2 to the load. The duration of the on state is $T_{ON} = D \times T$, [24] where D is the duty cycle set by the control driver, T is the switching cycle. Duty cycle, D is the ratio between T_{ON} and T. Current paths and directions are shown in Satage-1 of figure 5.7.

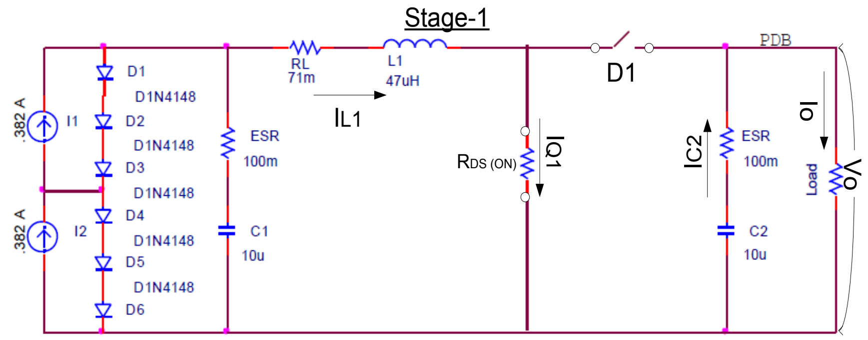

Figure 5.8: Power stage-1 of the proposed boost converter

MOSFET OFF state

During this stage the control driver turns off the MOSFET switch Q1 and diode D1 is turned on. Current flows through the inductor L1 and diode D1 to the output filter capacitor C2 and load. The duration of the off state is $T_{OFF} = (1–D) \times T$. During this state, current paths and directions are shown in Satage-2 of figure 5.8.

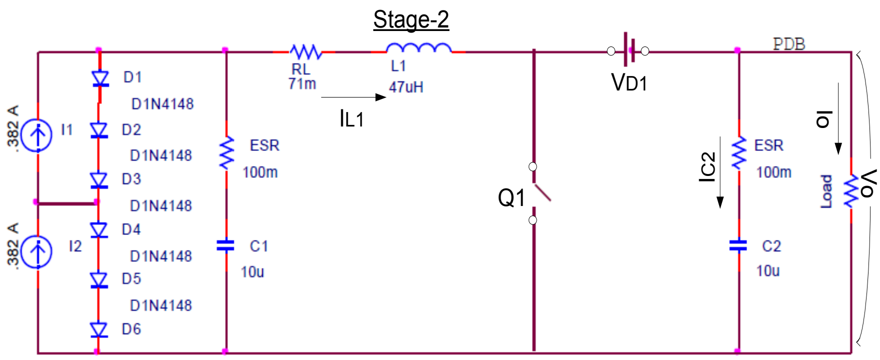

Figure 5.9: MOSFET OFF state of the proposed boost converter.

5.6 Boost converter components selection on the basis of power loss analysis

Improper selection of components for the boost converter can lead to useless design. Components should be selected through a precise and accurate selection method. In this paper, components for the boost converter were selected on the basis of minimum dimension and losses. After the selection of proper components and calculation of their losses efficiency was computed for the whole system.

In this design, components responsible for the efficiency of the boost converter is input and output capacitors, inductor, diode and transistor switch. Power losses through the driver components are very low and can be ignored.

Power loss analysis of different components was done and selected the best one with minimal losses [25].

5.6.1 MOSFET Power Loss Analysis

An n-channel MOSFET is used as a switch in this design. The main advantage of using n-channel MOSFET is that its properties are close to an ideal switch. It has a very low ON resistance as compared to p-channel MOSFET and other transistors. In ON state it is almost short circuit due to lower R_{DS} (on). While in off state it is an open switch. So power loss is very low in n-channel MOSFET [26].

MOSFET has three major power losses. Power loss due to drain to source on resistance (R_{DS} (on)) of the MOSFET when the switch is closed. Gate to source internal capacitance power loss and third one is due to the rise and fall times of the MOSFET switch.

Different MOSFET devices were used and analyzed on the basis of these three parameters for the boost converter and selected the best one. These parameters values are given in table 5.1 for different devices.

MOSFET MODEL	MOSFET TYPE	R_{DS}(on) (mΩ)	Rise Time (ns)	Fall Time (ns)	Q_{GS} (nC)	Dimensions
IRF7750	P-Channel	55	54	210	5.8	3×6.4×1.2
IRLU7807	N-Channel	18.2	28	3.5	7.00	6.7×10.4×2.4
FDP6030B	N-Channel	24	20	16	3.2	9.5×15.9×4.8
IRF7807	N-Channel	25	1.2	2.2	2.86	5×6.5×1.75
SI7112	N-Channel	8.2	15	15	6.2	3.3×3.3×1.12
IRL7833	N-Channel	4.5	50	6.9	13.8	11.4×17.8×4.8

Table 5.1: MOSFET devices tested on the basis of low power loss and small dimensions

5.6.1.1 Conduction Power Loss

Conduction power loss is due to drain to source internal resistance (R_{DS} (on)) of the MOSFET, when the switch is closed. The lower the value for R_{DS} (on) the lower will be the conduction power loss through the MOSFET.

In table 5.1 R_{DS} (on) values for different MOSFET devices are given. It is clear that the P-channel MOSFET have very high R_{DS} (on) value as compared to N-channel MOSFET. MOSFET model IRL7833 has the lowest R_{DS} (on) value, but it is not suitable for the design discussed in this paper because of higher dimensions. SI7112 was selected for this project because of low dimensions and comparatively low R_{DS} (on) value.

The power loss through the R_{DS} (on) is given by (5-1).

$$P_{cond} = I^2{}_{RMS} \times R_{DS}(on) \tag{5-1}$$

Where I_{RMS} is the root mean square (RMS) value of current through MOSFET and is given by (5-2) below [27];

$$I_{RMS} = \sqrt{\frac{(\mathrm{I_{max}})^2}{3} \times \frac{T_{ON}}{T}} \tag{5-2}$$

Where I_{MAX} is maximum current value through the MOSFET. It is obtained from the PSpice simulation of the boost converter. PSpice simulation current through MOSFET is shown in figure 5.9.

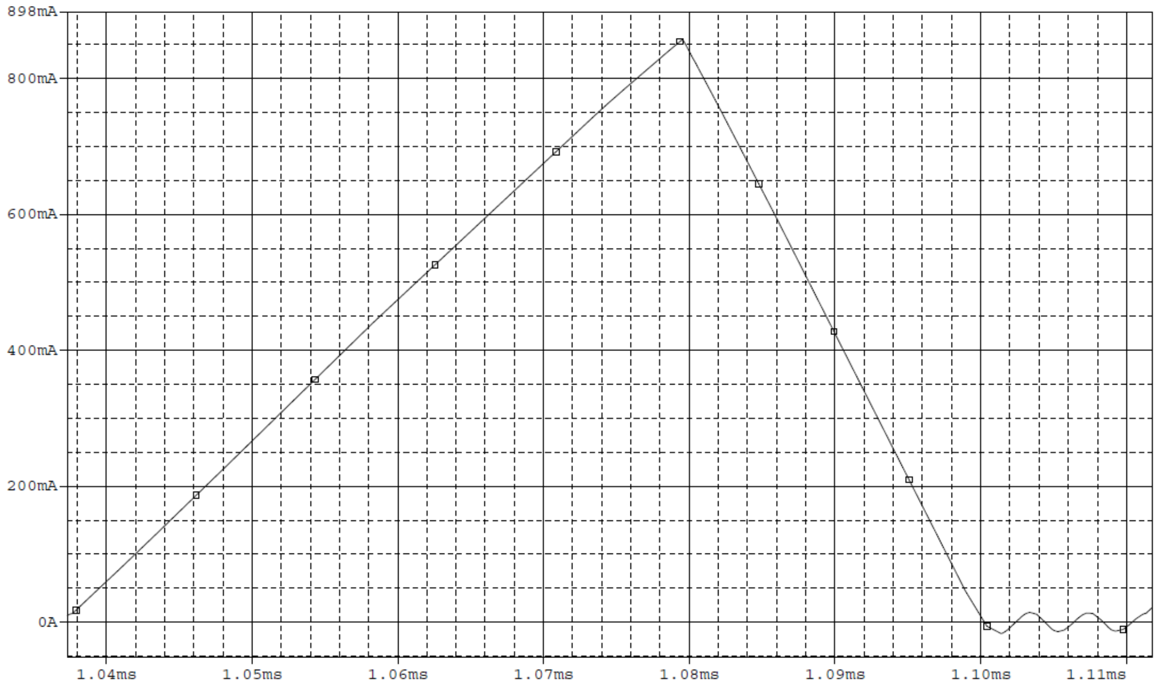

Figure 5.10: PSpice simulation current through MOSFET

Table 5.2 shows the conduction power loss and other parameters required for its calculation.

R_{DS}(on) (mΩ)	I_{MAX} (mA)	I_{RMS} (mA)	T (msec)	T_{ON} (msec)	P_{cond} (mW)
8.2	864	366	0.074	0.04	1.10

Table 5.2: Different parameters of MOSFET SI7112

5.6.1.2 Gate Power Loss

Charge is accumulated in Gate to source junction capacitor (C_{GS}) when a MOSFET is switched on. During on state it allows current to flow from the drain to source junction. A specific amount of charge is required to accumulate on gate to source junction before the switch is closed. It depends on the Q_{GS} parameter of the MOSFET. Larger Q_{GS} value will required greater amount of charge. Similarly during the switching off of the MOSFET, first you have to remove all the accumulated charge on the gate to source junction. This process results in power loss which is related with the switching speed of the MOSFET. The power loss in gate to source junction of the MOSFET during switching is calculated and given by (5-3) [28];

$$P_{Gate} = Q_{GS} V_{GS} f \tag{5-3}$$

Q_{GS} (C)	V_{GS} (V)	f (kHz)	P_{Gate} (mW)
6.2×10^{-9}	5	14	0.434

Table 5.3: Different parameters for SI7112 MOSFET gate power loss

5.6.1.3 Switching Power Loss

MOSFET cannot be switched on and off in zero time. Each MOSFET has its own rise and fall time to achieve the supply and ground voltages. While the device is switched on and off, the voltage and current are not zero. So there is a power loss associated with the switching of the MOSFET, we call it rise and fall time or switching power loss. Parameters require for its calculations are given in table 5.4.

τ_{rise} (ns)	τ_{fall} (ns)	V_{DS} (V)	I_{DS} *(mA)*	f *(kHz)*	P_{SW} (mW)
15	15	14	366	14	1.08

Table 5.4: Parameters for rise and fall time power loss

The power loss of the MOSFET during the rise and fall time is given by (5-4) below [28];

$$P_{SW} = K(\tau_{rise} + \tau_{fall}) \times V_{DS} \times I_{DS} \times f \tag{5-4}$$

Where K is a constant factor whose value is from 1/6 up to 1/2. Here we choose it 1/2.

5.1.1.1.Total Power Loss in MOSFET

By adding three losses in (5-1), (5-3) and (5-4), total power loss of the MOSFET is given by (5-5) below;

$$P_{MOSFET} = P_{cond} + P_{Gate} + P_{SW} \tag{5-5}$$

5.6.2 Input and output Capacitor Power Loss

The function of capacitor in boost converter is to maintain a constant voltage level and minimize the ripples. The equivalent series resistance (ESR), equivalent series inductance (ESL) and capacitance (C) are the main parameters which limits the output voltage ripples.

Power loss in capacitor is mainly due to the ESR. In order to have low power loss in capacitor, one has to select the capacitor with lower ESR. Ceramic capacitors have extremely low ESR than others such as tantalum or electrolytic components. Low is the ESR of capacitor, higher will be the ripple current capability of the component. Further, the ESR associated with capacitors has a direct relationship to the capacitor's ability to deliver energy when needed. So the lower the ESR, the more efficient the component is.

Apart from ESR we have also to see the capacitor size. In table 5.5 different capacitors are given along with their sizes and ESR values. First, different Tantalum capacitors were used, but they have higher ESR values and as a result high losses. The minimum ESR value of a Tantalum capacitor appropriate for this project is 250mΩ, which is still too high and is not suitable. Ceramic capacitors have low ESR values as compare to Tantalum capacitors of the same capacitance. Its ESR is very low and is suitable for this project. The dielectric material for the ceramic capacitor should be X5R or better. In case of low dielectric material, there will be losses in capacitance due to DC bias or temperature. So it was decided to use chip capacitor with part number "C1210C106K3RAC". It is a ceramic capacitor with temperature coefficient X7R.

ESR value of ceramic capacitors is related with the operating frequency. We found from the vender datasheets that at 14 kHz (operating frequency), the ESR value for C1210C106K3RAC is 100mΩ as shown in table 5.5.

Capacitor Type	Model Number	Capacitance (µF)	Dimensions (mm×mm×mm)	ESR (mΩ)
Ceramic	C1206C106K4RAC	10	3.2x1.6x1.6	100
Ceramic	C0805C106K4PAC	10	2x1.25x1.25	100
Ceramic	C1210C106K3RAC	10	3.2x2.5x2.5	100
Tantalum	T491C106K035AT	10	6.0x3.2x2.8	1600
Tantalum	T491A106M016AT	10	3.2x1.6x1.8	700
Tantalum	T495X106K035AT	10	4.3x7.3x4	250

Table 5.5: Different Ceramic and Tantalum capacitors dimension and ESR values

Power loss through the input capacitor (P_{C1}) and output capacitor (P_{C2}) are given by (5-6) below [27];

$$P_{C1}, P_{C2} = I^2{}_{RMS} \times ESR \tag{5-6}$$

I_{RMS} of input and output capacitors can be obtained from (5-2), while the maximum value of current for these capacitors are obtained from the PSpice simulation and is given in table 5.6. PSpice simulation current through input capacitor is shown in figure 5.10.

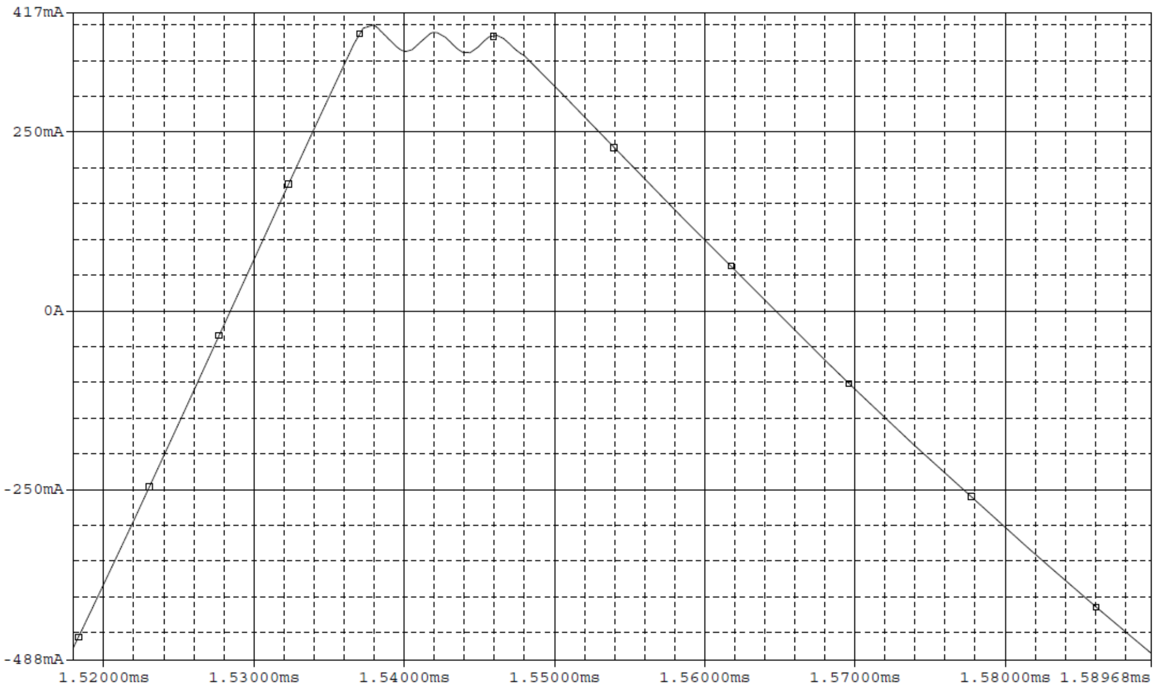

Figure 5.11: PSpice simulation current through input capacitor (C1)

I_{MAX}(C1) (mA)	I_{MAX}(C2) (mA)	I_{RMS}(C1) (mA)	I_{RMS}(C2) (mA)	P_{C1} (mW)	P_{C2} (mW)
875	564	762	324	32	10.5

Table 5.6: Parameters for input and output capacitors power loss.

5.6.3 Inductor Power Loss

In boost converter, the function of inductor is to maintain a constant current or to avoid abrupt change in current. Inductor stores energy in its magnetic field due to the flow of current and de-energize when the input current value decreases, in order to maintain constant current.
Internal resistance is responsible for power loss through the inductor. The boost efficiency decrease as the value of internal resistance increases. As a result, the smaller the internal resistance of the inductor, the smaller the power loss will be. Internal resistance is associated with the size of the wire gauge of the inductor. As the wire gauge increases the internal resistance decreases which allows more current to pass through the inductor.

When ac voltage is applied across the inductor, power is also dissipated in the inductor's core, called core loss. But in our design we are not concern with core loss because we are not working on ac voltage. Parameters for inductor power loss are given in table 2.7.

Different inductors were analyzed and inductor with part number 513-1050-1-ND was selected for this project. It has an inductance value of 47µH and an internal resistance of 71.9mΩ. The power loss through the inductor is given by (5-7) below [28];

$$P_L = I^2{}_{RMS} \times R_{\text{internal}} \tag{5-7}$$

I_{RMS} (mA)	R_{internal} (mΩ)	P_L (mW)
452	71.9	14.7

Table 5.7: Parameters for inductor power loss.

5.6.4 Diode Power Loss

Power losses in a power diode are [29];

- Conduction power loss
- Switching power loss
- Reverse leakage current power loss

Conduction power loss is due to the forward voltage drop on diode. Switching losses occurs when a diode switch from conducting state to off state or vice versa. These states changes normally take some time which results in power loss. Power diodes also conduct current when reversed biased. This reverse leakage current results in power loss which is temperature dependant.

Schottky diode is used instead of a normal silicon diode because it has a very low forward voltage drop due to metal-semiconductor junction. Low forward voltage drop result in less power consumption. In low voltage applications switching losses are almost zero in Schottky diodes.

Reverse leakage current losses are also negligible in these diodes. So we considered only conduction power losses in Schottky diodes.

Schottky diode B320A with a forward voltage drop V_F=0.35V is selected for this project. Power loss through diode [29] is only conduction losses and is given by (5-8).

$$P_D = I_{avg} \times V_F \tag{5-8}$$

Where I_{avg} is the average current through the diode which is obtained from PSpice current simulation through the diode. Parameters for the diode power loss are given in table 5.8.

I_{avg} (mA)	V_F (V)	P_D (mW)
122	0.35	42.7

Table 5.8: Parameters for diode power loss.

5.6.5 Total Power Loss

Total power loss through the boost converter is obtained by adding power losses through the individual components, is given by (5-9). Power losses and dimensions of the components used in boost converter design are given in table 5.9.

$$P_{LOSS} = P_{MOSFET} + P_{C1} + P_{C2} + P_L + P_D \tag{5-9}$$

Selected Components	Losses (mW)	Dimensions (mm^3)
MOSFET, SI7112 (Q_9)	2.614	3.3×3.3×1.12
Input Capacitor (C_{32})	32	Package 1210
Output Capacitor (C_{33})	10.5	Package 1210
Inductor (L_2)	14.7	12.50×12.50×7.00
Diode, B320A (D_7)	42.7	2.896×4.597×2.438

Table 5.9: Selected components for the boost converter on the basis of power losses and dimensions.

5.6.6 Boost converter simulation results

Efficiency of the boost converter depends on the losses in the converter. Lower the losses higher will be the efficiency [30]. Power flow of the converter is given by (5-10)

$$P_{in} = P_{out} + P_{LOSS} \tag{5-10}$$

Where P_{in} is the input power, P_{out} is the output power and P_{LOSS} is the power wasted inside the converter calculated in the previous section.

Input power to the boost converter (P_{in}) is fed from the solar cells. PSpice simulation circuit diagram of the proposed boost converter is shown in figure 5.6**.** Two solar cells supply an input current of 0.382mA and total voltage of 4.2V. P_{in} is given by (5-11).

$$P_{in} = I_{in}V_{in} \tag{5-11}$$

Output power of the boost converter (P_{out}) is obtained from the PSpice simulations of the output voltage (V_o) and output current (I_o) waveforms are shown in figure 5.11 and figure 5.12 respectively. P_{out} is given by (5-12).

$$P_{out} = I_oV_o \tag{5-12}$$

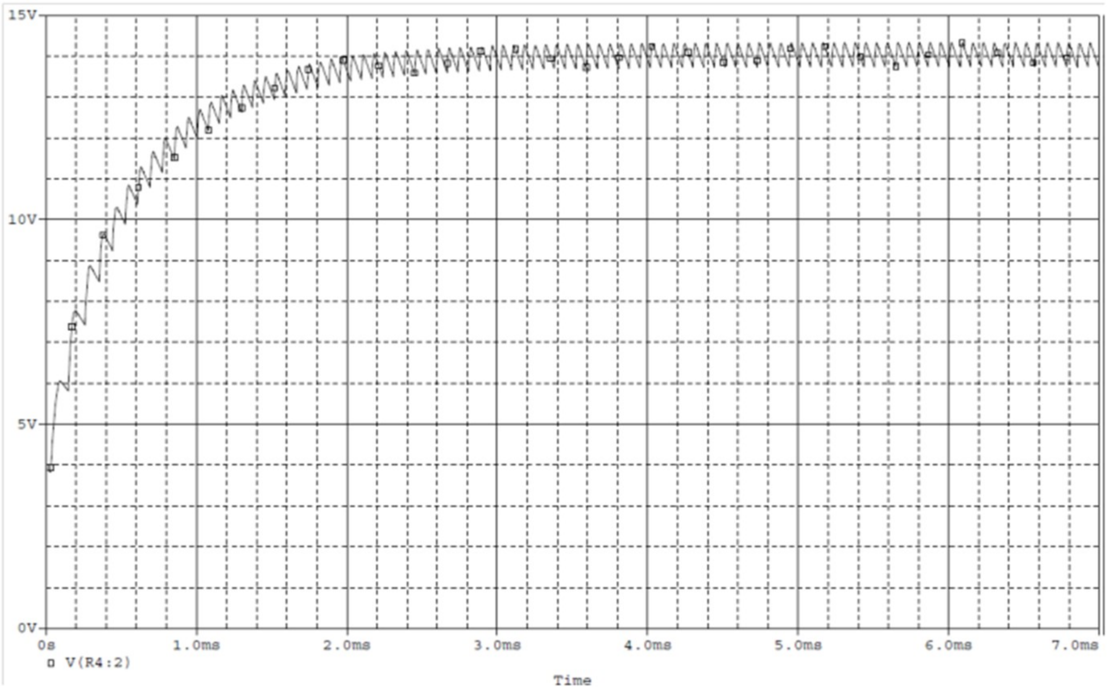

Figure 5.12: Output voltage waveform of the Boost converter PSpice Simulations

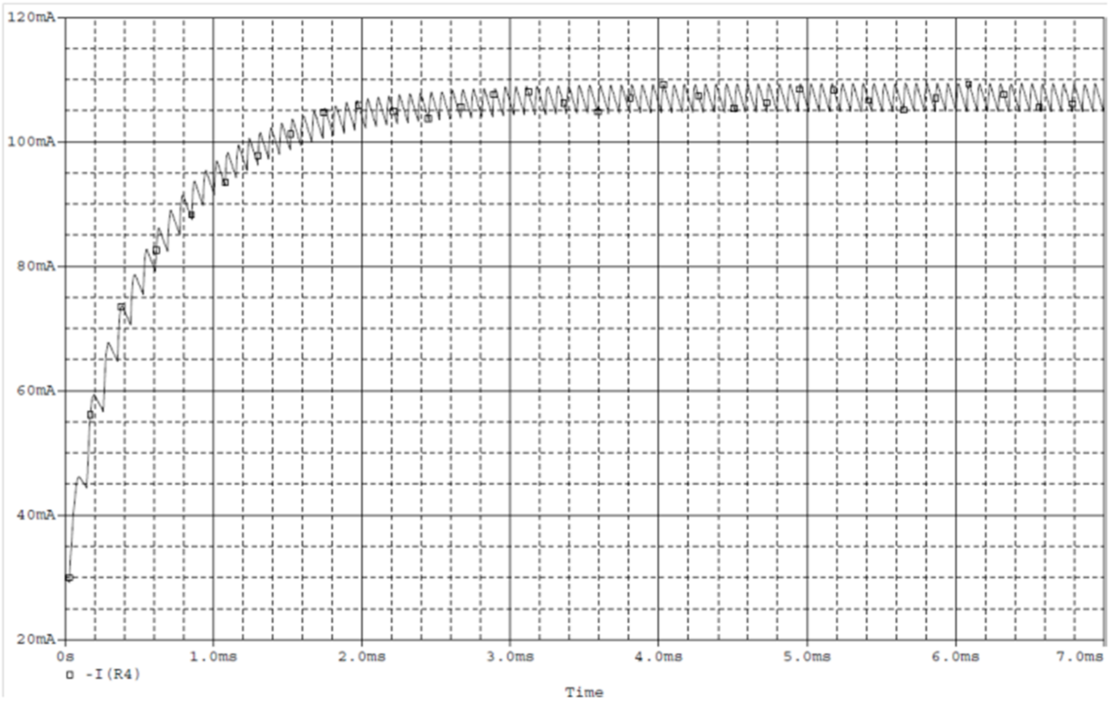

Figure 5.13: Output current waveform of the Boost converter PSpice Simulations

Efficiency (η) is the ratio between output and input power. There is no perfect DC-DC converter, which has zero losses and 100% efficiency. Efficiency is given by (5-13);

$$\%\eta = \frac{P_o}{P_{in}} \times 100 \tag{5-13}$$

Boost converter discussed in this paper, achieved an efficiency of 93% by using suitable low loss components and circuit techniques. Powers and efficiency values of the boost converter are given in the following table 5.10.

P_{in} (mW)	P_{LOSS} (mW)	P_{OUT} (mW)	*Efficiency (η)*
1604	103	1498	93%

Table 5.10: Power and efficiency values of the converter.

5.7 Implemented Boost Converter

After achieving the desired simulation results, the boost converter was implemented using the selected components as the schematic is shown in figure 5.13. A brief operation of the MPPT boost converter is described here. Solar panel charges boost converter input capacitor (C_{32}). Voltage on C32 is scaled by the resistive divider network (R30 and R32) and applied to the non-inverting input (IN+) of the comparator (U7) [31]. A constant voltage of 2.9V was applied to the inverting input (IN-) of the comparator through the pads of the resistors R80 and R89 as shown in the schematic of the implemented boost converter of figure 5.12. For the inverting input voltage a PWM-DC-converter block can also be used, but for the testing purpose a constant voltage was applied. When voltage on C32 becomes 4.165V, IN+ terminal voltage of U7 becomes 3V (greater than the inverting input (IN-) voltage (2.9V)), the output of U7 goes high and turns on MOSFET (Q9). During this stage C32 discharges through inductor (L2) and Q9 to GND. When C32 reaches 3.835V, IN+ terminal of U7 goes below IN- terminal and turns off Q9. During this stage, once again C32 voltage increases and when reaches 4.165V, the cycle repeats as shown in figure 8.3. The input and output voltage waveforms of the boost converter are shown in figure 8.4.

The Switching of *U7* at two different input voltage limits V_H= 4.165V and V_L =3.83V is due to hysteresis window (V_{HB}) set by the resistive network (R_{30}, R_{31} & R_{32}). Usually internal hysteresis is designed into comparators which keep them away from oscillation due to noise signal [32]. Here an external hysteresis is generated by resistive network and is used to switch the comparator at two different input voltage levels. Charge and discharge of C_{32} from the solar panel after a definite interval depends on the hysteresis window (V_{HB}) define by the comparator resistive network R_{30}, R_{31} and R_{32}. The suitable V_{HB} for the designed boost converter is 330mV at V_{cc} = 4V. Here by selecting R_{31}=26.7KΩ, one can find R_{30} = 2.2kΩ from (5-14) :

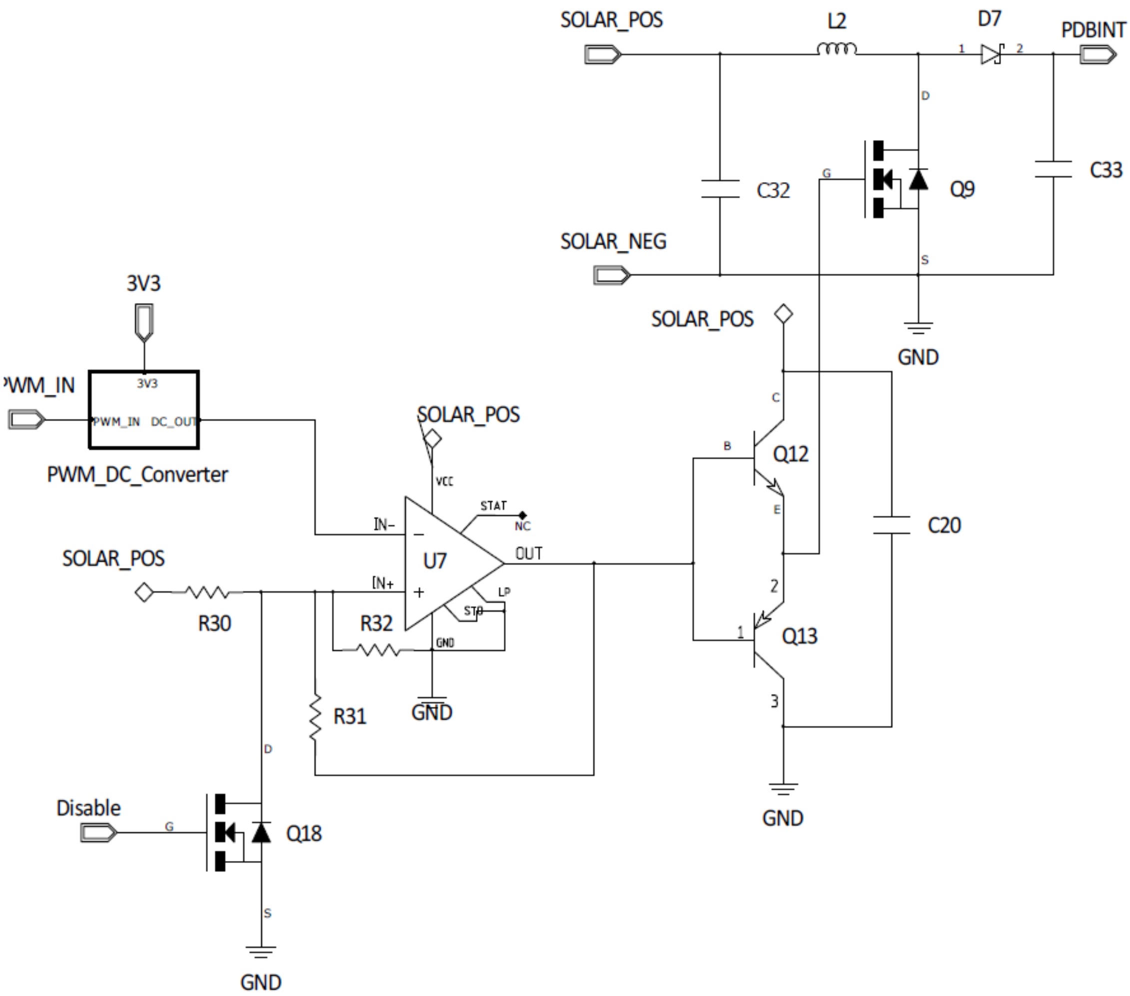

Figure 5.14: Schematic of the implemented boost converter

$$R_{30} = R_{31}\left(\frac{V_{HB}}{V_{CC}}\right) \tag{5-14}$$

Reference voltage (V_{ref}) value for the comparator can be found from (5-15):

$$V_H > V_{ref}\left(1+\frac{V_{HB}}{V_{CC}}\right) \tag{5-15}$$

Here $V_{ref} < 3.8$V, and is fixed to 3V. R_{32} found using (5-16) is 5.6kΩ.

$$R_{32} = \frac{1}{\left[\left(\frac{V_H}{V_{ref}\times R_{30}}\right)-\left(\frac{1}{R_{30}}\right)-\left(\frac{1}{R_{31}}\right)\right]} \tag{5-16}$$

In figure 5.13 transistors Q_{12} and Q_{13} drive MOSFET Q_9 in order to provide the V_{cc} and ground voltage levels on switching of U7. Transistor Q_{18} disables the boost converter on a disable signal from tile processor. Figure 5.15 shows the UML class diagram of the implemented switching boost (1B1121D).

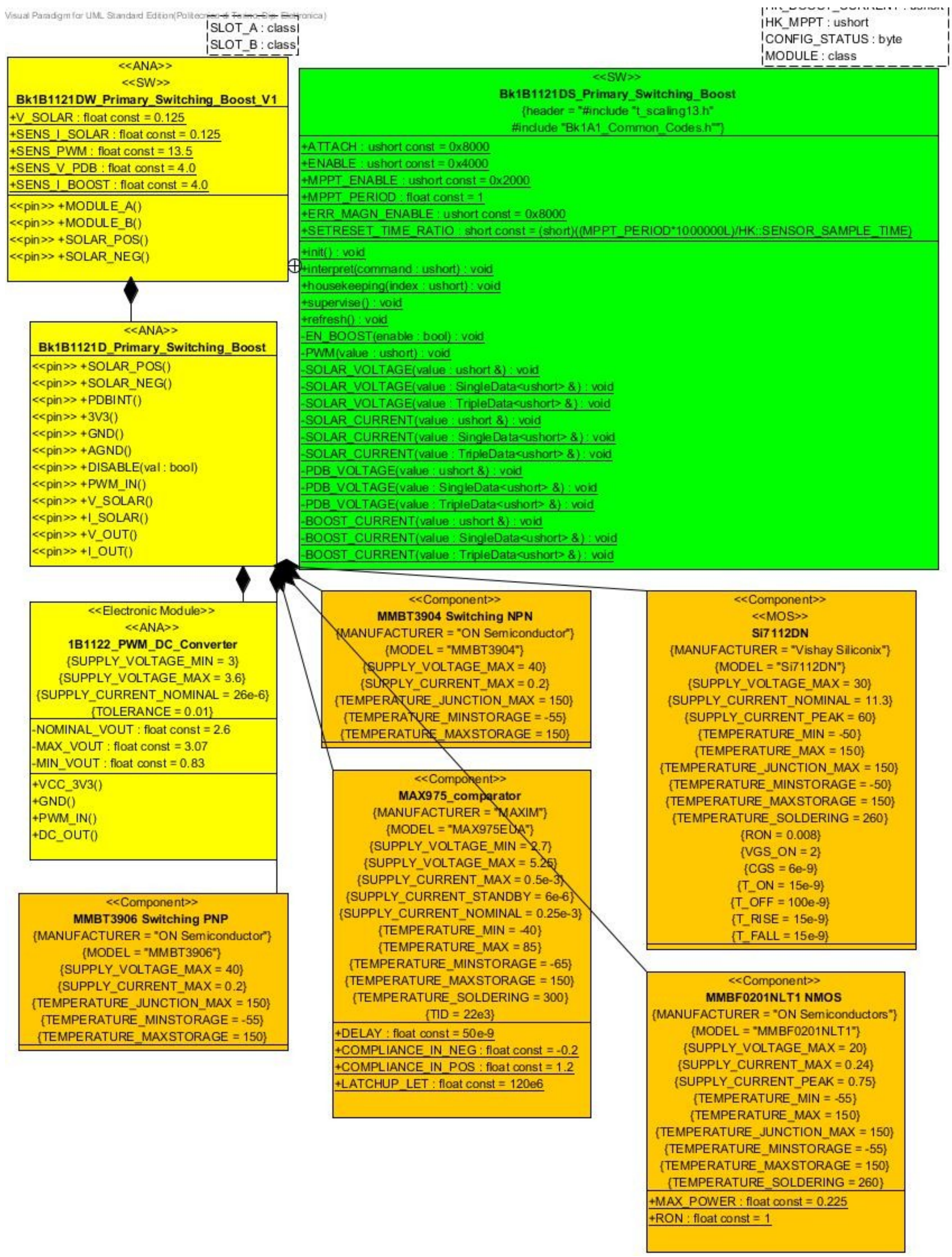

Figure 5.15: Primary switching boost UML class diagram.

5.8 1B121E Bi-directional Load Switch

Batteries are connected to the PDB through bi-directional load switch. This switch charge the batteries from the PDB when solar power is available, while in absence of solar power batteries provide power to the PDB through the bi-directional load switch. This switch is enabled from the tile processor. Schematic of the load switch is given in Appendix A.

5.9 Batteries

Energy is stored on a single pack of NiCd [33] rechargeable batteries (external to the 1B8_CubePMT module). The pack contains ten NiCd elements each provides 1.2V. Storage capacity of each NiCd cell is 0.9Ah. Batteries are charged from PDB through bi-directional load switch and provide power to AraMiS-C1 satellite in the absence of solar power. A pack of 10 NiCd batteries is shown in figure 5.16.

Figure 5.16: A pack of 10 NiCd batteries used on AraMiS-C1

5.10 1B115B Over Voltage Protection

Over voltage protection circuit keeps the PDB voltage within the operation limits. For this purpose two series connected zener diodes were used. Each of the diode has a break down voltage limit of 10V and their series connection keep the PDB voltage below 20V. The schematic is shown in Appendix A.

5.11 1B1251 Small Power Regulators

The PDB voltage level has to be down converted to low voltage levels (i.e. 3V, 3.3V and 5V) used by different subsystem components. For this purpose, 1B8_CubePMT has two linear and two switching regulators. Linear regulators have small dimensions and require little number of auxiliary components but they have lower efficiencies and hence high power losses. Linear regulators result in low power losses when, either there is a low voltage difference between input and output of the regulator or low current is drawn from the regulator. Switching regulators have higher efficiencies but have higher dimensions and require more auxiliary components [34]. The choice between linear and switching regulators depends on the application. Figure 5.17 shows the UML class diagram of small power regulators (1B1251).

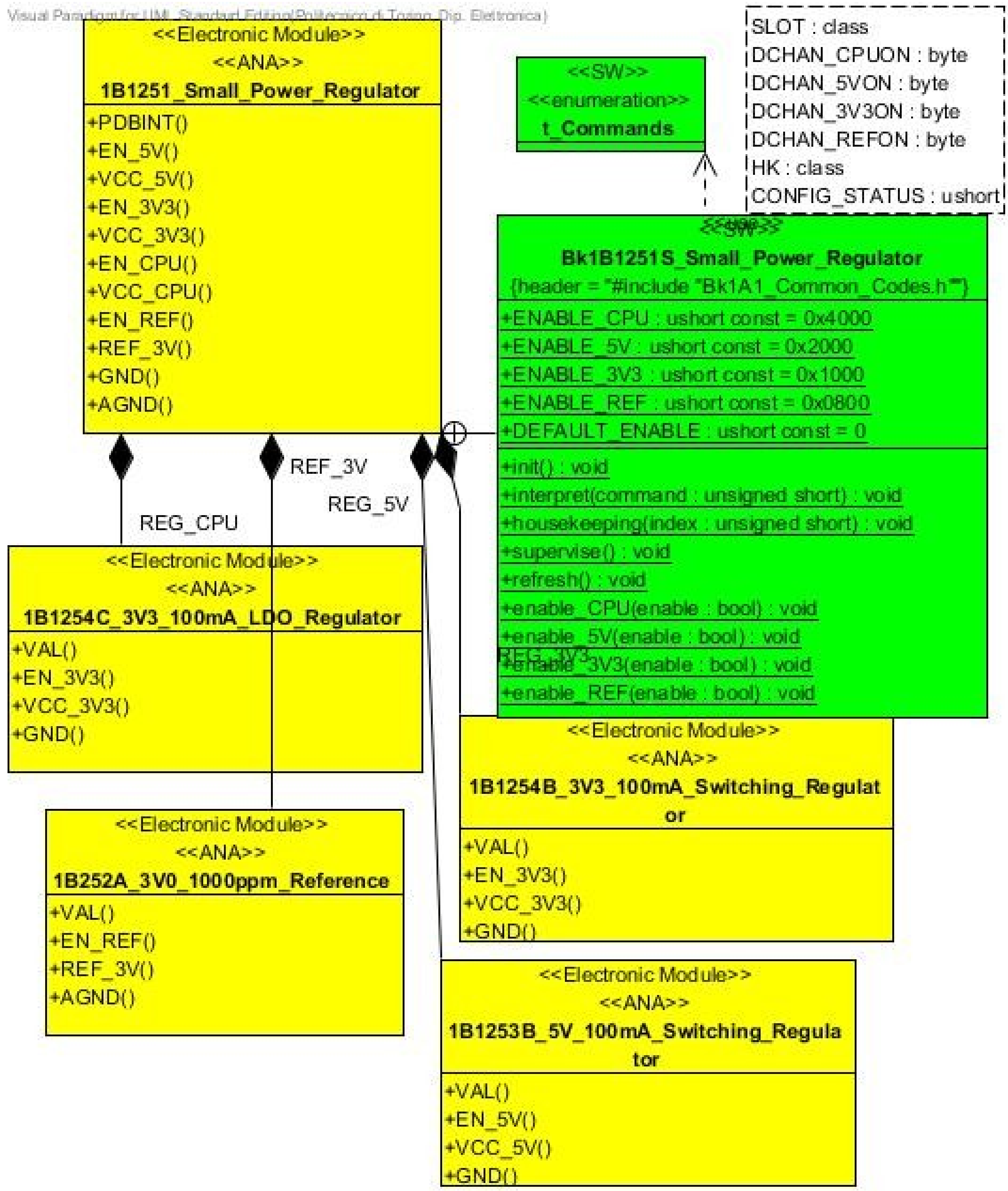

Figure 5.17: Small Power Regulators UML class diagram

5.11.1 1B1252A 3V Reference Regulator

One linear regulator is used for the 3V reference voltage supply. It steps down 5V input to 3V reference voltage. Output current and input/output voltage difference is low which results in negligible power loss, therefore a linear regulator is used. It is enabled from the tile processor. The schematic of the 3V reference voltage supply [35] is shown in figure 5.18.

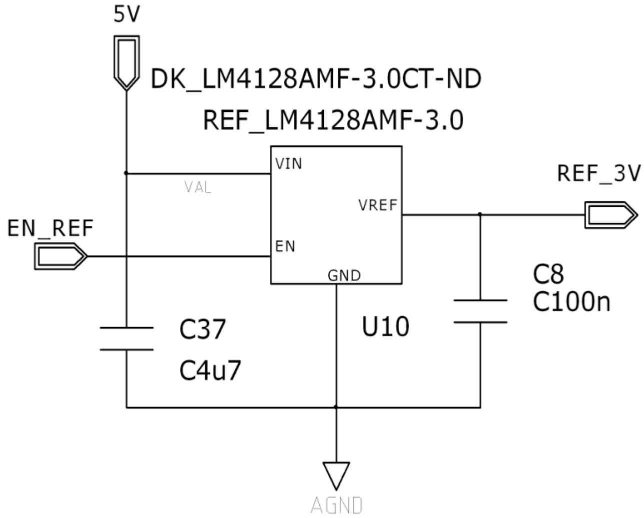

Figure 5.18: Schematic of the 3V reference voltage supply

5.11.2 1B1254C 3.3V Linear Regulator

Second linear regulator converts PDB voltage to 3.3V. This regulator gives supply to tile processor. The input/output voltage difference is high but the supply current is very low (312µA in active mode), which results in negligible power loss. The purpose of using separate regulator for tile processor is to make it independent on other subsystems and whenever PDB is available, the tile processor is ready for its job. This regulator is enabled from the PDB. The schematic of the 3.3V supply [36] is shown in figure 5.19.

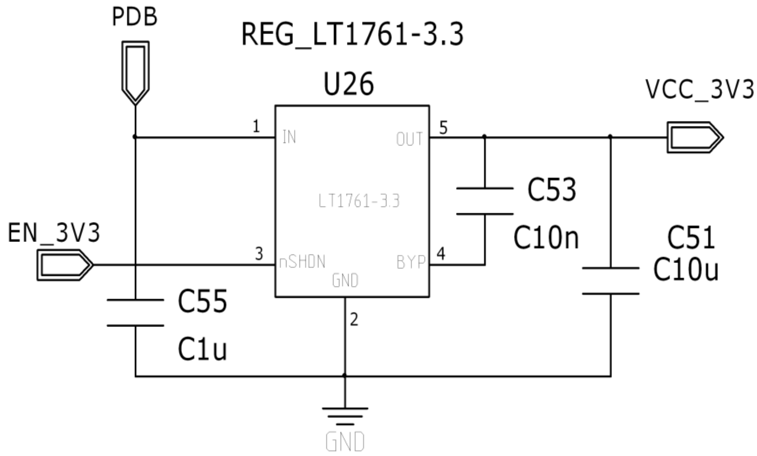

Figure 5.19: Schematic of the 3.3V voltage supply

5.11.3 1B1254B 3.3V Switching Regulator

One switching regulator provides 3.3V to all the subsystem components except the tile processor (separate 3.3V regulator is used for tile processor). High current is drawn from this supply; therefore a switching regulator is used. It converts PDB voltage level to 3.3V and enables from tile processor. The schematic of the 3.3V voltage supply [37] is shown in figure 5.20.

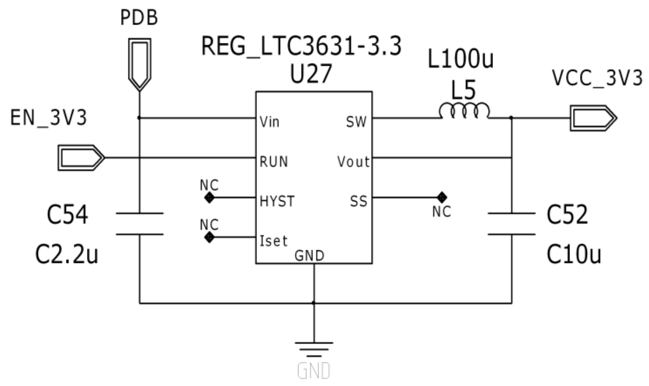

Figure 5.20: Schematic of the 3.3V voltage supply

5.11.4 1B1253B 5V Switching Regulator

Second switching regulator provides 5V to all the subsystems components. Again a high current is drawn; therefore a switching regulator is used. It also converts PDB voltage level to 3.3V and enables from the tile processor. The schematic of the 5V voltage supply [37] is shown in figure 5.21.

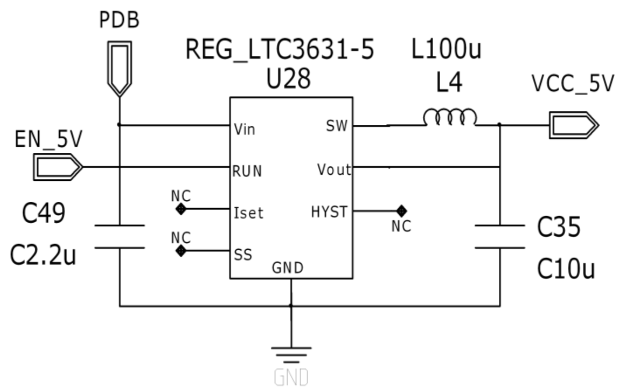

Figure 5.21: Schematic of the 5V voltage supply

1B8_CubePMT regulators testing results are given in chapter 8.

5.12 1B121 Load Switches

In order to control the power consumption of the subsystems, load switches are mounted at the input of each subsystem. These switches supply and cutoff power from the subsystems through enable signal from the tile processor. There are two types of load switches on the 1B8_CubePMT module. One is for high voltage (PDB) supply and the second is for low voltage (5V/3.3V/3V). The schematic of the load switch is given in Appendix A.

5.13 Housekeeping Sensors

For housekeeping and monitoring purposes, the 1B8_CubePMT module incorporates voltage, current and temperature sensors. These sensors are mounted at different points on the module. In case of anomalies, the tile processor takes necessary actions to protect system from any possible damage.

5.13.1 1B131B & 1B131C Voltage Sensors

1B8_CubePMT module consists of two voltage sensors having voltage limits 10V (1B131B) and 20V (1B131C). These sensors constantly monitor the output voltage of solar panel and boost converter. UML class diagram of 1B131 voltage sensors is shown in figure 5.22. Schematics of the 10V and 20V voltage sensors mounted on the output of the solar panel and PDB are shown in figure 5.23.

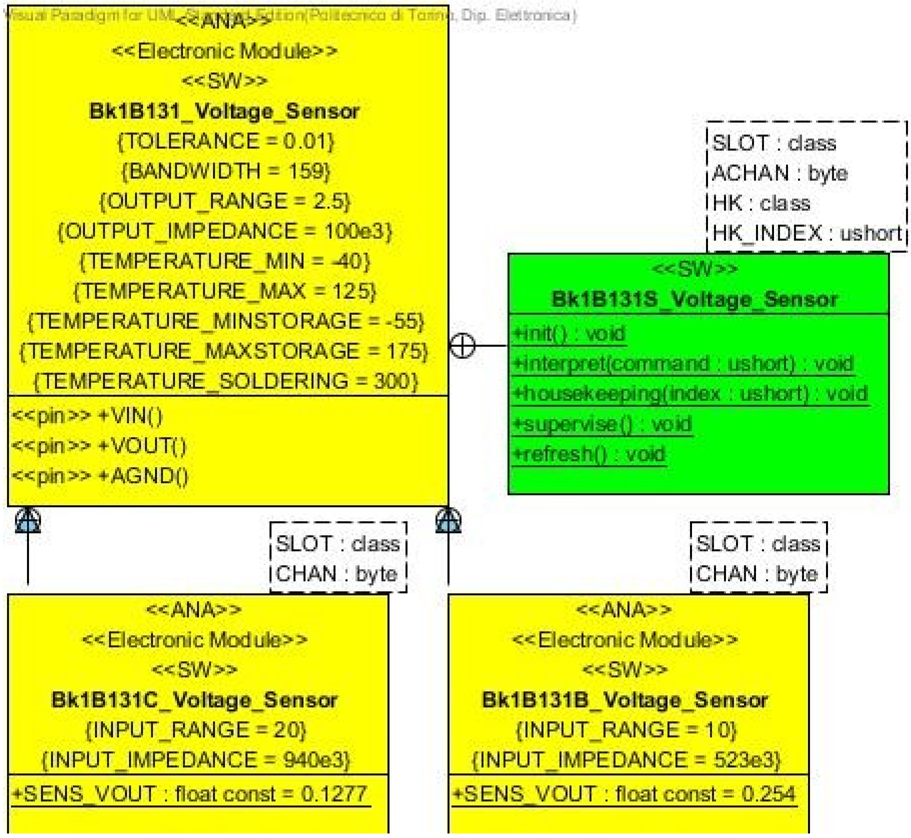

Figure 5.22: UML class diagram of 1B131 voltage sensors

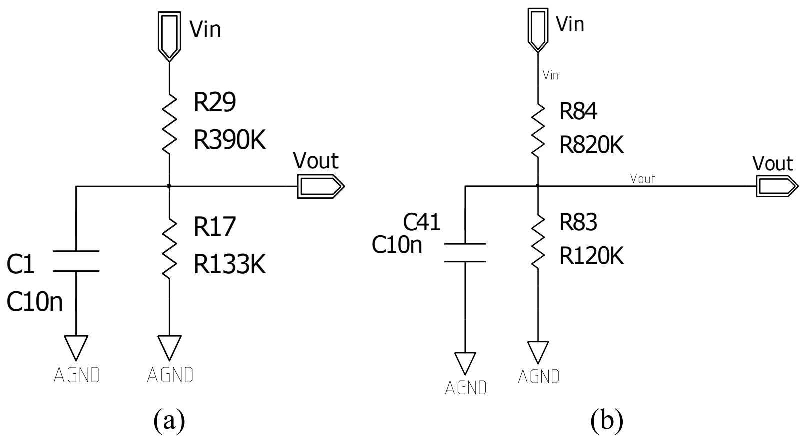

Figure 5.23: Schematic of voltage sensors (a) 10V (b) 20V

Analog output voltage (V_{out}) connected to ADC of tile processor, is given by (5-17);

$$V_{out} = V_{in} \times \frac{R_{17}}{R_{17} + R_{29}} \tag{5-17}$$

By observing schematic from the output side, it behaves as a low pass filter. The sampling frequency ($f_{sampling}$) is set by the value of C1 and R_{eq} (*R17//R29*). In order to avoid aliasing, the criteria given in (5-18) should be satisfied;

$$f_{sampling} \geq 2 \times \frac{1}{2\pi C_1 R_{eq}} \tag{5-18}$$

From (5-18) it is evident that $f_{sampling} \geq 321$Hz in order to avoid aliasing. Figure 5.24 shows that ADC internal circuit of the MSP430 microcontroller, has a internal resistor (R_i) and a capacitor (C_i).

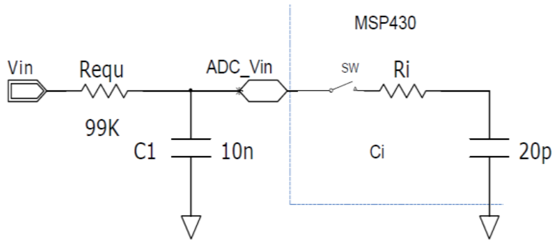

Figure 5.24: Equivalent circuit of 10V voltage sensor attached on MSP430 ADC pin

R_i has a small value around 10Ω and can be neglected, while C_i is coming in parallel with C_1 and can add error. It shifts sampling frequency point and can add aliasing to the system. To avoid aliasing, a suitable value of C_1 should be chosen. The charge distribute between C_1 and C_i: when switch is open charge at C_i (Q_i) is zero and at C_1(Q_1) has the total charge Q_t as given in (5-19):

$$Q_i = C_i V_i = C_i \times 0 = 0$$
$$Q_1 = C_1 V_1 = Q_t \tag{5-19}$$

When switch (SW) is closed, C_i start charging from Q_t. During transitional state the two capacitors are at the same voltage as given by (5-20):

$$\begin{aligned} Q_i &= C_i V_x = \Delta Q \\ Q_1 &= Q_t - \Delta Q = C_1 V_x \end{aligned} \tag{5-20}$$

Where V_x is the C_1 voltage after SW closing and is given by (5-21);

$$V_x = V_1 \frac{C_1}{C_1 + C_i} \tag{5-21}$$

In order to find out the relative error introduce by C_i, compare the difference (V_1-V_x) with original signal V_1, given by (5-22):

$$e_{V1} = \frac{\Delta V}{V_1} = \frac{|V_1 - V_x|}{V_1} = \frac{C_i}{C_i + C_1} \tag{5-22}$$

In order to reduce the error, C_{17} should have a very high value as compared to C_i. MSP430 with 12bit ADC and supply voltage of 3.3V has a quantization error 0.0805%. The voltage error (e_{v1}) should be smaller than the quantization error (0.0805%). It reflects that C_1 value should be very high as compare to C_i, in order to keep the error smaller. The selected C_1 value is 500 times greater than Ci.

5.13.2 1B132A & 1B132D Current Sensors

1B8_CubePMT contains two current sensors that monitor the solar panel output (1B132A) and output of boost converter (1B132D) having maximum current limit of 625mA and 152mA, respectively. Figure 5.25 shows the UML class diagram while figure 5.26 shows generic current sensor schematic where output voltage (V_o) is connected to the ADC of the tile processor and is given by (5-26) [38];

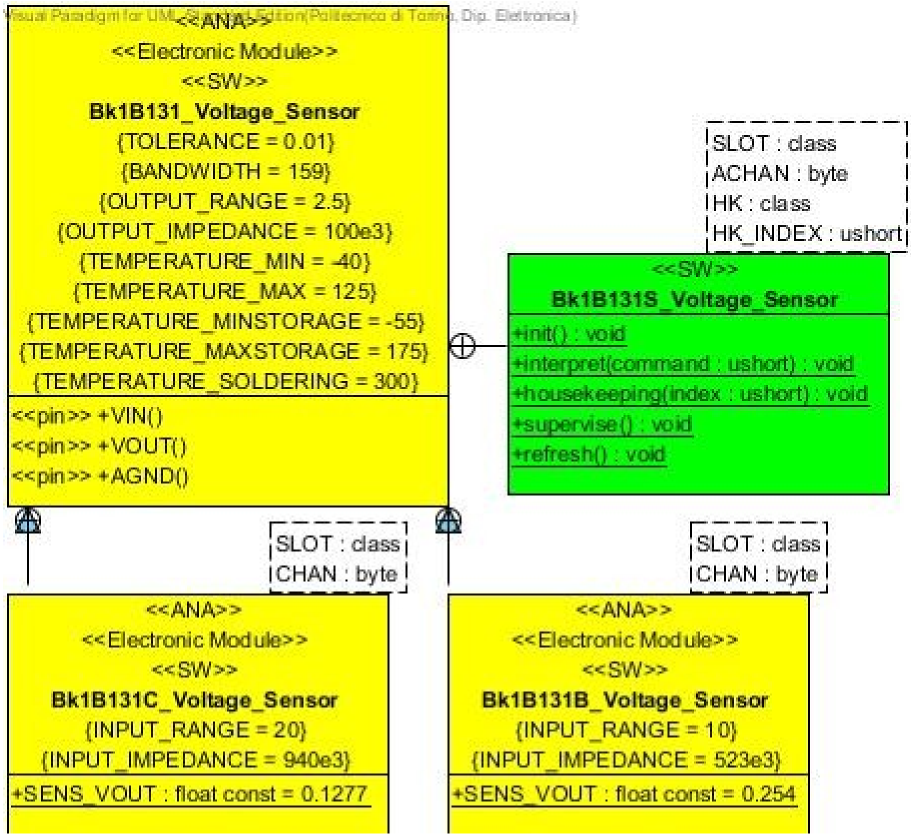

Figure 5.25: UML class diagram of 1B131 Current sensors

$$V_o = \frac{I_{\_Sense} \times R_{\_Sense} \times R_{\_out}}{5k\Omega} \tag{5-23}$$

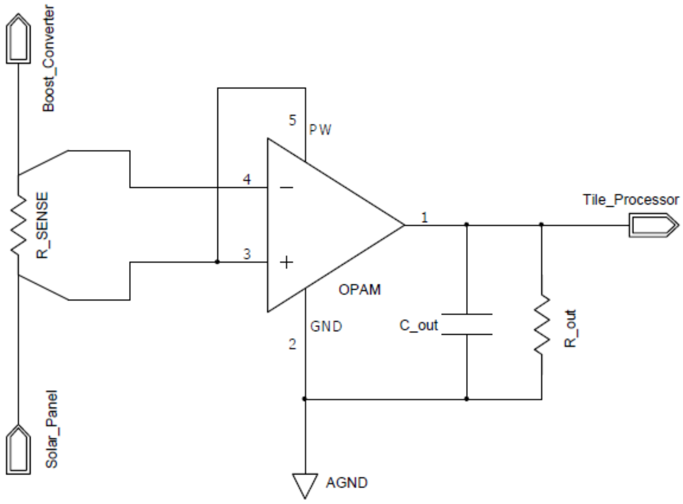

Figure 5.26: Current sensor of 1B8_CubePMT module (Mentor Graphics schematic).

By observing schematic in figure 5.19 from the output side, it behaves as low pass filter. The sampling frequency ($f_{sampling}$) is set by the value of *C_out* and *R_out*. In order to avoid aliasing, criteria in (5-24) should be satisfied:

$$f_{sampling} \geq 2 \times \frac{1}{2\pi C_{\_out} R_{\_out}} \tag{5-24}$$

5.13.3 1B133A Temperature Sensor

1B8_CubePMT module has one temperature sensor which is a glass protected NTC thermistor and has a temperature range from -30˚C to 70˚C. Output voltage of the sensor is linearly proportional to temperature. Its resistance range varies between 2.2kΩ ~100kΩ, highly accurate with 1% of tolerance. Output voltage of the sensor is linearly proportional to the temperature. Mentor Graphics schematic of the implemented temperature sensor is shown in figure 5.27 while UML class diagram is shown in figure 5.28. Temperature versus output voltage and power curves of the temperature sensor are shown in figure 5.29.

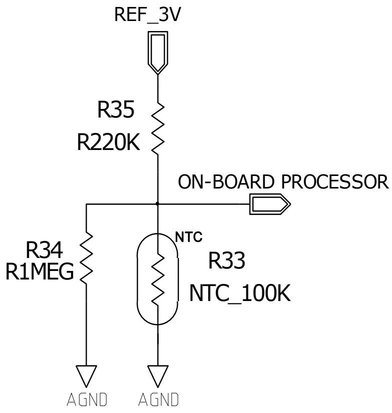

Figure 5.27: Schematic of the temperature sensor

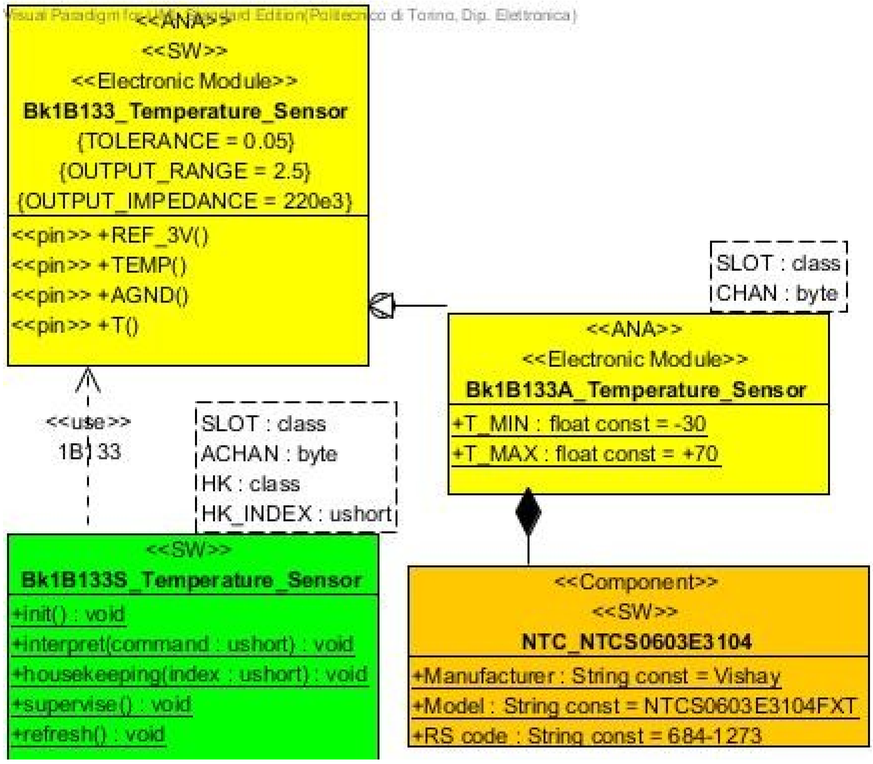

Figure 5.28: UML class diagram of 1B33A temperature sensor

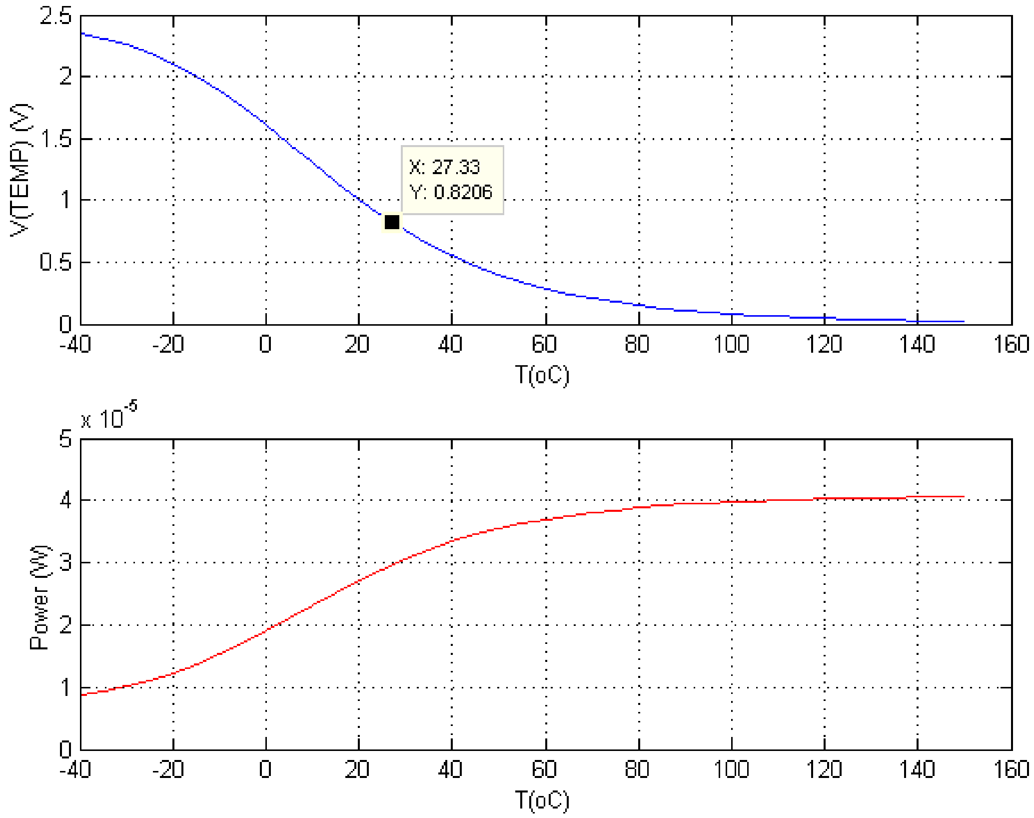

Figure 5.29: Temperature versus voltage and power curves of 1B133A Temperature Sensor

5.14 AraMiS-C1 Power Budget

5.14.1 Power Sources

The only power source of AraMiS-C1 are the four solar panels, which cover as many faces of the satellite. Each solar panel is about 2×70×40mm^2 that is 5600mm^2.
Sun power density at LEO is about 1362 W/m^2, and the average persistence of satellite in the day is about 60%. By taking into account that only one or at most two panels are exposed at a time at sunlight.

- When one panel, it is perpendicular to sunlight and has an equivalent panel surface of 5600mm^2, average power from sun is about 7.63W. Average efficiency of the solar cell is 26% which gives 1.98W power at output terminal.
- When two panels are 45^o from sunlight, the total equivalent panel surface, taking into account their size and their average inclination is about 7840mm^2. Optical power from the sun is10.678W. Average efficiency of the solar cell is 26% which gives 2.77W power at output terminal.

5.14.2 Energy Storage

Energy is stored on a single pack of NiCd rechargeable batteries. This pack contains ten NiCd element each 1.2V, for a total of 12V. Battery capacity of each NiCd is 0.9Ah. Maximum available energy is then 10.8Wh, equivalent to 38.9kJ.
All these batteries are charged from the power distribution bus which in turn is charged from the four solar panels via an hysteretic switching boost converter. Efficiency of the boost converter is 93%, therefore 1.84W is the expected average power available at the PDB, which is used to recharge batteries. Expected recharge time is therefore for the single cell is 5.8h for the whole system is 58h. Worst case efficiency (discharge energy/charge energy) of battery, over the temperature range and radiation environment is 80%. It results an average power available for all electronic systems of 8.64W.

5.14.3 Power Sinks

AraMiS-C1 is designed for low power consumption. All components have been chosen in commercial low-power domain. Typical power consumption of the tile systems (power management tile, communication tile and payload) is summarized in table 5.11, where both peak and average power are measured respectively. Subsystem that consume high power such as in the case of magnetorquer subsystem given in table 5.12, the solution is to keep the other subsystems either in idle state or completely switched off when magnetorquer subsystem is active.

Subsystems	Power sink	Duty cycle (%)	Power when active (mW)	Number of Subsystems	Total active Power (mW)	Avg. power (mW)
Power Management Tile	Magnetometer	1	89.3	4	357.2	3.572
	Gyroscope	5	45	4	180	9
	Housekeeping Sensors	5	5	4	20	1
	Tile Processor	100	5.5	4	22	22
Communication Tile	UHF Communication (Receive Mode)	8.33	50	1	50	5
	S-Band Communication 2.4GHz receiver	8.33	50	1	50	5
	Standard telemetry transmission, 435MHz: active max. 2s every minute	3.33	5600	1	5600	185
	Standard telemetry transmission, 2.4GHz: active max. 2s every minute	3.33	3000	1	3000	100
Payload		100	5	1	5	5

Table 5.11: Peak and average power of AraMiS-C1 subsystems

Magnetorquer System	Power Sink (W)	Activation time per month (s)	Energy (joule)
Magnetic Torque Actuator	0.254	21	5.59
Magnetorquer Coil (Four coils in series)	1.35	21	83.7

Table 5.12: Energy per maneuver for the magnetorquer system of AraMiS-C1

5.14.4 Budget Verification

The NanoSatellite power budget can be verified by satisfying the criteria concluded in the following three steps.

1. Peak power consumed (P_{peak}) by all the subsystems should always be less than the maximum power available from the batteries (P_{max_bat}).
2. Average power consumed (P_{avg}) by all the subsystems should always be less than the average solar power (P_{solar_avg}).
3. Energy required per satellite night (E_{night}) should always be less than the battery energy storage (E_{store}).

Power budget calculated for AraMiS-C1 is given in table 5.14.

Peak Power Consumed (P_{peak})	5.627W
Average Power Consumed (P_{avg})	335.57mW
Energy/night (E_{night})	1.19kJ
Peak Solar Power (P_{solar_peak})	2.77W
Average Solar Power (P_{solar_avg})	1.98W
Battery Energy Storage (E_{store})	38.9kJ
Battery Maximum Power (P_{max_bat})	10.8W
Battery Energy Life Cycle ($LC_{battery}$)	4.3years (500cycles)
Packet Energy (S-band @ 500kbps, 256 Bytes)	4.096mJ
Packet Energy (UHF @ 9600bps, 256 Bytes)	213.3mJ

Table 5.13: Power Budget of AraMiS-C1

Maximum power (5.6W) is consumed during active UHF transmission. During this stage all other subsystems are switched off except tile processor and payload. The power consumed during this stage is peak power given in the above table. Satellite orbit period is 100 minutes, and about 40% of the total time, it remains in dark zone. The enegy consumed per night is 1.19kJ. Battery energy storage is 38.9kJ which results in battery energy life cycle of 4.3 years.

P_{peak}, P_{avg} and E_{night} are less than P_{max_bat}, P_{solar_avg} and E_{store} respectively as clear from table 5.13. Power budget calculated for AraMiS-C1 satisfy the power budget criteria. This means that EPS of AraMiS-C1 will guarantee nominal operation without troubles.

Chapter 6

Attitude Determination Sensors (ADS)

6.1 Introduction

Attitude determination and control system (ADCS) is the fundamental element for successful mission in modern satellites. The ADCS can be further subdivided into two different subsystems, Attitude Determination System (ADS) and Attitude Control System (ACS). The ADS provides adequate satellite orientation information to the tile processor. The tile processor compares the present attitude with the predefined state and compute the time and amount of torque. This comparison output is then used by the ACS which rotates the satellite into desired direction. ADCS block diagram is shown in figure 6.1.

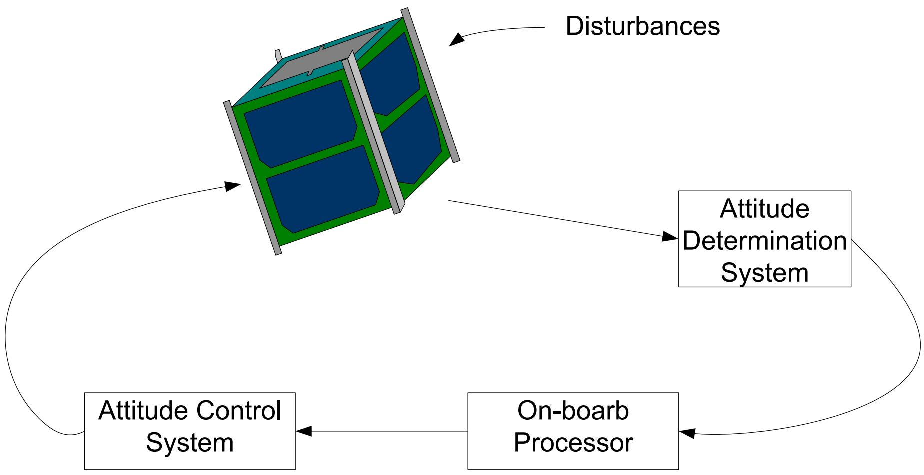

Figure 6.1: ADCS block diagram.

In this chapter we will discuss three types of attitude sensors designed for AraMiS-C1.

6.2 Attitude Determination System

The most commonly used references for satellite attitude determination are the sun, the center of the Earth, a known star or the magnetic field of the Earth [39]. Due to constraints on budget, size and power consumption for 1B8_CubePMT, inexpensive COTS components and unique algorithms has been utilized for reliable attitude determination. 1B8_CubePMT has three types of attitude sensors which are:

- Sun directional sensor
- Two-axis magnetometer and

- Gyroscope.

1B8_CubePMT is mounted on the external four faces of AraMiS-C1. Table 6.1 shows the number of attitude sensors in each axis of AraMiS-C1 satellite.

Type of Attitude Sensor	Number of attitude sensors in each axis		
	X-axis	Y-axis	Z-axis
Magnetometer	2	2	4
Gyroscope	2	2	0
Sun Sensor	2	2	1

Table 6.1: Number of attitude sensors in each axis

6.2.1 1B235 Sun Sensor

Solar cell CPC1822 is utilized as sun detector [40]. It is a monolithic photovoltaic string of solar cells. In presence of sun or artificial light it generates a voltage at its output which is sufficient to drive ADC of tile processor. Sun sensor was tested at AM0 (solar simulator available in our laboratory), has an open circuit voltage of 4.75V and short circuit current of 75uA. Output resistor keeps the output voltage value within the range of tile processor (0V~2.5V). Figure 6.2 shows schematic of the sun sensor. The open circuit voltage of a solar cell is proportional to the cosine of the angle of incident light as given in (6-1). Schematic of sun sensor is shown in figure 6.2.

$$V_o = V_{max} \cos(\theta) \tag{6-1}$$

Where V_{max} = 1.65V +/- 20%.

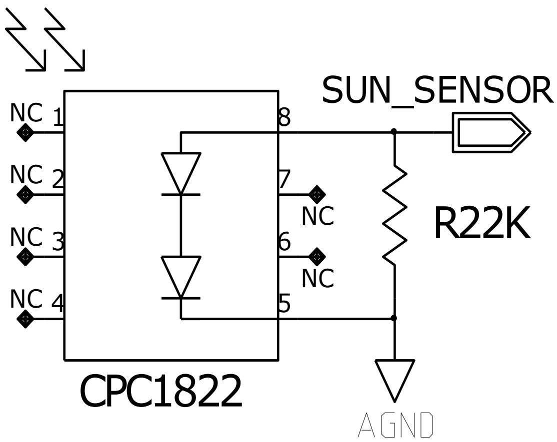

Figure 6.2: Schematic of sun sensor.

6.2.2 Magnetometer

In LEO satellites, interaction with earth magnetic field is a significant means of controlling orientation. Magnetometers are extensively used as attitude sensor for NanoSatellites because of their low-price, light weight and low power consumption [41]. Magnetometer measures the earth magnetic field and tile processor compares it with the predefined values.

6.2.3 Magnetometer technologies

Due to the widespread utilization of small magnetic sensors in the field of automobile, aerospace, mobile phones, medical devices etc, for different purposes, they are continuously evolving. At the moment, numerous types of magnetic sensor technologies are available in the market for geomagnetic field mapping. They may be categorized according to the magnetic properties, applications, measurement capabilities (vector or scalar) etc.

Amongst different technologies, the commercially available (COTS) magnetic sensors are AMR (Anisotropic Magneto Resistance), FG (Fluxgates), GMR (Giant Magneto Resistance), MI (Magneto Impedance) and TMR (Tunnel Magneto Resistance) or SDT (Spin Dependent Tunnel). Fluxgates are able to measure the magnetic field in the range of mT~nT and have frequency operating range from DC to several kHz. They are vector magnetometers with dynamic range of ±64000nT. These features reflect that Fluxgates have excellent magnetic properties but the problem is that, they are heavier (500mg) and consume high power (2W) which makes them incompatible with 1B8_CubePMT tile. Secondly, they are expensive and available from few manufacturers. GMR also have good sensing properties and repeatability but they posses high hysteresis (up to 10%) and thus their use for low magnetic field sensing is not trivial. TMR has good sensitivities, high magnetic field range and good resolution. But the problem is that TMR is a new developed, immature technology and COTS are not very widely spread yet. AMR sensors are the one with a long commercial history. They are not expensive and COTS are easily available in the market. They achieved higher maturity in the field of automotive and mobile communications. Commercially available AMR sensors produced by Honeywell (HMCxxx series) have high dynamic ranges (hundred of µT), high resolution (in the order of 1nT) and higher sensitivities in the order of $10mV/mT/V_{bridge}$ with Set/Reset pulses [42-43].

6.2.4 1B221 Magnetometer

Keeping in mind the advantages of AMR technology, magnetometer sensor used on 1B8_CubePMT module is Honeywell HMC1002 magnetic two-axis sensors, designed for low magnetic field sensing. The HMC1002 sensor utilizes Honeywell's Anisotropic Magneto Resistive (AMR) technology. It has very high sensitivity and is reliable sensor for low magnetic field measurement. It measures the magnitude of earth's magnetic fields in the range -2~2 G [44]. UML class diagram of the 1B221 magnetometer is shown in figure 6.3.

Figure 6.3: UML block diagram of the 1B221 Magnetometer

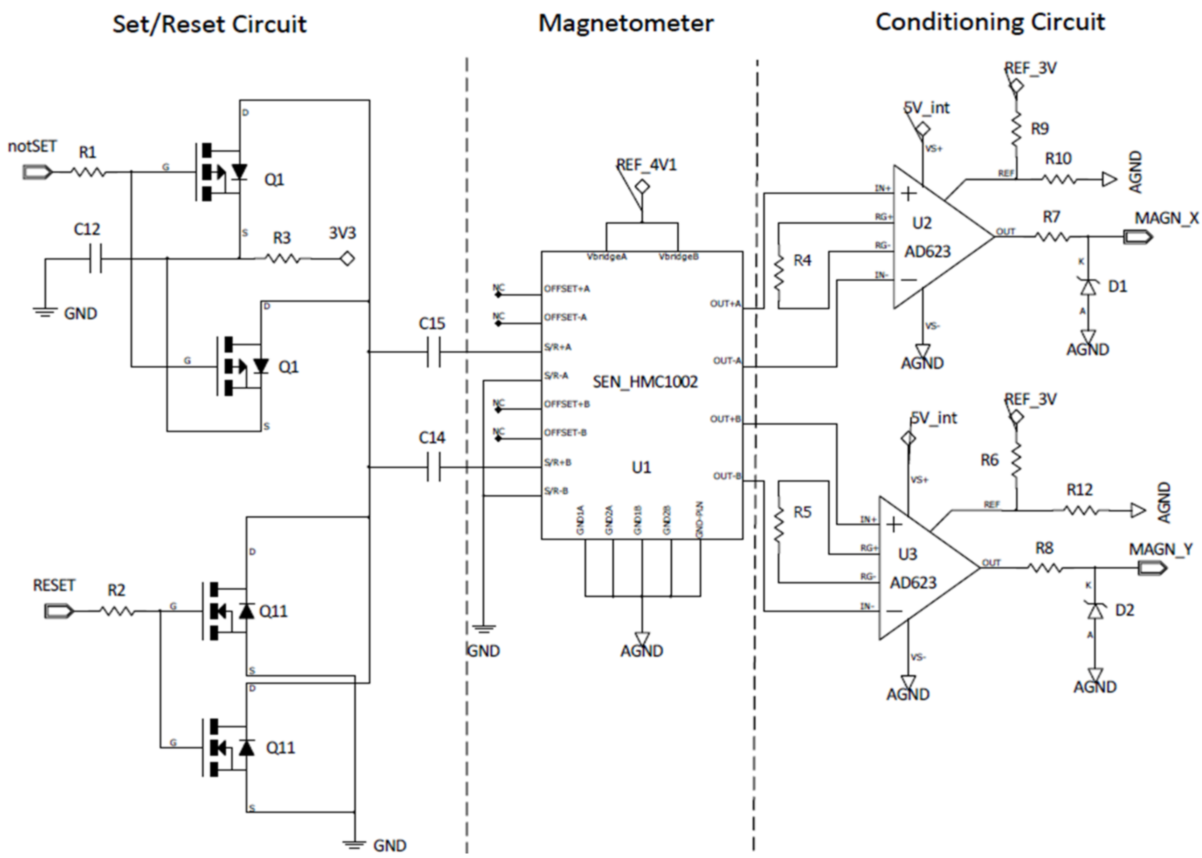

Figure 6.4: Schematic of the magnetometer subsystem.

1B8_CubePMT magnetometer subsystem schematic is shown in figure 6.4. It comprises of magnetic sensor HMC1002, conditional circuit and a set/reset circuit. Here, it is assumed that the incident magnetic field is in the range of -0.625~0.625 G [45]. The conditional circuit converts it to the ADC dynamic range (0 ~ 2.5V). HMC1002 has a Wheatstone bridge to measure the magnetic field. It converts any incident magnetic field in the sensitive axis directions to differential voltage outputs, which is given by (6-2);

$$V_A = OUT(A+) - OUT(A-)$$
$$V_B = OUT(B+) - OUT(B-) \qquad (6\text{-}2)$$

Where V_A and V_B are the differential output voltages of two Wheatstone bridges. The two Wheatstone bridges have identical features, therefore measurements will be done only on V_A and will be valid for V_B also. From the Wheatstone bridge V_A is obtained using (6-3);

$$V_A = K_M . B_x + V_{off} \qquad (6\text{-}3)$$

Where K_M is the magnetic sensitivity of each bridge in mV / G, V_{off} is the bridge offset voltage in mV and B_x is the magnetic field measured by the bridge A and expressed in G. All the three parameters have maximum, typical and minimum values. So V_A will also have three ranges as given in (6-4);

$$V_{A\_MAX} = K_{M\_MAX}.B_{x\_MAX} + V_{off\_MAX}$$

$$V_{A\_TYP} = K_{M\_TYP}.B_{x\_TYP} + V_{off\_TYP} \tag{6-4}$$

$$V_{A\_MIN} = K_{M\_MIN}.B_{x\_MIN} + V_{off\_MIN}$$

These parameters values given in HMC1002 datasheet are described for 8V supply. In case of 5V, the relative maximum and minimum values obtained for V_{off} by linear interpolation are 18.75 mV and -37.5mV respectively. By inserting these values in (7), the resultant values of V_{A_MAX} and V_{A_MIN} are 31.25mV and -50mV respectively. When V_A is applied to the instrumentation amplifier, output is given by (6-5),

$$MAGN\_X = V_A \times A_D + V_{REF} \tag{6-5}$$

Where A_D is the differential gain and V_{REF} is offset voltage of the instrumentation amplifier. Desired values of gain and offset are obtained by imposing conditions given in (6-6),

$$V_A = V_{A\_MIN} \Rightarrow MAGN\_X = 0$$

$$V_A = V_{A\_MAX} \Rightarrow MAGN\_X = 2.5V \tag{6-6}$$

Rearranging the above equations, results in (6-7);

$$A_D.(-50mV) + V_{REF} = 0$$

$$A_D.(31.25mV) + V_{REF} = 2.5V \tag{6-7}$$

The values obtained for gain, A_D =30.77 and offset voltage, V_{REF} =1.538V of the instrumentation amplifier (AD623). External resistors R_4 and R_5 can be found using (6-8) as provided in AD623 datasheet [46].

$$A_D = 1 + \frac{100K\Omega}{R_G} \tag{6-8}$$

The values of these resistors are given by (6-9):

$$R_4 = R_5 = \frac{100K\Omega}{A_D - 1} = 3.36K\Omega \tag{6-9}$$

The values used for R_4 and R_5 are 3.3KΩ. Thus, gain of the amplifier will slightly change (A_D=31.3). The resulting reference voltage V_{REF}, obtained by voltage divider resistors R_9 and R_{10}

(similarly between R_6 and R_{12}) in figure 6.4. These resistors have values 1kΩ±1%. The nominal value obtained for the offset voltage is given in (6-10):

$$V_{REF} = REF\_3V.\frac{R_{10}}{R_{10}+R_9} = 1.5V \tag{6-10}$$

It slightly deviates from the desired theoretical value. It is thus possible to obtain three different dynamic values of the output signal from magnetometer, depending on whether the sensor has a typical behavior or working in maximum or minimum range. The range of theoretical values obtained are given in (6-11);

$$\begin{gathered} Typical \Rightarrow MAGN\_X_{TYP} = [0.894 \sim 1.52]V \\ MAX \Rightarrow MAGN\_X_{MAX} = [1.7 \sim 2.48]V \\ MIN \Rightarrow MAGN\_X_{MIN} = [-0.065 \sim 0.72]V \end{gathered} \tag{6-11}$$

In all three cases the range of output voltages is measured corresponding to the range of variation of magnetic field -0.625 ~0.625G. There is also a negative value in the minimum range but it is relative to a value of magnetic field -0.625G which is almost impossible to achieve, and even if applied to the magnetometer, ADC would recognized it as 0V. Rest of the values are within the dynamic range of ADC. For further protection, zener diodes are employed that limits output voltage of the conditioning circuit to 3V. Set/reset pulses refresh the sensor. They maintain sensitivity of the sensor by eliminating memory effect of the magnetic elements and reducing effects of the strong interference fields. The magnetometer testing and magnetic field measurement results are given in table 8.6.

6.2.5 1B211B Gyroscope

The third type of attitude determination sensor used on 1B8_CubePMT module is gyroscope. Gyroscope is a device for measuring angular velocity. Yaw rate digital gyroscope ADIS16080, with dynamic range ±80°/sec, is used in this project. It is connected through a Serial Peripheral Interface (SPI) bus with tile processor. The digital data available at the SPI port of gyroscope is proportional to the angular rate about normal axis to the top surface of ADIS16080 IC [47]. Gyroscope block diagram is shown in figure 6.5.

The 1B8_CubePMT gyroscope is used in the operating range ±2rpm and occasionally up to ±6rpm (e.g. at satellite deployment). It has a noise density rate of 0.05°/sec/√Hz in the frequency range from 0.1Hz to 40Hz. After applying a software filter of 1Hz, the RMS value of the resulting noise becomes approximately 0.0025rpm, which is about 0.1% of the full scale. The resulting noise is low enough for envisaged application which is attitude stabilization. Filter bandwidth can be software programmed for lower bandwidth (more accuracy) or higher bandwidth (fast maneuvers). For accurate pointing other sensors including sun sensor and magnetometer can be used.

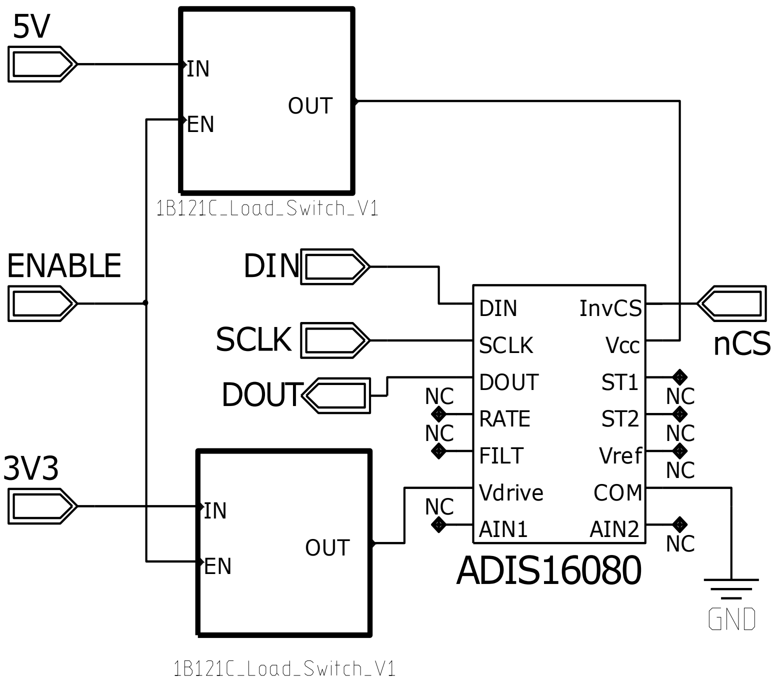

Figure 6.5: Gyroscope block diagram.

Chapter 7

Attitude Control System (ACS)

7.1 Introduction

The ACS manages satellite orientation, in order to point its antenna toward ground station or solar panels toward sun. For this purpose normally permanent magnets, reaction wheels and magnetic rods are used [48-49]. Permanent magnets are cheap, simple, light and consuming no power. But they have inadequate pointing accuracy and give very little choices on the pointing direction. Reaction wheels and magnetic rods have better pointing accuracy and can orientate satellite in any direction but their price, weight and size make them incompatible with CubeSats standard NanoSatellites like AraMiS-C1.

A reconfigurable magnetorquer coil has been designed and implemented for the 1B8_CubePMT module. Magnetorquer coil is a better choice for attitude control and stabilization of NanoSatellites. The goal of this work is to provide CubeSats with a magnetorquer coil which has small dimensions, weight and low heat dissipation. The designed magnetorquer coil is reconfigurable and integrated within the PCB internal layers occupying no excess space on CubeSats. Coils in each layer are treated separately and can be attached/detached through straps. Changing the arrangement of these straps, one can use either single, two, three or four coils in series, parallel or any hybrid combination. This reconfigurable design provides option for generating different amount of magnetic moment and resultant torque to stabilize and rotate satellite.

In this chapter magnetorquer coil design, magnetic moment generated and power dissipated will be discussed in detail. Power dissipation and the corresponding temperature increase of the 1B8_CubePMT module is evaluated by thermal modeling. Emissivity of the 1B8_CubePMT module was also found through a laboratory experiment.

7.2 Magnetorquer System

Magnetorquer system is designed for the 1B8_CubePMT module whose block diagram is shown in figure 7.1.

Magnetorquer system can be divided into two parts:

- Magnetorquer Coil Driver
- Magnetorquer Coil

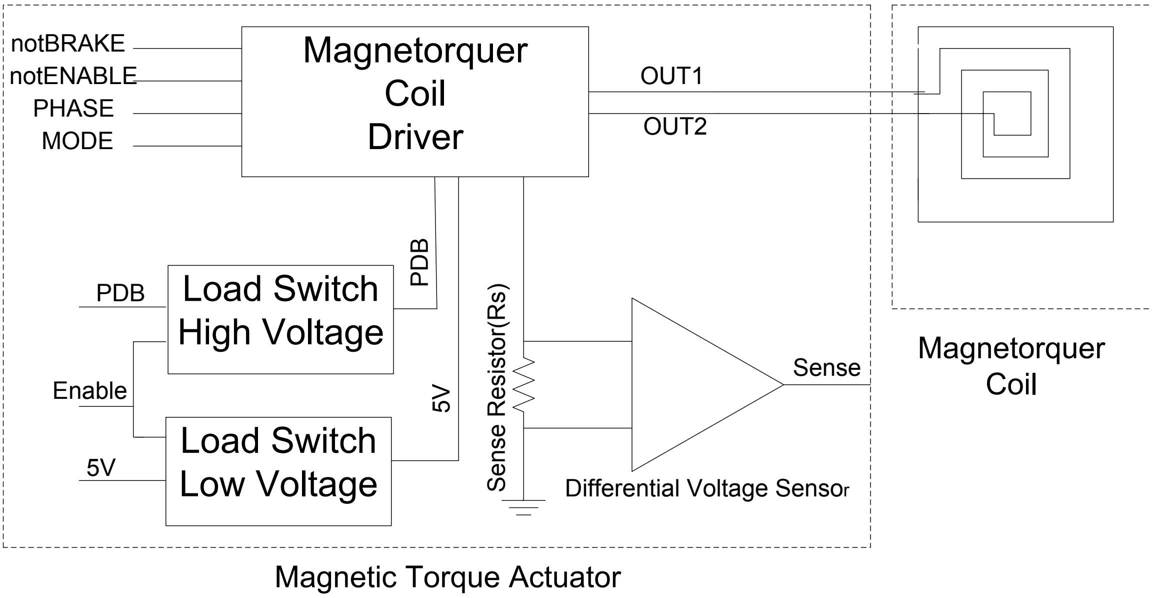

Figure 7.1: Magnetorquer subsystem block diagram.

7.3 1B222 Magnetic Torque Actuator

PWM motor driver IC 'A3953' [50] is used as magnetorquer coil current driver which controls the amount and direction of current flow. The driver pins OUT1 and OUT2 are connected with magnetorquer coil. Digital signals from tile processor (notBRAKE, PHASE, MODE and notENABLE) are used for driving the coil in different modes such as sleep, standby, brake_and forward /reverse, fast/slow current-decay mode. Differential voltage sensor monitors high current flow. Load switches provide and cutoff power to magnetorquer coil on enable signal from the tile processor.

The coil driver circuit has a transistor bridge as depicted in figure 7.3. The bridge topology allows bi-directional current flow through magnetorquer coil (L). Transistors Q1 and Q3 allow the current flow from left to right (shown through a solid line from supply 'V' to GND). Transistors Q2 and Q4 are opened during this stage. In case of reverse current flow, transistors Q2 and Q4 are closed and current flows through the coil from right to left (indicated by dashed line from supply 'V' to GND) . During this stage Q1 and Q3 are opened. The freewheeling diodes (D1, D2, D3 and D4) help in de-energizing the coil. The UML class diagram of the magnetorquer system is shown in figure 7.2.

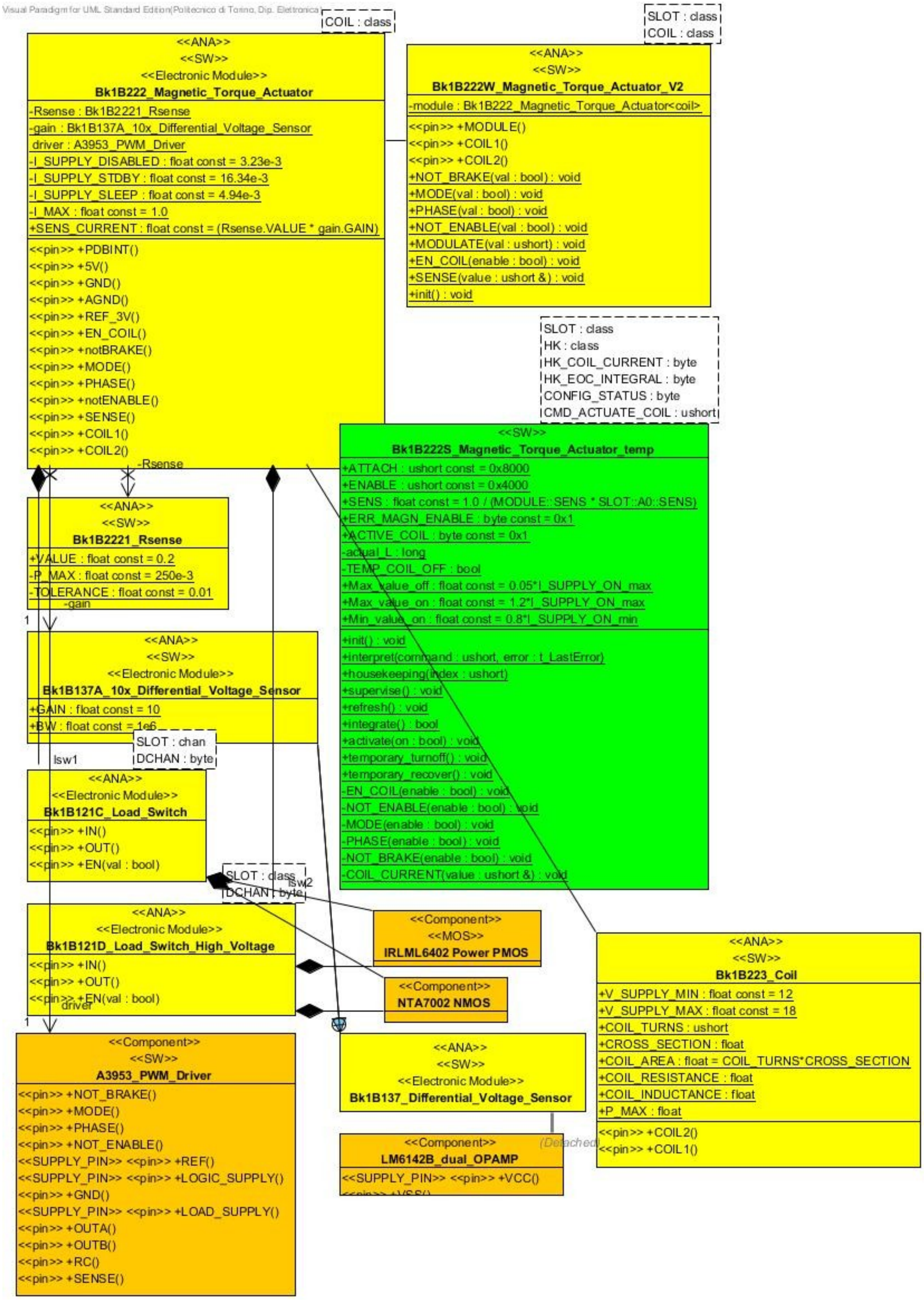

Figure 7.2: UML class diagram of the Magnetorquer system

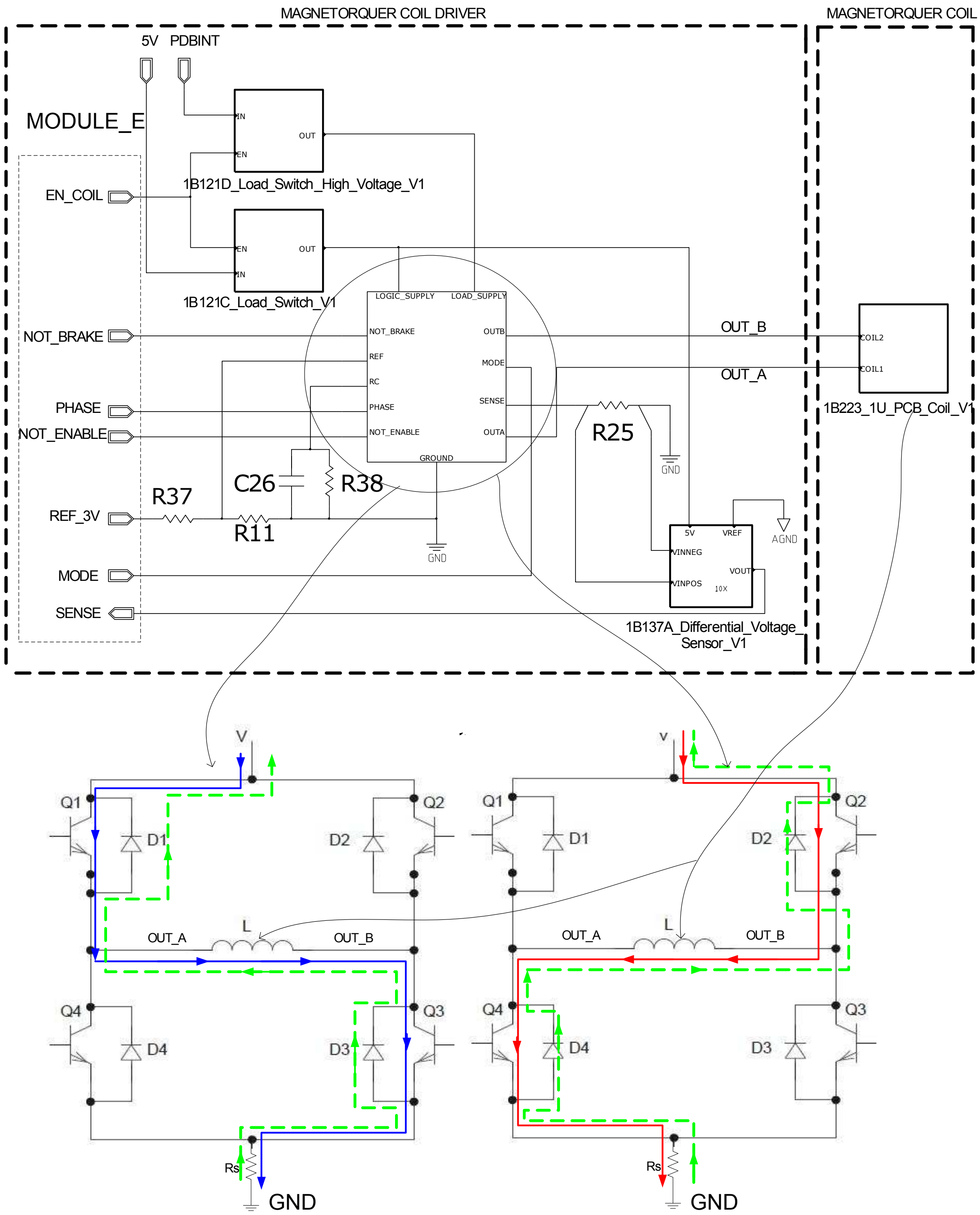

Figure 7.3: Coil driver (A3953) circuit current paths through coil (L)

7.4 1B223 Magnetorquer Coil

Considering, the dimensions and weight restrictions for NanoSatellites of CubeSat standard, a magnetorquer coil is designed and integrated inside the four internal layers of 1B8_CubePMT tile. 1B8_CubePMT is an eight layers PCB with four subcoils in second, third, fourth and fifth layers. Each coil has 50 turns therefore 1B8_CubePMT module has a total of 200 turns in the four internal layers. All the other subsystems are mounted on the top and bottom layers. Top layer hosts solar panel and sun sensor while bottom layer contains nessary electronics subsystems.

Sixth layer is dedicated for ground plane which isolates all the subsystem components from the magnetic field generated by the magnetorquer coils. As four 1B8_CubePMT modules are mounted to build 1U AraMiS-C1. The corresponding 1B8_CubePMT is energized to attain the required orientation.

7.4.1 Working Principle

Magnetorquer coil generates magnetic field which interacts with the earth magnetic field and the resulting torque is used to orient the satellite in any desired direction. Theoretically, when current flows through a solenoid, magnetic moment ($\vec{D}$) is generated which is given by (7-1):

$$\vec{D} = N.S.I \tag{7-1}$$

Where N is the number of turns, S is the area of the single turn and I is the current through the coil. The direction of $\vec{D}$ is given by right hand rule [51], i.e. hold the solenoid in right hand such that curled fingers point in the direction of current (clockwise), thumb along the axis of solenoid points to the direction of $\vec{D}$ (toward paper)as shown in figure 7.4.

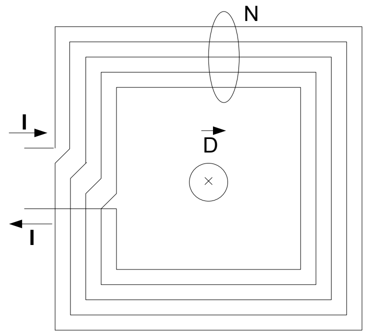

Figure 7.4:Direction of magnetic moment ($\vec{D}$) of a current carrying coil

When current carrying coil is placed in a magnetic field ($\vec{B}$), it generates a torque ($\vec{\tau}$) given by the vector product between $\vec{D}$ and $\vec{B}$ as given by (7-2):

$$\vec{\tau} = \vec{D} \times \vec{B} = \left|\vec{D}\right|\left|\vec{B}\right| \sin\theta \hat{n} \tag{7-2}$$

Where, θ is the angle between $\vec{D}$ & $\vec{B}$ and $\hat{n}$ is unit vector normal to the plane containing $\vec{D}$ & $\vec{B}$. The amount of $\vec{\tau}$ exerted on the coil depends on the magnitude of $\vec{D}$, $\vec{B}$ and θ . The resulting $\vec{\tau}$ is maximum when $\vec{D}$ and $\vec{B}$ are perpendicular (θ=90˚) as shown in figure 7.5 (a) and minimum when they are parallel (θ=0˚) as apparent from figure 7.5 (b).

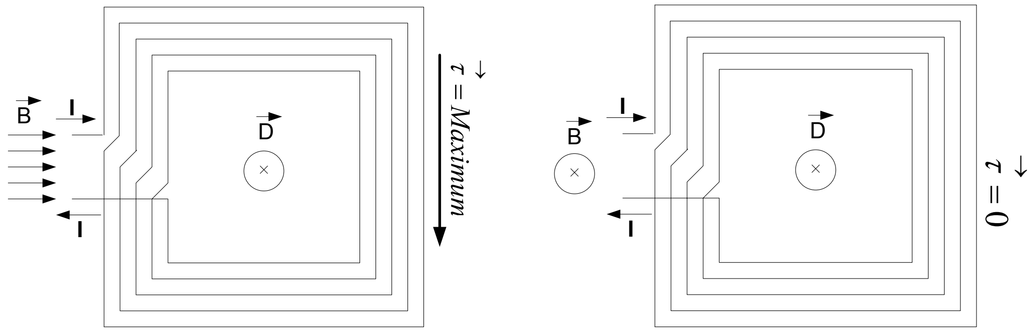

Figure 7.5: Magnetic field ($\vec{B}$), magnetic moment ($\vec{D}$) and resultant torque.

Magnetorquer coil utilizes earth magnetic field for attitude control and stabilization of NanoSatellites. Earth magnetic field varies with altitude and inclination angle. At an altitude of 800 km and inclination angle of 89°, it varies between 0.15G and 0.45G [52]. Magnetorquer coil generates magnetic moment which interferes with the earth magnetic field and provides torque to stabilize and rotate the satellite in its orbit. When current flows through magnetorquer coil in clockwise direction, it generates magnetic moment ($\vec{D}$) as shown in figure 7.6. According to Right Hand Rule, the direction of $\vec{D}$ will be in the negative z-axis (i.e. into the paper). If the earth magnetic field ($\vec{B}$) is along y-axis, then the resulting $\vec{\tau}$ will be along x-axis.

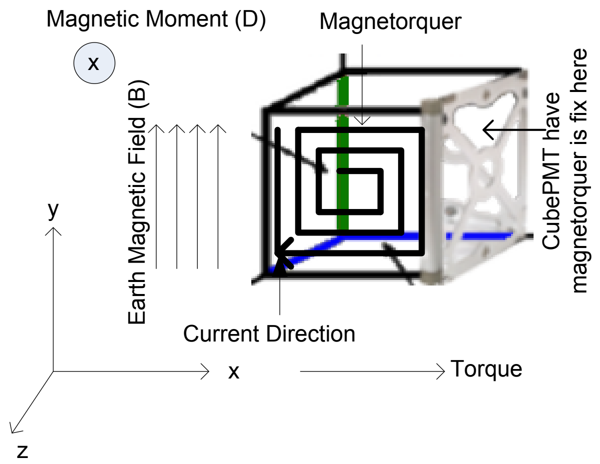

Figure 7.6: Earth magnetic field interaction with magnetorquer coil magnetic moment

7.4.2 Magnetorquer Coil Design

As already mensioned that magnetorquer coil is inserted inside second, third, fourth and fifth layers of 1B8_CubePMT module [53]. Coil in each layer has 50 turns therefore 1B8_CubePMT four internal layers has a total of 200 turns. Each coil trace has a width of 0.3mm and a thickness of 18µm. Space between adjacent traces is 0.2mm. Trace area (width & thickness), length and number of turns of each coil effect the resistance of magnetorquer coil which is related with magnetic moment, power cosumption and heat generated inside the 1B8_CubePMT. All these parameters are discussed in the coming sections. A cross sectional view of the 1B8_CubePMT module shows magnetorquer coil traces, is given in figure 7.7.

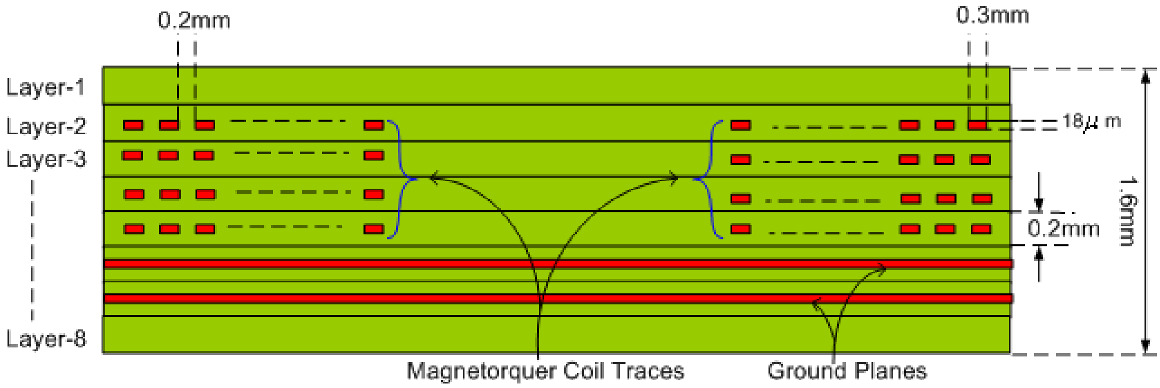

Figure 7.7: Magnetorquer Coil traces inside the 1B8_CubePMT module.

The main focus of the magnetorquer coil design is to make it compatible with the 1B8_CubePMT dimensions by not only being lighter but also being able to generate the intended magnetic moment. Schematic of the coil in single layer is depicted in figure 7.8 which also shows its dimensions. Table 7.1 highlights the key parameters of the magnetorquer coil design.

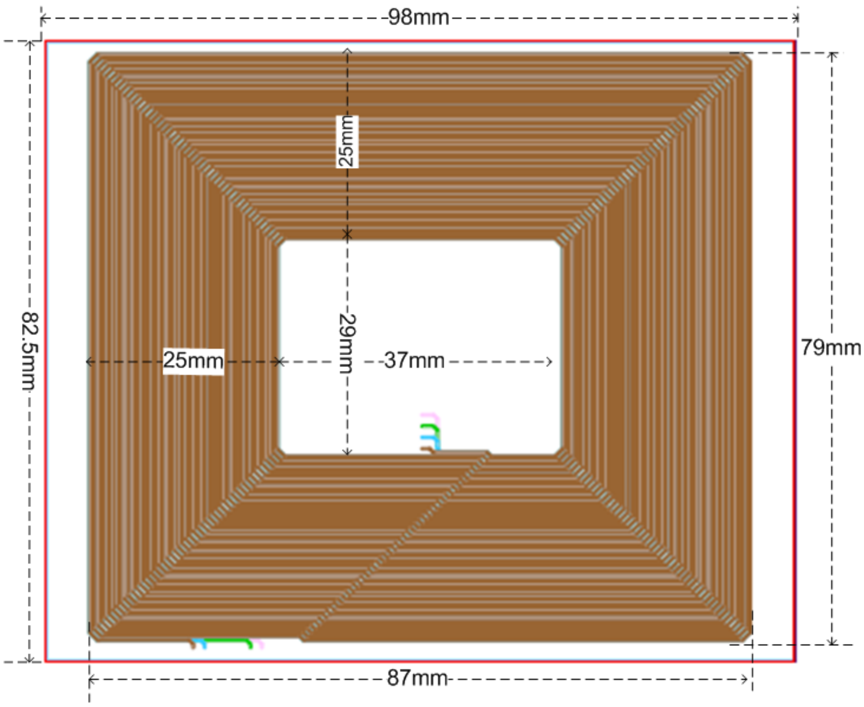

Figure 7.8: Schematic and dimensions of a single magnetorquer coil

Parameter	Values
Single turn average length; l_{avg}	230mm
Total length of single coil; L_t	11.5m
Trace cross sectional Area; $A=w\times t$	0.3mm×18µm
Total area occupied by single coil	$0.1675m^2$
Distance between two adjacent traces	0.2mm
Bundle width (50 traces)	25mm
Copper resistivity (from manufacturer), ρ	$3\times10^{-8}\Omega m$
Single coil resistance, R_o	64±3 Ω

Table 7.1: Dimension parameters of the magnetorquer coil

7.4.3 Reconfigurable Design

One of the main objective of this design is to make it reconfigurable and compatible with the 1B8_CubePMT dimensions. Therefore the coil is divided into four subcoils (L1, L2, L3 and L4) as shown in figure 7.9. Each subcoil is integrated in a separate internal layer of the PCB. They are connected through configurable *0* Ohm resistors. Each resistor can either be mounted or detached. Changing the arrangements of these resistors, one can use either a single coil or any other hybrid combination. Table 7.2 shows different combinations of *0* Ohm resistors to get the intended coil configurations. There is the possibility to arrange:

- Up to four coils connected in series
- Up to four coils connected in parallel
- Hybrid combination of series and parallel connected coils

This reconfigurable design allows to configure power consumption, magnetic moment, torque and heat dissipated by the coil inside the PCB. According to the specific mission requirements, possible arrangements can be evaluated on the basis of these parameters.

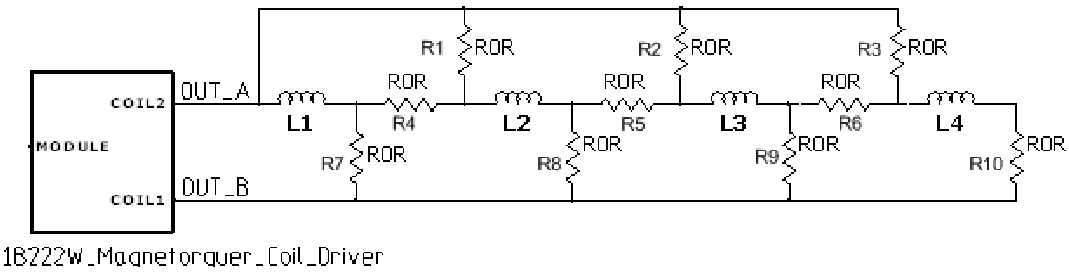

Figure 7.9: Magnetorquer sub-coils connected through 0 Ohm resistors

Coils Arrangements	*0* Ohm Resistor Arrangements									
	R1	*R2*	*R3*	*R4*	*R5*	*R6*	*R7*	*R8*	*R9*	*R10*
Single Coil							*X*			
4-coils in series				*X*	*X*	*X*				*X*
4-coils in parallel	*X*	*X*	*X*				*X*	*X*	*X*	*X*
4-coils in 2x2-hybrid		*X*		*X*		*X*		*X*		*X*

Table 7.2: Resistors to be mounted in order to get the corresponding coil arrangements

Figure 7.10 shows 1B8_CubePMT magnetorquer coil conneceted in different configurations (single, four in series, parallel and hybrid). In order to maintain a constant current (I_o) through m parallel connected coils, the applied voltage is kept same as that of a single coil (V_o). Similarly, in order to flow I_o through n series connected coils, the applied voltage is nV_o. While in case of $n \times m$ hybrid combination, the applied voltage is kept nV_o.

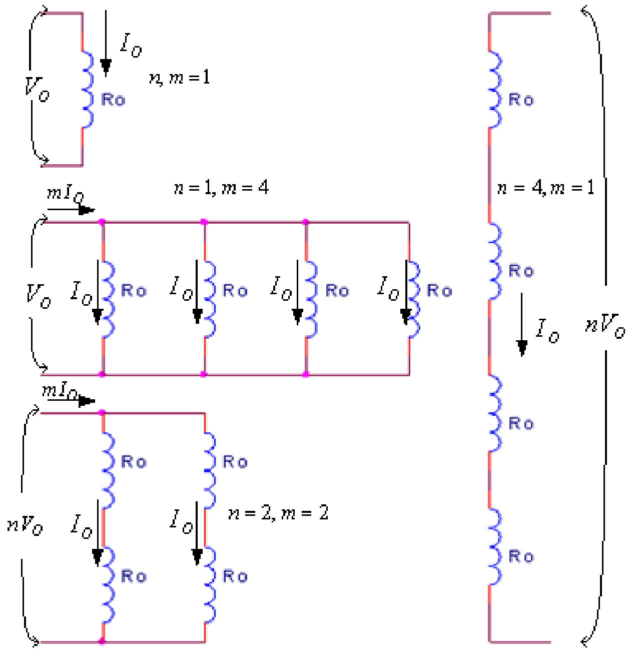

Figure 7.10: Required voltages to ensure the flow of constant current (I_o) through different combination of the magnetorquer coils.

7.4.4 Magnetic moment versus Power Dissipated

When current flows through the magnetorquer coils, magnetic moment is generated at the expense of power dissipation. Magnetic moment of the single coil $\vec{D}_o$ is given by (7-1). In case of M coils connected in series, parallel or any hybrid combination, the magnetic moment $\vec{D}$ is given by (7-3).

$$\vec{D} = M \cdot \vec{D_o} \tag{7-3}$$

Where M is the number of coils connected in any possible combination.
Similarly, power consumed by a single coil is given by (7-4).

$$P_o = {I_o}^2 R_o \qquad \because R_o = \rho \frac{L_t}{A} \tag{7-4}$$

Where I_o is the current through single coil, R_o is the resistance of the single coil and P_o is the power consumed by single coil. Power dissipated by M coils connected in any possible combination is given by (7-5).

$$P = MP_o \qquad \begin{aligned} &\because I = mI_o \\ &V = nV_o \\ &M = m \times n \end{aligned} \tag{7-5}$$

Where P is the power dissipated by M coils, V_o is the applied voltage to single coil and n & m are the number of coils connected in series and parallel respectively.
The ratio between magnetic moment generated and power dissipated is given by (7-6).

$$\frac{D_o}{P_o} = \frac{N \cdot S \cdot I_o}{R_o \cdot {I_o}^2} = \left(\frac{N.S}{R_o}\right) \cdot \frac{1}{I_o} \tag{7-6}$$

$${D_o}^2 = \frac{(N \cdot S)^2}{R_o} \cdot P_o \tag{7-7}$$

$$D^2 = n \cdot m \cdot \frac{(N \cdot S)^2}{R_o} \cdot P = k \cdot P \tag{7-8}$$

Where k is a constant parameter, depends on the number of coils connected in series or parallel and their dimensions. D^2/P_o or k is considered an important performance evaluation parameter for magnetorquer coils.

7.4.5 Torque Generated

As already mentioned, a magnetic moment is generated when current flows through the magnetorquer coil. In presence of the earth magnetic field a torque will be exerted on the 1B8_CubePMT module placed on four exterior faces of the AraMiS-C1. This torque is used to orient and stabilize the satellite in any desired direction. Torque generated is given by (7-9):

$$\tau = |B| \cdot |D| \cdot \sin\theta = |B| \cdot \sin\theta \cdot N \cdot S \cdot I \tag{7-9}$$

Torque exerted mainly depends on the amount of current flow through different combination of coils. Torque exerted versus current flowing through different combinations of the magnetorquer coil is shown in figure 7.11. Torque generated by the single coil and four coils in series is same but the current draw by the single coil is very high which results in high power consumption. Similarly single coil and 2x2 hybrid connected coils draw same current but the torque generated by the 2x2 hybrid combination is very high.

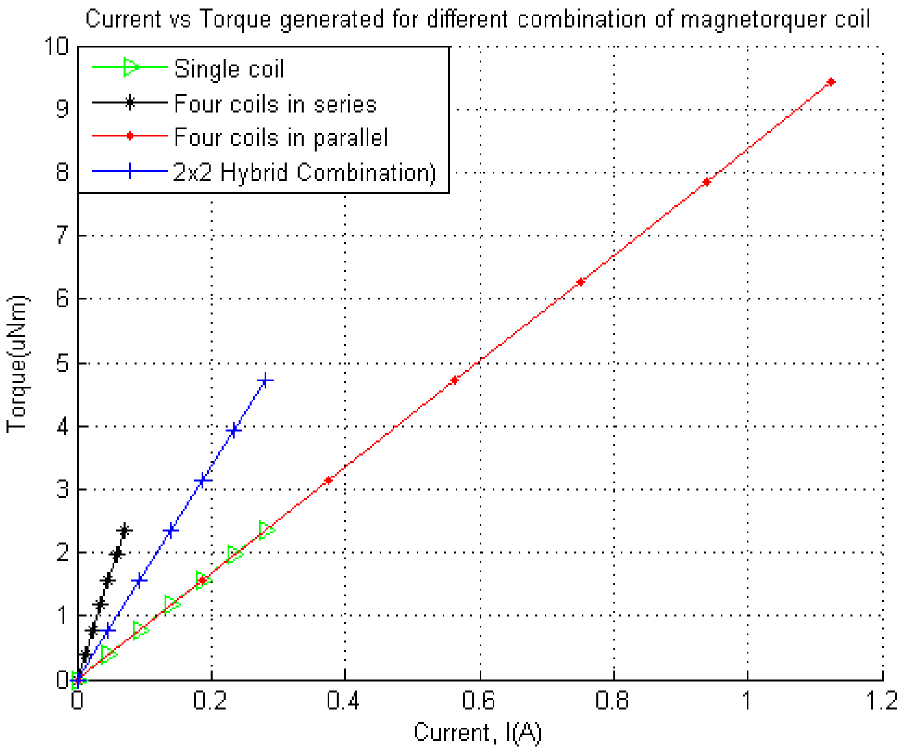

Figure 7.11: Current versus torque with applied voltage of 18V

Table 7.3 depicts that when the number of coils is increased, either in series or parallel, the magnetic moment and power dissipated also increase with same ratio. The current remains constant in case of series connected coils and voltage is constant in case of parallel connected coils. The ratio of magnetic moment and power dissipation remains constant for any number of coils connected in series or in parallel.

Coil Arrangement	Current I	Voltage V	Magnetic Moment |D|	Power Dissipated P	$\frac{\|D\|}{P}$	$\frac{V}{\|D\|}$
Single coil	I_o	V_o	D_o	P_o	$\frac{D_o}{P_o}$	$\frac{V_o}{D_o}$
Four coils in series	I_o	$4\,V_o$	$4\,D_o$	$4\,P_o$	$\frac{D_o}{P_o}$	$\frac{V_o}{D_o}$
Four coils in parallel	$4\,I_o$	V_o	$4\,D_o$	$4\,P_o$	$\frac{D_o}{P_o}$	$0.25\frac{V_o}{D_o}$
Four coils in hybrid	$2\,I_o$	$2\,V_o$	$4\,D_o$	$4\,P_o$	$\frac{D_o}{P_o}$	$0.5\frac{V_o}{D_o}$

Table 7.3: Comparison of current, voltage, magnetic moment and power consumption for different combinations with reference to the single coil.

7.4.6 Rotation Procedure

The angular speed (ω) of the satellite depends on the torque exerted and moment of inertia (J) of the satellite. Suppose the satellite has to be rotated by an angle (φ). Figure 7.12 shows that by applying a constant torque (τ_{max}) for a certain time (T / 2), the satellite angular speed (ω) increases linearly. In order to stop the satellite, an opposite torque of the same magnitude ($-\tau_{max}$) and duration (T/2) is applied. The opposite torque performs a braking action against the satellite spin, so as to seize the satellite spin after covering exactly the desired angle (φ).

According to the Newton's second law of rotation :

$$\tau = J\dot{\omega} \tag{7-10}$$

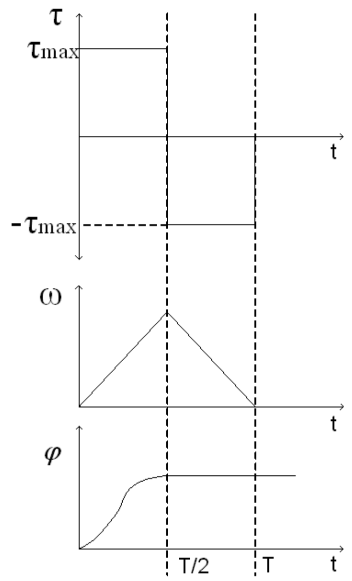

Figure 7.12: Actuation of the magnetorquer coil to rotate the satellite in ideal case.

The following expression illustrates angular position (φ):

$$\varphi = \dot{\omega}\left(\frac{T}{2}\right)^2 + \dot{\omega}\left(\frac{T}{2}\right)^2 = \frac{1}{2}\frac{\tau}{J}T^2 \tag{7-11}$$

The time T required for the magnetorquer coil to rotate the satellite through a certain angle φ can be obtained and is given by (7-12):

$$T = \sqrt{\frac{2J\theta}{\tau}} \tag{7-12}$$

It is apparent from (7-12) that torque exerted and time taken to rotate the satellite are inversely proportional. Figure 7.13 shows the torque generated and the corresponding time to rotate AraMiS-C1 through an angle of 90˚ by energizing different combinations of coils. The value of J for AraMiS-C1 is 0.0059kgm^2. The torque generated by four coils in parallel is 9.4 µNm which takes 45s to rotate AraMiS-C1 satellite through an angle of 90˚. In case of single and four coils connected in series generated torque is 2.45µNm which takes 89s to rotate the satellite through an angle of 90˚. In case of 2×2 hybrid combination, torque generated is 4.7µNm which requires 63s for 90˚ rotation.

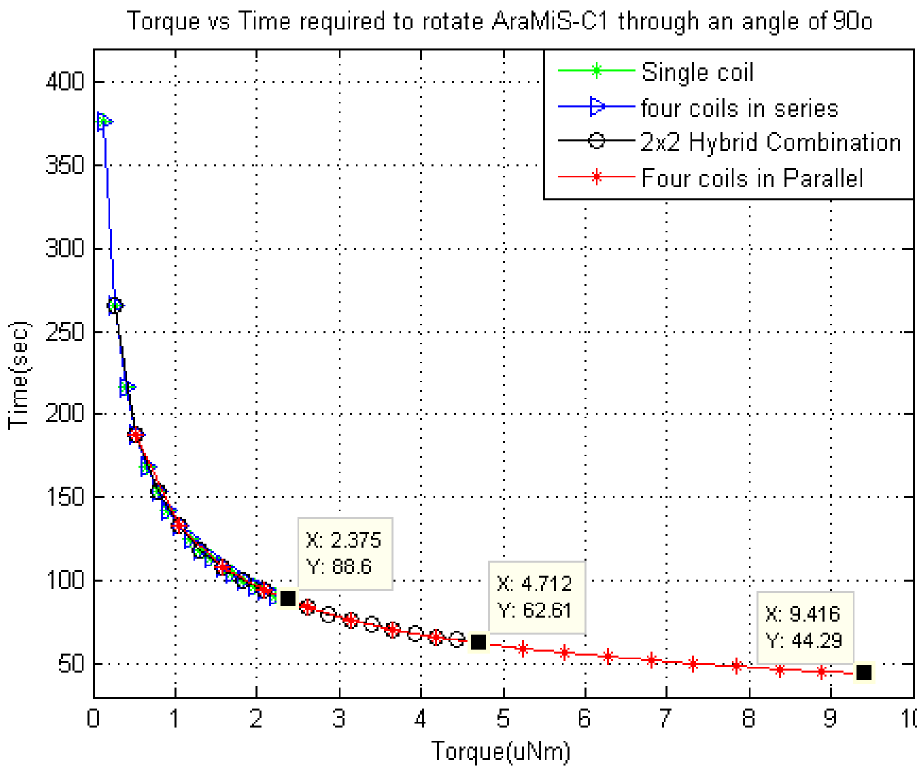

Figure 7.13: Time required to rotate AraMiS-C1 through an angle of 90˚

7.4.7 Thermal Modeling

Thermal modeling is considered an important element in designing a magnetorquer coil integrated inside the PCB. When magnetorquer coil is energized, power is dissipated in the form of heat which in turn increases the overall temperature of 1B8_CubePMT. This temperature increase should be confined within certain limits to avoid system performance degradation [54].

Thermal modeling provides detailed analysis about power dissipation and corresponding temperature variation of the PCB. Power dissipation is controlled by monitoring the amount of current that flows through the coil. Current flow also restricts the magnetic moment. Thus, temperature and magnetic moment are inter-related parameters. Higher magnetic moment can be achieved at the expense of increased PCB temperature [55].

Like any other thermal system, 1B8_CubePMT module also radiates and absorbs heat to and from the surroundings. Heat energy absorbed by the PCB from the surroundings is added to the heat generated by the coils. This additional energy tends to increase overall temperature of the PCB. In thermal equilibrium condition the total radiated power from the PCB to the surroundings (P_o) is equal to the electrical power dissipated by the coil inside the PCB (P_d) and power absorbed from the surroundings (P_I) depicted in figure 7.14 and given in (7-13) .

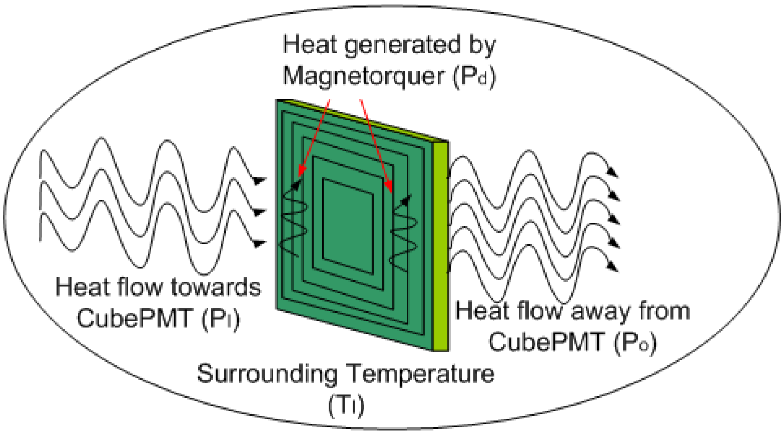

Figure 7.14: Heat flow through 1B8_CubePMT module.

$$P_o = P_d + P_I \tag{7-13}$$

The power dissipated by M coils is given by (7-4) and the power radiated from the PCB surface shown in figure 7.15 (b), can be deduced from the Stefan-Boltzmann's law [56]:

$$P_o = \alpha_o \sigma T_o{}^4 S + \alpha_L \sigma T_o{}^4 S_L \tag{7-14}$$

Where σ is the Stefan-Boltzmann constant ,

T_o is the PCB surface temperature in Kelvin,

S is the PCB surface area (both sides)

α_o is the emissivity of the PCB material at radiated wavelength λ_o

S_L is the lateral surface area and

α_L is the emissivity of the lateral surface.

Combining (7-13) and (7-14), results in (7-15):

$$\alpha_o \sigma T_o^4 S + \alpha_L \sigma T_o^4 S_L = P_d + P_I \tag{7-15}$$

In thermal equilibrium state, when no current flows through the coil, P_d = 0, and (7-16) becomes:

$$\alpha_I \sigma T_I^4 S + \alpha_L \sigma T_I^4 S_L = P_I \tag{7-16}$$

Where α_I is the emissivity of the PCB surface at the heat absorption wavelength λ_I.
Inserting P_I value from (7-16) into (7-15) results in (7-17).

$$\alpha_o \sigma T_o^4 S + \alpha_L \sigma T_o^4 S_L = P_d + \alpha_I \sigma T_I^4 S + \alpha_L \sigma T_I^4 S_L \tag{7-17}$$

In thermal equilibrium $\alpha_0 = \alpha_I = \alpha$. Rearranging (7-18) will give a relation between P_o and T_o as given in (7-18).

$$T_o = \sqrt[4]{\frac{P_d + \alpha \sigma T_I^4 S + \alpha_L \sigma T_I^4 S_L}{\alpha \sigma S + \alpha_L \sigma S_L}} \tag{7-18}$$

In order to find relation between P_o and T_o, it requires emissivity (α), as given in (7-19).

$$\alpha = \frac{P_d - \alpha_L \sigma S_L \left(T_o^4 - T_I^4\right)}{\sigma S \left(T_o^4 - T_I^4\right)} \tag{7-19}$$

In order to have the emissivity (α) value, it required surrounding temperature (T_I) , PCB surface temperature (T_o) and power dissipated inside the magnetorquer coil (P_d). These parameters are found through a measurement setup explained in next section 7.4.8.

7.4.8 Emissivity (α) measurement at Infra Red Wavelength

The emissivity of a material is the relative ability of its surface to emit energy by radiation [57]. Surfaces with different colors have different emissivity values [58-59]. The emissivity value of the bottom layer of 1B8_CubePMT module is found through a measurement setup shown in figure 7.15 (a). Arrangement of two 1B8_CubePMT modules used in emissivity measurement is shown in figure 7.14 (b). The emissivity value for the lateral surface (9.2mm) between two tiles is assumed to be 1 (α_L=1).
The measurements of emissivity (α) have been performed inside a vacuum chamber. A voltage of 17V is applied to the magnetorquer coils of the two 1B8_CubePMT modules. A temperature sensor is attached to the 1B8_CubePMT surface in order to record the increase in temperature due to flow of current in the coil. The applied voltage, amount of current flow and corresponding increase in temperature have been captured through a data acquisition system shown in figure 7.15 (a). These parameters are plotted against time as shown in figure 7.16. The temperature at normal atmospheric pressure is 20.2˚C when no voltage is applied to the coil. At time t_1, vacuum was generated in the vacuum chamber and the corresponding temperature suddenly dropped a few degrees as apparent from figure 7.15. After that the temperature started rising and reached steady state at time t_2. At this stage, both magnetorquer coils were energized with 17V. As a result, there was an exponential increase in the temperature until time t_3. At this point the system reached

steady state condition and there was negligible increase in temperature as function of time. At time t_4 the power supply was cut off which resulted in exponential decrease in temperature.

From the thermal measurement results of figure 7.16, all the parameters required for emissivity measurement in (7-19), were obtained as given in table 7.4. The resulting emissivity (α) value for the PCB surface was calculated using (7-19) is 0.9. This emissivity value is used in the results given in section 7.4.9.

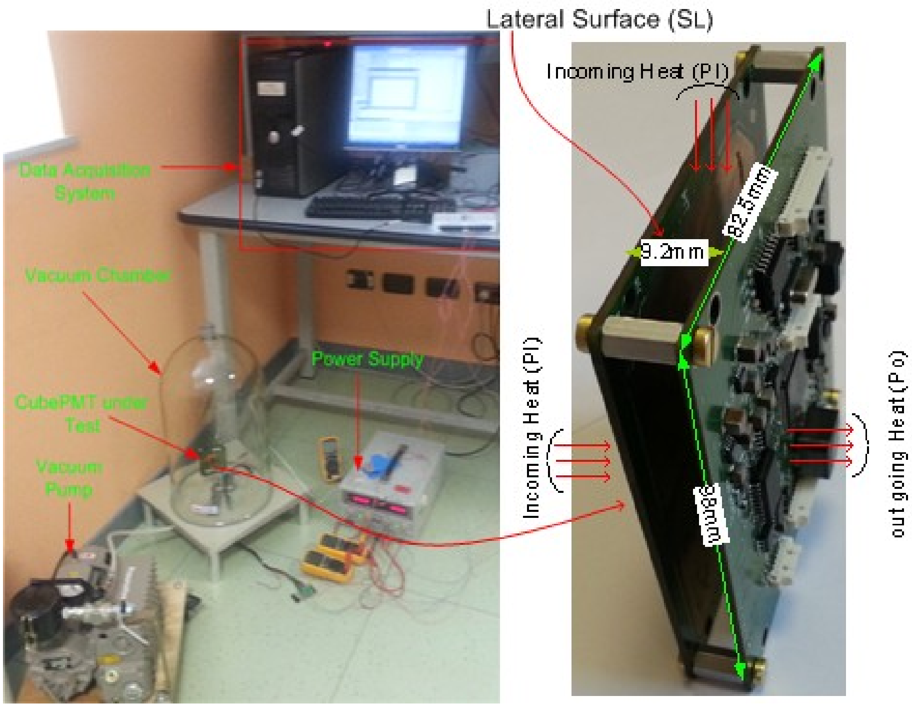

Figure 7.15: Photograph of emissivity measurement setup

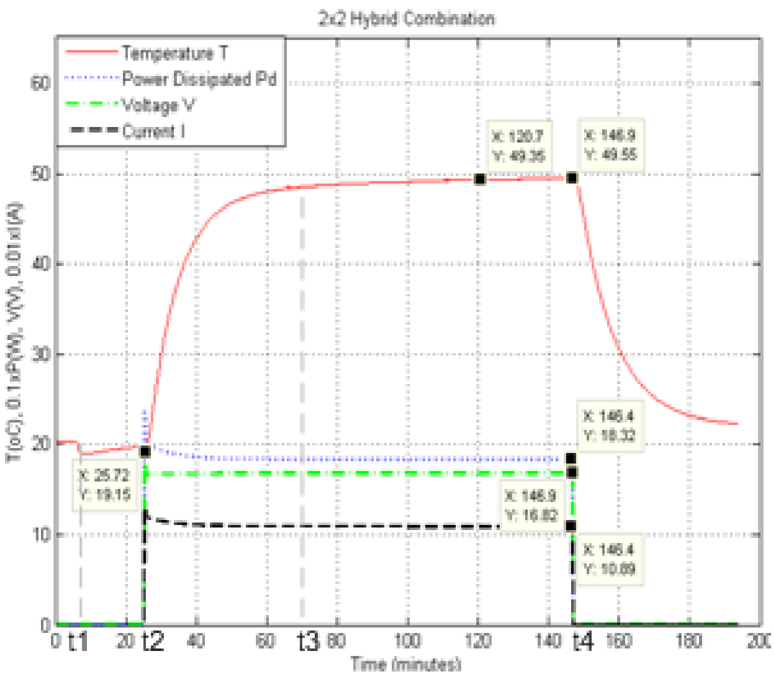

Figure 7.16: Thermal measurement results of magnetorquer coil.

Parameter	Value
σ	$5.6703\times10^{-8}Wm^{-2}K^{-4}$
T_I	$292.34K$
T_o	$322.69K$
S	0.01617m^2
S_L	0.003321m^2
P_d	3.623W
α_L	1

Table 7.4: Parameters used in thermal modeling of magnetorquer coil

From figure 7.15, thermal time constant of 1B8_CubePMT module can be obtained. At t2, a voltage of 17V was applied to the magnetorquer coil and 1B8_CubePMT temperature started to increase exponentially. At t_3, 1B8_CubePMT temperature attained a steady state value (49˚C). So it took 45 minutes to reach a steady state point.

7.4.9 Results

Magnetorquer coil driver controls the flow of current through the magnetorquer coils as a function of applied voltage. 1B8_CubePMT module has a maximum 18V power distribution bus voltage. The temperature increase of 1B8_CubePMT module, magnetic moment and torque generated, power dissipated and current flowing through the magnetorquer coils are plotted against applied voltage in figure 7.17 and figure 7.18 for different combination of the magnetorquer coil.

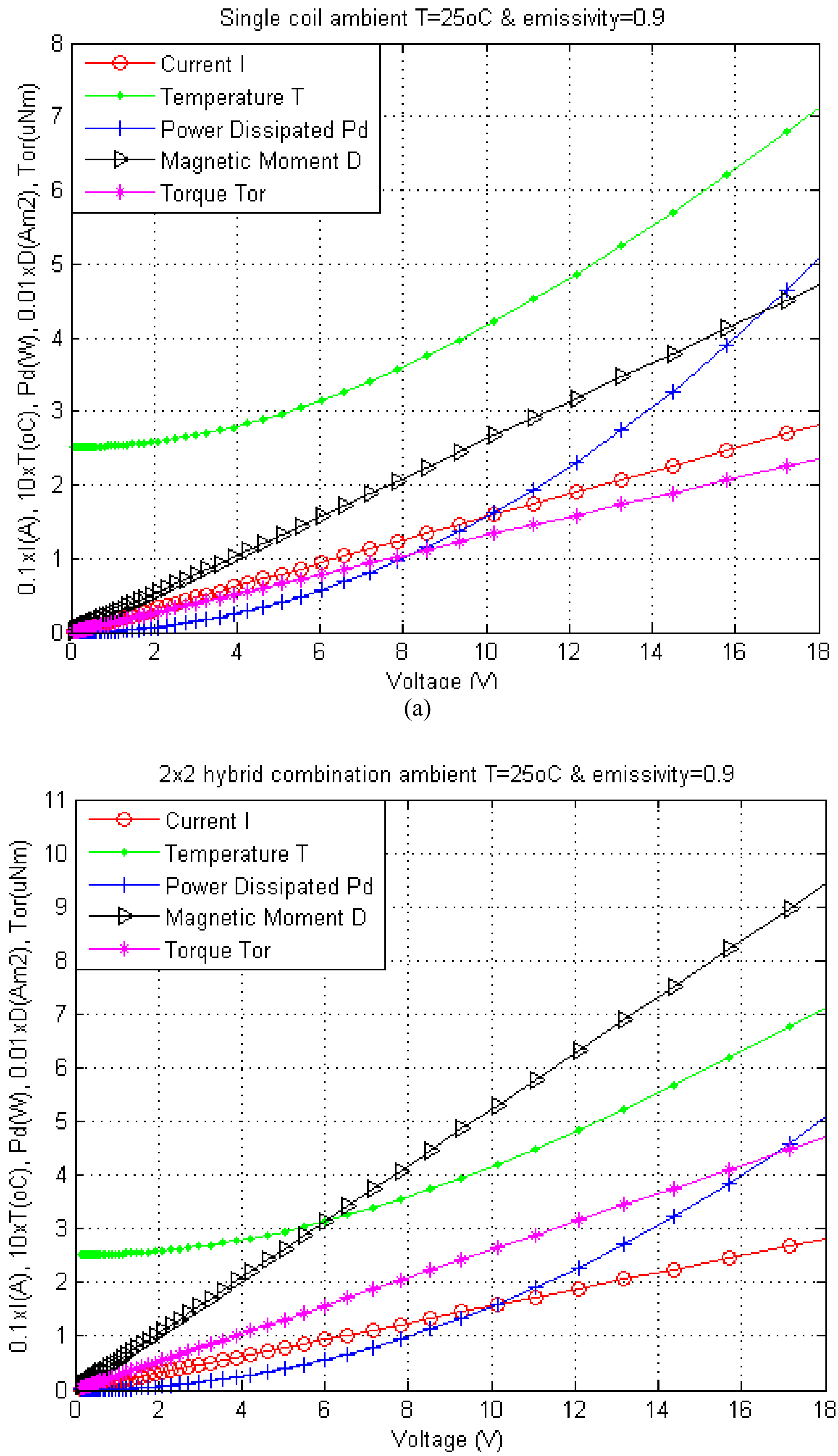

(a)

(b)

Figure 7.17: Magnetorquer plots (a) Single coil (b) 2x2 hybrid combination

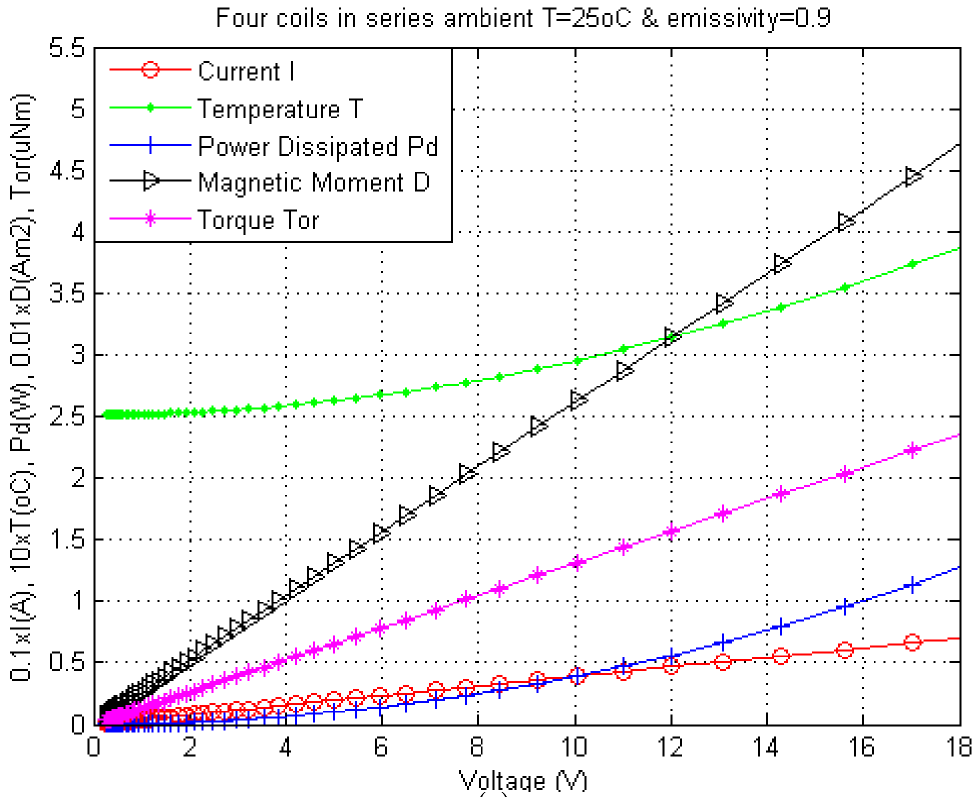

(a)

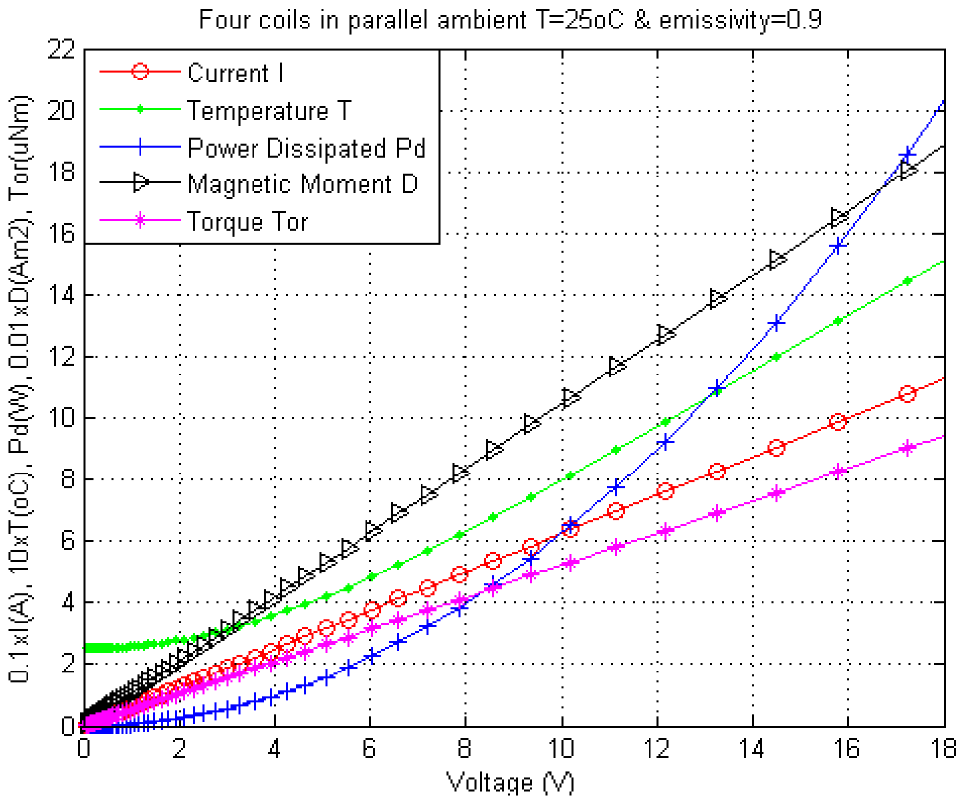

(b)

Figure 7.18: Magnetorquer plots (a) four coils in series and (b) four coils in parallel.

Coils Combination	Applied Voltage (V)	Current (mA)	Magnetic Momet (Am^2)	Power Dissipation (W)	Temp (˚C)	Torque (μNm)	Time to rotate by 90˚ (Seconds)
Single	10	158	0.026	1.58	42	1.32	120
Four in series		39	0.026	0.39	29	1.32	120
Hybrid (2x2)		156	0.052	1.56	41	2.6	84
Four in parallel		626	0.1	6.26	79	5.2	60
Single	18	278	0.05	5	71	2.45	89
Four in series		70	0.05	1.26	38	2.45	89
Hybrid (2x2)		280	0.099	5	71	4.9	63
Four in parallel		1120	0.2	20.2	151	9.8	44

Table 7.5: Results of different combinations of magnetorquer coils at applied voltage of 10V and 18V.

Applied voltage controls all the remaining parameters of the magnetorquer coil. At a particular voltage one can get the corresponding current, power dissipated, magnetic moment and temperature increase. For example, when 18V is applied to a single coil, the corresponding current is 278mA, dissipated power is 5W, magnetic moment generated is $0.05Am^2$ and temperature of PCB is increased to 71˚C as shown in as apparent from table 7.5 and figure 7.17 (a). The generated torque at earth magnetic field of 50μT is 2.45μNm. This amount of torque will take 89s to rotate AraMiS-C1 through an angle of 90° as given in figure 7.13. For all other combinations of figure 7.17 and figure 7.18, the corresponding parameters are given in table 7.5.

In case of four parallel coils, the temperature of 1B8_CubePMT module is increased up to 151˚C. It is temperature at steady state condition i.e. when the coil remained energized for 45 minutes. But in actual conditions, the coil is energized for just 63s in order to rotate AraMiS-C1 through angle of 90˚. It is apparent from figure 7.16 that when four coils in parallel are energized for 63 sec the temperature of the satellite increases by only 4˚C (from 19.2˚C to 23˚C), which is quite acceptable.

7.4.10 Comparison

Comparison results of the 1B8_CubePMT magnetorquer coil with already available systems in the market are given in table 7.6. The main parameters for these systems are weight, dimensions, occupied area and magnetic moment versus power ratio. CubeSat magnetic rod [60] has best magnetic moment versus power ratio but is expensive, heavier and occupy extra space on the spacecraft which is not suitable for 1U NanoSatellites like AraMiS-C1. NanoPower Solar P100U [61] is internal to the PCB but has worse magnetic moment versus power ratio. The magnetorquer discussed in this paper is lighter and requires no excess space in the satellite because it is integrated inside the four internal layers of the PCB. It also possesses better magnetic moment versus power ratio.

Parameter	Price	Power Consumed (W)	Magnetic Moment (Am^2)	Weight (mg)	Dimensions (mm)	Area Occupied Inside the PCB (m^2)	$\frac{D^2}{P}\left(\frac{(Am^2)^2}{W}\right)$
CubeSat Magnetic Rod	€1200	0.2	0.2	30000	Length = 70 Diameter = 9	External to PCB	0.2
NanoPower Solar P100U	Internal to PCB (No extra price)	2.31	0.05	Internal to the PCB (almost weightless)	Internal to the PCB (No space occupation)	1.6	0.001
1B8_CubePMT Magnetorquer Coil	Internal to PCB (No extra price)	1.25 (4 coils in series)	0.05	Internal to the PCB (almost weightless)	Internal to the PCB (No space occupation)	0.67	0.002

Table 7.6: Comparison of the Magnetorquer Coil of 1B8_CubePMT with the available systems in the market

Chapter 8

1B8_CubePMT Subsystems Testing

8.1 Introduction

In this chapter we will discuss in detail the testing procedures and testing results of all the subsystems of 1B8_CubePMT.

8.2 EPS Testing

EPS composed of two triple junctions GaAs solar cells connected in series to achieve an output voltage of approximately 4.4V (each cell generating 2.2V). Boost converter step up the solar panel voltage to PDB voltage level (14V). The PDB voltage level is down converted by different switching and linear regulator to low voltage levels (i.e. 3V, 3.3V and 5V) used by different subsystem components.

8.2.1 Solar Cells Simulator

During testing, solar cells were not mounted on the 1B8_CubePMT tile. The solar cells behavior was implemented with a solar cells simulator. Schematic of the solar cells simulator is shown in figure 8.1 and the implemented circuit is shown in figure 8.2. Six diodes are connected in series in such a manner that the cathode of one diode is connected to the anode of the next one. The combination of these six diodes can withstand a forward voltage up to 4.2V. A power supply was used in constant current mode and applied to the tile through the solar cells simulator. The simulator was connected to the tile through a four pin connector (labeled as J6 on the 1B8_CubePMT).

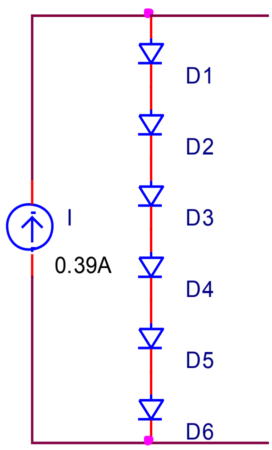

Figure 8.1: Solar cells simulator schematic

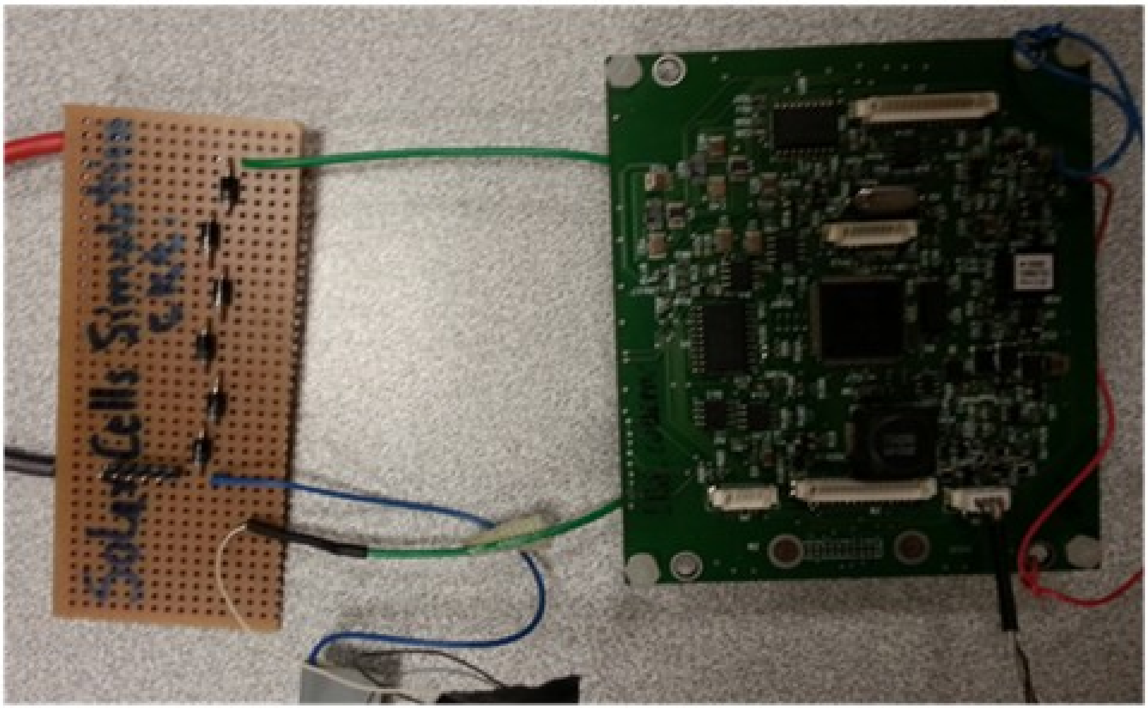

Figure 8.2: Solar cells simulator circuit with 1B8_CubePMT module.

8.2.2 1B1121D_Primary_Switching_Boost_V1

The solar cells simulator discussed in previous section is attached to the 1B8_CubePMT module through 4-pins Molex connector with reference designator J6 as shown in figure 8.2. This setup will connect the simulator output to the boost converter inputs SOLAR_POS and SOLAR_NEG as shown in figure 5.13. The current from the simulator charges the boost converter input capacitor (C32). Voltage on C32 is scaled by the resistive divider network (R30 and R32) and applied to the non-inverting input (IN+) of the comparator (U7). A constant voltage of 2.9V was applied to the inverting input (IN-) of the comparator through the pads of the resistors R80 and R89 as shown in the schematic of the implemented boost converter of figure 5.13. For the inverting input voltage a PWM-DC-converter block can also be used, but for the testing purpose a constant voltage was applied. When voltage on C32 becomes 4.165V, IN+ terminal voltage of U7 becomes 3V (greater than the inverting input (IN-) voltage (2.9V)), the output of U7 goes high and turns on MOSFET (Q9). During this stage C32 discharges through inductor (L2) and Q9 to GND. When C32 reaches 3.835V, IN+ terminal of U7 goes below IN- terminal and turns off Q9. During this stage, once again C32 voltage increases and when reaches 4.165V, the cycle repeats as shown in figure 8.3. The output of the boost converter was checked at the test point TP6 of the 1B8_CubePMT module. The input and output voltage waveforms of the boost converter are shown in figure 8.4.

S. No	Actions
1	Apply a constant current of 0.39A through solar simulator on 4 pins connector J6.
2	Apply a constant voltage of around 4V on the pads of resistors R88 or R90 connected through a voltage divider to the inverting input of comparator U7.
3	Observe the input voltage waveform on test point TP7 and switching of the MOSFET on the oscilloscope screen using probes.
4	Observe the output waveform of the boost converter on TP6 through the oscilloscope probes.

Table 8.1: Steps for testing of 1B1121D_Primary_Switching_Boost.

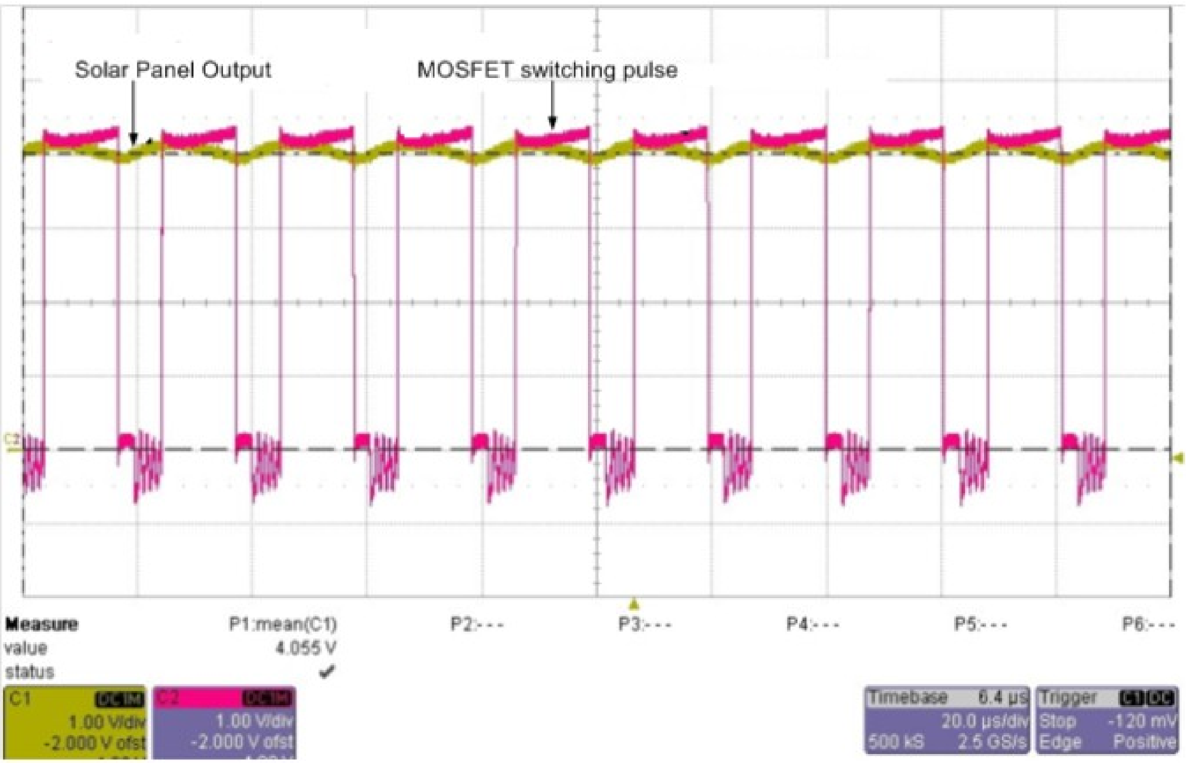

Figure 8.3 : Testing results of solar panel output and MOSFET (Q9) input switching pulse

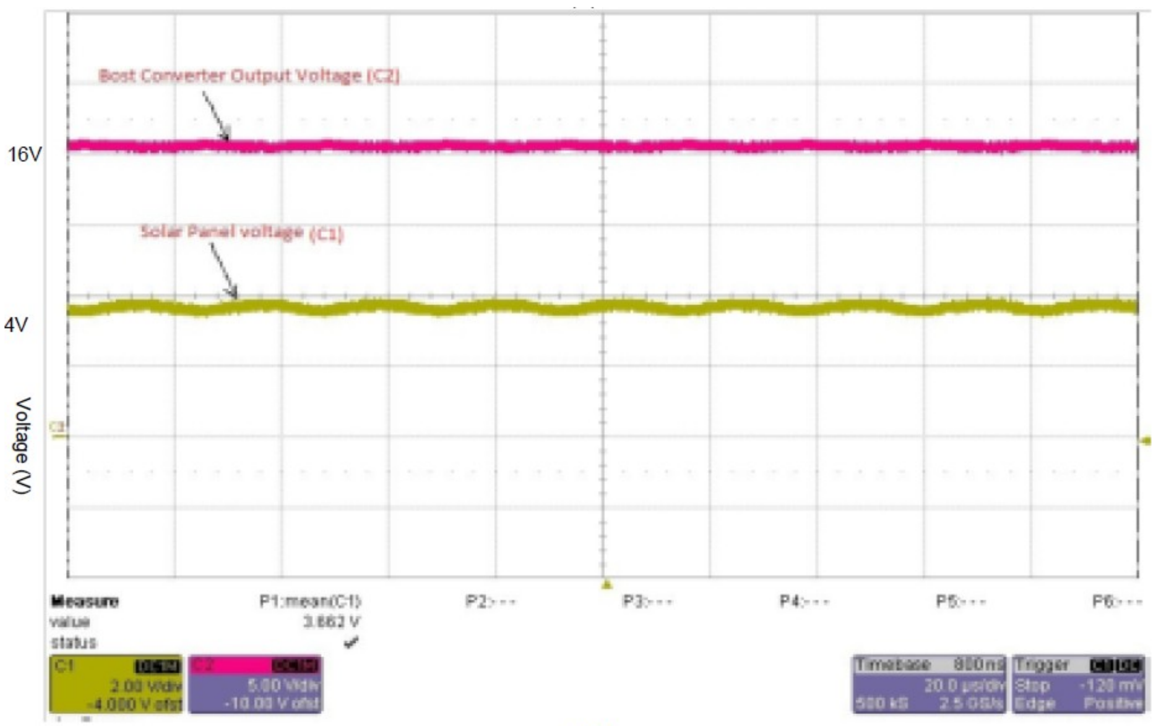

(b)

Figure 8.4: Testing results of the Boost Converter output waveform.

8.2.3 1B1251 Small Power Regulators

The PDB voltage level has to be down converted to low voltage levels (i.e. 3V, 3.3V and 5V) used by different subsystem components. For this purpose, 1B8_CubePMT has two linear and two switching regulators. These regulators were tested by applying different input voltage values.

8.2.4 1B1253B 5V Switching Regulator

It is a switching regulator, converts the PDB voltage level (14V) to 5V, which is used by all the components of the 1B8_CubePMT subsystems require 5V. It is a linear technology component with part number LTC3631EMS8E-5#PBF-ND and reference designator U28. The schematic is shown in figure 5.18, while PCB layout is shown in figure 8.5. Testing results are given in table 8.2.

We applied different voltages on the PDB as shown in table 8.2. Enable signal was applied from the tile processor. Checked the output at TP5 of the 1B8_CubePMT module. Testing results are given in table 8.2.

Rated Input Voltage (V)	Applied Input Voltage (V)	Applied Enable signal (V)	Measured output Voltage (V)
4.5~45	10 14 16	From tile processor (2.5)	5

Table 8.2: Testing results of 1B1253B_5V_100mA_Regulator_V1

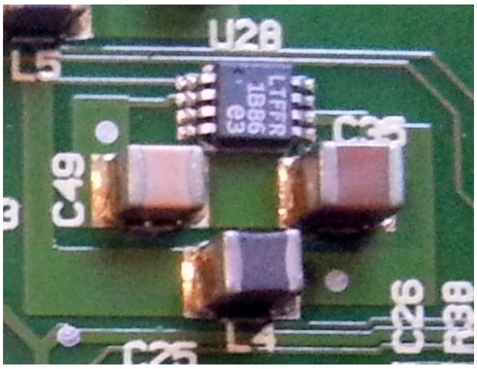

Figure 8.5: PCB layout of 1B1253B_5V_100mA_Regulator_V1

8.2.5 1B1252A 3V Reference Regulator

It is a linear regulator, provides 3V reference voltage to the 1B8_CubePMT subsystems. National Semiconductor component with part number LM4128AMF-3.0CT-ND is used for this regulator. On the PCB layout it has reference designator U10. The schematic is shown in figure 5.15, while the PCB layout is shown in figure 8.6.
In order to apply 5V input to this regulator we also enabled 5V regulator (1B1253B_5V_100mA_Regulator_V1) which gives input to this regulator. Applied enable signal from the tile processor and check the output at TP3 of the 1B8_CubePMT module. Testing results are given in table 8.3 below.

Rated Input Voltage (V)	Applied Input Voltage (V)	Applied Enable signal (V)	Measured output Voltage (V)
4.5~45	5	From tile processor (2.5)	3.293

Table 8.3: Testing results of 1B1252A_3V0_1000ppm_Regulator_V1

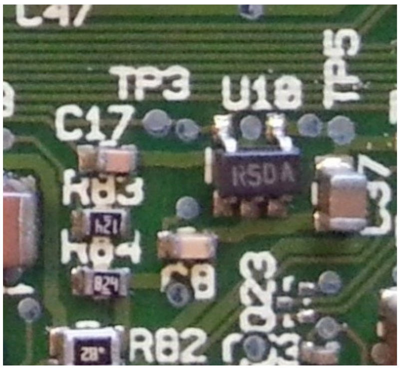

Figure 8.6: PCB layout of 1B1252A_3V0_1000ppm_Regulator_V1

8.2.6 1B1254C 3V3 Linear Regulator

This is linear regulator supply 3.3V to the tile processor. It is a linear technology component with part number LT1761ES5-3.3#TRMPBFCT-ND and reference designator U26. The schematic is shown in figure 5.16, while PCB layout is shown in figure 8.7. This regulator provides input supply to the tile processor, therefore should be enable from the PDB. But during its design mistakenly its enable signal was also applied from the tile processor. During testing R16 resistor is removed from the CubePMT and PDB voltage is applied to the enable signal of this regulator. Applied different voltages on PDB and checked the output voltage on TP12. The results are shown in the table 8.3.

Rated Input Voltage (V)	Applied Input Voltage (V)	Applied Enable signal (V)	Measured output Voltage (V)
3.8~20	6 10 15 18	PDB	3.3

Table 8.4: Testing results of 1B1254C_3V3_100mA_LDO_Regulator_V1

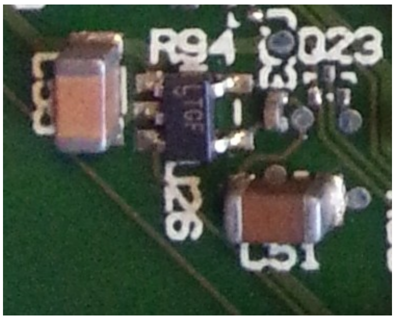

Figure 8.7: PCB layout of 1B1254C_3V3_100mA_LDO_Regulator_V1

8.2.7 1B1254B 3V3 Switching Regulator

This regulator provides 3.3V voltage level to all the 1B8_CubePMT subsystems. Linear technology component with part number DK_LTC3631EMS8E-3.3#PBF-ND and reference designator U27 is used for this supply. It converts the PDB voltage level (14V) to 3.3V, which is used by all the components of the 1B8_CubePMT system require 3.3V except tile processor (which uses separate 3.3V linear regulator). The schematic is shown in figure 5.17, while the PCB layout is shown in figure 8.8. Apply enable signal from the tile processor and check the output at TP11 of the 1B8_CubePMT module. Testing results are given in table 8.5.

Rated Input Voltage (V)	Applied Input Voltage (V)	Applied Enable signal (V)	Measured output Voltage (V)
4.5~45	10 14 16	From tile processor (2.5)	3.29

Table 8.5: Testing results of 1B1254B_3V3_100mA_ Regulator_V1

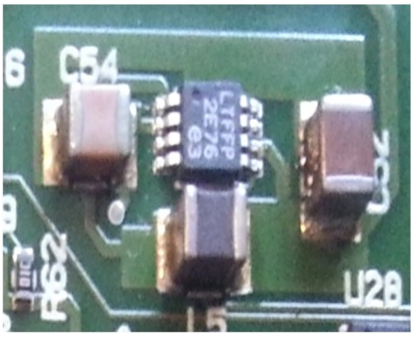

Figure 8.8: PCB layout of 1B1254B_3V3_100mA_ Regulator_V1

8.3 Housekeeping Sensors Testing

CubePMT contains two current and two voltage sensors and a single temperature sensor as already mentioned.

TEST SETUP

In order to test housekeeping sensors, first of all we attached the 1B8_CubePMT to the PC through IAR debug interface. Applied 14V to the PDB. Applied 3.3V to pin No. 4 of J- tag connector (J4). This pin should be connected to the power supply of tile processor (1B1254C_3V3_100mA_LDO_Regulator_V1), but in our case it is connected to the general 3.3V supply (1B1254B_3V3_100mA_Regulator_V1). Care should be taken that the general 3.3V supply is off.
This test setup is used for all the housekeeping sensors testing.

8.3.1 1B131C Voltage Sensor

This voltage sensor is mounted on the PDB of 1B8_CubePMT. After arranging the test setup, executed the 1B131C_Voltage_Sensor_V1 program in the 1B_CubePMT from IAR embedded workbench as given in Appendix B. Read the memory register value: in this case ADCS12MEM0 = 0BD5 hex. Equivalent decimal value is 3029. Converted this value to voltage (V) using (8-1) [11]:

$$V_{in} = N_{ADC} \frac{V_{REF}}{2^{12}} \tag{8-1}$$

Where N_{ADC} is the decimal value acquired through IAR debug interface and
V_{REF} in the reference voltage which is 2.5V.

The output value of the voltage sensor acquired through USB debug interface is 1.84V. During this test voltage on PDB was 14V. According to the schematic of voltage sensor shown in figure 5.19(b) the output voltage should be 1.79V. For further verification of the acquired results, the output of the voltage sensor is measured through a multimeter on the 1B8_CubePMT module. The value measured through multimeter is 1.78V. The acquired, calculated and measured values are almost the same, which reflects that the implemented sensor is working properly.

8.3.2 1B131B Voltage Sensor

This voltage sensor is mounted on the on the output of the solar panel. After arranging the test setup, executed the 1B131B_Voltage_Sensor_V1 program in the 1B_CubePMT from IAR embedded workbench as given in Appendix B. Read the memory register value: in this case ADCS12MEM0 = 06D1 hex. Equivalent decimal value is 1745. Converted this value to voltage (V) using (8-1), the resultant voltage is 1.06V. According to the schematic of voltage sensor shown in figure 5.19(a) the output voltage should be 1.02V. For further verification of the acquired results, the output of the voltage sensor is measured through a multimeter on the 1B8_CubePMT module. The value measured through multimeter is 1.02V. The acquired, calculated and measured values are almost the same, which reflects that the implemented voltage sensor is working properly.

8.3.3 1B132D Current Sensor

This current sensor is mounted on the PDB. After arranging the test setup, executed the 1B132D_Current_Sensor_V1 program through the 1B8_CubePMT from IAR embedded workbench as given in Appendix B. Read the memory register value: in this case ADCS12MEM0 = 0007 hex. Equivalent decimal value is 7. Convert this value to voltage (V) using (8-1), the resultant voltage is 4.27mV. For practical reading from the CubePMT module: measured voltage on C40 using multimeter. The value is 5.1mV. Measured and acquired values are very close which shows that the implemented current sensor is working properly.

8.3.4 1B132A Current Sensor

This current sensor is mounted on the output of solar panel. After arranging the test setup, executed the 1B132A_Current_Sensor_V1 program through the CubePMT from IAR embedded workbench as given in Appendix B. Read the memory register value: in this case ADCS12MEM0 = 0013 hex. Equivalent decimal value is 19. Converted this value to voltage (V) using (8-1), the resultant voltage is 11.6mV. For practical reading from the CubePMT module: measured voltage on R78 using multimeter. The value is 10mV. Measured and acquired values are very close which shows that the implemented current sensor is working properly.

8.3.5 1B133A Temperature Sensor

After arranging the test setup, executed the 1B133A Temperature Sensor program through the 1B8_CubePMT from IAR embedded workbench as given in Appendix B. Read the memory register value: in this case ADCS12MEM0 = 0596 hex. Equivalent decimal value is 1430. Converted this value to voltage (V) using (8-1), the resultant voltage is 873mV. For practical reading from the 1B8_CubePMT module: measured voltage across R34 using multimeter which was 820mV. From the output voltage versus temperature behavior of the temperature sensor shown in figure 5.22, temperature at 820mV is 27°C.
Measured and acquired values are very close which shows that the implemented temperature sensor is working properly.

8.4 ADCS Testing

TEST SETUP

In order to test each housekeeping sensor, first of all we attached the 1B8_CubePMT to the PC through IAR debug interface. Applied 14V to the PDB. Applied 3.3V to pin No. 4 of J- tag connector (J4). This pin should be connected to the power supply of tile processor (1B1254C_3V3_100mA_LDO_Regulator_V1), but in our case it is connected to the general 3.3V supply (1B1254B_3V3_100mA_Regulator_V1). Care should be taken that the general 3.3V supply is off.
This test setup is used for all the housekeeping sensors testing.

8.4.1 1B235 Sun Sensor

After arranging the test setup, we executed the 1B235 Sun Sensor program through the 1B8_CubePMT from IAR embedded workbench as given in Appendix B. Testing procedure and results of the sun sensor are giving in table 8.6.

Step No		Actions	Results	
			Hexadecimal	Decimal
1	i	Keep the 1B8_CubePMT sun sensor at 0° angle in front of the solar simulator at AM0 intensity.		
	ii	Acquire the value through IAR embedded workbench	055C	1372
	iii	Convert this value to voltage using (8-1)		837mV
	iv	Measure the value of voltage across R62 on the 1B8_CubePMT module		871mV
2	i	Keep the 1B8_CubePMT sun sensor at 45° angle in front of the solar simulator at AM0 intensity.		
	ii	Acquire the value through IAR embedded workbench	040D	1037
	iii	Convert this value to voltage using (8-1)		633mV
	iv	Measure the value of voltage across R62 on the 1B8_CubePMT module		653mV
3	i	Keep the 1B8_CubePMT sun sensor at 90° angle in front of the solar simulator at AM0 intensity.		
	ii	Acquire the value through IAR embedded workbench	010F	271
	iii	Convert this value to voltage using (8-1)		165mV
	iv	Measure the value of voltage across R62 on the 1B8_CubePMT module		171mV

Table 8.6: Testing procedure and results of sun sensor

8.4.2 B221 Magnetometer Testing

After arranging the test setup, we executed the 1B221Magnetometer program through the 1B8_CubePMT module from IAR embedded workbench as given in Appendix B. Read the memory register value: in my case ADCS12MEM0 = 090E hex. Equivalent decimal value is 2318. Now rotate the 1B8_CubePMT module by 180˚ and read ADCS12MEM0 = 07F7 hex. Equivalent decimal value is 2039.
Convert these values to voltages (mV) using (1):

$$V_{in\_MAX} = 2318 \frac{2500mV}{4096} = 1414.79mV$$

$$V_{in\_MIN} = 2039 \frac{2500mV}{4096} = 1244.5mV$$

$$\Delta V = \frac{V_{in\_MAX} - V_{in\_MIN}}{2} = \frac{170.28mV}{2} = 85.14mV$$

Divide ΔV with the gain of the OPAM (30).

$$V_{out} = \frac{\Delta V}{30} = \frac{85.14mV}{30} = 2.84mV$$

Sensitivity of the Magnetometer is 3.2mV/V/gauss and at 4.1V supply the bridge output response will be 3.2×4.1=13.12mV/gauss.
To get earth magnetic field (B), divided V_{out} with the bridge output response. As Earth Magnetic field is at 60˚ inclination in Turin, therefore:

$$B\cos 60° = \frac{V_{out}}{bridge\_response} = \frac{2.84mV}{13.12mV\,/\,gauss} = 0.2164gauss$$

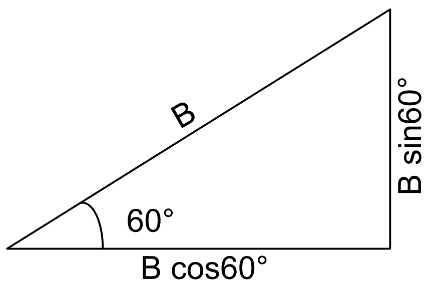

$$B = \frac{0.2164gauss}{\cos 60°} = 0.4328gauss$$

So the Earth Magnetic field in Turin is 0.4328gauss.

Chapter 9

Thermal Modeling of CubeSat Standard NanoSatellites

9.1 Introduction

The challenging aspects for NanoSatellites are their small surface area for heat dissipation due to their limited size. There is not enough space for mounting radiators for heat dissipation. As a result thermal modeling becomes a very important element in designing a small satellite. A generic thermal model of a CubeSat satellite is presented in this chapter. Detailed and simplified thermal models for NanoSatellites have been discussed. The detailed model takes into account all the thermal resistors associated with the respective layer while in the simplified model the layers with similar materials have been combined together and represented by a single thermal resistor. The thermal model of complete CubeSat has been presented. The proposed models have been applied to AraMiS-C1. Thermal resistances measured through both models are compared and the results are in close agreement. The absorbed power and the corresponding temperature differences between different points of the single panel and complete satellite are measured. In order to verify the theoretical results, the thermal resistance of the AraMiS-C1 is measured through an experimental setup. Both values are in close agreement.

9.2 Thermal Resistance

Heat is generated by the satellite as well as absorbed from the environment. Some portion of the heat energy is trapped inside the satellite while the remaining energy is lost to the surrounding. The trapped heat energy increases the overall temperature of the satellite which degrades the performance and reduces the life time of the satellite subsystems. The increase in temperature depends on the thermal resistance of the satellite. If the satellite material has greater thermal resistance, more heat is trapped inside and less energy is lost to the surrounding. The thermal resistance is related with the spacecraft structure material and the design dimensions. Thermal resistance and the resulting temperature difference between different points of the satellite can be found using thermal modeling, which help in visualizing the thermal behavior of the satellite. Therefore, these two parameters are very important for the structural design of NanoSatellites.

Thermal resistance can be found using the Fourier's Law for heat conduction [62], and is given by (9-1).

$$\theta_{th} = \frac{L}{K \times S} \tag{9-1}$$

Where θ_{th} is the thermal resistance,

L is the length of the object,

K is the thermal conductivity and

S is the cross sectional area of the object perpendicular to heat flow as shown in figure 9.1.

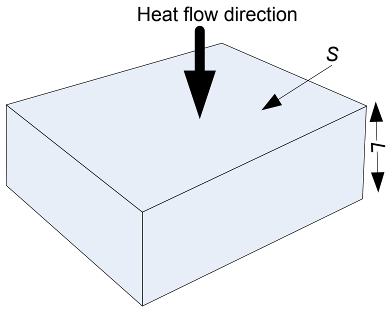

Figure 9.1: Object with cross sectional area S and length L

It is clear from (9-1) that thermal resistance of any material is directly proportional to its length and is inversely proportional to its cross sectional area. Whereas thermal conductivity is physical property and is constant for a given type of material.

9.3 Temperature Difference

When an object is exposed to the solar power, some portion of the solar power is absorbed by the object and the remaining power is reflected back from the object surface. Absorbed power (P) is given by (9-2):

$$P = \alpha \cdot P_d \cdot S \tag{9-2}$$

Where α is the absorption coefficient of the exposed surface,

P_d is the solar power density,

S is the exposed surface area and

P is the power absorbed by the surface.

When solar panel are exposed to the solar power, they absorb some portion of the incoming solar power and the remaining power is transmitted to the satellite subsystems. The power absorbed by solar panel is transformed to useful energy where as the power transmitted to the satellite is stored as unwanted heat energy. The unwanted absorbed power (P) depends on the solar power density (P_d), solar panel conversion efficiency (η), absorption coefficient (α) and area(S) of the exposed surface, given by (9-3).

$$P = P_d \cdot S \cdot (1-\eta) \cdot \alpha \tag{9-3}$$

Based on the similarity of thermal parameters and electrical parameters, in thermal domain, Ohm's law [63] is given by (9-4).

$$\Delta T = P \cdot \theta_{th} \tag{9-4}$$

Where ΔT is the temperature difference across an object and P is the power dissipated.

Thermal systems can be modeled as a network of thermal resistors and thermal capacitors. Let suppose that an object is composed of two materials attached with each other as shown in figure 9.2.

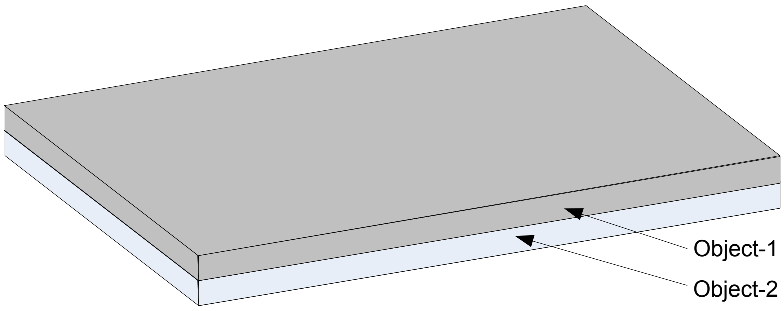

Figure 9.2: Object is composed of two materials attached with each other

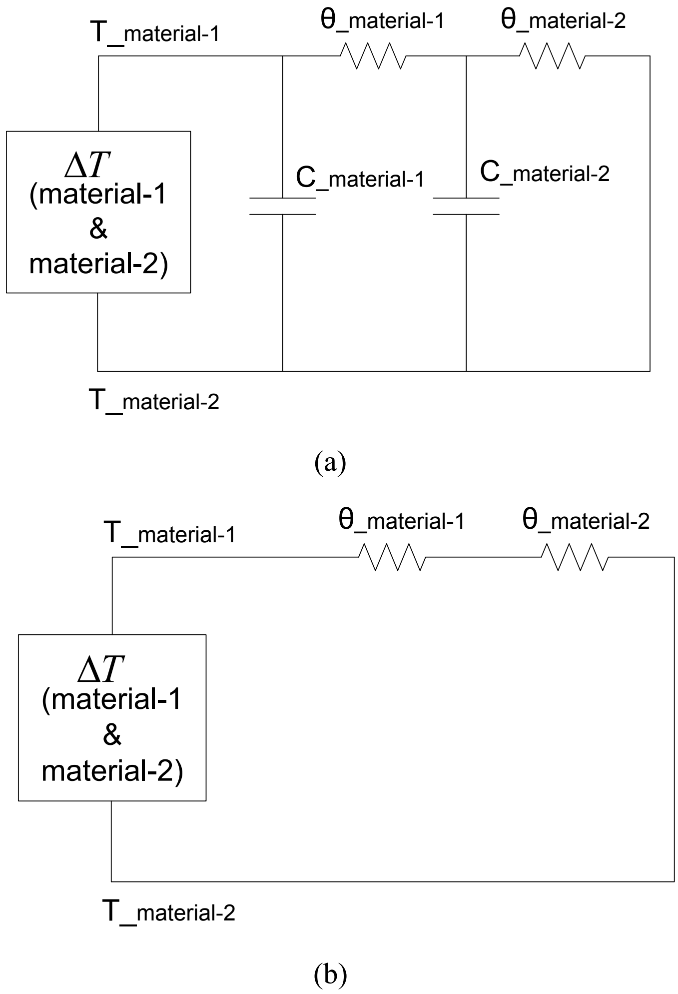

Figure 9.3: Thermal model (a) transient (b) steady state

Thermal model between top surface of material-1 and bottom surface of material-2 of the object shown in figure 9.2 is given in figure 9.3 (a).

Where *ΔT* is the temperature difference between material-1 and material-2,
T-material-1 is the top surface temperature of material-1,
T-material-2 is the bottom surface temperature of material-2,
θ-material-1 is the thermal resistance of material-1,
θ-material-2 is the thermal resistance of material-2,
C-material-1 is the thermal capacitance of material-1 and
C-material-2 is the thermal capacitance of material-2.

In steady state, the power and temperature reach constant levels ultimately thermal capacitors are fully charged. Therefore these capacitors can be neglected from the circuit model. Figure 9.3 (b) shows the steady state thermal model.

9.4 Thermal model of the CubeSat

CubeSat designed by different universities and SMEs have same dimensions but the six sides covered by the panels may have different materials. In thermal modeling consideration the CubeSat is supposed to be equipped with identical panels which are dual purpose: generating power as well as providing mechanical structure of the satellite. These panels are combined together into a cube structure with the help of aluminum rails. 1U CubeSat and aluminum rail to combine the CubeSat panel together are shown in figure 9.4.

Generalized thermal models have been presented for a generic CubeSat panel architecture and CubeSat satellite. The composition of materials and their dimensions may vary from satellite to satellite.

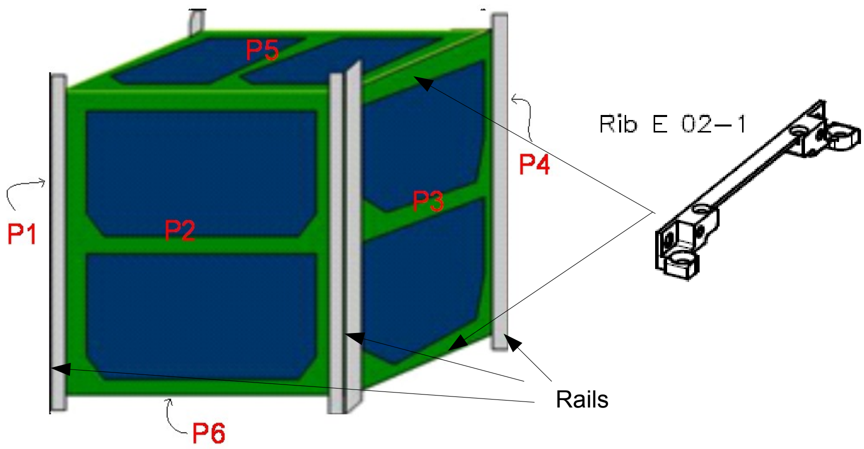

Figure 9.4: 1U CubeSat model and aluminum ribs and rails

9.5 CubeSat panel structure

As already mentioned that the CubeSat panel material and structure may be different, designed by different manufacturers. Here we are going to make a supposition that the panel may be composed of composed of four layers and four different types of materials, such as;

- FR4 printed circuit board (PCB)
- GaAs solar cells

- Resin
- Copper traces and ground plan

All four layers have FR4 material. Two solar cells are attached on layer-1 using a thermally conductive resin. Layer-2 and 3 have copper traces inserted in FR4 material. The internal layers may have different number of copper traces of certain dimensions. The traces may be used for connecting the components on external PCB surface or as magnetorquer coil. The ground plane is embedded in layer 4. Thermo mechanical model of CubeSat panel and its cross sectional view are shown in figure 9.5.

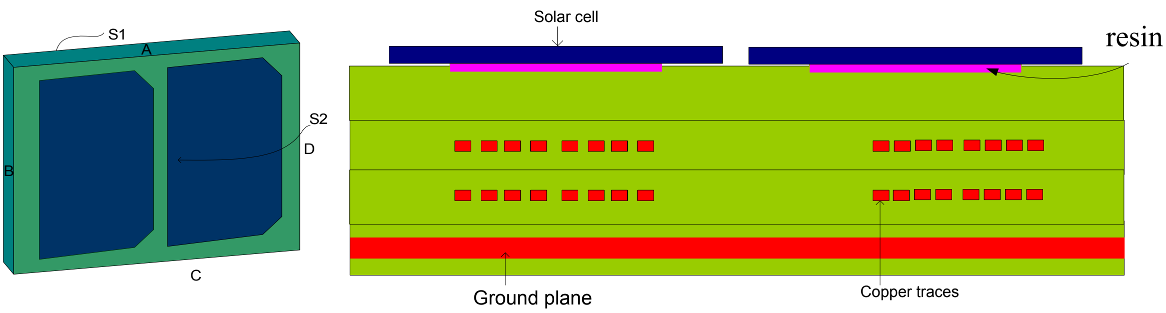

Figure 9.5: Thermo mechanical model and Cross sectional view of the CubeSat panel

9.6 CubeSat panel thermal model

Thermal model of the CubeSat panel was presented through two different models,

- Detailed thermal model
- Simplified thermal model

In the detailed thermal model, the type of panel material in each layer is identified. A separate thermal resistor is assigned to the material in each layer. A thermal resistors model is obtained by combining the resistors associated with each layer materials. This model is composed of different combination of series and parallel thermal resistors. At last a mathematical model is obtained from the thermal resistors network.

In simplified model, first similar materials of different layers are merged together and a single resistor is assigned. This technique results in a very few number of thermal resistors in the final thermal model. Thus in simplified model the number of thermal resistors reduce and computation becomes easier. The equivalent resistances of both these models should have the same value. The closeness of the two models resulted resistances values verify the authentication of these models.

9.7 Top to bottom thermal model of CubeSat panel

From top to bottom thermal model of the CubeSat panel has been found through the detailed and simplified models as presented in the subsequent sections.

9.7.1 Detailed thermal model

The cross sectional view of the generalized structure of CubeSat panel and the related detailed model are shown in figure 9.6.

In order to get a detailed model, the panel has been divided into different subsections with respect to the type of material. Each subsection has an associated thermal resistance as depicted in detailed model of figure 9.6(a). The value of the thermal resistance depends on the length, width and material type of the respective subsection. In the detailed model, a single solar cell resistor (θ_s) is in series with its resin resistor (θ_R) while the combination of these two is in parallel with the second solar cell and resin series resistors.

In thermal resistor representation, θ denotes the resistor, F represents FR4 while Cu represents copper, alphabets (a, b, c, d, e) represent the respective subsection and numbers ($1, 2, 3, 4$) represent the relevant layer. For example $\theta_{F\text{-}a2\text{-}3}$ represents the thermal resistor of FR4 material in subsection a of layers 2 and 3.

Detailed thermal model of figure 9.6(b) is written in mathematical form as given in (9-5).

$$\begin{aligned} \theta_{th-S1S2} &= \frac{\theta_S + \theta_R}{2} + \theta_{F-1} + \theta_{F-a2-3} // (\theta_{Cu-b2-3} + \theta_{F-b2-3}) // \\ &\theta_{F-c2-3} // (\theta_{Cu-d2-3} + \theta_{F-d2-3}) // \theta_{F-e2-3} + \theta_{Cu\_4} + \theta_{F-4} \end{aligned} \tag{9-5}$$

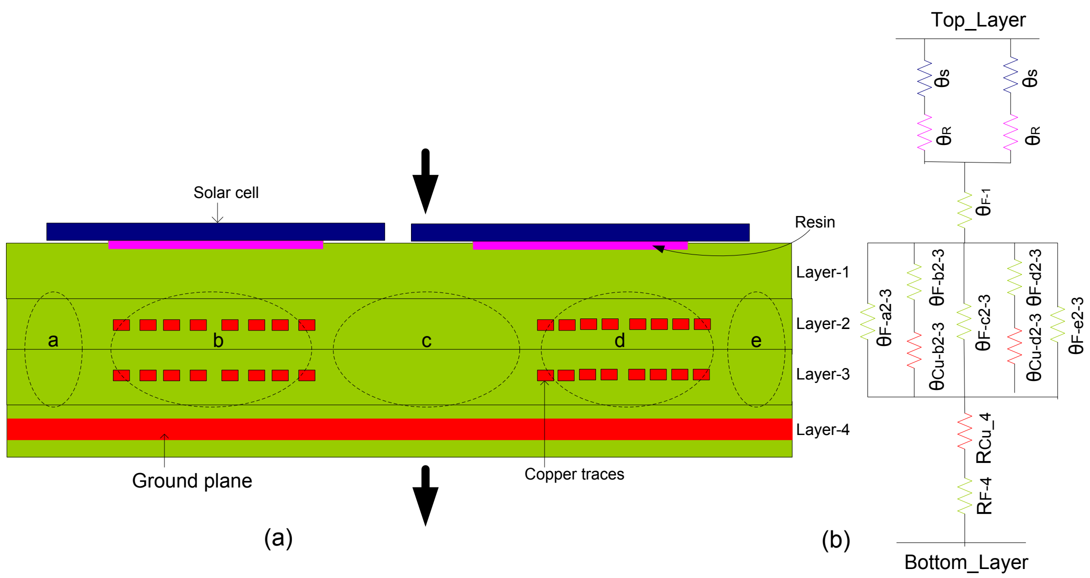

Figure 9.6: CubeSat panel (a) cross sectional view (b) detailed model.

9.7.2 Simplified thermal model

The simplified thermal model is obtained by merging different subsections of the panel with same material. Copper traces of different layers are merged into a single trace, similarly FR4 material is also combined together. As a result, the FR4 and copper reduces to four subsections (*a, b, c & d*) as shown in figure 9.7(a). Subsections '*a*' and '*b*' have FR4 material while subsections '*c*' and '*d*' have copper.

The simplified model is shown in figure 9.7(b). The parallel combination of two solar cells resistors is represented by a single thermal resistor (θ_S) and the associated resin resistors are also represented by a single thermal resistor (θ_R).

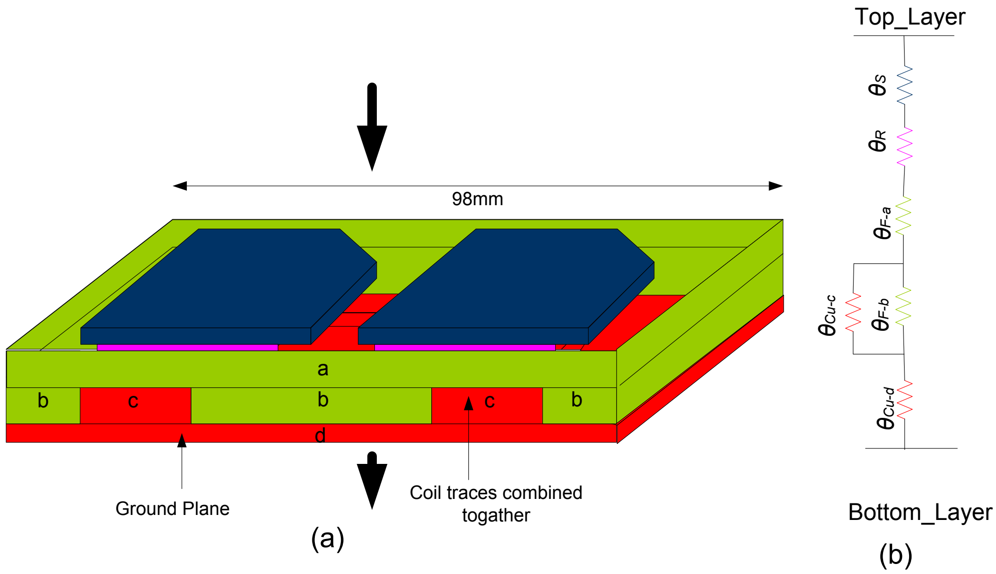

Figure 9.7: (a) Panel top to bottom cross sectional view and (b) panel simplified model.

In thermal resistor representation, θ denotes the resistor, *F* represents FR4 while *Cu* represents copper and alphabets (*a, b, c, d*) represent the respective subsection. Thermal model of figure 8.7(b) is written in mathematical form as given in (9-6).

$$\theta_{th-S1S2} = \theta_S + \theta_R + \theta_{F-a} + \theta_{Cu-c} // \theta_{F-b} + \theta_{Cu-d} \tag{9-6}$$

9.8 Edge to edge thermal model of CubeSat panel

Thermal resistance between the two edges '*B*' and '*D*' of the panel, is found using the proposed models discussed in the subsequent sections.

9.8.1 Detailed thermal model

The panel has been divided into small subsections of different lengths with respect to the type of material as shown in figure 9.8. Subsection 'a' and 'e' have pure FR4 material in layers 1, 2 and 3 while ground plane is embedded in layer 4. Similarly subsections 'b', 'c' and 'd' consist of both FR4 and copper traces. In subsections 'b' and 'd' the individual resistance of the copper traces is in series with each other while in subsection 'c', copper traces resistances are in parallel with each other. Subsection 'f' has the FR4 material of layer 1 and 4 while subsection 'g' has the ground plane. Thermal model is obtained by combining the thermal resistances associated with each subsection. Solar panel internal view, side view and edge to edge detailed thermal model are shown in figure 9.8.

Thermal model of figure 9.8(c) is written in mathematical form as given in (9-7) where '*i*' represents the number of layers have copper traces and '*j*' represents the number of ground planes.

$$\theta_{th-BD} = \left\{ \begin{array}{l} 2(\theta_R // \theta_S) + \theta_{POS}) // \left(\dfrac{\theta_{F-b} // \theta_{Cu-b} + \theta_{F-c} // \theta_{Cu-c} + \theta_{F-d} // \theta_{Cu-d}}{i} \right) \\ // \theta_{F-f1} // \theta_{F-f4} + \theta_{F-a1-4} + \theta_{F-e1-4} \end{array} \right\} // \frac{\theta_{Cu-g4}}{j} \tag{9-7}$$

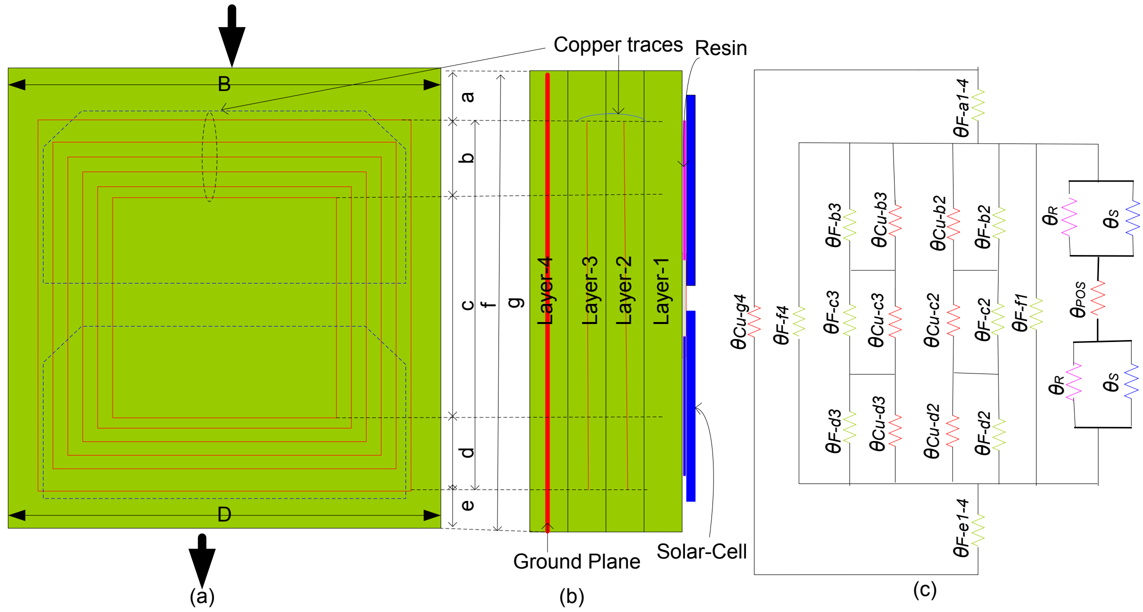

Figure 9.8: Panel (a) internal view (b) side view (c) detailed thermal model

9.8.2 Simplified thermal model

Detailed thermal model from edge to edge of the panel is very complicated and requires complex computations of resistors as it is apparent from figure 9.8(c). Through simplified model the complex system is made simpler by combining different subsections of the panel having similar material. The copper traces in different layers are merged together into a single trace. Similarly, FR4 material is also shifted and combined together.

The equivalent thermal model for the half portion of the panel is shown in figure 9.9(b), which is identical to the second half. Subsection ‘a’ has pure FR4 material while subsections ‘b’ and ‘c’ consist of copper traces and FR4 material.

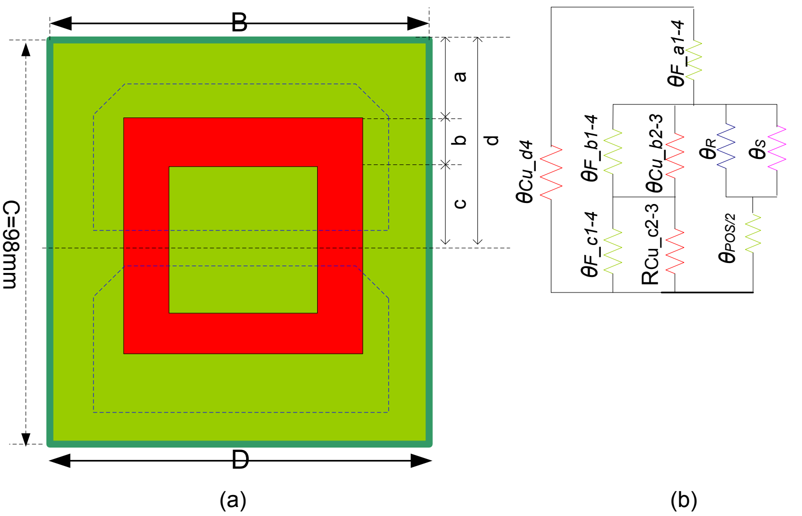

Figure 9.9: (a) Panel shape after combining similar material (b) Panel half portion simplified model

The simplified thermal model of complete panel is given in (8-8).

$$\theta_{th-BD} = 2[(\theta_{F\_a1-4} + (\theta_{F\_b1-4} // \theta_{Cu\_b2-3} + \theta_{F\_c1-4} // \theta_{Cu\_c2-3}) // (\theta_s // \theta_R + \frac{\theta_{POS}}{2})) // \theta_{Cu\_d4}] \quad (9\text{-}8)$$

9.9 Centre to edge thermal model of CubeSat panel

Before going into the details of centre to edge thermal model, let first understand the thermal resistance between two circles as shown in figure 9.10. Solar power is impinging on circle with radius R_1 and spreads to the circle with radius R_2.

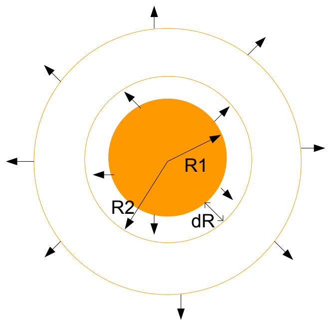

Figure 9.10: Thermal resistance between two circles

The solar power (P) absorbed by the circle with radius R is given by (8-9);

$$P = P_d \alpha \pi R^2 \quad (9\text{-}9)$$

Where, P_d is the solar power density and

α is the absorption coefficient of the circle with radius R.

Temperature difference (ΔT) of the length dR is give by (8-10).

$$\begin{aligned}
&dT = Pd\theta \\
&dT = P\frac{dR}{K2\pi R.h} \\
&dT = P_d \alpha \pi R^2 \frac{dR}{K2\pi R.h} = \frac{P_d \alpha}{2Kh} RdR \\
&\int_{R_1}^{R_2} dT = \frac{P_d \alpha}{2P_d Kh} \int_{R_1}^{R_2} RdR = \frac{\alpha(R_2{}^2 - R_1{}^2)}{4K \cdot h} \\
&\Delta T = \frac{\alpha P_d}{4Kh}(R_2{}^2 - R_1{}^2)
\end{aligned} \quad (9\text{-}10)$$

Where K is the thermal conductivity of the material

h is the thickness of the circular section.

Thermal resistance of the section with length dR, as shown in figure 9.10, is given by (9-11).

$$\Delta\theta = \frac{\Delta T}{P} \tag{9-11}$$

$$\Delta\theta = \frac{\frac{\alpha P_d R_T^2}{4Kh}}{P_d \cdot \pi \cdot R_T^2} = \frac{\alpha}{4\pi Kh}$$

Therefore, the thermal resistance of a circular section depends on the thickness of that section and the material absorption coefficient.

9.9.1 Detailed thermal model

Assuming the panel to be consist of three concentric circles with radius R_1, R_2 and R_3 respectively with centre R_o as shown in figure 9.11. The section between the radii R_1 and R_0 contains FR4 material and also ground plane (extended in layer 4). The subsection between circle R_1 and R_2 contains copper traces, FR4 material as well as ground plane. While the subsection between circles R_2 and R_3contains FR4 material and ground plane. Centre to edge detailed thermal model is shown in figure 9.11(c). In thermal resistor representation, θ denotes the resistor, F represents FR4 while Cu represents copper, numbers ($1, 2, 3, 4$) represent the relevant layer and R_i R_j (i, j= 1, 2, 3, 4) represents the subsection between the two circles. For example $\theta_{F\text{-}2\text{-}R1R2}$ represents the thermal resistor of FR4 material in layer 2 of subsection between circles R_1 and R_2.

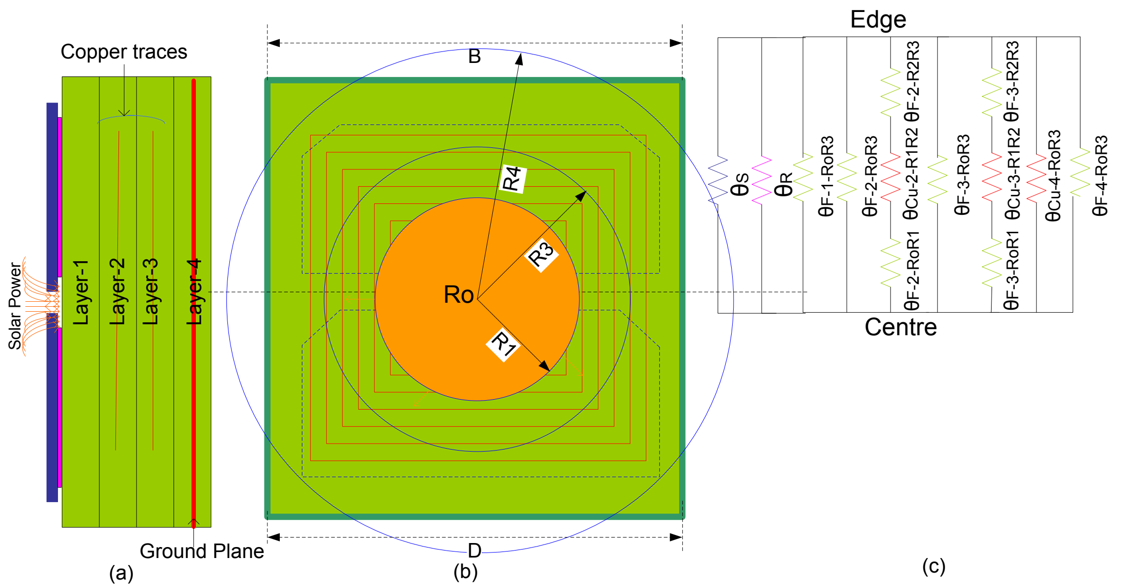

Figure 9.11: Panel (a) side view (b) internal view (c) detailed model.

Thermal model of figure 8.11(c) is written in mathematical form as given in (8-12).

$$\theta_{th-CE} = \theta_S // \theta_R // \theta_{F\_1-R_0R_3} // \theta_{F\_2-R_0R_3} //(\theta_{F\_2-R_0R_1} + \theta_{Cu\_2-R_1R_2} + \theta_{F\_2-R_2R_3}) // \theta_{F\_3-R_0R_1} //(\theta_{F\_3-R_0R_1} + \theta_{Cu\_3-R_1R_2} + \theta_{F\_3-R_2R_3}) // \theta_{Cu\_4-R_0R_3} // \theta_{F\_4-R_0R_3}$$

(9-12)

9.9.2 Simplified thermal model

Detailed model from centre to edge of the panel is also complex and requires to compute large number of resistors as it is apparent from figure 9.11(c). In simplified model the system is made simpler by combining different subsections of the panel having similar material. The copper traces are merged into a single trace. Similarly, FR4 material is also shifted and combined together. The panel shape after simplification process and the related simplified model are shown in figure 9.12(b). Centre to edge simplified thermal model is given in figure 9.12(c).

Thermal model of figure 9.12 (c) is written in mathematical form as given in (9-13). In thermal resistor representation, θ denotes the resistor, F represents FR4 while Cu represents copper, numbers (*1, 2, 3, 4*) represent the relevant layer and $R_i\,R_j$ (i, j= 1, 2, 3, 4) represents the subsection between the two circles. For example $\theta_{F\text{-}2\text{-}R1R2}$ represents the thermal resistor of FR4 material in layer 2 of subsection between circles R_1 and R_2.

$$\theta_{th-CE} = \theta_S \,//\, \theta_R \,//\, \theta_{F-4-R_0R_3} \,//\, \theta_{Cu-4-R_0R_3} \,//(\theta_{F-2-3-R_0R_1} + \theta_{Cu-2-3-R_1R_2} + \theta_{F-2-3-R_2R_3}) \tag{9-13}$$

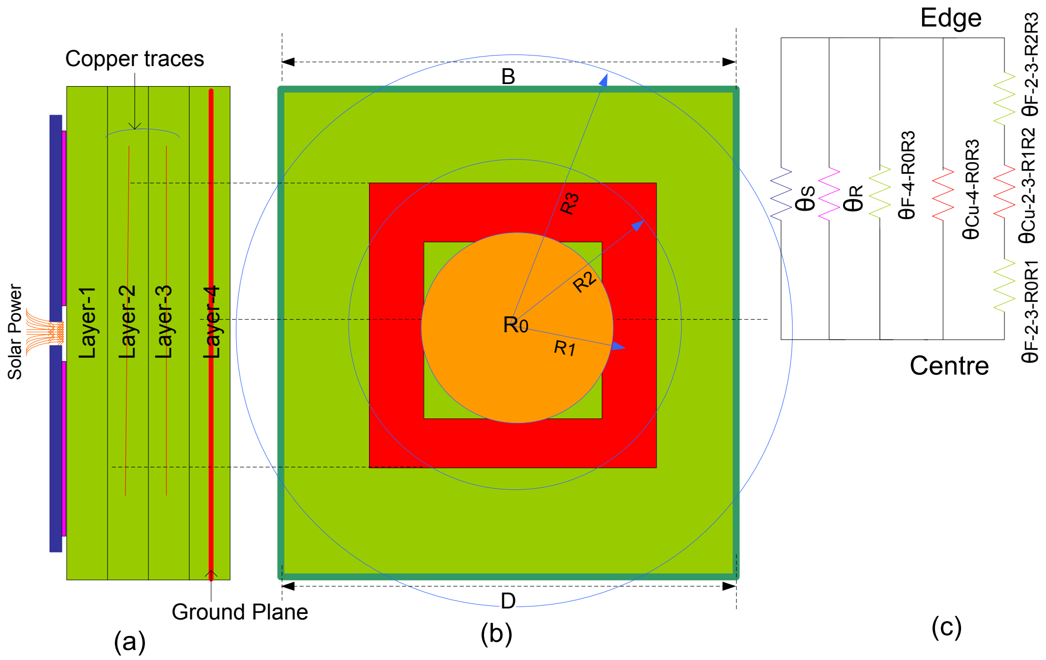

Figure 9.12: Panel (a) side view (b) internal view (c) simplified model

9.10 CubeSat thermal model

As already mentioned that CubeSat 1U is generally composed of six panels on the outer faces, combined together with aluminum rails using screws as shown in figure 9.4. In order to find CubeSat thermal model, let consider that the solar power is impinging on the panel centre on one face of the satellite and flows to the coolest point on the opposite face of the satellite. This power is equally distributed between all the six faces as shown in figure 9.13. Here the power flows through all the six panels, rails and screws. Each panel and rails have associated thermal resistances. CubeSat thermal resistors with the satellite panels, rails and screws are shown in figure 9.13. where

θ_{CE} : centre to edge thermal resistance of the panel,
$\theta_{CE\text{-}q}$: centre to edge thermal resistance of the panel on equipotential surface
$\theta_{Rail\text{-}1}$: aluminum rail to rail thermal resistance
$\theta_{Rail\text{-}1\text{-}q}$: aluminum rail to rail thermal resistance on equipotential surface
$\theta_{Rail\text{-}2}$: aluminum rail to panel thermal resistance
$\theta_{Rail\text{-}2\text{-}q}$: aluminum rail to panel thermal resistance on equipotential surface and
θ_{Screw} : screw thermal resistance.

There are surfaces on the CubeSat which are at the same temperature and called equipotential surfaces. These surfaces are shown with red lines in the CubeSat thermal model shown in figure 9.14. The resistors on the equipotential surfaces are represented with subscript 'q'. The temperature difference across the equipotential surfaces resistance is zero, therefore these resistors do not contribute to the thermal model and can be neglected from the CubeSat thermal model. The CubeSat thermal model without equipotential thermal resistors is shown in figure 9.15. In this thermal model the centre of each tile is represented with a circle with cross (×) and the corners of the satellite are represented with a circle with dot (●). The centre of the rails are represented with small circle as shown in figure 9.15.

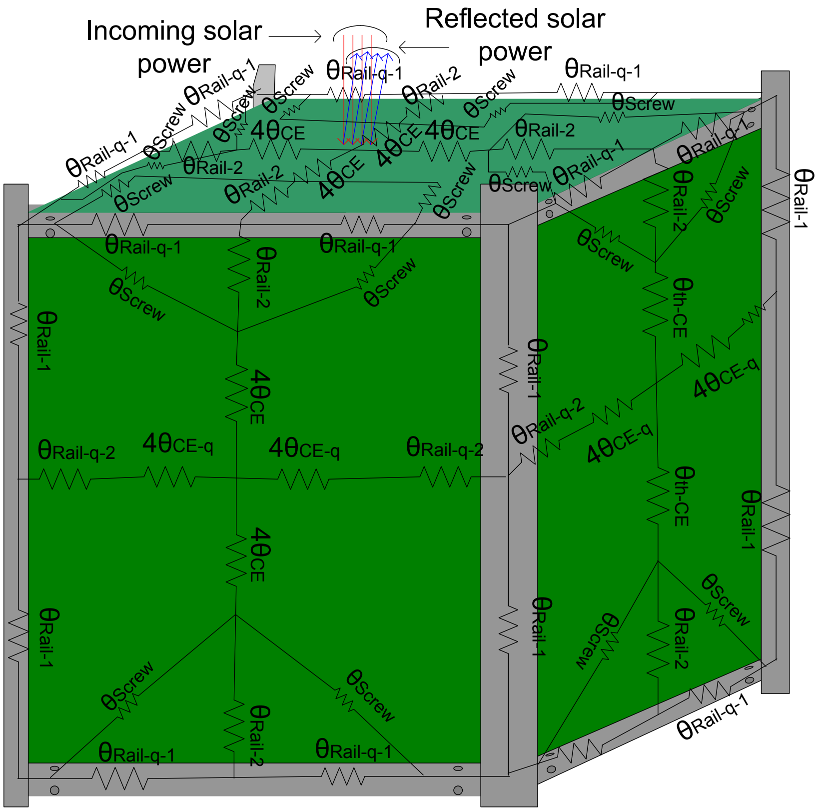

Figure 9.13: CubeSat with thermal resistors

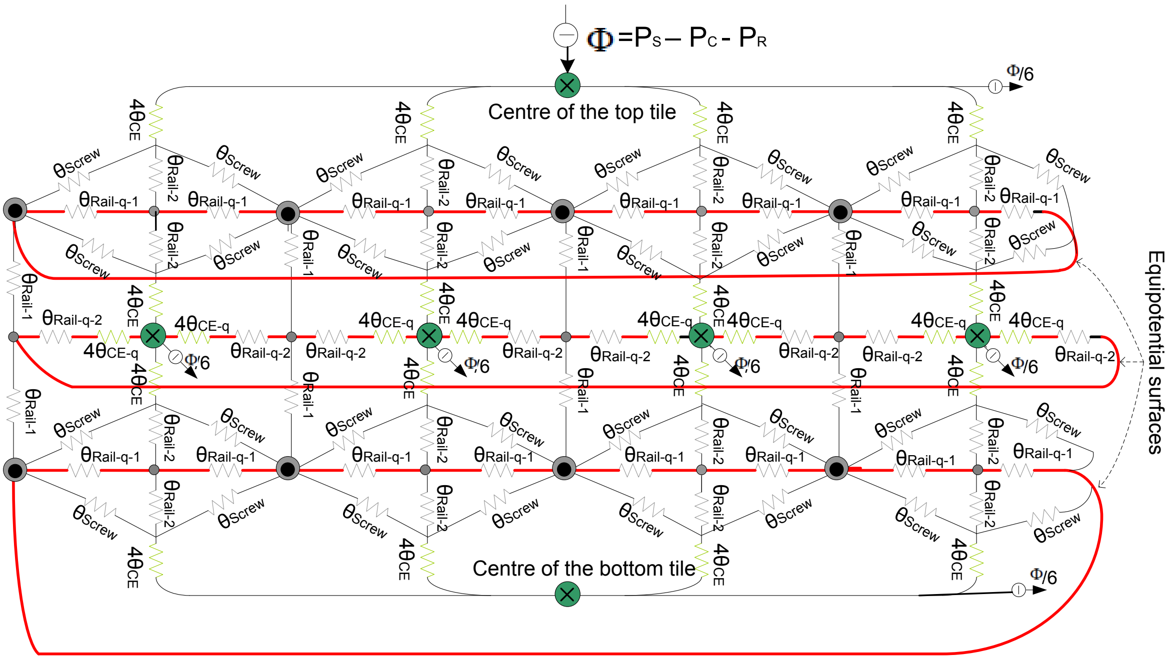

Figure 9.14: CubeSat thermal model along with equipotential surfaces resistors

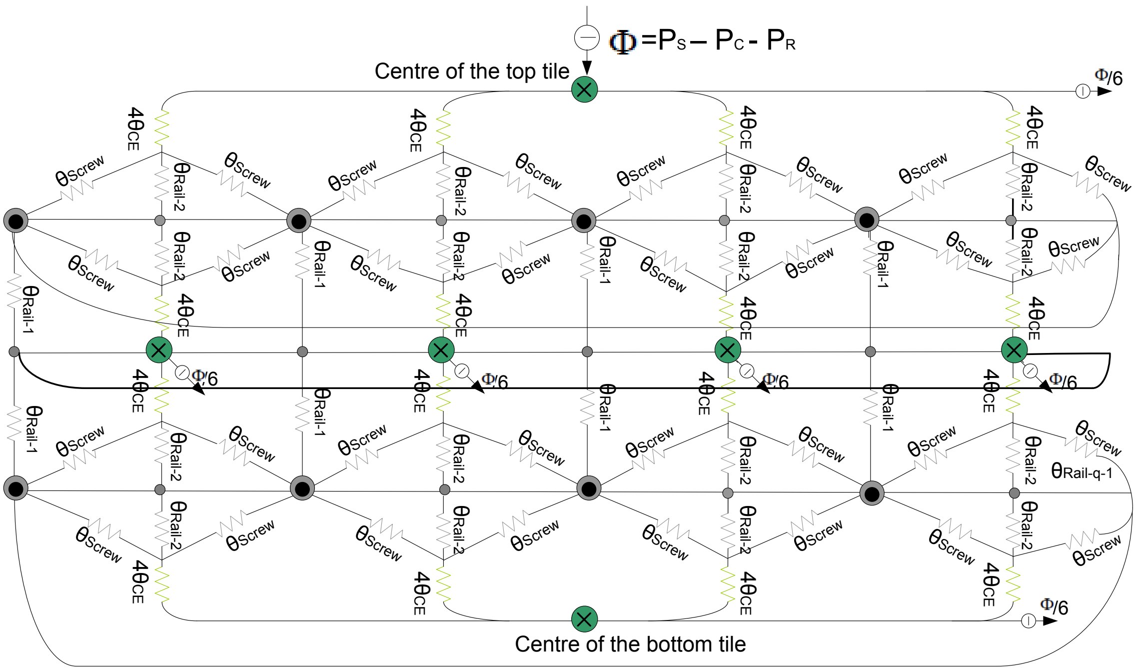

Figure 9.15: CubeSat thermal model without equipotential surfaces resistors

Thermal model of figure 9.15 is written in mathematical form as given in (9-14).

$$\theta_{th} = 2\left(\frac{4\theta_{CE} + \theta_{Rail\text{-}2} \,//\, \dfrac{\theta_{Screw}}{2}}{4}\right) + 2\left(\frac{4}{4\theta_{CE} + \theta_{Rail\text{-}2} \,//\, \dfrac{\theta_{Screw}}{2}} + \frac{4}{\theta_{Rail\text{-}1}}\right)^{-1} \tag{9-14}$$

9.11 Solar Power absorbed by CubeSat

The only power source of the CubeSat are the six solar panels covering as many faces of the satellite. By taking into account that only one panel is exposed at a time to sunlight. There are two cases where the power absorbed by the panel may be different.

- When solar panel is converting solar power to electrical power, it absorbs some portion of the incoming solar power (P_S) and the remaining power is reflected (P_R) from the surface. The amount of absorbed power depends on the absorption coefficient (α) of the exposed surface. Some portion of the absorbed power is converted to useful energy (P_C) which depends on the efficiency (η) of the solar panel. The remaining absorbed power is transmitted to the satellite which is the unwanted energy (Φ) as shown in figure 8.15 and is given by (9-15):

$$\begin{aligned} &\Phi = P_S - P_R - P_C \\ &P_S - P_R = \alpha P_d S \\ &P_C = \eta(P_S - P_R) = \eta\alpha P_d S \\ &\Rightarrow \Phi = \alpha P_d S(1-\eta) \end{aligned} \tag{9-15}$$

Where P_d is the solar power density at LEO (low earth orbit) is about 1366 W/m^2 and
S is the area of the exposed surface.

- When solar panel is off, no power is converted to useful energy (P_c=0) and all the absorbed power is transferred to the satellite.

$$\Phi = \alpha P_d S \tag{9-16}$$

The unwanted energy (Φ) start flowing to the coolest point on the satellite which is the centre point on the opposite face as shown in figure 9.15. The unwanted energy (Φ) flows to all the six faces and equally distributed amongst them ($\Phi/6$ to each face). This power tends to increase the overall temperature of the satellite.

9.12 Thermal resistance of AraMiS-C1 using CubeSat model

Thermal model presented in the previous section, is applied to AraMiS-C1. As already mentioned that four sides of AraMiS-C1 are equipped with identical 1B8_CubePMT tiles and the remaining two sides have 1B9_CubeTCT . In order to find thermal resistance of AraMiS-C1, first thermal resistances of 1B8_CubePMT and 1B9_CubeTCT are required.

For 1B8_CubePMT and 1B9_CubeTCT thermal resistances computation, thermal model presented for the CubeSat panel in the previous sections will be applied here.

9.12.1 Top to bottom thermal resistance of 1B8_CubePMT

1B8_CubePMT module has the same type of material as that of CubeSat solar panel, just the number of layers, copper traces and ground planes have been increased. Changing the number of layers and traces will modify the dimensions of the respective subsections which will result in different thermal resistance values for 1B8_CubePMT as compared to CubeSat panel. The thermal resistance model will remain the same as that of CubeSats solar panel presented in section 9.6. 1B8_CubePMT module top to bottom cross sectional view is shown in figure 9.16.

9.12.1.1 Using CubeSat panel detailed model

First we used the detailed model of CubeSat panel presented in section 9.7.1, in order to find top to bottom thermal resistance of 1B8_CubePMT module as given in (9-17). As it is clear from (9-17) that the model is same, just the number of layers have been increased in case of 1B8_CubePMT.

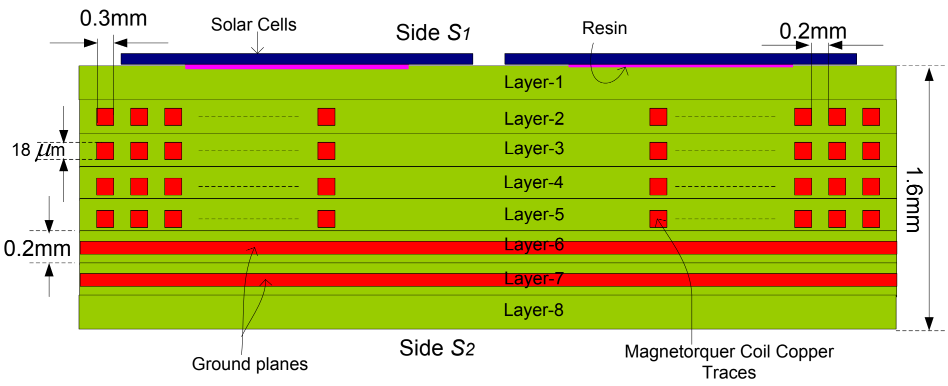

Figure 9.16: 1B8_CubePMT module top to bottom cross sectional view.

$$\theta_{th-S1S2} = \frac{\theta_{Solar-cell} + \theta_{\text{Resin}}}{2} + \theta_{F-1} + \theta_{F-a2-5} // (\theta_{Cu-b2-5} + \theta_{F-b2-5}) // \theta_{F-c2-5} // (\theta_{Cu-d2-5} + \theta_{F-d2-5}) // \theta_{F-e2-5} + \theta_{Cu\_g} + \theta_{F-6-7-8} \quad (9\text{-}17)$$

Each subsection thermal resistance was found by inserting the length and thickness parameters of the corresponding subsection.

$$\theta_{Solar-cell} = \frac{L}{K_{GaAs} \times S} = \frac{0.15 \times 10^{-3}}{55 \times (70 \times 10^{-3} \times 40 \times 10^{-3})} = 0.97 \times 10^{-3} K/W$$

$$\theta_{\text{Resin}} = \frac{L}{K_{\text{Resin}} \times S} = \frac{0.5 \times 10^{-3}}{0.282 \times (30 \times 10^{-3} \times 25 \times 10^{-3})} = 2.36 K/W$$

$$\theta_{F\_1} = \frac{L_1}{K_{FR4} \times S_1} = \frac{0.2 \times 10^{-3}}{0.24 \times (82.5 \times 10^{-3} \times 98 \times 10^{-3})} = 0.1 K/W$$

$$\theta_{F\_a2-5} = \frac{L_{2-5}}{K_{FR4} \times S_{F\_2-5}} = \frac{(0.2 \times 4) \times 10^{-3}}{0.24 \times (82.5 \times 10^{-3} \times 5.5 \times 10^{-3} + 98 \times 10^{-3} \times 1.75 \times 10^{-3})} = 5.54 K/W$$

$$\theta_{F\_e2-5} = \frac{L_{2-5}}{K_{FR4} \times S_{F\_2-5}} = \frac{(0.2 \times 4) \times 10^{-3}}{0.24 \times (82.5 \times 10^{-3} \times 5.5 \times 10^{-3} + 98 \times 10^{-3} \times 1.75 \times 10^{-3})} = 5.54 K/W$$

$$\theta_{F\_b2-5} = \frac{L_{2-5\_b}}{K_{FR4} \times S_{F\_2-5\_b}} = \frac{4(0.2 \times 10^{-3} - 18 \times 10^{-6})}{0.24 \times ((25-10) \times 10^{-3} \times 79 \times 10^{-3} + (25-10) \times 10^{-3} \times 18.5 \times 10^{-3})} = 2 K/W$$

$$\theta_{F\_d2-5} = \frac{L_{2-5\_d}}{K_{FR4} \times S_{F\_2-5\_d}} = \frac{4(0.2\times10^{-3} - 18\times10^{-6})}{0.24\times(25\times10^{-3}\times79\times10^{-3} + 25\times10^{-3}\times18.5\times10^{-3})} = 2K/W$$

$$\theta_{Cu-b2-5} = \frac{L_{c2-5}}{K_c S_{c2-5}} = \frac{4\times18\times10^{-6}}{355\times(50\times0.3\times10^{-3}\times79\times10^{-3} + 2\times50\times0.3\times10^{-3}\times18.5\times10^{-3})} = 11.65\times10^{-5} K/W$$

$$\theta_{Cu-d2-5} = \frac{L_{d2-5}}{K_c S_{d2-5}} = \frac{4\times18\times10^{-6}}{355\times(50\times0.3\times10^{-3}\times79\times10^{-3} + 2\times50\times0.3\times10^{-3}\times18.5\times10^{-3})} = 11.65\times10^{-5} K/W$$

$$\theta_{F\_c2-5} = \frac{L_{F\_c2-5}}{K_{FR4} S_{F-c2-5}} = \frac{(0.2\times4)\times10^{-3}}{0.24\times((37+5)\times10^{-3}\times(29+5)\times10^{-3})} = 2.33K/W$$

$$\theta_{Cu\_g} = \frac{L_{cg}}{K_c S_{cg}} = \frac{2\times18\times10^{-6}}{355\times(82.5\times10^{-3}\times98\times10^{-3})} = 1.25\times10^{-5} K/W$$

$$\theta_{F\_7-8} = \frac{L_{6-7-8}}{K_{RF4} S_{6-7-8}} = \frac{(0.2\times2 - 0.018\times2)\times10^{-3}}{0.24\times98\times10^{-3}\times82.5\times10^{-3}} = 0.19K/W$$

$$\boxed{\theta_{th-S1S2} = 2.07K/W}$$

Thermal resistors values of top to bottom using detailed model is *2.07 K/W* .

9.12.1.2 Using CubeSat panel simplified model

Now we will used the simplified model presented for the CubeSat panel in section 9.7.2, in order to find top to bottom thermal resistance of 1B8_CubePMT module.

$$\theta_{th-S1S2} = \theta_S + \theta_R + \theta_{F-a} + \theta_{Cu-c} // \theta_{F-b} + \theta_{Cu-d} \tag{9-18}$$

$$\theta_S = \theta_{Solar-cell} // \theta_{Solar-cell} = 0.05\times10^{-3} K/W$$

$$\theta_R = \theta_{\mathrm{Resin}} // \theta_{\mathrm{Resin}} = 1.18K/W$$

$$\theta_{F\_a} = \frac{L_a}{K_{FR4} \times S_{F\_a}} = \frac{(1.6 - 6\times0.018)\times10^{-3}}{0.24\times(82.5\times10^{-3}\times98\times10^{-3})} = 0.77K/W$$

$$\theta_{F\_b} = \frac{L_b}{K_{RF4} S_b} = \frac{(0.2\times4)\times10^{-3}}{0.24\times((37+10)\times10^{-3}\times(29+10)\times10^{-3} + 7\times10^{-3}\times2(92+80)\times10^{-3})} = 1.57K/W$$

$$\theta_{Cu-c} = \frac{L_c}{K_{Cu} S_c} = \frac{4\times18\times10^{-6}}{355\times2\times(62+54)\times10^{-3}\times15\times10^{-3}} = 5.8\times10^{-5} K/W$$

$$\theta_{Cu\_d} = \frac{L_d}{K_{Cu} S_d} = \frac{2\times18\times10^{-6}}{355\times(82.5\times10^{-3}\times98\times10^{-3})} = 1.25\times10^{-5} K/W$$

$$\boxed{\theta_{th.S1S2} = 2K/W}$$

Top to bottom thermal resistor value of 1B8_CubePMT using simplified model is *2.07 K/W* . So thermal resistances found through simplified and detailed models have almost same values. This reflects the authentication of the proposed models.

9.12.2 Thermal resistance from centre to edge

Thermal resistance from centre to edge of the 1B8_CubePMT module is found by using the detailed and simplified models of CubeSat panel given in section 9.9.

9.12.2.1 Using detailed thermal model

From center to edge thermal resistance of the 1B8_CubePMT module was found using the detailed thermal model of CubeSat panel given in 9.9.1. As the number of layers have been increased, so the mathematical form of the model will become as given in (9-19).

$$\begin{aligned} \theta_{th-CE} &= \theta_S // \theta_R // \theta_{F\_1-R_0R_3} // \theta_{F\_2-3-4-5-R_0R_3} //(\theta_{F\_2-3-4-5-R_0R_1} \\ &+ \theta_{Cu\_2-3-4-5-R_1R_2} + \theta_{F\_2-3-4-5-R_2R_3}) // \theta_{F\_6-7-8-R_0R_3} // \theta_{Cu\_6-7-R_0R_3} \end{aligned} \tag{9-19}$$

$$\theta_S = \frac{0.9}{4\pi \times 55 \times 150 \times 10^{-6}} = 8.68K/W$$

$$\theta_R = \frac{0.9}{4\pi \times 0.282 \times 500 \times 10^{-6}} = 507K/W$$

$$\theta_{F\_1-R_0R_3} = \frac{0.9}{4\pi \times 0.24 \times 0.2 \times 10^{-3}} = 1492K/W$$

$$\theta_{F\_2-3-4-5-R_0R_1} = \frac{0.9}{4\pi \times 0.24 \times 4(0.2-0.018) \times 10^{-3}} = 400K/W$$

$$\theta_{Cu\_2-3-4-5-R_1R_2} = \frac{0.9}{4\pi \times 355 \times 4 \times 0.018 \times 10^{-3}} = 2.8K/W$$

$$\theta_{F\_2-3-4-5-R_2R_3} = \frac{0.9}{4\pi \times 0.24 \times 4(0.2-0.018) \times 10^{-3}} = 400K/W$$

$$\theta_{F\_6-7-8-R_0R_3} = \frac{0.9}{4\pi \times 0.24 \times 4(3 \times 0.2 - 2 \times 0.018) \times 10^{-3}} = 529K/W$$

$$\theta_{Cu\_6-7-R_0R_3} = \frac{0.9}{4\pi \times 355 \times 2 \times 0.018 \times 10^{-3}} = 5.6K/W$$

$$\boxed{\theta_{CE} = 3.31K/W}$$

The thermal resistance value found is 3.31K/W.

9.12.2.2 Using simplified thermal model

From center to edge thermal resistance of the 1B8_CubePMT module was found using the simplified thermal model of CubeSat panel given in 9.9.2.

$$\theta_{CE-P} = \left(\theta_{F-3} + \theta_{Cu-2} + \theta_{F-1}\right) // \theta_{Cu-4} // \theta_{F-5} // \theta_S // \theta_R$$

$$\theta_{CE-P} = \left(\frac{0.9}{4\pi \times 0.24 \times 72 \times 10^{-6}} + \frac{0.9}{4\pi \times 355 \times 72 \times 10^{-6}} + \frac{0.9}{4\pi \times 0.24 \times 72 \times 10^{-6}}\right) // \frac{0.9}{4\pi \times 355 \times 36 \times 10^{-6}}$$

$$// \frac{0.9}{4\pi \times 0.24 \times 1.492 \times 10^{-3}} // \frac{0.9}{4\pi \times 55 \times 150 \times 10^{-6}} // \frac{0.9}{4\pi \times 0.282 \times 500 \times 10^{-6}}$$

$$\boxed{\theta_{CE} = 3.32 K / W}$$

The thermal resistance using simplified found is 3.32K/W.

Thermal resistances values found through detailed and simplified models are almost the same. The closeness of these values show the accuracy of the proposed models.

9.12.3 Thermal Resistance of AraMiS-C1

In order to measure equivalent thermal resistance of AraMiS-C1, a heat source is required to supply thermal power to the satellite equivalent to the incoming solar power. For this purpose solar simulator can be used but these measurements will be performed inside a vacuum chamber. In that case, it is impossible to take solar simulator inside the vacuum chamber. For that purpose a 2.2Ω and 100W resistor was used to raise the satellite one face temperature equivalent to the temperature increase by the sun light at AM0. This resistor was attached with the telecommunication tile (1B9_CubeTCT) through an aluminum piece as shown in figure 9.17.

9.12.4 Theoretical Measurement of AraMiS-C1 utilizing CubeSat Model

For the theoretical measurement of equivalent thermal resistance of AraMiS-C1, the thermal resistance model of CubeSat presented in section 9.10. A little modification can be seen in this model from that of CubeSat. A new thermal resistor that of aluminum piece (θ_{Al}) has been added in parallel with the top tile and the thermal resistance from centre to edge θ_{CE} has been modified with θ_{CE-C} and θ_{CE-P}, which represent 1B9_CubeTCT centre to edge thermal resistance and 1B8_CubePMT centre to edge thermal resistance respectively.

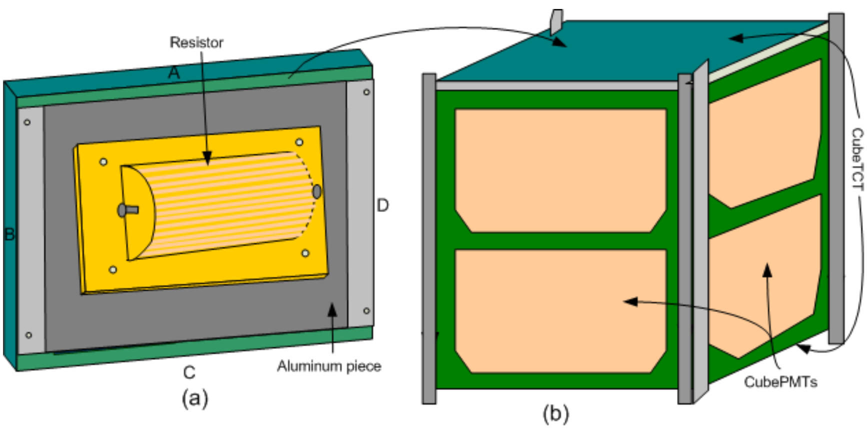

Figure 9.17: Measurement arrangements (a) Power resistor attached with 1B9_CubeTCT through aluminum tile (b) AraMiS-C1 with four 1B8_CubePMT without solar cells and two 1B9_CubeTCT tiles.

The equivalent thermal model of the AraMiS-C1 satellite with the measurement arrangement is shown in figure 9.18.

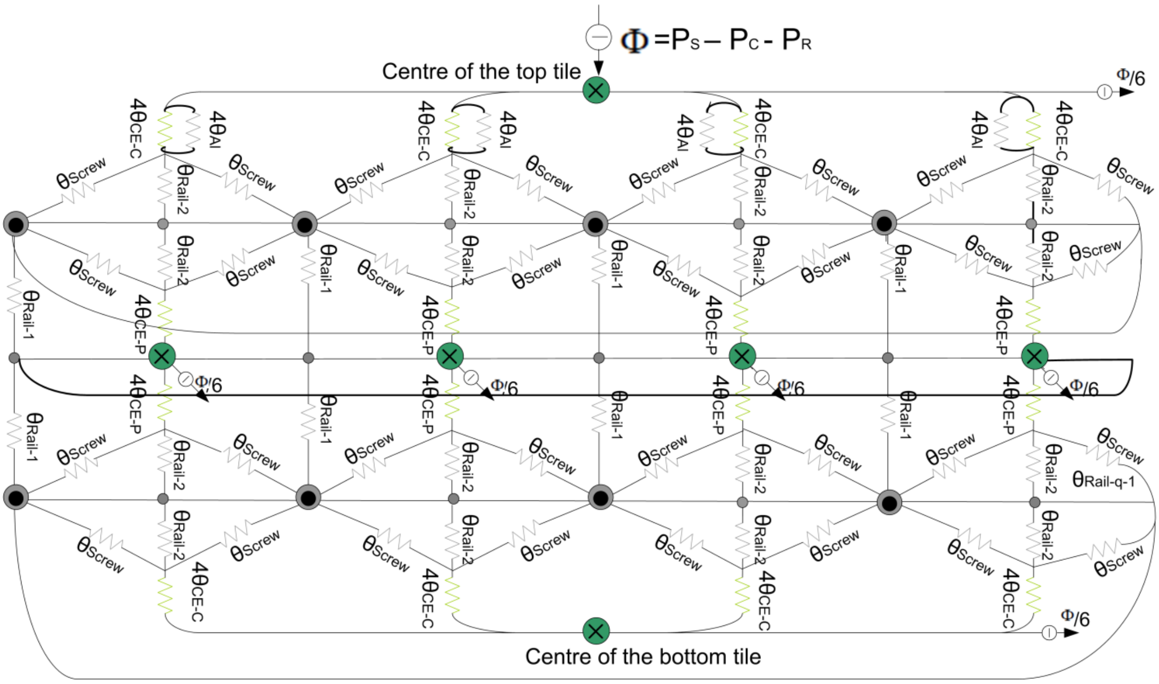

Figure 9.18: Equivalent thermal model of the measurement arrangement.

Thermal model of figure 9.18 is mathematically expressed in (9-20).

$$\theta_{th} = \left(\left(\frac{4\theta_{CE-C} \,//\, 4\theta_{Al} + \theta_{Rail-2} \,//\, \frac{\theta_{Screw}}{2}}{4} \right) + \left(\frac{4\theta_{CE-C} + \theta_{Rail-2} \,//\, \frac{\theta_{Screw}}{2}}{4} \right) + 2\left(\frac{4}{4\theta_{CE-P} + \theta_{Rail-2} \,//\, \frac{\theta_{Screw}}{2}} + \frac{4}{\theta_{Rail-1}} \right) \right)^{-1}$$

(9-20)

Where θ_{CE-C} center to edge thermal resistance of 1B9_CubeTCT,

θ_{CE-P} center to edge thermal resistance of 1B8_CubePMT,

θ_{Al} thermal resistance of aluminum tile,

θ_{Rail} thermal resistance of rail and

θ_{Screw} is the screw thermal resistance.

This model is almost the same as that of the CubeSat thermal model except the aluminum resistor in parallel with the 1B9_CubeTCT tile. In the CubeSat model there was 1B8_CubePMT thermal resistor instead of 1B9_CubeTCT and aluminum thermal resistors parallel combination.

In thermal measurements the 1B8_CubePMT was without solar cells and resins. Therefore these two resistors can be neglected in the theoretical measurements. All the required resistors for the AraMiS-C1 thermal model theoretical measurements are given in the following equations.

$$\theta_{CE-P} = (\theta_{F-3} + \theta_{Cu-2} + \theta_{F-1}) // \theta_{Cu-4} // \theta_{F-5} // \theta_{POS}$$
$$\theta_{CE-P} = \left(\frac{0.9}{4\pi \times 0.24 \times 72 \times 10^{-6}} + \frac{0.9}{4\pi \times 355 \times 72 \times 10^{-6}} + \frac{0.9}{4\pi \times 0.24 \times 72 \times 10^{-6}} \right) \quad (9\text{-}21)$$
$$// \frac{0.9}{4\pi \times 355 \times 36 \times 10^{-6}} // \frac{0.9}{4\pi \times 0.24 \times 1.492 \times 10^{-3}} // \frac{0.9}{4\pi \times 355 \times 18 \times 10^{-6}}$$

$$\boxed{\theta_{CE-P} = 3.66 K/W}$$

$$\theta_{CE-C} = \theta_{Cu} // \theta_F$$
$$\theta_{CE-C} = \frac{0.9}{4\pi \times 355 \times 71 \times 10^{-6}} // \frac{0.9}{4\pi \times 0.24 \times 1.479 \times 10^{-3}} \quad (9\text{-}22)$$

$$\boxed{\theta_{CE-C} = 0.28 K/W}$$

$$\theta_{Al-Tile} = \frac{0.9}{4\pi \times 210 \times 6 \times 10^{-3}} = 0.056 K/W$$
$$\theta_{Screw} = \frac{6mm}{210W/(Km) \times \pi \times (1.27mm)^2} = 5.64 K/W$$
$$\theta_{Rail-A} == \frac{L}{K_{Al} \times S} = \frac{100mm}{210W/mK \times (2mm \times 10mm + 2mm \times 8mm)} = 13.23 K/W$$
$$\theta_{Rail-1} = \frac{\theta_{Rail-A}}{2} = 6.6 K/W$$
$$\theta_{Rail-B} = \frac{L}{K_{Al} \times S} = \frac{12mm}{210W/mK \times (2mm \times 100mm)} = 0.3 K/W$$
$$\theta_{Rail-2} = 2 * \theta_{Rail-B} = 0.6 K/W$$

By inserting all the required resistors values in (9-20), the equivalent thermal resistance of AraMiS-C1 is 2.86K/W as given below.

$$\boxed{\theta_{th} = 2.86 K/W}$$

This is the theoretical thermal resistance value of AraMiS-C1from centre of the one 1B9_CubeTCT tile to the centre of the second 1B9_CubeTCT tile mounted on opposite side.

9.12.5 Experimental value of AraMiS-C1 thermal resistance

In the previous section theoretical thermal resistance value of AraMiS-C1 was found using thermal model presented for the CubeSat standard NanoSatellites. In order to verify the theoretical results, a practical value of the AraMiS-C1 thermal resistance was found using the setup shown in figure 8.19.

From the introduction of this chapter, it is clear that for thermal resistance of an object we need power absorbed and temperature difference. For AraMiS-C1 thermal resistance measurement, a constant power will be provided to one side of the satellite inside vacuum chamber. Temperature difference between the tile where power is provided and the opposite side of the satellite will be measured. If the power applied and the resultant temperature difference are known, one can find thermal resistance of AraMiS-C1 using (9-4).

The measurement setup is composed of:

- AraMiS-C1 with measurement arrangements
- Vacuum chamber
- Vacuum pump
- Temperature sensors

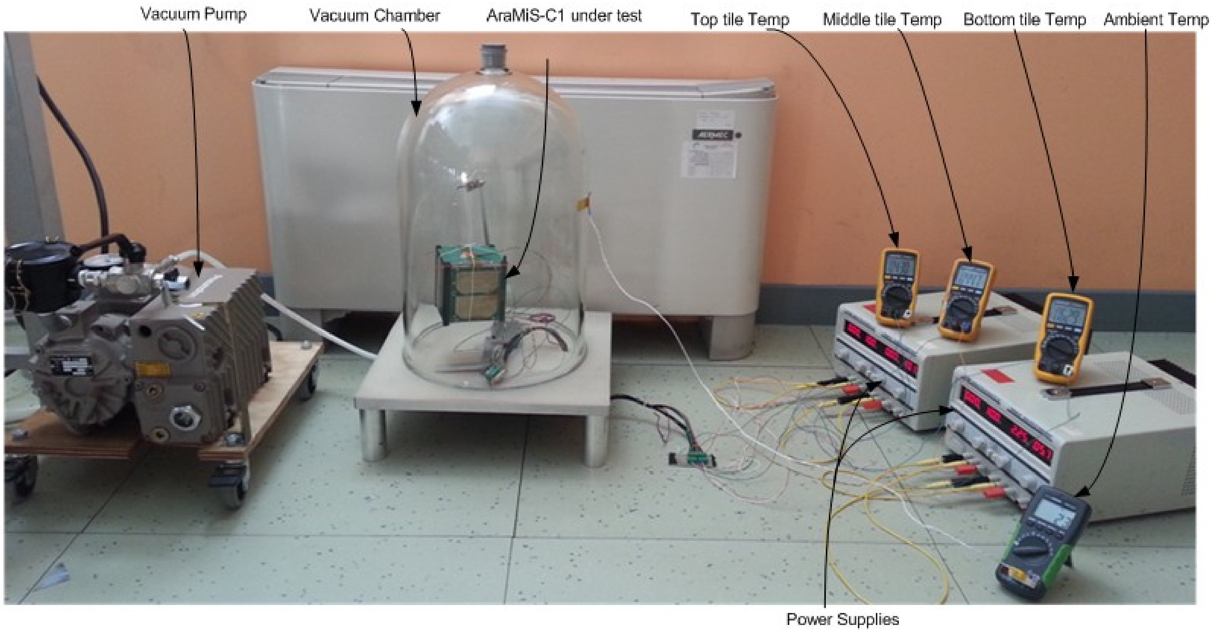

Figure 9.19: AraMiS-C1 thermal resistance measurement experimental setup

AraMiS-C1 with measurement arrangements is shown in figure 9.17. A power resistor is attached to the 1B9_CubeTCT in order to provide power to the top tile of AraMiS-C1 equivalent to the solar power provided by the AM0 intensity light in LEO.

Solar power density at LEO, P = 1365W/m^2
Area of the AraMiS-C1 exposed to sun, A = 98mm×82.5mm = 0.008085m^2
Power absorbed by AraMiS-C1 $P_{absorbed} = P.A$ = 1365W/m^2×1365W/m^2 = 11W

In order to provide 11W power to AraMiS-C1, a constant current of 5A is drawn through 2.2Ω power resistor. Three temperature sensors are attached to the top and bottom 1B9_CubeTCT tiles and side 1B8_CubePMT tile. Power supplies are used to supply power to the temperature sensors and power resistor. Multimeters are used to display the temperature sensors values. Ambient temperature is recorded through a thermo couple and is also displayed through a multimeter.

AraMiS-C1 with measurement arrangements is shown in figure 9.17, was placed inside the vacuum chamber. After generating vacuum inside the chamber, a constant current of 5A was drawn through the power resistor. The temperatures of the top 1B9_CubeTCT tile, opposite bottom 1B9_CubeTCT tile and side 1B8_CubePMT tiles were recorded. Temperatures of all three

Time	**Temp sensor A (bottom)˚C**	**Temp sensor B (middle)˚C**	**Temp sensor C (top) ˚C**	**ΔT (top-bottom) ˚C**	**ΔT (top-middle) ˚C**	**θ_{th} (top-bottom) ˚C/W**
11:47	21.3	21	23.5	2.2	2.5	0.2000121
12:04	20.44	19.36	22.42	1.98	3.06	0.1800109
12:06	20.21	20.07	23.03	2.82	2.96	0.2563792
12:08	20.56	20.61	23.98	3.42	3.37	0.31092
12:11	20.96	21.12	28.11	7.15	6.99	0.6500395
12:13	21.37	21.67	31.8	10.43	10.13	0.9482394
12:17	22.58	23.24	38.47	15.89	15.23	1.4446332
12:19	23.55	24.4	41.8	18.25	17.4	1.6591917
12:21	24.68	25.71	45	20.32	19.29	1.8473850
12:26	26.96	28.28	50.4	23.44	22.12	2.1310386
12:28	27.65	29.05	51.8	24.15	22.75	2.1955880
12:31	29.25	30.82	55	25.75	24.18	2.3410514
12:36	31.5	33.37	59.1	27.6	25.73	2.5092434
12:40	32.9	34.8	61.3	28.4	26.5	2.5819751
12:43	33.50	35.5	63.50	30.00	28	2.7274385
12:46	35.07	37.12	64.8	29.73	27.68	2.7028916
12:49	36.23	38.34	66.5	30.27	28.16	2.7519855
12:53	37.32	39.52	68.2	30.88	28.68	2.8074434
12:55	37.89	40	69	31.11	29	2.8283537
12:57	38.2	40.4	69.6	31.4	29.2	2.8547190
12:59	38.7	40.9	70.3	31.6	29.4	2.8729019
13:01	39.2	41.5	71.1	31.9	29.6	2.9001763
13:05	40	42.2	72.1	32.1	29.9	2.9183592
13:08	40.6	42.9	73	32.4	30.1	2.9456336
13:10	40.9	43.2	73.5	32.6	30.3	2.9638165
13:13	41.4	43.7	74.1	32.7	30.4	2.9729080
13:16	41.8	44.1	74.7	32.9	30.6	2.9910909
13:18	42.1	44.4	75.1	33	30.7	3.000182
13:22	42.6	45	75.8	33.2	30.8	3.0183653
13:25	43	45.4	76.3	33.3	30.9	3.0274567
13:27	43.2	45.7	76.7	33.5	31	3.0456397
13:31	43.6	45.1	77.2	33.6	32.1	3.0547311
13:36	44.1	46.6	77.8	33.7	31.2	3.0638226
13:39	44.3	46.7	78	33.7	31.3	3.0638226
13:43	44.6	47	78.3	33.7	31.3	3.0638226
13:46	44.9	47.3	78.8	33.9	31.5	3.0820055
13:54	45.3	47.8	79.3	34	31.5	3.0910970
14:00	45.6	48.1	79.7	34.1	31.6	3.1001884
14:04	45.8	48.2	79.9	34.1	31.7	3.1001884

14:08	45.9	48.4	80.1	34.2	31.7	3.1092799
14:11	46	48.5	80.2	34.2	31.7	3.1092799
14:13	46.1	48.6	80.3	34.2	31.7	3.1092799

Table 9.1: Data of experimental results

tiles, their difference with the top tile temperature and the top to bottom thermal resistance go on increasing with time as shown in table 9.1. After some time thermal resistance attained the steady state value, as clear from the table during time 14:04 to 14:17.

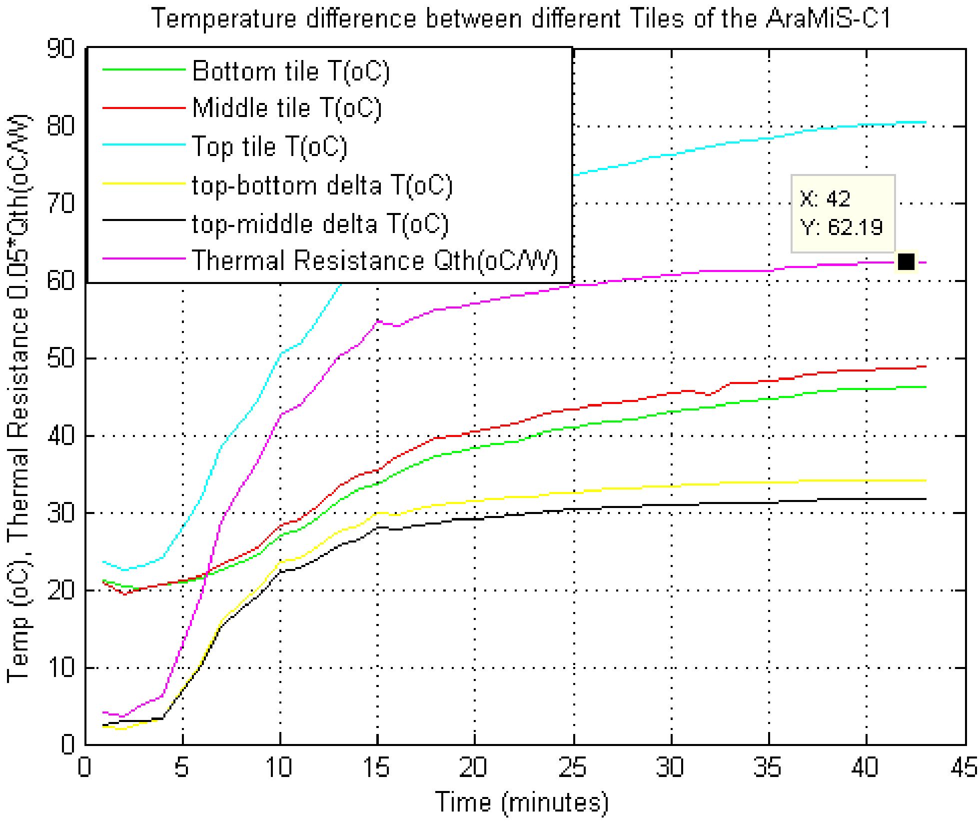

Figure 9.20: Thermal resistance and temperature difference between different faces of AraMiS-C1 Satellite

Figure 9.20 shows temperatures of top, middle and bottom tiles and their temperature differences. This figure also shows thermal resistance between top and bottom tiles, which is 3.1 °C/W.

The thermal resistance of AraMiS-C1, found through CubeSat mathematical model and experimental setup, has almost the same value.

9.13 Solar Power Absorbed by AraMiS-C1

The only power source of AraMiS-C1 are the six solar panels covering as many faces of the satellite. Each solar panel has an area of about 2×70×40mm^2. Sun power density at LEO (low earth orbit) is about 1366 W/m^2. By taking into account that only one panel is exposed at a time to sunlight. There are two cases where the power absorbed by 1B8_CubePMT single module may be different.

- When solar panel is on, it absorbs *26%* of power and remaining *74%* power is lost through 1B8_CubePMT module. Power lost can be found using (9-3). All the parameters in (9-3) are known except absorption coefficient (α), which is found through an experimental setup presented in chapter 9. Inserting parameters in (9-3), the power absorbed by AraMiS-C1 is 5.1W.
- When solar panel is off, all the radiating power is transferred to the 1B8_CubePMT module. The absorption area (A) is the 1B8_CubePMT surface area ($98\times82.5mm^2$) and solar cell efficiency (η) will become zero in (9-3). The power absorbed by AraMiS-C1 is 11W.

9.14 Temperature Difference

In order to find temperature difference (ΔT) between different points of an object, thermal resistor and solar power absorbed are required as given in (9-4).

9.14.1 1B8_CubePMT

Temperature difference (ΔT) between various sides of the 1B8_CubePMT module can be found using (9-4) in two different cases:

- When solar panel is on: ΔT from top to bottom layer of the 1B8_CubePMT is (5.1W×2K/W) 10.2K while from centre to edge ΔT is (5.1W×3.2K/W) 16.3K.
- When solar panel is off: ΔT from top to bottom layer of the 1B8_CubePMT is (11W×2K/W) 22K while from centre to edge ΔT is (11W×3.2K/W) 35.2K.

9.14.2 AraMiS-C1

In AraMiS-C1 case we consider that power is absorbed through a single 1B8_CubePMT module perpendicular to the incoming solar radiations. All the other tiles are in dark. Temperature difference (ΔT) from top to bottom of AraMiS-C1 using (8-4)can be found in two different cases:

- In case when solar panel is on: ΔT value is (5.1W×3K/W) 15.3K.
- When solar panel is off: ΔT value is (11W×3K/W) 33K.

Chapter 10

Preliminary Thermal and Orbital Spin Analysis of NanoSatellites

10.1 Introduction

In space thermal environment, satellite thermal control is required in order to maintain mechanical structure and electronic subsystems integrity over long period of times. Satellite thermal design proceeds by identifying sources of heat and minimizing their effects by releasing and rejecting heat such that all systems components remain within temperature permissible limits. Heat is generated by the satellite as well as absorbed from the environment. Components generating heat are electronic devices, motors and batteries. Heat from the environment is mainly due to solar radiations. Thus satellite thermal control requires the selection of suitable structural material and devices. The material and devices should maintain a balance between heat absorbed and emitted to the environment.

In space thermal environment, NanoSatellites are exposed to many heat sources which continuously increase satellite temperature. Normally radiators are used to release heat, but due to space and weight constraints with NanoSatellites, it is impossible to mount radiators. This problem signifies the importance of thermal analysis of a NanoSatellite in space environment. So the ultimate goal is to measure the effect of all heat sources and to ensure satellite will be functioning in their safe range of temperatures. Primarily this chapter focuses on general thermal analysis of NanoSatellites called AraMiS standard, developed at Politecnico di Torino. Then this analysis will be applied to the CubeSat standard NanoSatellite called AraMiS-C1. Secondly, this chapter presents a preliminary analysis of induced spin which is produced by CubeSats standard satellites due to asymmetrical colors (different absorption coefficient) of satellite outer surface. The substantial contributors for induced spin have been considered and the estimated spin has been measured.

A satellite is exposed to harsh space thermal environment as soon as it is launched. During cold space environment, heaters are used to keep the satellite subsystems above the acceptance temperature limits. However during hot space condition, NanoSatellite has no coolers to keep the subsystems temperature under the permissible temperature limits. The only choice for NanoSatellites is the balance thermal control design which adopts passive thermal control systems. So it is better to know the space environment heat sources and design our satellite according to the space thermal conditions [64-65].

In this chapter, we will present the satellite thermal analysis in space environment and will discuss all the heat sources. We will find a thermal equilibrium equation for the satellite. Temperature of the satellite will be found for different cases like thermal equilibrium and no heat generation by satellite subsystems etc. Absorption coefficient of the AraMiS-C1 satellite will be found and thermal analysis will be applied to AraMiS-C1. AraMiS-C1 temperature will be found in different cases of steady state and transient analysis. At the end orbital spin analysis will be presented on the basis of color difference between two edges of the satellite.

10.2 Satellite Thermal Analysis in Space Environment

Main feature of the space environment is high vacuum where the molecular free path becomes comparable to their distance. The heat transfer is by radiation only and there is a negligible convective heat transfer [66]. When a NanoSatellite orbiting Earth, it has several heat sources considering substantial contributions due to:

- Heating due to solar radiation depending on sun distance, with a mean value around 1366 W/m^2.
- Heating due to Earth's albedo reflected radiation. It is the fraction of the incident solar radiation returned from the earth. Earth's albedo varies with it surface conditions. For Earth, the mean reflectivity is around 30% which varying up to 40 to 80% above shiny clouds and from 5 to 10% for ocean and forests.
- Heating due to thermal terrestrial radiation. Earth can be modeled as an equivalent black-body emitting at 255 K.
- Heating due to internal heat generation in electronic components (Joule effect).
- Heat capacity of the system
- Cooling due to heat radiation
- Cooling due to the conversion of solar energy into electricity

The satellite will be in thermal equilibrium state when the heat energy received from the first five sources is equaled by the last two cooling sources. The temperature at thermal equilibrium state is called radiation equilibrium temperature. This temperature is used in the design analysis of the satellite for system feasibility. Satellite thermal balance can be achieved by the required degree of radiation balance between internal power dissipation and heat generation, and the balance between the absorption (α) and emission (ε) coefficients.

The satellite temperature periodically varies along its orbit. During eclipse stage only two heat sources; thermal terrestrial radiations and internal heat generation in electronic components are present. Therefore the satellite is cooler during the eclipse and hotter in sunshine. The system is considered to be completely isothermal.

10.2.1 Assumptions and Conditions

The detailed thermal analysis of the satellite in space is extremely complex. However, the starting point of satellite thermal analysis like in any other analytical process, are some assumptions and boundary conditions.

Let assume that system is composed of N isothermal faces oriented in space. Each face is characterized by an absorption coefficient between zero and one ($0 < \alpha < 1$), photoelectric efficiency (γ) between zero and one ($0 < \gamma < 1$), a transmittance $\tau = 0$ and reflectance $\rho = 1 - \alpha$. The data we know is that,

- Solar radiation outside the atmosphere is $F_S = 1366$ W/m^2.
- Average terrestrial albedo is slightly lower than 0.4. Since the LEO satellites are sufficiently close to the earth's surface (say a distance of less than 1/5 of Earth's radius), one can assume that the radiation due to Earth is given by the product of solar radiation by Earth's albedo: $F_T = F_S * 0.4 = 546$ W/m2 (at a height of 800km this is reduced by approximately 80%).

- The radiation intensity, F (T) emitted by a body immersed in vacuum (refractive index 1) is given by Stefan-Boltzmann's law:

$$F(T) = \sigma\alpha T^4 \tag{10-1}$$

Where $\sigma = 5.78\times10^{-8}$ W/m^2 / K^4 is the Stefan-Boltzmann's constant,
α is the absorption coefficient of the surface and

T its absolute temperature.

In reality, the Stefan-Boltzmann using the emissivity of the surface instead of its absorption coefficient, but the Kirchhoff's law states that the two parameters are equal.

10.2.2 Thermal Equations

Let suppose that the satellite is a closed system, therefore the algebraic sum of the powers that come in any form (radiation and emission) in the system must be equal to the sum of the internal power (converted into chemical energy inside batteries and generated internally by Joule's effect).

Solar radiation on each face lit of the satellite (P_i^R) is given by;

$$P_i^R = \alpha_i F_S S_i \tag{10-2}$$

Where the subscript '*i'* denotes the *i*th face whose surface is S_i and F_S is the solar radiation intensity.

Similarly, terrestrial radiation incident on the each face lit of the satellite (P_i^T) is given by;

$$P_i^T = \alpha_i F_T S_i \tag{10-3}$$

So the total incoming radiation (P_i^S) on each face lit (assuming solar radiation and terrestrial incidents on the same face, for simplicity) is given by:

$$\begin{aligned} P_i^S &= P_i^R + P_i^T \\ P_i^S &= \alpha_i (F_S + F_T) S_i \end{aligned} \tag{10-4}$$

Emitted thermal radiation from each face of the satellite can be deduced from Stefan-Boltzmann's law:

$$P_i^E(T) = \sigma\alpha_i T^4 S_i \tag{10-5}$$

Thermal radiation due to the emission from the earth is difficult to assess, but it may be overestimated in order to get a conservative guess of the temperature of the satellite. The following simplified model has been used:

- The earth emits thermal radiation due to its surface temperature (average temperature of Earth's surface 287K [67]), according to the Stefan-Boltzmann above.
- The earth albedo is 0.4, and then absorption coefficient of the earth is α = 1-0.4 = 0.6.
- The power density decreases with the square of the distance from the center of the earth, then at an altitude h it is reduced by a factor of [R / (R + h)] ^ 2, where R is the radius of the Earth. In case of the LEO satellite, *h* is considered to be 800km.
- The face of the satellite parallel to the earth's surface receives all the power density emitted, decreased by the absorption coefficient of the satellite's surface and taking into account the altitude.
- The side faces of the satellite get a lower power density which is not trivial to judge, but this contribution is overestimate assuming that each side wall is parallel to the earth's surface (conservative assumption), but receives energy only from half of the Earth surface, since the other half is shielded from the rest of the satellite.

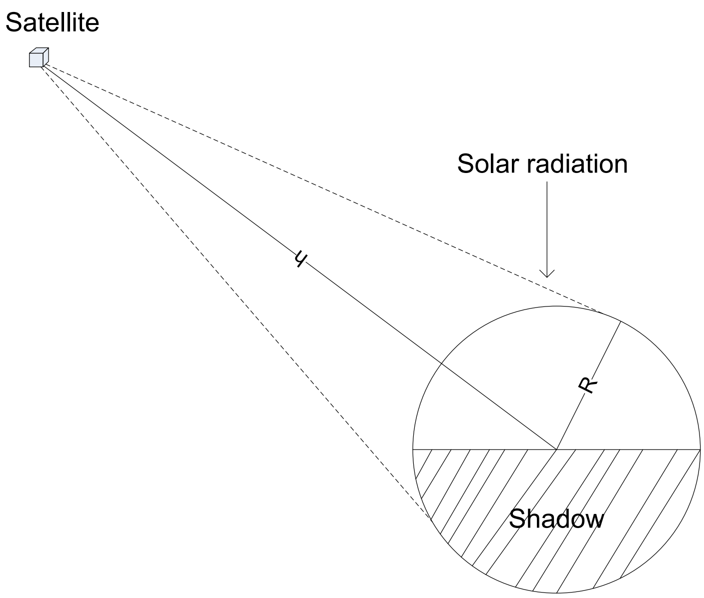

Figure 10.1: Spacecraft irradiation

- The wall farther from the Earth does not receive energy;
- So one can consider an equivalent area equal to the sum of the surface facing the Earth, plus half of the lateral faces.

On the basis of the above model, the following mathematical relation can be achieved for the thermal radiation power due to the emission of the earth (P^T).

$$P^T = \sigma\alpha_T T_T^{\,4}\left(\frac{R}{R+h}\right)^2\left(\alpha_{aff}S_{aff} + \alpha_{lat}\frac{S_{lat}}{2}\right) = F_E\left(\alpha_{aff}S_{aff} + \alpha_{lat}\frac{S_{lat}}{2}\right) \qquad (10\text{-}6)$$

Where earth's radiation (F_E) at altitude h is given by:

$$F_E = \sigma \alpha_T T_T^{\,4} \left(\frac{R}{R+h} \right)^2 \tag{10-7}$$

Where T_T is the temperature of the earth,
α_T is the absorption coefficient of the earth,
S_{aff} is the surface area of the satellite face towards (parallel with) earth surface and
S_{lat} is the surface area of the satellite face lateral with earth surface respectively.

that is, with previous data, F_E = 185 W/m^2;

Conversion of light energy into electricity and its chemical storage, for each face lit (assuming solar and terrestrial radiation incident on the same face, for simplicity):

$$P_i^P = \gamma_i (F_S + F_T) S_i \tag{10-8}$$

Heat will be accumulated inside the satellite ($P^C(t)$) depends on the mass of the system (m), its specific heat (c) and temperature (T):

$$P^C(t) = \frac{d}{dt} mcT = mc \frac{d}{dt} T \tag{10-9}$$

Internal heat generation (P^J) is due to the electronic circuits, except that for energy conversion of the panels, which have been already taken into account in the photoelectric efficiency.

10.2.3 Thermal Equilibrium Equation

When a system is exposed to thermal environment, some portion of the incoming radiations is accumulated inside the system and the remaining energy is emitted back to the environment. So, the equation of thermal equilibrium can therefore be written as:

$$\sum_{face\_illuminated} \left(P_i^S - P_i^P \right) + P^J + P^T - \sum_{all\_faces} \left(P_i^E(T) \right) = P^C(T) \tag{10-10}$$

By expanding the above equation, one can get:

$$\sum_{face\_illuminated} \left((\alpha_i - \gamma_i)(F_S + F_T) S_i \right) - \sum_{all\_faces} (\alpha_i S_i) \sigma T^4 + P^J + F_E \left(\alpha_{aff} S_{aff} + \alpha_{lat} \frac{S_{lat}}{2} \right) = mc \frac{d}{dt} T \tag{10-11}$$

Now we are going to consider different cases in which the satellite might be during its flight.

10.2.4 Different Cases

<u>Case 1</u>: Thermal equilibrium, no generation or accumulation of heat inside the satellite

Let first take the system in thermal equilibrium with no heat is generated and accumulated inside the satellite.

Then $\frac{dT}{dt} = 0$, $P^J = 0$, $\gamma = 0$.

$$\sum_{face\_illuminated}\left(\alpha_i\left(F_S+F_T\right)S_i\right)++F_E\left(\alpha_{aff}S_{aff}+\alpha_{lat}\frac{S_{lat}}{2}\right)=\sum_{all\_faces}\left(\alpha_i S_i\right)\sigma T^4 \tag{10-12}$$

Now we are going to elaborate this case and take different possible conditions.

Case 1a: Take a worst case: "black mirror" condition, i.e. a thin sheet with one side ideally black (α = 1) exposed to solar-terrestrial radiation, and one of the same area, ideally reflecting (α = 0) towards the dark:

$$\left(F_S+F_T+F_E\right)=\sigma T^4 \tag{10-13}$$

Therefore T = 436.5K = +163.3 °C.

Case 1b: Take a cube of uniform color (thus α equal for all faces), with one face exposed to solar-terrestrial radiation and five faces, obviously of the same surface, facing the darkness, one facing the earth, four facing sideways:

$$\left(F_S+F_T+F_E\left(1+\frac{4}{2}\right)\right)=6\sigma T^4 \tag{10-14}$$

Therefore T = +6.3 °C

Case 1c: Solid-color cube with two faces exposed to solar-terrestrial radiation which are not orthogonal. In this case the total equivalent area seen from the sun being $1.41S_i$. The other faces of the satellite have the same surface area, facing the dark:

$$\sqrt{2}\left(F_S+F_T\right)+F_E\left(1+\frac{4}{2}\right)=6\sigma T^4 \tag{10-15}$$

Therefore T = +22.2 °C

Case 1d: Cube of uniform color with only one face exposed to Earth radiation and all the other faces have the same surface area, facing the dark:

$$F_T+F_E\left(1+\frac{4}{2}\right)=6\sigma T^4 \tag{10-16}$$

Therefore T = -44.7 °C

Case 1e: Cube of uniform color completely in the dark:

$$F_E\left(1+\frac{4}{2}\right)=6\sigma T^4 \tag{10-17}$$

Therefore T = -80.6 °C, but one should also consider Earth own radiation (thermal radiation) and the cosmic background radiation, but I would say that this case does not concern us ...

Case 1f: Planar structure very large compared to the thickness, uniform color, with a face exposed to solar-terrestrial radiation and the other one, obviously of the same surface, facing toward the darkness; no side wall:

$$F_T+F_E=2\sigma T^4 \tag{10-18}$$

Therefore T = +58.5 °C

Case 1g: Sphere of uniform color with a hemisphere exposed to radiation from solar-terrestrial (but not orthogonal to the surface; we considered the total “equivalent” area seen from the sun equal to the surface of the equatorial circle) and the total radiating area equal to 4 times the Equatorial surface:

$$\left(F_S+F_T+F_E\right)=4\sigma T^4 \tag{10-19}$$

Therefore T = +18.7 °C. On this figure I would not put my hand on fire, at least as regards the thermal radiation of the Earth.

10.3 AraMiS-C1: Example

Now we are going to do thermal analysis of a CubeSat standard NanoSatellite called AraMiS-C1. There is no need for structural details about AraMiS-C1 satellite as we already have them in chapter 1. As already mentioned that for thermal analysis of a satellite we need satellite thermal balance that can be achieved by the required degree of radiation balance between internal power dissipation and heat generation, and the balance between the absorption (α) and emission (ε) coefficients. We already have presented some cases of satellite thermal balance equations, now we are going to find the emissivity and absorption coefficient of the satellite surface.

AraMiS-C1 has four 1B8_CubePMT modules on the external faces, therefore emissivity and absorption coefficient of the 1B8_CubePMT module were found in the forthcoming sections.

10.3.1 Measurement of Absorption Coefficient (α) at Visible Light

Absorption coefficient (α) of top layer (solar panel side) was measured in visible light. The measurement setup is shown in figure 10.2. Measurements were performed in two steps. In the first part of this measurement, 1B8_CubePMT module was illuminated through a solar simulator which produces AM0 intensity light. The corresponding temperature increase due to solar light

Figure 10.2: Photograph of absorption coefficient measurement setup.

intensity was recorded using a temperature sensor. When the temperature value reached its steady state (74˚C), the solar simulator was switched off.

In the second part of the measurement, voltage was applied to the magnetorquer coil, the corresponding amount of current flowing through the magnetorquer coil and increase in temperature was monitored. The applied voltage was increased step by step and the corresponding temperature was measured. When the temperature reached at 74˚C, the corresponding voltage and current were recorded as given in table 10.1.

As the temperature increase due to solar light at AM0 is exactly the same as due to power dissipated through the magnetorquer coil, therefore solar power absorbed is equal to the electrical power lost through the coil as given in (10-20) and (10-21);

$$P_{solar} = P_{electrical} \qquad \because P_{solar} = a.P_D.S \ \& \tag{10-20}$$

$$\Rightarrow \alpha = \frac{V.I}{P_D.S} \qquad P_{electrical} = V.I \tag{10-21}$$

Parameter	Value
Applied Voltage (V)	14.24V
Current (I)	700mA
Solar Power Density (P_D)	1366.1W/m^2
1B8_CubePMT surface area (S)	0.008085m^2

Table 10.1: Parameters used in thermal modeling of magnetorquer coil

By inserting the values of table 10.1 in (10-21), the absorption coefficient (*a*) found is 0.903.

10.3.2 Different cases of AraMiS-C1 in thermal equilibrium state

Now we are going to take different conditions of AraMiS-C1 satellite utilizing the thermal balance condition and absorption coefficient value measured in the previous section.

Case 2: Thermal balance with internal heat generation.

Then $\dfrac{dT}{dt} = 0$, $P^J > 0$, $\alpha_i = 0.9$.

Let consider different cases:

Case 2a: Let first consider the case without heat accumulation ($\gamma = 0$) inside the satellite. Suppose that two faces are exposed to solar-terrestrial radiation and four faces of the same area, facing the darkness. The thermal balance equation will become:

$$\sqrt{2}\alpha(F_S + F_T) + \alpha F_E\left(1 + \frac{4}{2}\right) + \frac{P^J}{S} = 6\sigma\alpha T^4 \qquad (10\text{-}22)$$

Figure 10.3 shows the AraMiS-C1 equilibrium temperature versus power generated internally by the electronic subsystems of the satellite:

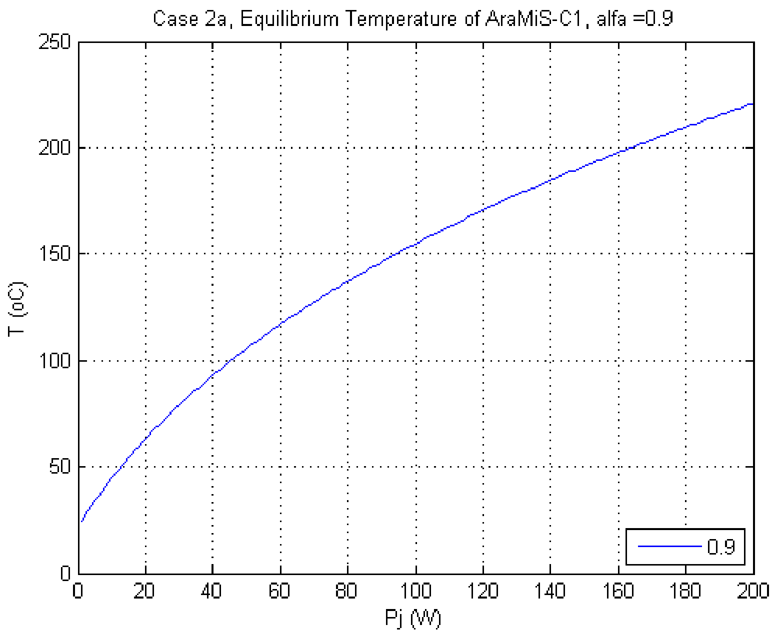

Figure 10.3: Equilibrium temperature versus heat generated: no heat accumulation (γ=0)

Figure 10.3 shows the external temperature of the AraMiS-C1 satellite. Temperature inside the satellite will be greater and depends on the thermal resistance between the point of heat generation and the outer surface.

Case 2b: AraMiS-C1 is a cube of 10cm with solar cells efficiency of 26% and switching regulator efficiency of 80% resulting in $\gamma = 0.26\times0.80$. Suppose that two faces are exposed to solar-terrestrial radiation and four faces of the same area, facing the darkness. Thermal balance equation will become:

$$\sqrt{2}(\alpha - \gamma)(F_S + F_T) + (\alpha - \gamma)F_E\left(1 + \frac{4}{2}\right) + \frac{P^J}{S} = 6\sigma\alpha T^4 \qquad (10\text{-}23)$$

Figure 10.4 shows the AraMiS-C1 equilibrium temperature versus power generated internally by the electronic subsystems of the satellite:

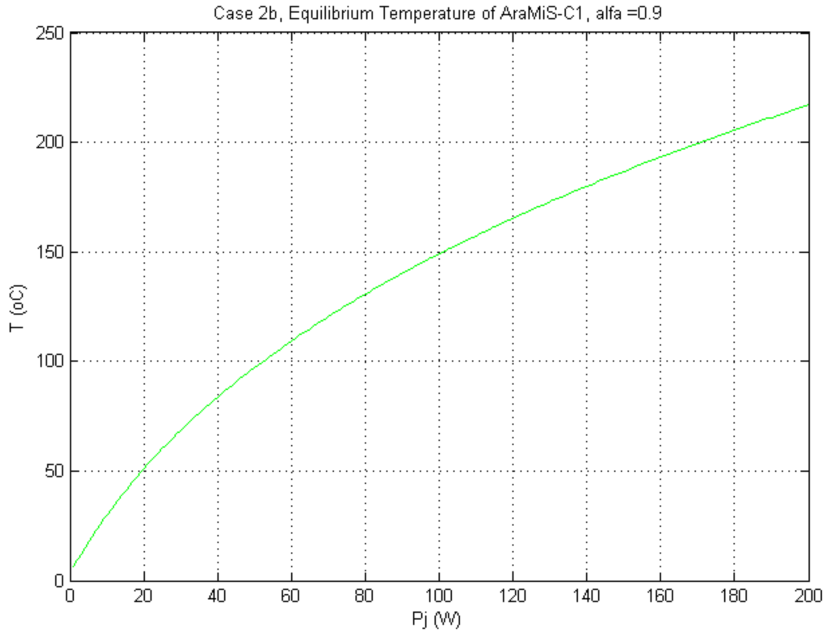

Figure 10.4: Equilibrium temperature versus heat generated: heat accumulation (γ=0.26x0.8)

10.3.3 Different cases of AraMiS-C1 in transient state

Case 3: Transient Analysis

Let consider that the system is not in thermal equilibrium state and dT/dt <> 0. The system equation is:

$$\sum_{illuminated\_face}\left(\left(\alpha_i-\gamma_i\right)\left(F_S+F_T\right)S_i\right)-\sum_{all\_faces}\left(\alpha_i\,S_i\right)\sigma T^4+F_E\left(\alpha_{aff}S_{aff}+\alpha_{lat}\frac{S_{lat}}{2}\right)+P^J=mc\frac{d}{dt}T \tag{10-24}$$

which is a first order non linear differential equation.

Consider the step response to one of the parameters:

- transition of F_S + F_T from 0 to 1366 * 1.4 W/m^2, and vice versa, that is, the effect of sunrise and sunset;
- transition of P^J from 0 to the nominal value and vice versa, that is, powering up and down a generator internal power;
- transition of γ from 0 to 0.26 * 0.8 and vice versa, that is, powering up and down of a solar panel ;

For simplicity we consider a linear system, the start and end equilibrium points of which are known (see cases 1 and 2 above), therefore we can calculate a time constant:

$$\tau = \theta C \tag{10-25}$$

where

$$\frac{1}{\theta} = \frac{dP}{dT} = \sum_{all\_faces} (\alpha_i S_i) \sigma 4T^3 \tag{10-26}$$

is the thermal resistance for radiation into space, while:

$$C = mc \tag{10-27}$$

is the heat capacity of the system. Then:

$$\tau = \frac{mc}{\sum_{all\_faces} (\alpha_i S_i) \sigma 4T^3} \tag{10-28}$$

As AraMiS-C1 is a 6-sided cube of side 10cm, α = 0.9, mass m = 1.2kg of FR4 with specific heat c = 600J/kg/K.

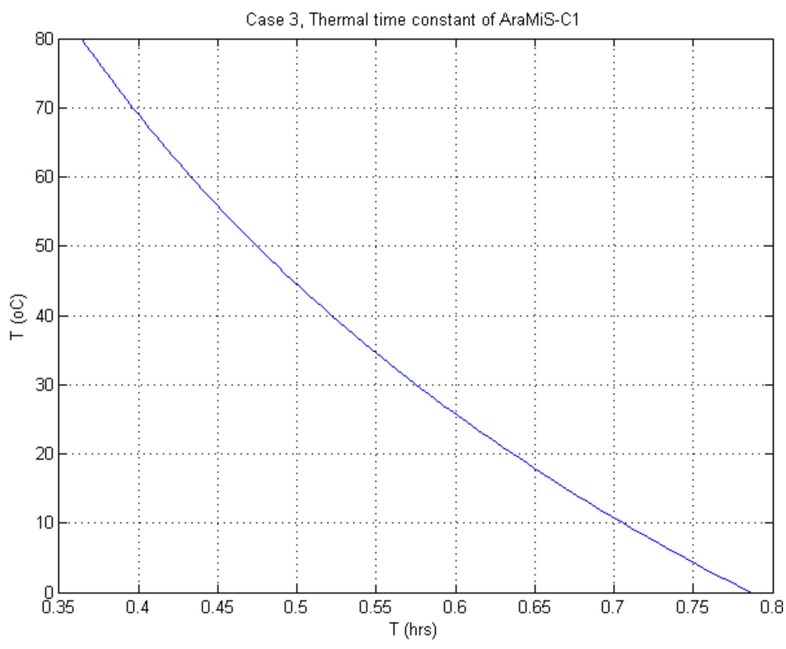

Figure 10.5: Thermal time constant of AraMiS-C1

The time required for AraMiS-C1 to attain the room temperature (23°C) is 37minutes. Therefore thermal time constant of AraMiS-C1 satellite is around 37 minutes.

10.4 Preliminary Spin Analysis led by a gradient of color

In this section we are going to present a preliminary spin analysis, induced by the color (absorption coefficient) asymmetry of the outer surface of the satellite. We will considered substantial contributions due to:

- Solar radiation and the Earth's albedo radiation
- Absorption coefficient difference on both sides of the bright face and
- Moment of inertia of the satellite

10.4.1 Preconditions

Let consider a system composed of *N* square faces of side *L*, adjacent to one another, arranged in a plane illuminated perpendicularly. Each face is characterized by a uniform absorption coefficient (α = 0.9) on all surfaces except on two symmetrical strips of width D, posed to the opposing edges whose absorption coefficients are α_1 and α_2 respectively, with null photoelectric efficiency γ = 0 (or any solar panels off), a transmittance τ = 0 (non-transparent surface) and a reflectance ρ = 1-α :

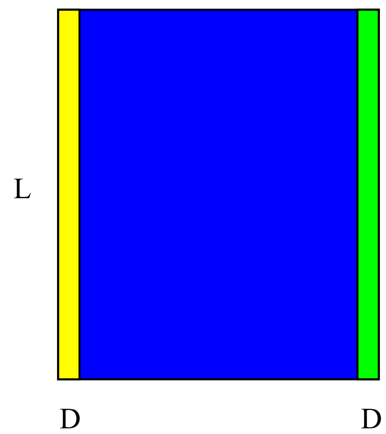

Figure 10.6: Structure with different colors.

We know that

- Solar radiation outside the atmosphere is F_S = 1366W / m^2 (solar constant).
- It can be assumed that the radiation due to Earth is given approximately by the product of solar radiation by the Earth's albedo $F_T = F_S * 0.4$ = 546W / m^2 (at a height of 800km this is reduced by 80 % approximately).
- The radiation pressure of light from the sun and reflected from the Earth, for a non-transparent body is:

$$p = \frac{F_S + F_T}{c}(2-\alpha) \qquad (10\text{-}29)$$

Where c = 2.998×10^8 m / s is the speed of light.

10.4.2 Mechanical Analysis of the mechanical momentum and the spin induced

We consider the following formulas:
The radiation pressure on the central face lit creates no momentum with respect to the center of the face as the absorption coefficient is uniform and the system is symmetric about its geometric center.

- The force acting on each of the two side bands will be given by the product of pressure to the surface of each colored band. Respectively

$$F_1 = \frac{F_S + F_T}{c}(2-\alpha_1)LD$$
$$F_2 = \frac{F_S + F_T}{c}(2-\alpha_2)LD \tag{10-30}$$

- While the moment of these two forces, supposed to be imposed on the geometric center of each band is given by their difference multiplied by the distance between the points of application:

$$M = \frac{F_S + F_T}{c}(\alpha_2 - \alpha_1)LD(L-D) \tag{10-31}$$

- While the angular acceleration due to the sum of N of these moments (as there are so many faces) will be:

$$\dot{\omega} = N\frac{M}{J} \tag{10-32}$$

  where J is the moment of inertia with respect to the axis of rotation, assuming for simplicity the tensor of inertia is diagonal (i.e. the momentum along one axis does not generate rotations along axes perpendicular to it).

- The time required to rotate the satellite, initially without spin, with an angular velocity ω_0 is given by:

$$T = \frac{\omega_0}{\dot{\omega}} = \frac{\omega_0 J}{NM} \tag{10-33}$$

- The moment of inertia is considered that of a uniformly filled sphere of radius R and mass m:

$$J = \frac{3mR^2}{5} \tag{10-34}$$

In case of AraMiS-C1, which is a cube of six identical faces: we consider N = 1, L = 100mm (side of the PCB), D = 10mm, $\alpha_2 - \alpha_1 = 0.3$ (i.e. a gradient of color that is already high), M = 1.2kg and R = 140mm;

In order to arrive at an angular rotation of ω = 1rpm, the time required is 0.2704 years.

Chapter 11

Conclusion

The work discussed in this thesis allows to understand how to accommodate EPS and ADCS subsystems of CubeSat standard satellite on a single tile. The design approach of AraMiS project is adopted in the design, implementation and testing of all the subsystems. The 1B8_CubePMT module is a fundamental step in designing and implementation of EPS and ADCS subsystems on a single tile for CubeSat standard NanoSatellites. It illustrates an ingenious solution for resolving conflicting constraints such as cost, power consumption and physical dimension. To implement such a large number of subsystems on single module is never a trivial job. Best suitable results have been achieved by proper selection of COTS devices with lower dimensions, cost and power consumption. All the subsystem components are selected on the basis of efficiency and power loss analysis.

The designed EPS is a fully functional system which can fulfill the power requirements of a CubeSat standard nano-satellite, AraMiS-C1. The main requirement of the design was to get higher efficiency and to reduce the overall size. To achieve this goal different COTS components were analyzed in PSpice simulation and selected the best one on the basis of minimum losses and small dimensions. This technique results in small space occupation and higher efficiency for the EPS. Power budget is calculated in order to evaluate the EPS performance for the AraMiS-C1 satellite. The power budget of AraMiS-C1satisfies the power budget criteria which means that the designed EPS will guarantee nominal operation of AraMiS-C1 without troubles.

The most interesting feature of 1B8_CubePMT module is the implementation of magnetorquer coil in PCB internal layers. The designed magnetorquer is totally reconfigurable. One can use any combination of the coils for control of rotation and stabilization of the satellite. This reconfigurable design gives a freedom in generating any amount of magnetic moment and control power dissipation and heat generation inside PCB. The designed magnetorquer is integrated inside the four internal layers of PCB and occupy no extra space in the spacecraft. The coils are copper traces of extremely small dimensions which result in very low weight. More importantly, the heat generated by the coils inside the PCB is quite low. It raises the PCB temperature just by few degrees which is within the design temperature limits of the 1B8_CubePMT module. This innovation not only reduces the overall weight and cost of the 1B8_CubePMT module but also provides significantly compact design. Thus, providing enough space to accommodate more subsystems. These attributes reflect that the designed magnetorquer coil is highly suitable for 1B8_CubePMT module of 1U AraMiS-C1 and other CubeSat standard NanoSatellites. 1B8_CubePMT also has different sensors in order to guarantee reliable and safe operation. All the subsystems of the 1B8_CubePMT were tested. The results are according to the requirements.

The second part of the thesis, presented thermal modeling and thermal analysis of CubeSat standard NanoSatellites. Thermal models have been presented for CubeSat and their panels. Detailed and simplified models were attained for a single CubeSat panel. The two models should have the same results. The corresponding models were applied to 1B8_CubePMT module and thermal resistances of the 1B8_CubePMT module were found. The difference between the resistances values measured through both models is very low which verify the authentication of the proposed models.

Thermal resistance of AraMiS-C1 satellite was found by employing the presented CubeSat thermal model. In order to verify the value of the thermal resistance measured through CubeSat model, AraMiS-C1 thermal resistance was measured inside a vacuum chamber. The two values are very close, which indicates the authentication of the model presented for CubeSat.

From thermal modeling we can conclude two things. First, the presented models are reliable and can be applied to CubeSat standard satellites. This conclusion is drawn on the basis of theoretical and laboratory measurements. Thermal resistance measured theoretically for AraMiS-C1 satellite using the proposed models have same result as that of measured through laboratory setup. Secondly, the thermal resistances of 1B8_CubePMT module and AraMiS-C1 satellites are very low.

The absorption coefficient was measured for 1B8_CubePMT module and the amount of power absorbed by 1B8_CubePMT module and AraMiS-C1 satellite under different conditions is calculated. Temperature difference between different points of the single tile and complete satellite were found.

Thermal analysis of a small satellite in space environment was performed different heat sources were discussed in detail. A thermal equilibrium equation for the satellite was found and satellite temperature was found for different cases like thermal equilibrium and no heat generation by satellite subsystems etc. AraMiS-C1 temperature was found in different cases of steady state and transient analysis.

At the end, orbital spin analysis was presented on the basis of color difference between two edges of the satellite. In light of these results, it can be concluded that the color gradient is not a problem and can be neglected. This implies that there is no need to worry about the color of the PCB of solar panels.

Appendix A

1B8_CubePMT Schematics

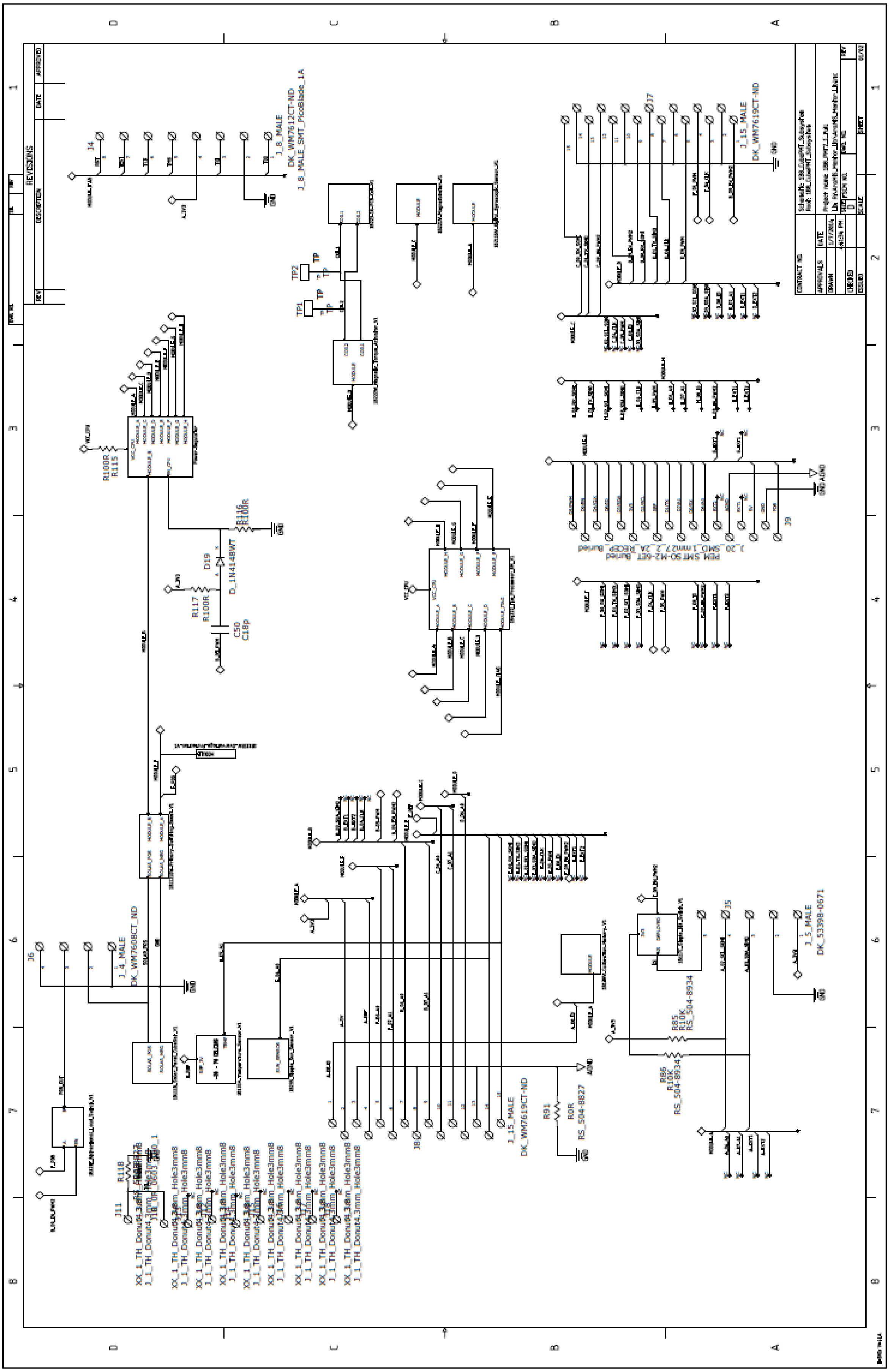
REVISIONS
J4
J_8_MALE
DK_WM7612CT-ND
J_8_MALE_SMT_PicoBlade_1A
J7
J_15_MALE
DK_WM7619CT-ND
TP1
TP2
R100R
R115
R116
R100R
D19
D_1N4148WT
R117
R100R
C50
C18p
J9
J_20_SMD_1mm27_2_2A_RECEP_Buried
PEM_SMTSO-M2-6ET_Buried
GND
AGND
J6
J_4_MALE
DK_WM7608CT-ND
J8
J_15_MALE
DK_WM7619CT-ND
R91
R0R
RS_504-8827
R85
R10K
RS_504-8934
R86
R10K
RS_504-8934
J5
J_5_MALE
DK_53398-0671
J11
R118

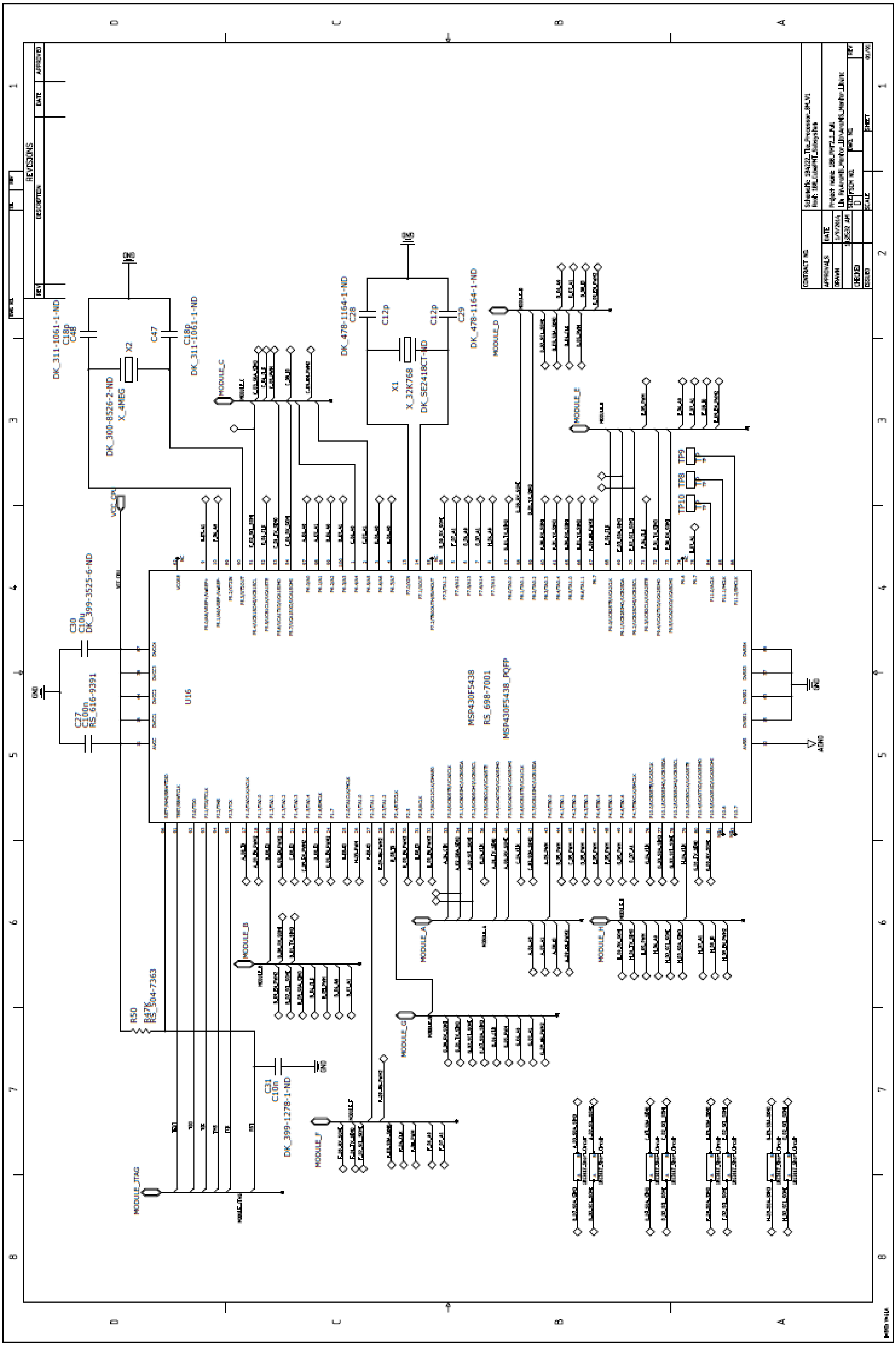
REVISIONS
U16
MSP430F5438
RS_698-7001
MSP430F5438_PQFP
MODULE_A
MODULE_B
MODULE_C
MODULE_D
MODULE_E
MODULE_F
MODULE_G
MODULE_H
MODULE_JTAG
X1
X_32K768
DK_SE2418CT-ND
X2
X_4MEG
DK_300-8526-2-ND
C28
C12p
DK_478-1164-1-ND
C29
C12p
DK_478-1164-1-ND
C48
C18p
DK_311-1061-1-ND
C47
C18p
DK_311-1061-1-ND
C30
C10u
DK_399-3525-6-ND
C27
C100n
RS_616-9391
R50
R47k
RS_504-7363
C31
C10n
DK_399-1278-1-ND
TP8
TP9
TP10
GND
AGND
VCC_CPU

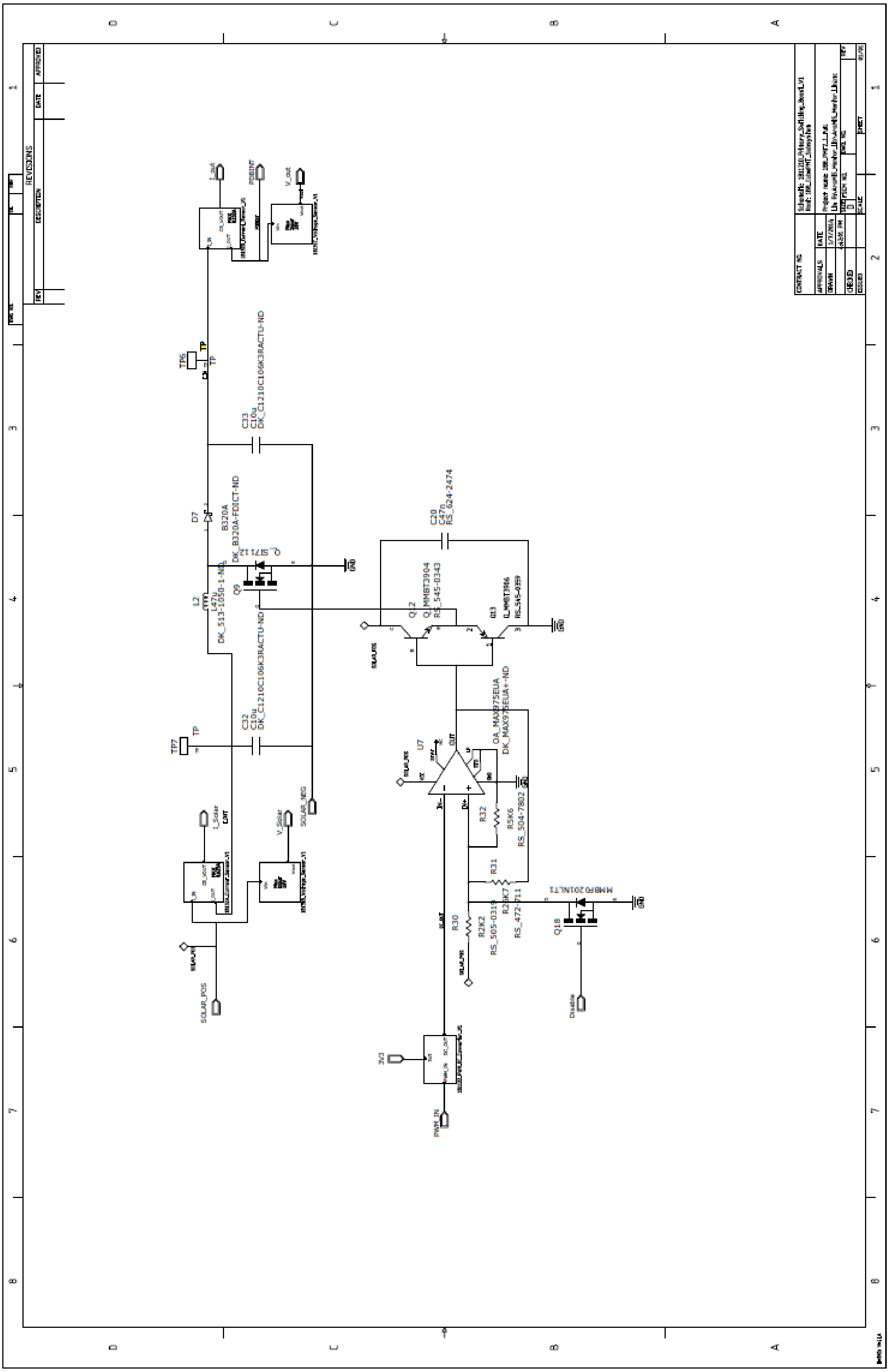
REVISIONS
D7
B320A
DK_B320A-FDICT-ND
C33
C10u
DK_C1210C106K3RACTU-ND
L2
L47u
DK_513-1050-1-ND
Q9
C32
C10u
DK_C1210C106K3RACTU-ND
C20
C47n
RS_624-2474
Q12
Q_MMBT3904
RS_545-0343
Q13
Q_MMBT3906
RS_545-0359
U7
OA_MAX975EUA
DK_MAX975EUA+-ND
R32
R5K6
RS_504-7802
R31
R26K7
RS_472-711
R30
R2K2
RS_505-0319
Q18
MMBF0201NLT1
TP6
TP7
TP
I_out
V_out
I_Solar
V_Solar
SOLAR_POS
SOLAR_NEG
3V3
PWM_IN
Disable
GND

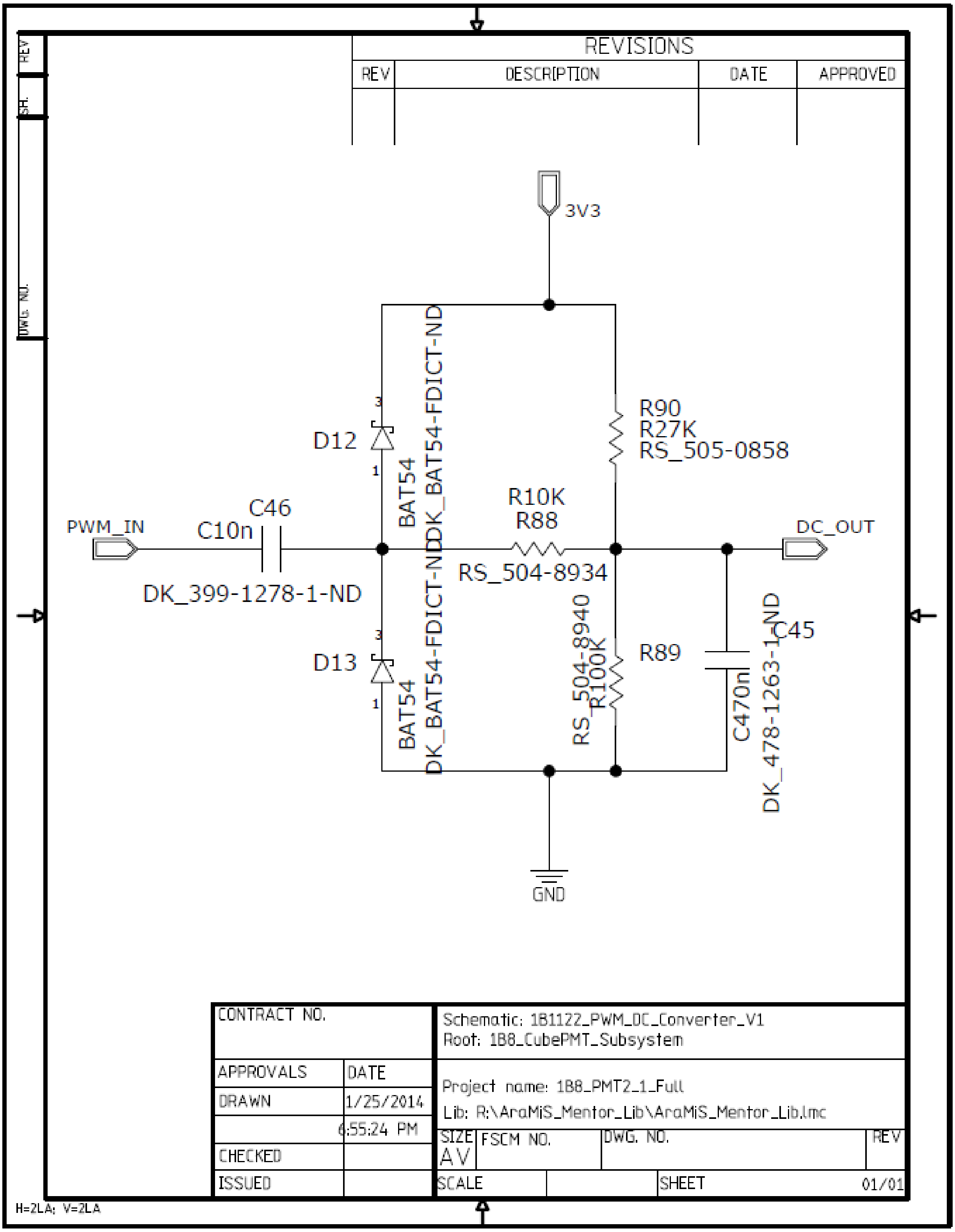
REVISIONS
REV
DESCRIPTION
DATE
APPROVED
3V3
D12
BAT54
DK_BAT54-FDICT-ND
R90
R27K
RS_505-0858
PWM_IN
C46
C10n
DK_399-1278-1-ND
R10K
R88
RS_504-8934
DC_OUT
D13
BAT54
DK_BAT54-FDICT-ND
RS_504-8940
R100K
R89
C45
C470n
DK_478-1263-1-ND
GND
CONTRACT NO.
APPROVALS
DATE
DRAWN
1/25/2014
6:55:24 PM
CHECKED
ISSUED
Schematic: 1B1122_PWM_DC_Converter_V1
Root: 1B8_CubePMT_Subsystem
Project name: 1B8_PMT2_1_Full
Lib: R:\AraMiS_Mentor_Lib\AraMiS_Mentor_Lib.lmc
SIZE
AV
FSCM NO.
DWG. NO.
REV
SCALE
SHEET
01/01
H=2LA; V=2LA
REV
SH.
DWG. NO.

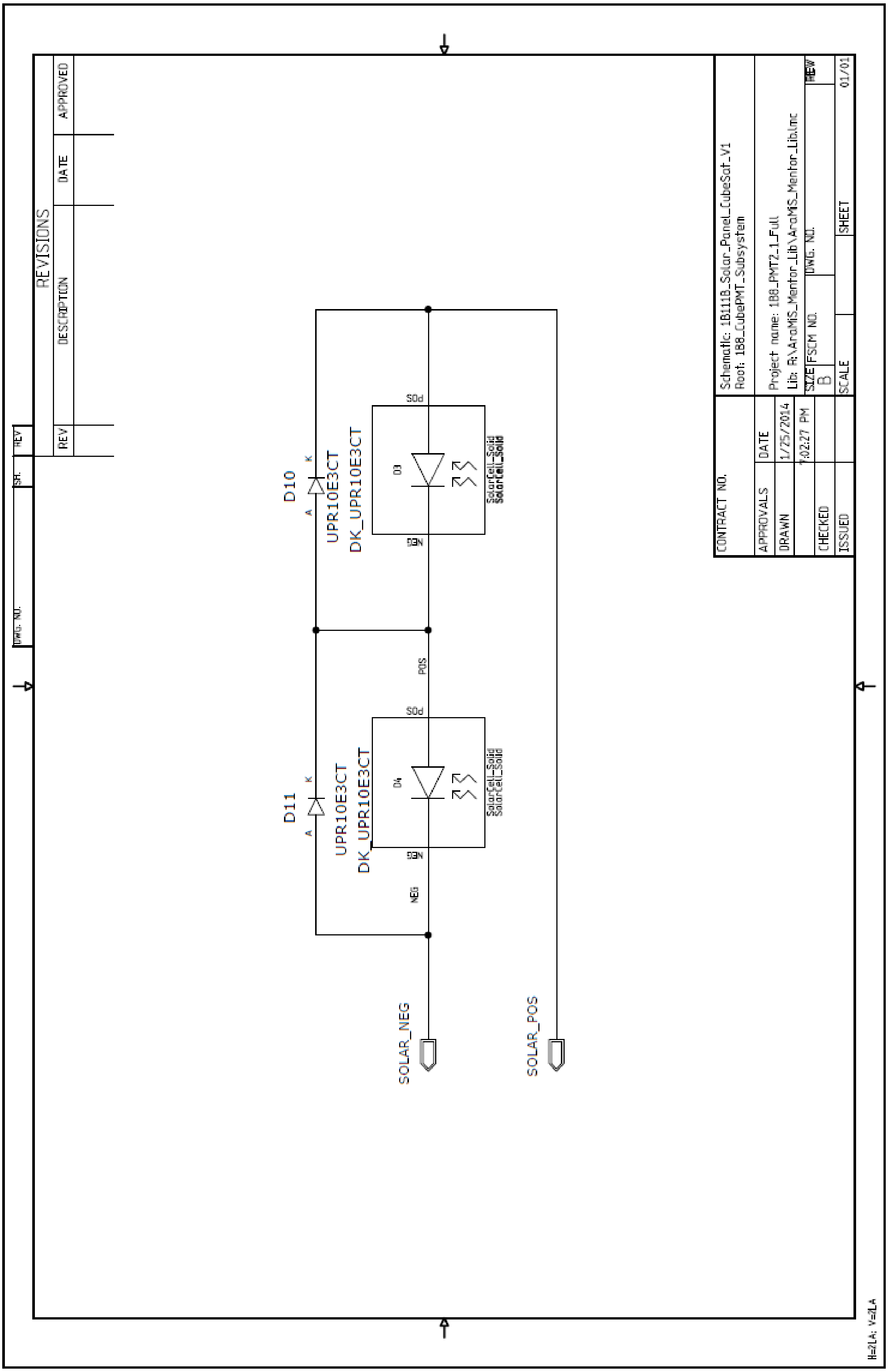
REVISIONS
REV
DESCRIPTION
DATE
APPROVED
D10
UPR10E3CT
DK_UPR10E3CT
D11
UPR10E3CT
DK_UPR10E3CT
D3
D4
SolarCell_Solid
POS
NEG
SOLAR_NEG
SOLAR_POS
CONTRACT NO.
APPROVALS
DATE
DRAWN
1/25/2014
CHECKED
ISSUED
Schematic: 1B111B_Solar_Panel_CubeSat_V1
Root: 1B8_CubePMT_Subsystem
Project name: 1B8_PMT2_1_Full
Lib: R:\AraMiS_Mentor_Lib\AraMiS_Mentor_Lib.lmc
SIZE
B
FSCM NO.
DWG. NO.
REV
SCALE
SHEET
01/01
H=2LA; V=2LA

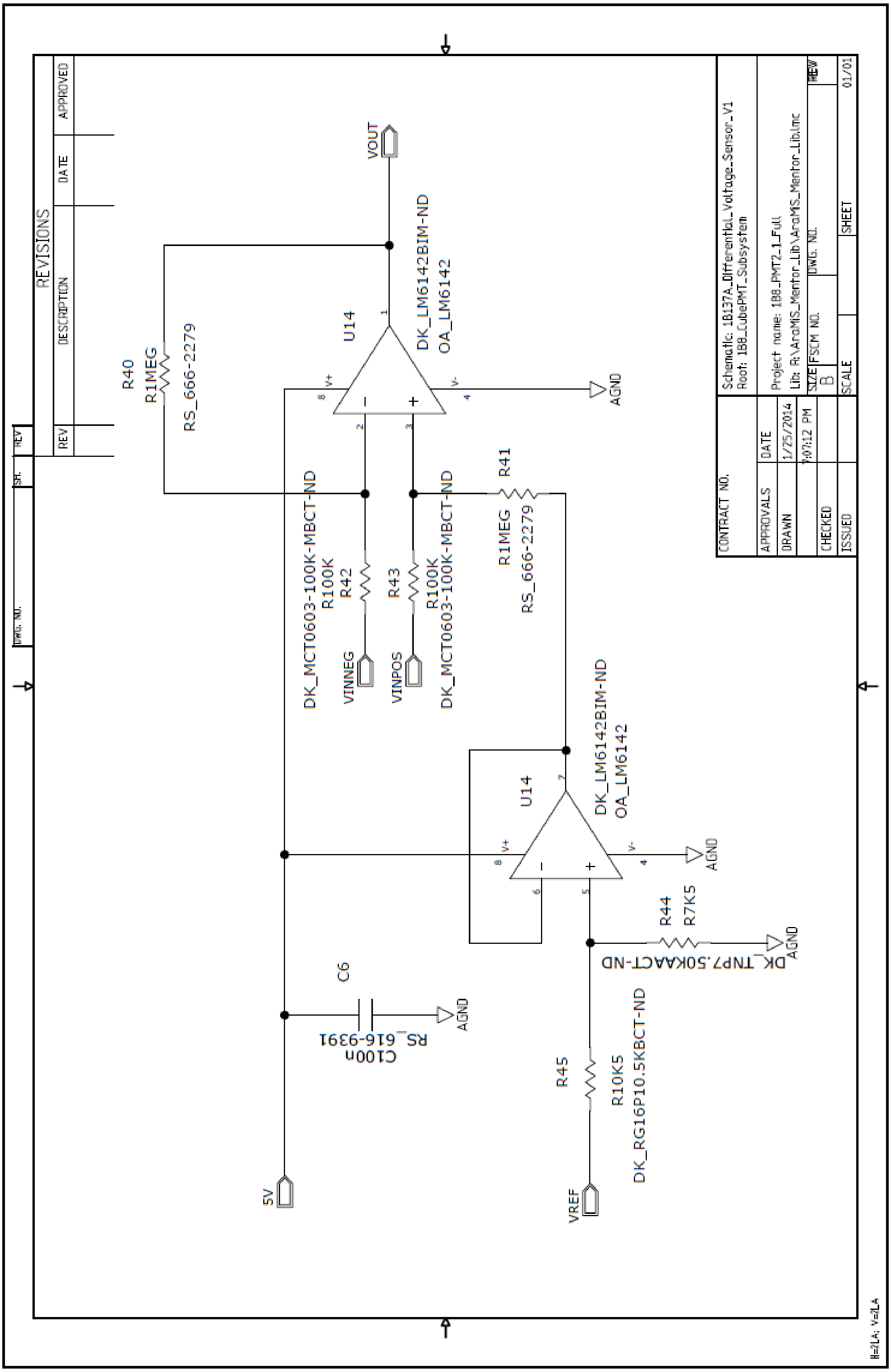
REVISIONS
REV
DESCRIPTION
DATE
APPROVED
DWG. NO.
SH.
REV
VOUT
R40
R1MEG
RS_666-2279
U14
DK_LM6142BIM-ND
OA_LM6142
AGND
R41
R1MEG
RS_666-2279
R42
R100K
DK_MCT0603-100K-MBCT-ND
R43
R100K
DK_MCT0603-100K-MBCT-ND
VINNEG
VINPOS
U14
DK_LM6142BIM-ND
OA_LM6142
AGND
R44
R7K5
DK_TNP7.50KAACT-ND
AGND
C6
C100n
RS_616-9391
AGND
R45
R10K5
DK_RG16P10.5KBCT-ND
5V
VREF
CONTRACT NO.
APPROVALS
DATE
DRAWN
1/25/2014
CHECKED
ISSUED
Schematic: 1B137A_Differential_Voltage_Sensor_V1
Root: 1B8_CubePMT_Subsystem
Project name: 1B8_PMT2.1_Full
SIZE
B
FSCM NO.
DWG. NO.
REV
SCALE
SHEET
01/01
H=2LA; V=2LA

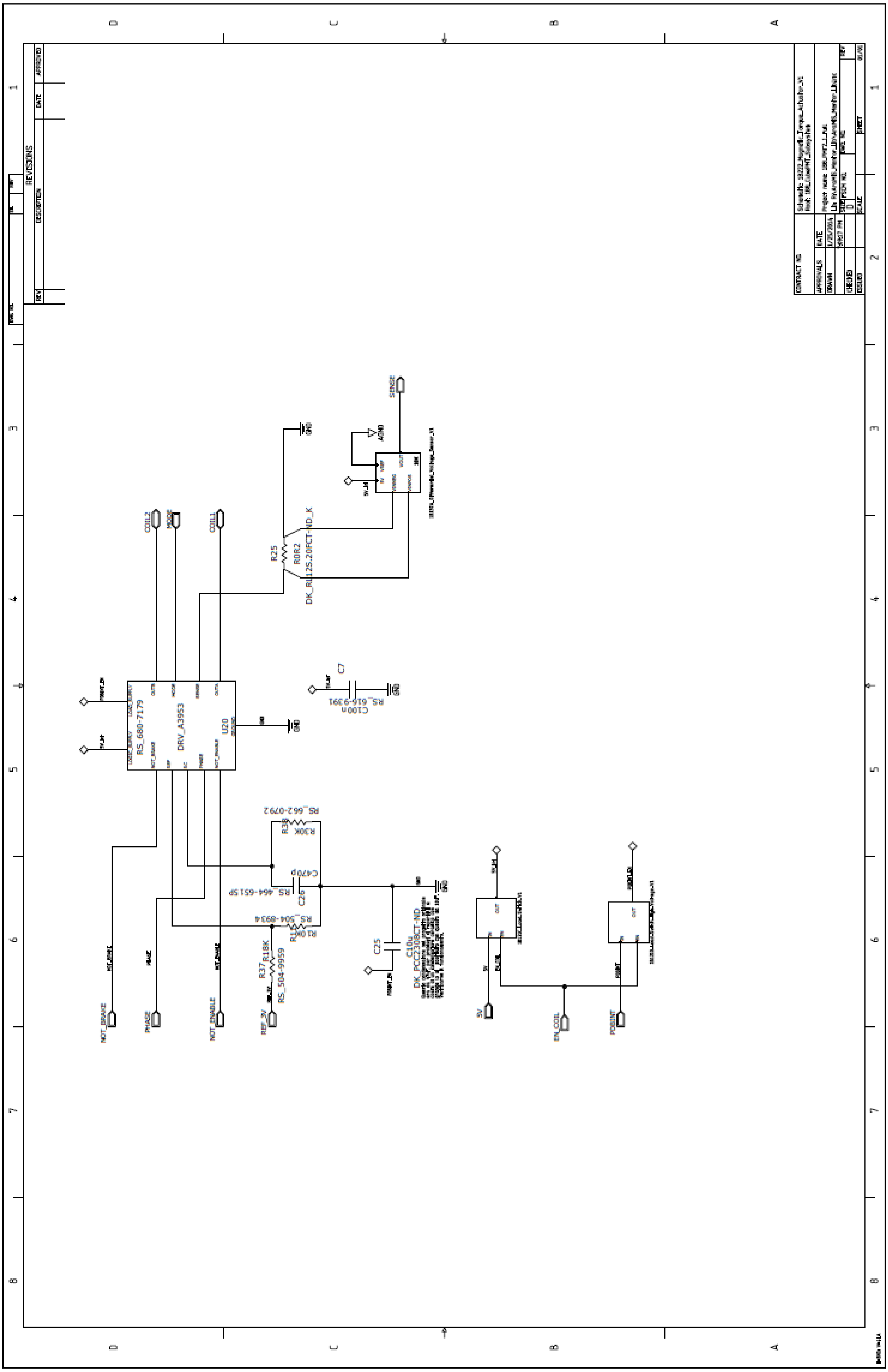
REVISIONS
DRV_A3953
U20
RS_680-7179
COIL2
MODE
COIL1
R25
SENSE
AGND
GND
C7
C100n
RS_616-9391
C26
C470p
R30K
RS_662-0792
C25
C10u
R37
R18K
RS_504-9959
NOT_BRAKE
PHASE
NOT_ENABLE
REF_3V
5V
EN_COIL

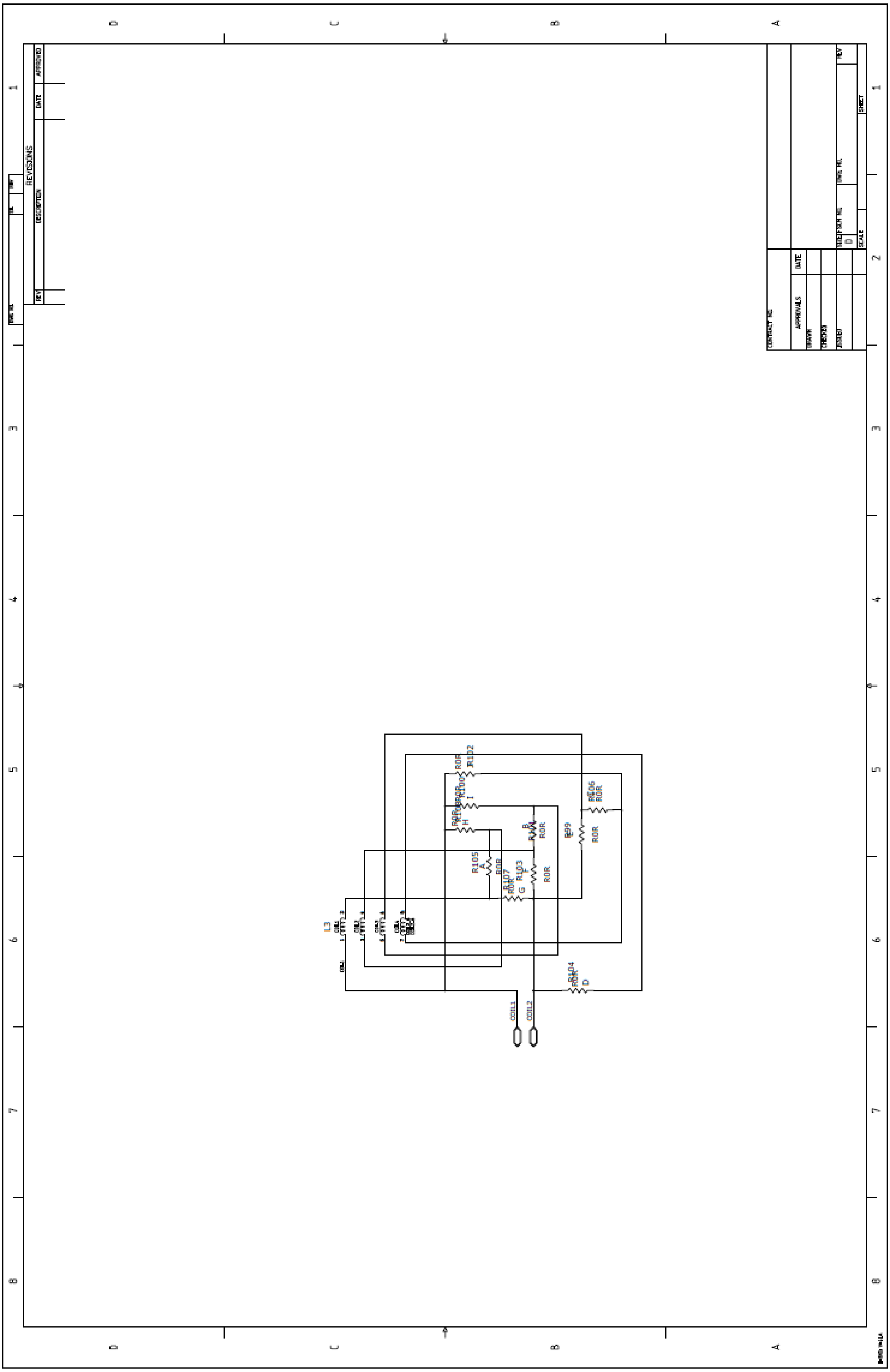
REVISIONS
R102
R105
R103
R107
R104
R99
L3
COIL1
COIL2

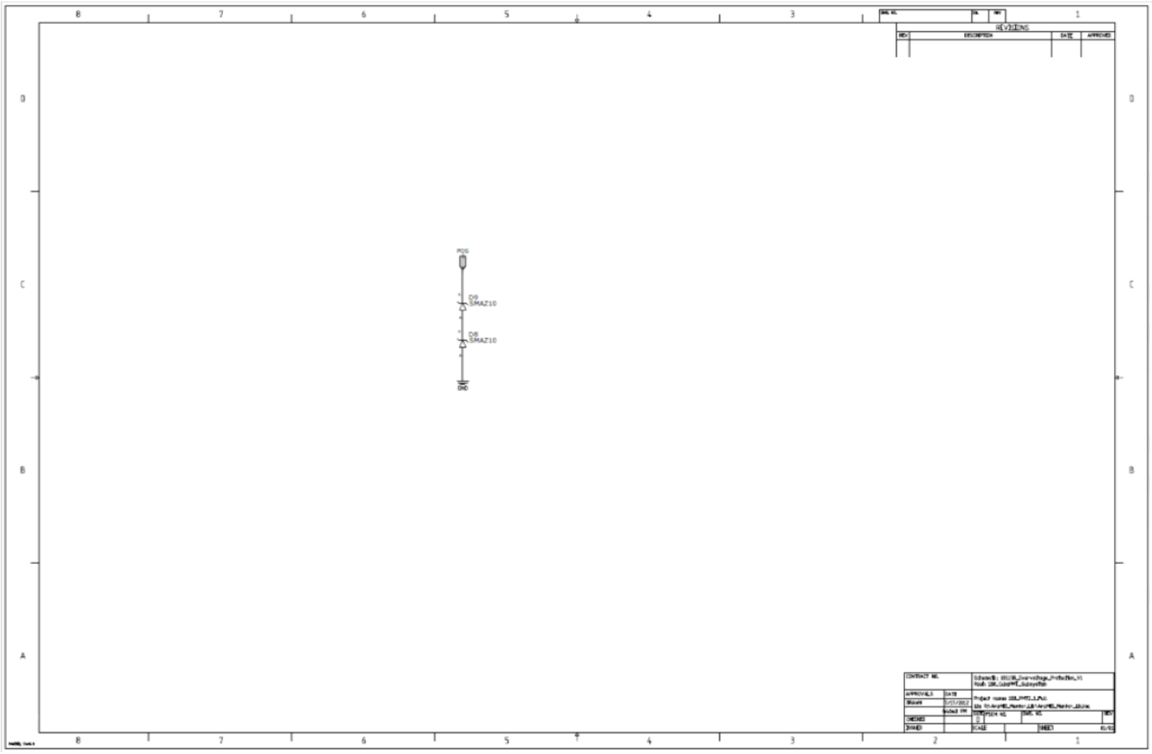
REVISIONS
POS
D9
SMAZ10
D8
SMAZ10
GND

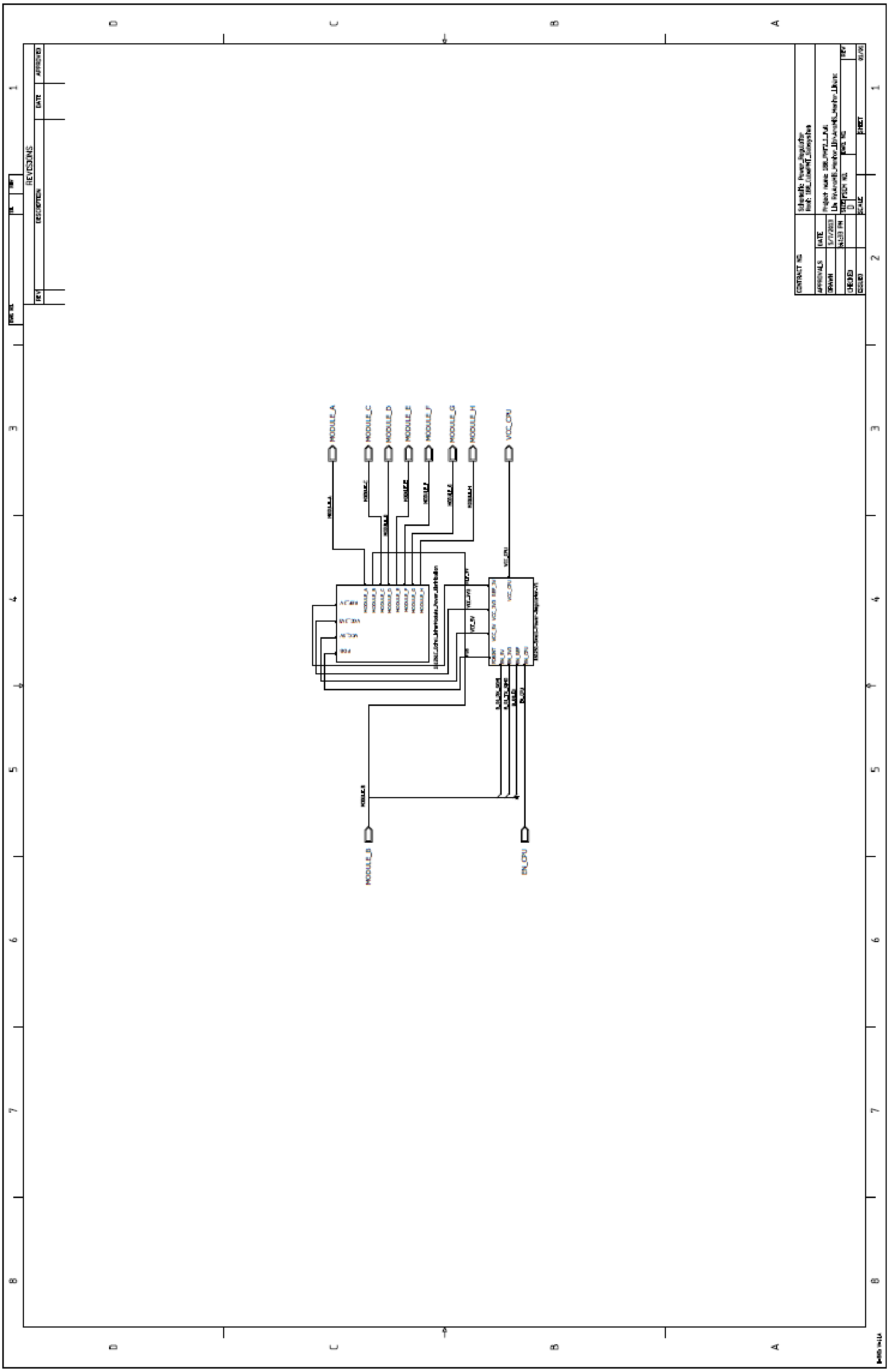
REVISIONS
MODULE_A
MODULE_C
MODULE_D
MODULE_E
MODULE_F
MODULE_G
MODULE_H
VCC_CPU
MODULE_B
EN_CPU

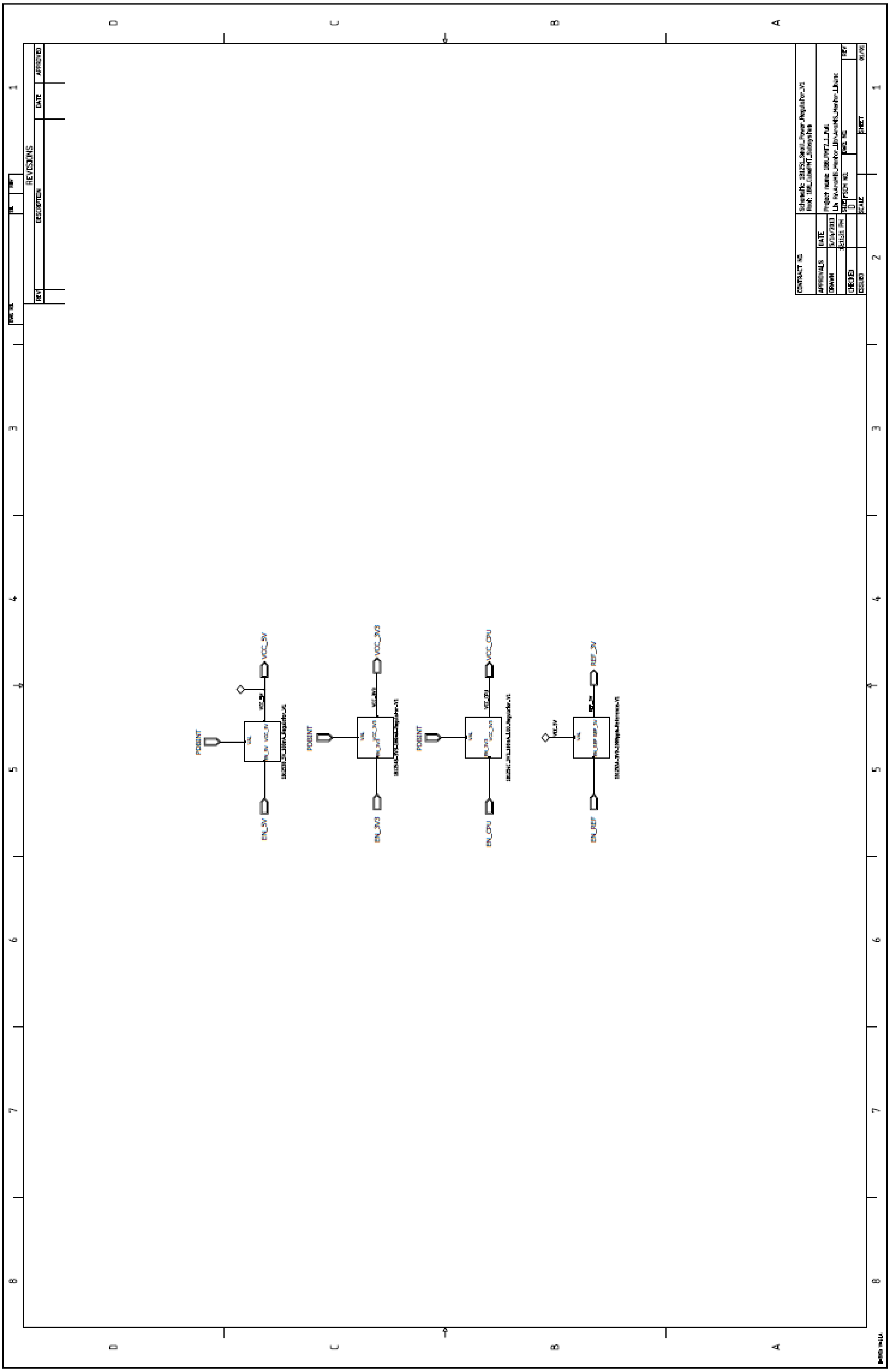

Appendix B

1B8_CubePMT Subsystems Testing Code

Testing Code: 1B235 Simple Sun Sensor

```
#include "io430.h"
int main( void )
{
  volatile unsigned int i;
  // Stop watchdog timer to prevent time out reset
  WDTCTL = WDTPW + WDTHOLD;



  P5SEL |= BIT1;
  P5DIR &= ~BIT1;
  UCSCTL4 |= SELM_5;
  ADC12CTL1 = ADC12SSEL_2;
  ADC12CTL0 = ADC12ON + ADC12SHT02 + ADC12REFON + ADC12REF2_5V;
                                    // Turn on ADC12, Sampling time-
                                    // On Reference Generator and set to
                                    // 2.5V
  ADC12CTL0 &= ~ADC12ENC;
  ADC12CTL2 |= 0x0020;
  //ADC12MCTL4 = ADC12SREF0*1 | ADC12INCH0*4 | ADC12INCH0*5;
  ADC12MCTL0 |= 0x19;
  ADC12CTL1 = ADC12SHP;                     // Use sampling timer
  /*ADC12MCTL0 = ADC12SREF_1;     */          // Vr+=Vref+ and Vr-=AVss

  for ( i=0; i<0x0F30; i++);                // Delay for reference start-up

  ADC12CTL0 |= ADC12ENC;                    // Enable conversions

  while (1)
  {
    ADC12CTL0 |= ADC12SC;                   // Start conversion
    while (!(ADC12IFG & BIT0));
   // __no_operation();                     // SET BREAKPOINT HERE
    for ( i=0; i<0x0F30; i++);              // Delay for reference start-up
  }
}
```

Testing Code: 1B131B Voltage Sensor

```
#include "io430.h"
int main( void )
{
  volatile unsigned int i;
  // Stop watchdog timer to prevent time out reset
  WDTCTL = WDTPW + WDTHOLD;

  P6SEL |= BIT7;
  P6DIR &= ~BIT7;
  UCSCTL4 |= SELM_5;
  ADC12CTL1 = ADC12SSEL_2;
  ADC12CTL0 = ADC12ON + ADC12SHT02 + ADC12REFON + ADC12REF2_5V;
                                          // Turn on ADC12, Sampling time-
                                          // On Reference Generator and set to
                                          // 2.5V
  ADC12CTL0 &= ~ADC12ENC;
  ADC12CTL2 |= 0x0020;

  ADC12MCTL0 |= 0x17;                     // Analog Channel No
  ADC12CTL1 = ADC12SHP;                   // Use sampling timer
  /*ADC12MCTL0 = ADC12SREF_1;    */       // Vr+=Vref+ and Vr-=AVss

  for ( i=0; i<0x0F30; i++);              // Delay for reference start-up

  ADC12CTL0 |= ADC12ENC;                  // Enable conversions

  while (1)
  {
    ADC12CTL0 |= ADC12SC;                 // Start conversion
    while (!(ADC12IFG & BIT0));
   // __no_operation();                   // SET BREAKPOINT HERE
    for ( i=0; i<0x0F30; i++);            // Delay for reference start-up
  }
}
```

Testing Code: 1B131C Voltage Sensor

```
#include "io430.h"

int main( void )
{
  volatile unsigned int i;
  // Stop watchdog timer to prevent time out reset
  WDTCTL = WDTPW + WDTHOLD;

  P6SEL |= BIT2;
  P6DIR &= ~BIT2;
  UCSCTL4 |= SELM_5;
  ADC12CTL1 = ADC12SSEL_2;
  ADC12CTL0 = ADC12ON + ADC12SHT02 + ADC12REFON + ADC12REF2_5V;
                                    // Turn on ADC12, Sampling time-
                                    // On Reference Generator and set to
                                    // 2.5V
  ADC12CTL0 &= ~ADC12ENC;
  ADC12CTL2 |= 0x0020;
  //ADC12MCTL4 = ADC12SREF0*1 | ADC12INCH0*4 | ADC12INCH0*5;
  ADC12MCTL0 |= 0x12;
  ADC12CTL1 = ADC12SHP;                   // Use sampling timer
  /*ADC12MCTL0 = ADC12SREF_1;     */           // Vr+=Vref+ and Vr-=AVss

  for ( i=0; i<0x0F30; i++);                 // Delay for reference start-up

  ADC12CTL0 |= ADC12ENC;                   // Enable conversions

  while (1)
  {
    ADC12CTL0 |= ADC12SC;                   // Start conversion
    while (!(ADC12IFG & BIT0));
   // __no_operation();                     // SET BREAKPOINT HERE
    for ( i=0; i<0x0F30; i++);                 // Delay for reference start-up
  }
}
```

Testing Code: 1B132A Current Sensor

```
#include "io430.h"
int main( void )
{
  volatile unsigned int i;
  // Stop watchdog timer to prevent time out reset
  WDTCTL = WDTPW + WDTHOLD;
   P5SEL |= BIT0;
  P5DIR &= ~BIT0;

  UCSCTL4 |= SELM_5;
  ADC12CTL1 = ADC12SSEL_2;
  ADC12CTL0 = ADC12ON + ADC12SHT02 + ADC12REFON + ADC12REF2_5V;
                                          // Turn on ADC12, Sampling time-
                                          // On Reference Generator and set to
                                          // 2.5V
  ADC12CTL0 &= ~ADC12ENC;
  ADC12CTL2 |= 0x0020;
  //ADC12MCTL4 = ADC12SREF0*1 | ADC12INCH0*4 | ADC12INCH0*5;
  ADC12MCTL0 |= 0x18;
  ADC12CTL1 = ADC12SHP;                   // Use sampling timer
  /*ADC12MCTL0 = ADC12SREF_1;     */           // Vr+=Vref+ and Vr-=AVss

  for ( i=0; i<0x0F30; i++);              // Delay for reference start-up

  ADC12CTL0 |= ADC12ENC;                  // Enable conversions

  while (1)
  {
    ADC12CTL0 |= ADC12SC;                 // Start conversion
    while (!(ADC12IFG & BIT0));
   // __no_operation();                   // SET BREAKPOINT HERE
    for ( i=0; i<0x0F30; i++);            // Delay for reference start-up
  }
}
```

Testing Code: 1B132D Current Sensor

```
#include "io430.h"

int main( void )
{
  volatile unsigned int i;
  // Stop watchdog timer to prevent time out reset
  WDTCTL = WDTPW + WDTHOLD;

  P6SEL |= BIT3;
  P6DIR &= ~BIT3;
  UCSCTL4 |= SELM_5;
  ADC12CTL1 = ADC12SSEL_2;
  ADC12CTL0 = ADC12ON + ADC12SHT02 + ADC12REFON + ADC12REF2_5V;
                                    // Turn on ADC12, Sampling time-
                                    // On Reference Generator and set to
                                    // 2.5V
  ADC12CTL0 &= ~ADC12ENC;
  ADC12CTL2 |= 0x0020;
  //ADC12MCTL4 = ADC12SREF0*1 | ADC12INCH0*4 | ADC12INCH0*5;
  ADC12MCTL0 |= 0x13;
  ADC12CTL1 = ADC12SHP;                   // Use sampling timer
  /*ADC12MCTL0 = ADC12SREF_1;     */            // Vr+=Vref+ and Vr-=AVss

  for ( i=0; i<0x0F30; i++);                 // Delay for reference start-up

  ADC12CTL0 |= ADC12ENC;                   // Enable conversions

  while (1)
  {
    ADC12CTL0 |= ADC12SC;                   // Start conversion
    while (!(ADC12IFG & BIT0));
   // __no_operation();                     // SET BREAKPOINT HERE
    for ( i=0; i<0x0F30; i++);                 // Delay for reference start-up
  }
}
```

Testing Code: 1B133A Temperature Sensor

```
#include "io430.h"

int main( void )
{
  volatile unsigned int i;
  // Stop watchdog timer to prevent time out reset
  WDTCTL = WDTPW + WDTHOLD;

  P7DIR |= BIT3;
  P7OUT |= BIT3;
  P1DIR |= BIT2;
  P1OUT |= BIT2;
  P7SEL |= BIT4;
  P7DIR &= ~BIT4;
  UCSCTL4 |= SELM_5;
  ADC12CTL1 = ADC12SSEL_2;
  ADC12CTL0 = ADC12ON + ADC12SHT02 + ADC12REFON + ADC12REF2_5V;
                                    // Turn on ADC12, Sampling time-
                                    // On Reference Generator and set to
                                    // 2.5V
  ADC12CTL0 &= ~ADC12ENC;
  ADC12CTL2 |= 0x0020;
  //ADC12MCTL4 = ADC12SREF0*1 | ADC12INCH0*4 | ADC12INCH0*5;
  ADC12MCTL0 |= 0x1C;
  ADC12CTL1 = ADC12SHP;                     // Use sampling timer
  /*ADC12MCTL0 = ADC12SREF_1;     */        // Vr+=Vref+ and Vr-=AVss

  for ( i=0; i<0x0F30; i++);                // Delay for reference start-up

  ADC12CTL0 |= ADC12ENC;                    // Enable conversions

  while (1)
  {
    ADC12CTL0 |= ADC12SC;                   // Start conversion
```

```
   while (!(ADC12IFG & BIT0));
  // __no_operation();                      // SET BREAKPOINT HERE
   for ( i=0; i<0x0F30; i++);                  // Delay for reference start-up
  }
}
```

Testing Code: 1B221 Magnetometer

```
#include "io430.h"

int main( void )
{
  volatile unsigned int i;
  // Stop watchdog timer to prevent time out reset
  WDTCTL = WDTPW + WDTHOLD;

   P1DIR |= BIT5;           // C_D9_EN_PWM-2 (Magnetometer enable)
  P1OUT |= BIT5;

  P1DIR |= BIT2;           // B_D8_ID (REF-3V_enable)
  P1OUT |= BIT2;

  P7DIR |= BIT3;           // B_D0_Rx_SOMI (5V_enable)
  P7OUT |= BIT3;

  P6SEL |= BIT5;           //MAGN_X
  P6DIR &= ~BIT5;

 //P6SEL |= BIT4;           //MAGN_y
 //P6DIR &= ~BIT4;

  ADC12CTL0 = ADC12ON + ADC12SHT02 + ADC12REFON + ADC12REF2_5V;
                                  // Turn on ADC12, Sampling time
                                  // On Reference Generator and set to
                                  // 2.5V
  ADC12CTL0 &= ~ADC12ENC;
```

```
  ADC12CTL2 |= 0x0020;
  //ADC12MCTL4 = ADC12SREF0*1 | ADC12INCH0*4 | ADC12INCH0*5;
  ADC12MCTL0 |= 0x15;
  // ADC12MCTL2 |= 0x14;
  ADC12CTL1 = ADC12SHP;                     // Use sampling timer
  /*ADC12MCTL0 = ADC12SREF_1;     */            // Vr+=Vref+ and Vr-=AVss

  for ( i=0; i<0x0F30; i++);                 // Delay for reference start-up

  ADC12CTL0 |= ADC12ENC;                    // Enable conversions

  while (1)
  {
    ADC12CTL0 |= ADC12SC;                   // Start conversion
    while (!(ADC12IFG & BIT0));
   // __no_operation();                     // SET BREAKPOINT HERE
    for ( i=0; i<0x0F30; i++);               // Delay for reference start-up
  }
}
```

Bibliography

[1] Riki Munakata, CubeSat Design Specifications, Rev.12, California State Polytechnic Univerity, 2009.

[2] Passerone C., Tranchero M., Speretta S., Reyneri L., Sansoe C., Del Corso D., Design Solutions for a University Nano-satellite, Aerospace Conference, 2008 IEEE , vol. no. pp.1,13, 1-8 March 2008

[3] Stefano Speretta, Leonardo M. Reyneri, Claudio Sanso´e,Maurizio Tranchero, Claudio Passerone, Dante Del Corso, Modular Architecture for Satellites, 58th IAC , Hyderabad, India, 24 - 28 September 2007.

[4] Satellite Classification. http://centaur.sstl.co.uk/SSHP/sshp_classify.html

[5] Jake A. Schaffner. The electronic system design, analysis, integration and constriction of the cal poly state university cp1 cubesat. Technical report, Cal Poly State University, 2002.

[6] Stefano Speretta, Project solutions for low cost space missions, PhD thesis, March 2010

[7] Haider Ali, Telecommunication Subsystem Design for Small Satellites, PhD thesis, Politecnico di Torino, Italy, February 2014.

[8] Muhammad Rizwan Mughal, Onboard Communication Systems for Low Cost Small Satellites, PhD thesis, Politecnico di Torino, Italy, February 2014.

[9] M. Muhammad Rizwan Mughal; Anwar Ali; Haider Ali; L. Reyneri. A smart honeycomb tile for small satellites. pages 1–7. IEEE Aerospace conference,2014.

[10] Anwar Ali, M. Rizwan Mughal, Haider Ali, Leonardo M. Reyneri, Innovative power management, attitude determination and control tile for CubeSat standard NanoSatellites, Acta Astronautica,Volume 96, March–April 2014, Pages 116–127

[11] UML tutorial: http://www.tutorialspoint.com/uml/index.htm

[12] Mughal, M.R.; Reyneri, L.M.; Ali, A., "UML based design methodology for serial data handling system of NanoSatellites," Satellite Telecommunications (ESTEL), 2012 IEEE First AESS European Conference on , vol., no., pp.1,6, 2-5 Oct. 2012 doi: 10.1109/ESTEL.2012.6400194

[13] T. Instruments, MSP430 User's Guide, Texas Instruments, Tech. Rep.,SLAU208H, Dec 2010.

[14] Anwar Ali, Leonardo M. Reyneri, Juan Carlos de los Rios, Haider Ali, Innovative Power Management Tile for NanoSatellites , 63rd International Autronautical Congress, Naples Italy, 1-5 Oct. 2012.

[15] Anwar Ali, M. Rizwan Mughal, Haider Ali, Leonardo M. Reyneri, Innovative Electric Power Supply System for NanoSatellites, 64rd International Astronautical Congress, Beijing, China.

[16] Elliott Ivan Gurrola, Sourabh Dongaonkar, "SPICE Simulation of Thin-Film Solar Cell Modules" Network for Computational Nanotechnology, NCN.

[17] Jaycar Electronics Reference Data Sheet, "dc-dc converters: a primer" 2001

[18] Richard A. Cullen, What is Maximum Power Point Tracking (MPPT) and How Does it Work?, Blue Sky Energy

[19] A. Dolara, R. Faranda, S. Leva, Energy Comparison of Seven MPPT Techniques for PV Systems, J. Electromagnetic Analysis & Applications, 2009,3: 152-162.

[20] Daniel M. Erb, Samir A. Rawashdeh, James E. Lumpp, Jr., Evaluation of Solar Array Peak Power Tracking Technologies for CubeSats, paper SSC11-VI-11, 25 Annual AIAA/USU Conference on Small Satellites.

[21] G. Bonin, D. Sinclair, R. E. Zee, Peak Power Tracking on a NanoSatellite Scale: The Design and Implementation of Digital Power Electronics on the SFL Generic NanoSatellite Bus, paper SSC09-XI-9, 23rd Annual AIAA/USU Conference on Small Satellites.

[22] F.Santoni, F.Piergentili, Design and test of a maximum power point tracking system for UNISAT-3 microsatellite, paper IAC-04-R.2.01, 55th International Astronautical Congress (IAC), Vancouver, Canada, 4-8 October 2004.

[23] Anwar Ali, Leonardo M. Reyneri, Haider Ali and M. Rizwan Mughal, Components selection for a simple boost converter on the basis of power loss analysis, 63rd International Autronautical Congress, Naples Italy, 1-5 Oct. 2012.

[24] "An alternative approach to higher-power boost converter" Power Designer 127.

[25] Eric Anderson, Chris Dohan, "Solar panel peak power tracking system" Worcester Polytechnic Institute, March 12 2003.

[26] Wilson Allan Thomas Eberle, "MOSFET current source gate drivers, switching loss modeling and frequency dithering control for MHz switching frequency dc-dc converters" PhD thesis, Queen's University Kingston, Ontario, Canada February, 2008.

[27] Application Note, "ESR Losses in Ceramic Capacitors" by Richard Fiore, Director of RF application engineering American Technical Ceramics.

[28] Nelson Garcia, "Determining Inductor Power Losses" Coilcraft, Document 486 Revised 12/20/05.

[29] "SMPS components and their effects on system design" web seminar 2006 Microchip technology incorporated.

[30] Jaycar Electronics Reference Data Sheet, "dc-dc converters: a primer" 2001.

[31] Max975 datasheet, URL, http://datasheet.eeworld.com.cn/pdf/MAXIM/14380_MAX975-MAX977.pdf

[32] Adding Extra Hysteresis to Comparators, URL, http://www.ece.rochester.edu/courses/ECE216/Adding%20Extra%20Hysteresis%20to%20Comparators.pdf

[33] NiCd rechargible batteries, URL, "http://media.digikey.com/pdf/Data%20Sheets/Sanyo%20Energy/KR-900AAEC.pdf".

[34] Chester Simpson, Linear and Switching Voltage Regulator Fundamentals, National Semiconductor.

[35] Linear regulator, 3V, LM4128, URL, http://media.digikey.com/pdf/Data%20Sheets/National%20Semiconductor%20PDFs/LM4128.pdf

[36] Linear regulator, 3.3V, LT1761, URL, http://cds.linear.com/docs/en/datasheet/1761sff.pdf

[37] Switching regulator, 3.3V, LTC3631, URL, http://cds.linear.com/docs/en/datasheet/3631fe.pdf

[38] INA138 datasheet, High-Side Measurement Current Shunt Monitor, Burr Brown Products from Texas Instruments

[39] Marco Schmidt, Karthik Ravandoor, Oliver Kurz, Stephan Busch, Klaus Schilling, Attitude Determination for the Pico-Satellite UWE-2, Proceedings of the 17th World Congress. The International Federation of Automatic Control Seoul, Korea, July 6-11, 2008.

[40] Sun sensor, CPC1822 datasheet, URL,

http://www.clare.com/home/pdfs.nsf/0/4EC381FBC6760F3585256E6900649D38/$file/CPC1822.pdf
[41] Ceren Kaplan, LEO satellites: Attitude Determination and Control Components ; some linear attitude control techniques, A thesis submitted to the Graduate School of Natural and Applied Sciences of Middle East Technical University.
[42] Marina Díaz-Michelena, Small Magnetic Sensors for Space Applications, Sensors 2009, 9, 2271-2288; doi:10.3390/s90402271
[43] F. Santoni, F. Piergentili, "UniSat-3 Attitude Determination using Solar Panel and Magnetometer Data," Proceedings of the 56th IAC 2005, Fukuoda, Japan, Oct. 17-21, 2005, IAC-05-C1.2.06.
[44] HMC1002/1021/1022 datasheet, 1- and 2-Axis Magnetic Sensors, Honeywell, URL, http://www51.honeywell.com/aero/common/documents/myaerospacecatalog-documents/Missiles-Munitions/HMC_1001-1002-1021-1022_Data_Sheet.pdf
[45] SPENVIS, URL, http://www.spenvis.oma.be
[46] AD623 datasheet, Single-Supply, Rail-to-Rail, Low Cost Instrumentation Amplifier, Analog Devices, URL, http://www.oup.com/us/pdf/microcircuits/students/amps/ad623-analog.pdf
[47] ADIS16080 datasheet, Yaw Rate Gyroscope with SPI, Analog Devices, URL, http://www.bdtic.com/DataSheet/ADI/ADIS16080.pdf
[48] Fredrik Alvenes, Satellite Attitude Control System, Department of Engineering Cybernetics, 2012
[49] Robert Stengel, Spacecraft Sensors and Actuators Space System Design, MAE 342, Princeton University
[50] A3953 datasheet, Full-Bridge PWM Motor Driver, Allegro, URL, http://pdf.datasheetcatalog.com/datasheet/allegromicrosystems/3953.pdf
[51] U.A. Bakshi & M.V. Bakshi, “Electromechanical Energy Conversion & D.C Machines”. Tecnical Publications Pune, First Edition 2009 .
[52] SPENVIS. http://www.spenvis.oma.be
[53] Ali, A.; Reyneri, L.; de los Rios, J.C.; Ali, H.; Mughal, M.R., "Reconfigurable magnetorquer for the CubePMT module of CubeSat satellites," Multitopic Conference (INMIC), 2012 15th International , vol., no., pp.178,183, 13-15 Dec. 2012 doi: 10.1109/INMIC.2012.6511478
[54] Zhou Chen, Integrated Electrical and Thermal Modeling, Analysis and Design for IPEM, Faculty of the Virginia Polytechnic Institute and State University, February 6, 2004.
[55] Robert Siegel, Thermal Radiation Heat Transfer, Taylor & Francis, 4th edition, 2002.
[56] Mark Wellons, The Stefan-Boltzmann Law, Physics Department, The College of Wooster, Wooster, Ohio 44691, USA, May 9, 2007.
[57] What is emissivity and why is it important? http://www.npl.co.uk/reference/faqs/what-is-emissivity-and-why-is-it-important-(faq-thermal)
[58] Table of emissivity of various surfaces, Mikron Vertretung Schweiz
[59] Table of total emissivity http://www.monarchserver.com/TableofEmissivity.pdf
[60] CubeSat Magnetic Rod, online: http://www.cubesatshop.com/index.php?page=shop.product_details&flypage=flypage.tpl&product_id=75&category_id=7&keyword=magnetic+rod&option=com_virtuemart&Itemid=69

[61] NanoPower Solar P100-A/B, online: http://www.cubesatshop.com/index.php?page=shop.product_details&flypage=flypage.tpl&product_id=70&category_id=17&keyword=NanoPower+Solar+100&option=com_virtuemart&Itemid=79

[62] Fourier's law of heat conduction, URL, http://www.me.umn.edu/courses/old_me_course_pages/me3333/essays/essay%203.pdf

[63] Ohm's law in thermal domain, URL, ftp://ftp.dei.polimi.it/outgoing/Massimo.Ghioni/Power%20Electronics%20/Thermal/Advanced%20Power%20Dissipation%20and%20Dynamic%20Thermal%20Analysis.pdf

[64] Diego A. Melani Barreiro, A Small Satellite Thermal Control and Heat Shield Analysis, Department of Mechanical engineering, MIT, 2006.

[65] Kristina Hogstrom, State-of-the-Art Thermal Analysis Methods and Validation for Small Spacecraft, Literacy Servey, 2013.

[66] C1C Richard Lyon, LtCol Jerry Sellers, Craig Underwood, Small Satellite Thermal Modeling and Design at USAFA: FalconSat-2 Applications.

[67] Ross A. Henderson, Thermal Control of Spacecraft, Chapter 12, European Space Agency